FIRST MEASUREMENT OF THE LONGITUDINAL AND TRANSVERSE CROSS SECTIONS IN $^1H(e, e'K^+)\Lambda$

A Dissertation

by

GABRIEL NICULESCU

Submitted to the Graduate College of

Hampton University

in partial fulfillment of the requirements

for the degree of

DOCTOR OF PHILOSOPHY

December 1998

FIRST MEASUREMENT OF THE LONGITUDINAL AND TRANSVERSE CROSS SECTIONS IN $^1H(e, e'K^+)\Lambda$

A Dissertation

by

GABRIEL NICULESCU

This dissertation submitted by Gabriel Niculescu in partial fullfillment of requirements for the degree of Doctor of Phylosophy in Physics at Hampton University, Hampton, Virginia, is hereby approved by the committee under whom the work has been done.

Oliver K. Baker, Ph. D., Chair

Warren W. Buck, Ph. D., Member

Donald F. Geesaman, Ph. D., Member

Benjamin Zeidman, Ph. D., Member

Calvin W. Lowe, Sc. D.
Vice President for Research and
Dean of the Graduate College

Date

December 1998

Major Subject: Physics

ABSTRACT

First Measurement of the Longitudinal and Transverse cross sections in $^1H(e, e'K^+)\Lambda$.

(December 1998)

Chair of Advisory Committee: Dr. 0. K. Baker

Jefferson Laboratory experiment **E93-018** studied kaon electroproduction off hydrogen. The cross-section for the $e + p \rightarrow e' + K^+ + \Lambda$ reaction was studied at momentum-transfer values, Q^2, between 0.52 and 2.00 $(GeV/c)^2$. The longitudinal (σ_L) and transverse (σ_T) parts of the cross-section were separated using the Rosenbluth technique at Q^2 of 0.52, 0.75, 1.00, and 2.00 (GeV/c)^2. Extensive comparisons of these data with existing theoretical model calculations on strangeness leptoproduction are provided both in terms of the separated response function and the σ_L/σ_T ratio.

The **t** dependence of the cross-section was also investigated for Q^2 of 0.75, 1.00, and 1.25 (GeV/c)^2. Preliminary results, leading to an extraction of the kaon form factor, are shown here.

To my late father, Niculae Niculescu

ACKNOWLEDGMENTS

I would like to use this space to acknowledge those that supported/influenced my development both as a physicist and as a person.

The list must start with my parents who encouraged and supported me and my studies since my very first day in school. My younger brother, Ovidiu, was also supportive of my efforts. I do hope I managed to meet their expectations and made them proud.

Throughout the years I was fortunate to have many wonderful teachers that influenced me a great deal. Special thanks go to Mrs. Ioniţă, my grade school teacher, who guided my first shaky steps on the never ending path of knowledge, and to Mr. Tunaru, my high–school physics teacher, who helped spark my interest in physics.

From the many excellent physicists that instructed and provided guidance while at Bucharest University I would like to specially acknowledge A. Meşter, A. Hristev, T. A. Angelescu, O. Sima, and Al. Mihul. While doing research for my thesis diploma I had the chance to go for an extended work stage at the Joint Institute for Nuclear Research (JINR), in the (now defunct) USSR. From the people who welcomed and guided my work within the Laboratory of Nuclear Problems I would like to acknowledge Y. A. Budagov, the late A. A. Kuritchin, and G. Velev.

Special thanks go to Mel Month from Fermilab who provided me with the opportunity to attend the Harvard classes of the United States Particle Accelerator School in 1990 and to Warren Buck who was instrumental in recruiting my wife and I to join Hampton University.

Upon joining Hampton University in 1992 I had the opportunity to be taught by and interact practically with all the members of the NuHep group, all of them accomplished physicists whose skills and knowledge are only equaled by their kindness and willingness to work with and help their students. Therefore my thanks go to Warren Buck, Keith Baker, Khin Maung Maung, Liquang Tang, Jose Goity, and Cynthia Keppel for making my stay in Hampton an enjoyable as well as extremely instructive period. Special thanks also go to Vevelyn Nazario and to Carlane Pittman for their relentless efforts to help students deal with countless nagging bureaucratic issues, as well as to Martha Jalim and her staff in the International Student's Office for all her help. Off my fellow Hampton graduate student I had the pleasure to interact with I would like to acknowledge Steve Avery, Jinseok Cha, Mark Harvey, Wendy Hinton, Alicia Johnson, Win Naing, Yong Nguyen, and Ioana Niculescu. My hat goes off to the Hampton postdoctoral fellows, the work of which is frequently quoted in this dissertation: Paul Gueye, Ketevi Assamagan, and Robert Williams.

Being a part of the Hall C construction and commissioning effort almost from the beginning I must acknowledge the efforts of the Hall C staff scientists and postdocs, Roger Carlini, Joe Mitchell, David Mack, Keith Baker, Rolf Ent, Chen Yan, Steve Wood, and Jim Dunne. The efforts and dedication of the Hall C engineers and technicians, Joe Beaufait, Paul Brandza, Mike Fowler, Steve Hickson, Paul Hood, Steve Lassiter, led by the chief engineer Bill Vulcan, are also acknowledged. Among the physicists from various US and foreign institutions whose contributions were most notable during the building and commissioning of the Hall C spectrometers I would like to acknowledge the efforts of Don Geesaman, Roy Holt, Hal Jackson, David Potterveld, Kevin Bailey, Hamlet Mkrtchyan, Ben Zeidman, Mike Miller, Hayan Gao, Herbert Breuer, Elisabeth Beise, Joerg Reinhold, and many–many others.

Many thanks go to Don Geesaman, Steve Wood, Kevin Beard, Pat Welch, and John Arrington for providing not only a good framework, but also an excellent implementation of the Hall C analysis software; to Joe Mitchell and his cryotarget group: Dave Meekins, Jim Dunne, and Bart Terburg, for providing a reliable target system; and also to the people that helped shape the Hall C simulation software in its present form, Rolf Ent, Tom O'Neill, Naomi Makins, Rick Mohring, and Dipangkar Dutta.

This list would not be completed without the names of my fellow graduate students that formed the original Hall C "crew": John Arrington, Dave Meekins, Jinseok Cha, Dipangkar Dutta, Derek van Westrum, Kenneth Gustafsson, the three Chrises, Armstrong, Bochna, and Cothran, Wendy Hinton, Valery Frolov, Pawel Ambrozowicz, Rick Mohring, Doug Koltenuk, and Ioana Niculescu. I was very fortunate to have such a knowledgeable and dedicated group of co–workers; I wish you all luck and achievements in your young careers.

All the members of the **E93-018** collaboration (too many to list here) are to be commended for their relentless efforts that led to a successful experiment, despite significant technical difficulties, not mention sheer bad luck. During my data analysis Don Geesaman, Joe Mitchell, Dave Mack, Ben Zeidman, and Tatiana Angelescu provided me with many helpful hints and suggestions, as was my dissertation advisor (and **E93-018** spokesperson), Dr. Oliver Keith Baker. Rolf Ent was always available for questions and comments, his advice was invaluable for my analysis (now if only he could dribble that soccer ball better ...).

During countless discussions with fellow "kaon farmers" Joerg Reinhold, Paul Gueye, Jinseok Cha, Wendy Hinton, Rick Mohring, and Doug Koltenuk, many useful ideas that made their way into my analysis emerged. During the interpretation phase of the experiment, a lot of theoretical help, including programs and/or numerical predictions, was provided by Robert Williams, Bijan Saghai, Jean Marc Laget, Cornelius Bennhold, Warren Buck, and their respective collaborators, and I wish to thank them all.

Lastly, I can't close without mentioning the two persons most close to my heart and without which the present work would not exist: my daughter, Tatiana, and my wife, Ioana. This dissertation is as much theirs as it is mine. To my daughter Tatiana I am especially indebted for sitting-in in many of my quantum mechanics classes, becoming the "mascot" of the **E93-018** experiment, and generally coping with a way–too–busy dad. Being married to someone that is herself a nuclear physicist was both a blessing and a curse for many a time I ended up feeling at work while I was at home. Throughout it all, I felt Ioana's dynamic presence as accomplished physicist, as helpful and relentless co–worker, as loving wife, as devouted mother of my child, as skillful cook, providing all the help I needed in my work and giving a meaning to my existence.

Contents

List of Figures

List of Tables

INTRODUCTION AND PHYSICS MOTIVATION

1.1 Introduction

The objective of nuclear physics is the study of the structure of hadronic matter. The nucleus, as a collection of baryons in close proximity provides an ideal microscopic laboratory for testing the structure of fundamental interactions. Baryons themselves are now understood as complicated many body systems, comprised of quarks and gluons whose interaction are described by *quantum chromodynamics* (QCD). All forces known in nature are present in the nucleus; strong, electromagnetic, weak, and even gravitational if one stretches the definition of a nucleus to include condensed stellar objects (i.e. huge nuclei held together by gravity). As most of the mass and energy in the visible universe comes from nuclei and nuclear reactions, understanding nuclear physics is crucial for understanding the universe both in its formation (early universe, formation of elements), as well as its (sometimes explosive) later stages (supernovae, neutron stars).

Several levels of understanding of the nucleus and nuclear structure, (sometimes, but not always) reflecting the historical progress in the field, are available:

First, one has the non–relativistic, many–body system approach. In this framework one uses static potentials based on two–body scattering and bound–state data. The dynamics is described by non–relativistic, many–particle Schrödinger equations, while the electroweak currents come from the properties of free nucleons.

Second, one has relativistic many–body system approaches. Relativistic hadrons, mesons, and baryons form the degrees of freedom of these many–body representations. These quantum field theories based on hadronic degrees of freedom are sometimes called *quantum hadrodynamics* (QHD).

Lastly, one has the representation of the nucleus as a strongly coupled system of quarks and gluons. The interactions of quarks and gluons are described by a Yang–Mills theory based on an internal color symmetry (QCD). QCD has two remarkable (and intriguing) properties: *asymptotic freedom* (i.e. at very high momenta, or short interaction distances, the coupling constant becomes vanishingly small), and *confinement* (i.e. quarks and gluons, the QCD degrees of freedom, are confined to the interior of the hadrons). Another practical aspect of QCD is that, to date, it cannot be solved analytically except in its perturbative regime (pQCD).

1.1.1 Electromagnetic Interactions in Nuclear Physics

Electromagnetic probes (i.e. scattering of real or virtual photons) have proven ideal tools for studying nuclear structure and, given enough incident energy, the structure (and dynamics) of nucleons themselves.

The predominant interaction in electron scattering, the electromagnetic interaction, is governed by *quantum electrodynamics* (QED), the most accurate physical theory [4] . The electromagnetic interaction is relatively weak, thus producing only minimal disturbance to the target, at least compared with other means of investigation such as hadronic probes. Electromagnetic probes interact only with the local electromagnetic current density of the target, hence once knows what is measured. In practice one measures the Fourier transform (with respect to the momentum transfer) of the transition matrix element of the current density.

In particular, using virtual as opposed to real photons offers access to additional degrees of freedom/observables because the electron scattering variables, the initial and final electron energies, as well as the scattering angle can be conveniently modified in order to obtain variations in both the energy and the momentum transfers to the target.

By varying the polarization of the virtual photon one can separate the charge and current interactions. In addition to the Coulomb interaction with the charges in the target, in electron scattering one is also sensitive to the magnetic interactions with the convection current as well as the intrinsic magnetization of the target. By performing polarization experiments in electron scattering, one is sensitive to the interference between the photon, γ, and the Z^0 exchange. Thus one can measure the nuclear distribution of the weak nuclear current.

Deep inelastic (DIS) electron scattering experiments and the various scaling laws offered the first evidence on the point–like quark substructure of the hadrons. DIS provides a measurement of the quark momentum distribution, as well as a valuable testing ground for QCD predictions.

Last, but not least, the recent availability of medium energy, high intensity, high duty factor electron beams (such as those available at Jefferson Lab) enables systematic studies in areas of nuclear physics where only exploratory measurements were possible previously, including the kaon electroproduction experiments.

1.1.2 Kaons and Kaon Electroproduction

The K mesons[1] were "discovered" in the first half of the 20–th century (Rochester and Butler, 1947, claiming the first observation [5]). What was observed initially was a previously unknown particle produced in strong interactions but which sported a rather long lifetime (on the order of 10^{-8} s), characteristic of weak decays. To (partially) explain the properties of these particles, a new quantum number, the strangeness, S, was proposed by Gell Mann and Nishijima (see for example [6]). Strangeness is conserved in the strong and electromagnetic interactions, but not in the weak interaction. Conventionally the K^+ meson has a strangeness of +1, while the K^- meson (and, for that matter, the Λ hyperon) has a strangeness of -1. Later on Gell–Mann [7] and Zweig [8] proposed the quark model, in what turned out to be an important contribution to the advance of nuclear/particle physics.

[1] The K meson family is composed of the positive K^+ and negative K^- mesons, as well as the short lived K^0_S and longer lived K^0_L neutral kaons.

In the quarks and gluons language of QCD one can describe the K meson as the lightest quark–antiquark system in which a strange quark, s, is paired with an up, u, or a down, d quark (i.e. a K^+ meson is a $\overline{s}u$ pair).

After the discovery in the forties, strangeness physics was a very active field of study for about two decades. Despite some early successes, the field of electromagnetic production of strangeness was gradually abandoned in the mid–late 1970s, mainly due to a lack of adequate experimental facilities[2] and an apparently complicated reaction mechanism [9]. As a direct consequence of this lack of activity in the field, the experimental data is very scarce, and, for the most part, plagued by large statistical and systematic uncertainties.

In recent years, a new plethora of theoretical studies of electroproduction [10] (and photoproduction as well) emerged, fueled by the promise of understanding hadrons in terms of QCD and the construction of new accelerators capable of providing continuous wave, high–current, electron beams (unpolarized as well as polarized) in the few GeV range.

As Jefferson Lab (CEBAF at that time) became operational in 1994 and started its physics program in late 1995, this promise of a new generation of electron accelerators turned into palpable reality. Among the first experiments to take data at this new facility were two kaon electroproduction experiments, E91-016 and **E93-018** .

1.1.3 Experiment E93–018; Description and Goals

Experiment **E93-018** was designed to take advantage of the continuous wave (**CW**), high–intensity, (relatively) high energy, of the Jefferson Lab electron beam and provide a detailed study of elementary K^+ electroproduction in both the

$$e + p \rightarrow e' + K^+ + \Lambda \tag{1.1}$$

[2] As the cross sections involved in kaon electroproduction are small and also kaons are relatively heavy, high–luminosity, reasonably high (few GeV) facilities are needed. No electron accelerator from, say, a decade ago could fill that prescription; for example the Stanford Linear Accelerator, SLAC, certainly had/has multi–GeV capabilities, however the duty factor was too poor for $(e, e'K^+)$ coincidence experiments. On the other hand the Mainz Microtron, MAMI, certainly can provide high intensity, continuous beams, however the maximum energy is just below the Λ threshold.

and

$$e + p \rightarrow e' + K^+ + \Sigma^0 \tag{1.2}$$

reactions. The main physics goal of the experiment was to gain insight on the production mechanisms at work in kaon electroproduction, and possibly also to measure (directly or indirectly) the size of the charge distribution of a kaon (in other words measure the kaon electromagnetic form factor). In more concrete terms, the experimental goals of **E93-018** were:

- separate the longitudinal and transverse parts of the cross–section for a wide range of kinematic settings
- study the t–dependence[3] of the cross–section and gain some direct/indirect knowledge on the kaon form factor
- study the differences between the Λ and Σ^0 production in terms of coupling constants, possibly as a measure of the strangeness content of the proton
- accomplish all of the above with unprecedented statistical and systematic uncertainty, thus testing the validity of the theoretical models available (as well as seriously constraining future models)
- set the benchmark for future kaon electroproduction experiments (planned at Jefferson Lab as well as worldwide)
- provide a baseline/reference for subsequent kaon electroproduction experiments on nuclei, including hypernuclear experiments.

Experimentally the kaons produced by the interaction of the primary electron beam with the hydrogen target were detected in coincidence with the scattered/outgoing electrons. Using this technique, the differential cross-section was measured at four values of the four–momentum–transfer, $Q^2 = 0.52, 0.75, 1.00$ and $2.00 (GeV/c)^2$. For each Q^2

[3] For a definition of the Mandelstam variable t, as well as other quantities of interest for the present analysis see next section.

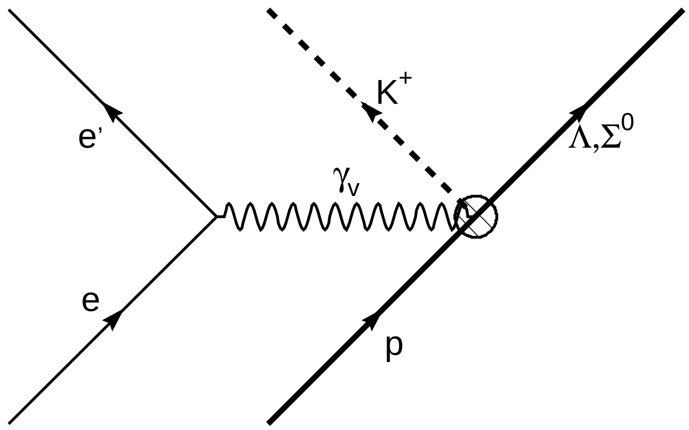

Figure 1.1: Feynman diagram representation of kaon electroproduction in the one–photon exchange approximation.

value measurements were carried out at three different virtual photon polarizations, ε, enabling the separation of the longitudinal and transverse parts of the cross-section. The cross–section was also studied in terms of its t dependence at Q^2 of 0.75, 1.00, and 1.25 (GeV/c)^2, aiming to extract information on the kaon form factor.

1.1.4 Theoretical Background and Kinematics

In this section the quantities relevant to the **E93-018** analysis are defined and the notations used throughout this work are described. In **E93-018** the reactions

$$e + p \rightarrow e' + K^+ + \Lambda/\Sigma^0 \tag{1.3}$$

were studied. To first order in the electromagnetic coupling constant $\alpha = 1/137$ (the so–called one photon exchange approximation), eq. (1.3) can be related to the associated photoproduction[4] reaction $\gamma_v + p \rightarrow K^+ + \Lambda/\Sigma^0$. Figure 1.1 shows the Feynman diagram representation of the kaon electroproduction in the one photon exchange approximation. In Fig. 1.2 the kinematic variables of the $(e, e'K^+)$ reaction (or, in general, any $(e, e'X)$

[4]Most of the formalism in this section can be re–written in general terms, i.e. the electroproduction of any meson.

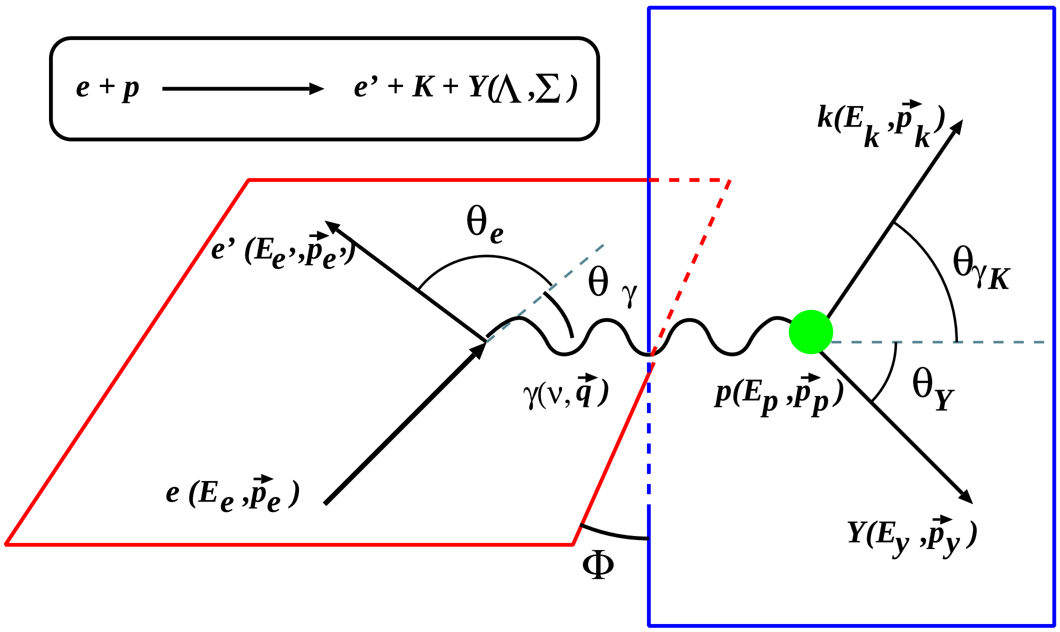

Figure 1.2: Definition of kinematic variables used in kaon electroproduction.

reaction) are shown[5]. The incident[6], $e = (E, \vec{p}_e)$ and the scattered electrons $e' = (E_{e'}, \vec{p}_{e'})$ define the scattering plane. The recoiling K^+ meson $k = (E_K, \vec{p}_K)$ and the residual system, Y, (a Λ or a Σ^0 hyperon) $= (E_Y, \vec{p}_Y)$ define the production plane. The target proton is characterized by $p = (m_p, \vec{0})$ (i.e. no initial momentum for the target proton in the laboratory system). One might note that the virtual photon lies in both planes. The angle between the scattering and the production planes, the out–of–plane angle, is denoted by Φ. The polar angle between the virtual photon and the kaon is denoted by $\theta_{\gamma K}$ while the angle between the incident and the scattered electron is θ_e. The four momentum transfer from the electron to the proton is denoted by q; $q = e - e'$. Its components are $E - E_{e'} = \nu$ (the electron energy loss in the laboratory system) and $\vec{q} = \vec{p}_e - \vec{p}_{e'}$. The square of the four momentum transfer $q^2 = -Q^2$, also known as the

[5]In Fig. 1.2 Y denotes the undetected baryon; for **E93-018** that would be either the Λ or the Σ^0 hyperon.

[6]Where the four vector, e, as well as its energy, E, and three momentum $\vec{p}_e$ are given. The notation is similar for all particles involved in reaction 1.3

mass of the virtual photon (as the photon is virtual it will have a non–zero mass. For the kinematic settings studied in **E93-018** $q^2 < 0$, i.e. space–like). Neglecting the mass of the electron[7] one can write q^2 as:

$$q^2 = -4EE' \sin^2(\theta_e/2). \tag{1.4}$$

Other quantities of interest are $W^2 = m_p^2 + 2m_p\nu - Q^2$, the mass squared of the system recoiling against the electron (i.e. the photon–proton system), and the Mandelstam variables $t = (q-k)^2 = q^2 + m_K^2 - 2qk$, $s = (e+p)^2 = m_p^2 + 2m_pE$, and $u = (k-p)^2$. One can also define the Björken scaling variable $x = \frac{Q^2}{2m_p\nu}$ (interpreted, in the quark parton model, as the fraction of the target nucleon's momentum carried by the struck quark).

Within the one-photon exchange approximation framework, the general differential cross section formula for electron scattering from a spin 1/2 target, when a kaon (or any other nucleon or meson) is detected in coincidence[8] with the outgoing electron can be deduced starting from the Feynman diagram in Fig. 1.2: It can be shown[9] that, for the case when none of the initial or final spins are detected, such as during the **E93-018** experiment, the coincidence cross–section can be written in the form[13]:

$$\frac{d^5\sigma}{dE' d\Omega_{e'} d\Omega_{K+}} = \Gamma(\sigma_T + \varepsilon\ \sigma_L + \varepsilon\ cos(2\phi)\ \sigma_{TT} + [\frac{\varepsilon\ (\epsilon + 1)}{2}]^{1/2}\ cos\ \phi\ \sigma_{LT}) \tag{1.5}$$

where $\Gamma = \frac{\alpha}{4\pi^2}\ \frac{E'\ (W^2 - m_p^2)}{Em_pQ^2\ (1-\epsilon)}$ is the virtual photon flux; σ_T is the unpolarized (transverse) cross section; σ_L is the longitudinal cross section; σ_{TT} is the transverse–transverse interference cross section; σ_{LT} is the longitudinal–transverse interference cross section; $\Omega_{e'}$ is the scattered electron solid angle; Ω_{K+} is the kaon solid angle; E' is the scattered electron energy; ε is the virtual photon polarization parameter; ϕ is the azimuthal angle between the scattering and production planes. The quantities $\sigma_T, \sigma_L, \sigma_{TT}$ and σ_{LT} completely characterize the dependence of the cross–section on the nucleon (nucleus). Generally they are functions of the kinematic variables Q^2, W, and t.

[7]As the lowest electron energy measured in **E93-018** is at least several hundred MeV this approximation works rather well.

[8]For a theoretical review of electron coincidence experiments see [11].

[9]The full theoretical derivation of eq. 1.5 from first principles is given, for example, in [12].

The separation of σ_T and σ_L, which is the main focus of the present analysis, is possible via the so–called Rosenbluth technique. First, let us observe that the last two terms of eq. (1.5) vanish if one integrates over ϕ between 0 and 2π. The integration has to be performed keeping Q^2, W, and t simultaneously constant. In practice one needs to average over some region around $\theta_{\gamma K} = 0$ so that the available phase–space for the reaction is non–zero. Repeating the procedure for different values of ε yields a very simple system of linear equations

$$\sigma^i(Q^2, W, t, \varepsilon) = \sigma_T(Q^2, W, t) + \varepsilon^i \sigma_L(Q^2, W, t) \quad i = 1, 2, \ldots \tag{1.6}$$

with the longitudinal and the transverse terms of the cross-section as the only unknowns[10]. Solving this system, using for example a least square fitting technique[11], yields the values for σ_T and σ_L.

Following this procedure, in experiment **E93-018** , three different ε settings were measured for each Q^2 value (W and t were kept constant as well). The complete set of L/T kinematics measured during **E93-018** is given in Table 1.1. Columns three and four in the table correspond respectively to the HMS (SOS) central momenta[12], while columns five and six show the HMS (SOS) central angles. For each setting the cross–section was first determined in the laboratory frame, then, integrating over ϕ and averaging over the available $\theta_{\gamma K}$ range the unseparated CM cross–sections were obtained. For each Q^2 value a linear least squares fit was used to fit a line through the three measured ε points. The slope of the line will then be the longitudinal component of the cross–section, σ_L, and the intercept at the origin will be the transverse part of the cross–section, σ_T.

Another quantity of interest in the present **E93-018** analysis is the kaon electromagnetic form factor (or kaon form factor for short). The form factors are generally defined as the Fourier transforms of the spatial charge and current distributions [6]. For example, one might consider the case of an electron interacting with (scattering off) a target (for simplicity a spinless target is considered here) having a charge distribution

[10] In eq. 1.6 the upper index i is used to differentiate between the ε points measured for each Q^2.

[11] The system becomes over-determined if more than two ε points are measured.

[12] Neglecting the mass of the electron with respect to its momentum, i.e. $E_{e'} \equiv p_{e'}$ introduces, for the lowest electron momenta measured in **E93-018** , an error of only $\sim 5 \times 10^{-7}$.

Q^2 $[GeV/c]^2$	E_e $[GeV]$	$E_{e'}$ $[GeV]$	p_k $[GeV/c]$	θ_e $[°]$	θ_γ $[°]$	W $[GeV]$	ε	x	$-t$ $[GeV/c]^2$
0.52	2.445	0.833	1.126	29.27	13.33	1.84	0.55	0.17	0.219
0.52	3.245	1.633	1.126	18.02	16.62	1.84	0.77	0.17	0.219
0.52	4.045	2.433	1.126	13.20	18.34	1.84	0.86	0.17	0.219
0.75	2.445	0.726	1.188	37.94	13.41	1.83	0.46	0.23	0.300
0.75	3.245	1.526	1.188	22.44	17.62	1.83	0.72	0.23	0.300
0.75	4.045	2.326	1.188	16.23	19.74	1.83	0.83	0.23	0.300
1.00	2.445	0.635	1.216	47.30	13.05	1.81	0.38	0.30	0.407
1.00	3.245	1.435	1.216	26.79	18.24	1.81	0.67	0.30	0.407
1.00	4.045	2.235	1.216	19.14	20.77	1.81	0.81	0.30	0.407
2.00	3.245	0.844	1.634	50.59	13.54	1.84	0.37	0.44	0.741
2.00	3.545	1.144	1.634	41.11	15.66	1.84	0.48	0.44	0.741
2.00	4.045	1.644	1.634	31.83	18.13	1.84	0.61	0.44	0.741

Table 1.1: Nominal kinematics for Experiment **E93-018** Longitudinal Transverse separation. The number of different ε values measurable was limited by the number of different beam energies available, while the range in ε achievable was restricted by the range of angles accessible for each spectrometer as well as the minimal opening angle between the spectrometers.

$\rho(x)$, normalized such as $\int \rho(x)dx = 1$, via the exchange of a photon. Let q^2 (defined as above) be the four momentum transfer of this interaction. Then the form factor is the Fourier transform of the charge distribution ρ: $F(q) = \int \rho(x)e^{-iqx}dx$. For this simple case the square of the form factor is proportional with the cross–section:

$$\frac{d\sigma}{d\Omega} = \left(\frac{d\sigma}{d\Omega}\right)_{\text{Mott}} (F(q))^2 \tag{1.7}$$

where $(\frac{d\sigma}{d\Omega})_{\text{Mott}}$ is the Mott cross–section (i.e. the cross–section for scattering off a point–like particle).

1.1.5 Kaon Electroproduction Models

Several groups in the theoretical community have put great efforts, over the last ten years or so, into building models capable of explaining the production of mesons in electromagnetic interactions. In this section a brief review of these models will be given. Although the language will be in terms of kaon production, one might bear in mind that, most of these models start out as pion production models (mainly because the pion database is much richer, thus offering ample opportunities to test ones models).

While the various models differ from each other (sometimes dramatically), there is, fortunately, a general consensus on the requirements that any successful model has to meet. These requirements are:

- Simultaneously explain (including polarization observables) all reactions of photo- and electro- production of kaons (in both the Λ and Σ channels), and, through charge conjugation, explain the radiative capture of K^- mesons as well:

$$\gamma + p \rightarrow K^+ + \Lambda$$

$$\gamma + p \rightarrow K^+ + \Sigma^0$$

$$\gamma + p \rightarrow K^0 + \Sigma^+$$

$$e + p \rightarrow e' + K^+ + \Lambda$$

$$e + p \rightarrow e' + K^+ + \Sigma^0$$

$$K^- + p \to \gamma + \Lambda$$

$$K^- + p \to \gamma + \Sigma^0$$

- Reproduce with a reasonable precision all available experimental data.
- Satisfy SU(3) symmetry constraints[13] for the two main coupling constants, $g_{K\Lambda N}$ and $g_{K\Sigma N}$.
- Provide a "smooth" transition towards higher Q^2 values and the perturbative regime of QCD.
- Obtain as simple a reaction mechanism as possible (i.e. a physical model for the reaction(s) and not a mathematical representation for the data).

The existing theoretical models can be classified into two main groups: isobaric models and Regge models.

In the isobaric model approach all amplitudes as expressed as Feynman diagrams. Using perturbation theory (to first order), each diagram corresponds to the exchange of one particle or resonance (the so–called tree approximation). These models include extended Born terms for p, K, and Y ($Y = \Lambda$ or Σ hyperons) exchange (plots a), b), and c) in Fig. 1.3), as well as resonant terms for N^* (for Σ production one has to take into account the Δ's as well), K^* (in some cases even K_1), and Y^* terms . Depending on the level of sophistication of the model, resonances with spins up to I = 5/2 are included (see Fig. 1.4. Notations are similar to those used in [1]). Each Feynman diagram shown in Figs. 1.3 and 1.4 leads to a gauge invariant amplitude, except for the kaon exchange diagram in the t channel (Fig. 1.3a). In order to restore gauge invariance one needs to include the exchange of charged baryons (i.e. protons) in the s channel (Fig. 1.3b) [1]. As seen in the case of pion electroproduction, the kaon exchange diagram (Fig. 1.3a) is expected to dominate, at least for forward kaon electroproduction (i.e. low t). These models reproduce reasonably well the available data. However, the main disadvantage of these models is the rather large number of input parameters that need to be fixed. As

[13] Broken at the ~20 % level.

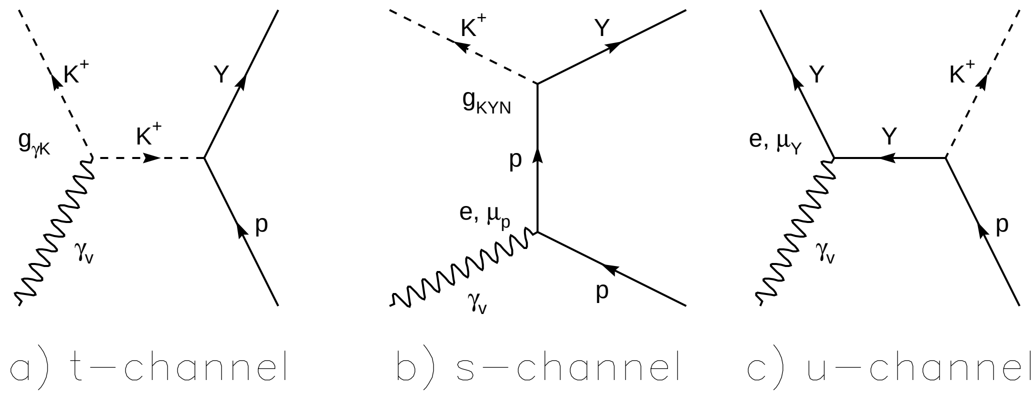

Figure 1.3: Extended Born terms for kaon electroproduction.

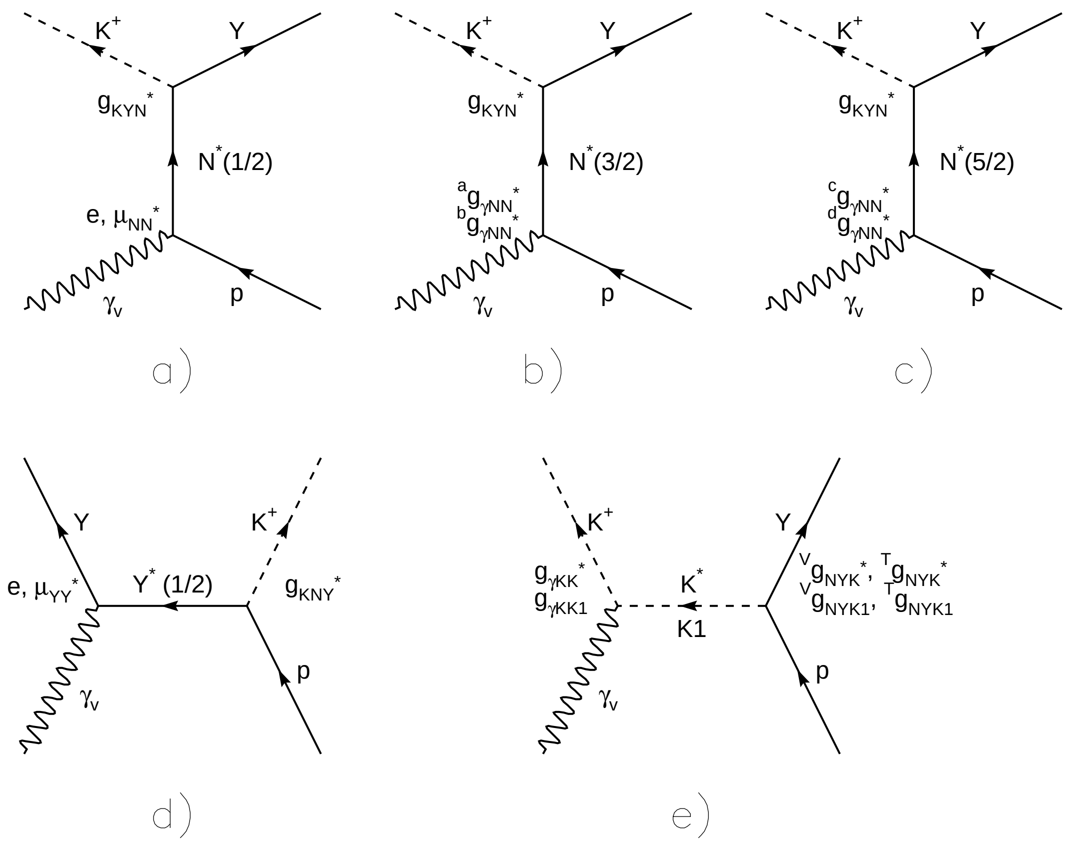

Figure 1.4: Resonant terms used in isobaric models. Notations used for coupling constants, etc. are as explained in [1].

the available data is rather scarce, there are little or no constraints imposed on some of these parameters. For example, the $g_{K\Lambda N}/4\pi$ coupling constant can be lower than 1 in some analyses, or higher than 4 in others. While a comprehensive list of pre–1990 models can be found in [9], here we shall list only the more recent efforts:

- Adelseck and Saghai [9] focussed only on Λ photoproduction for photon energies (in the laboratory system) below 1.5 GeV.

- Williams, Ji, and Cotanch (WJC) [14] studied all the reactions listed above except for K^0 production, while extending the energy range to ~ 2.1 GeV. This came as a revision of the previous WJC model [15].

- Mart, Bennhold, and Hyde–Wright produced a model [16] that, while covering the same energy range as the WJC model, focuses on the $K\Sigma$ photoproduction reactions, with special emphasis on K^0 production.

- David and collaborators improved upon the cited Adelseck and Saghai work to produce the so–called Saclay–Lyon (SL) model [1].

In contrast with the large number of parameter used in isobaric models, Regge (or "reggeized") models are parameter–free or contain a minimal number of parameter that need to be fixed from data. The exchange of high–spin, high–mass particles in the t (u) channels is economically taken into account by replacing the usual, pole–like Feynman propagator with the Regge propagator. For example, for K exchange, one has:

$$\frac{1}{t-m_K^2} \Rightarrow \P^K_{Regge} = \left(\frac{s}{s_0}\right)^{\alpha_K(t)} \frac{\pi\alpha'_K}{\sin(\pi\alpha_K(t))} \frac{\mathcal{S}+e^{-i\pi\alpha_K(t)}}{2} \frac{1}{\Gamma(1+\alpha_K(t))} \tag{1.8}$$

where s_0 is a mass scale (conventionally taken as $s_0 = 1$ GeV^2), $\mathcal{S}$ is the signature of the trajectory $\mathcal{S} = \pm 1$, α_0 and α' are the parameters of the Regge trajectory, and $\alpha(t) = \alpha_0 + \alpha'(t)$. The gamma function $\Gamma(\alpha(t))$ ensures the suppression of the poles of the propagator in the unphysical region. As in the case of isobaric models the gauge invariance of the t channel diagrams is restored by adding diagrams in the s channel (see Fig. 1.5a).

The latest Regge–type model for kaon (and pion) photo- and electroproduction is due to Vanderhaeghen, Guidal, and Laget [17, 18, 19] (VGL). This model is based on saturating Regge trajectories and includes, for kaon electroproduction, exchanges of K^+ and K^* trajectories (see Fig. 1.5b). The form factors for both K^+ and K^* are parameterized using a monopole representation

$$F_{K^+,K^*}(Q^2) = \frac{1}{1 + Q^2/\Lambda^2_{K^+,K^*}}. \tag{1.9}$$

This Regge model, despite its apparent simplicity, reproduces well the pion and kaon photo- and electroproduction data available.

1.2 Previous Data

In the past, the low duty factor of available electron accelerators, combined with the low cross-section (i.e. about three orders of magnitude lower than hadronic reaction cross-section), the relatively short lifetime of a K meson, and the usually high backgrounds made kaon electroproduction studies very difficult [20]. Given these conditions the existing world data on kaon electroproduction is very limited and usually the uncertainties are large [21, 22, 23, 24]. The available photoproduction data is somewhat more extensive although by no means exhaustive (an excellent compilation of these can be found in [9]). Only one previous attempt was made to separate the longitudinal and transverse components of the cross section[21], but the systematic uncertainties reported were large (due to the low duty factor one ε point was measured in one year and the other ε point was measured the next year - thus the large systematic errors). A summary of the existing total cross-section data is shown in Fig. 1.6 – 1.7 for Λ and Σ^0 respectively. while a list of all available measurements (as of 1994) for the 7 reactions mentioned in section 1.1.5 is given in Table 1.2[14]. Note that in order to compare results for different experiments the data points were extrapolated to a common W as explained in [21]. The results of the only previous attempt to separate the longitudinal and transverse parts of the cross–section (in Λ electroproduction) are shown in Fig. 1.8 [21]. The results of

[14]The number of experimental data points for Σ^0 electroproduction is roughly the same as for Λ electroproduction.

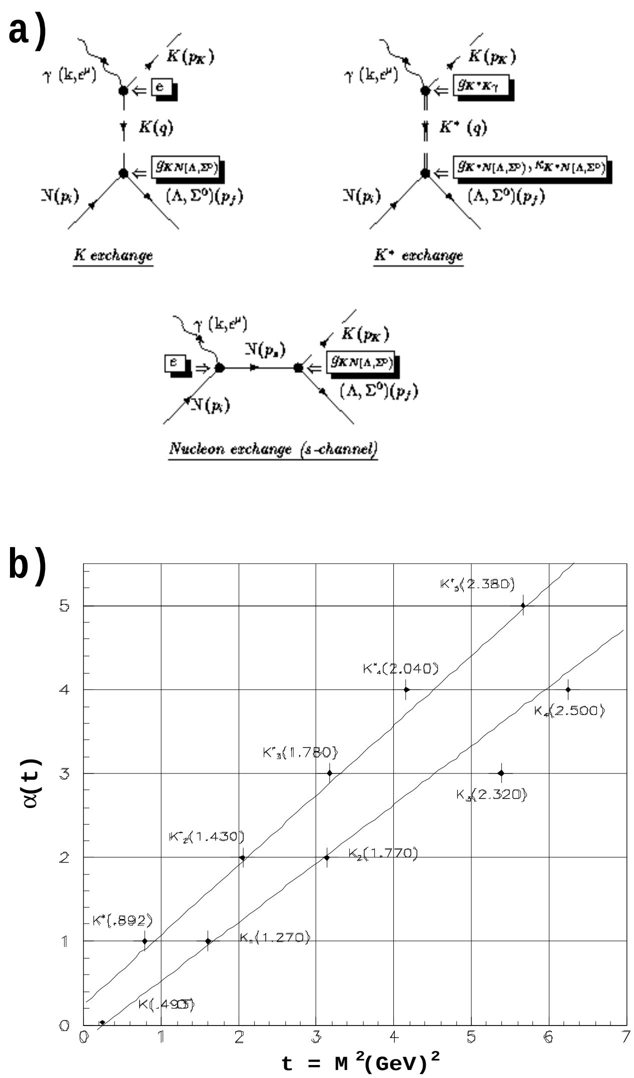

Figure 1.5: Feynman diagrams considered in the Regge model of Vanderhaeghen, Guidal, and Laget (panel a). Representation of the K^+ and K^* Regge trajectories considered in the model (panel b).

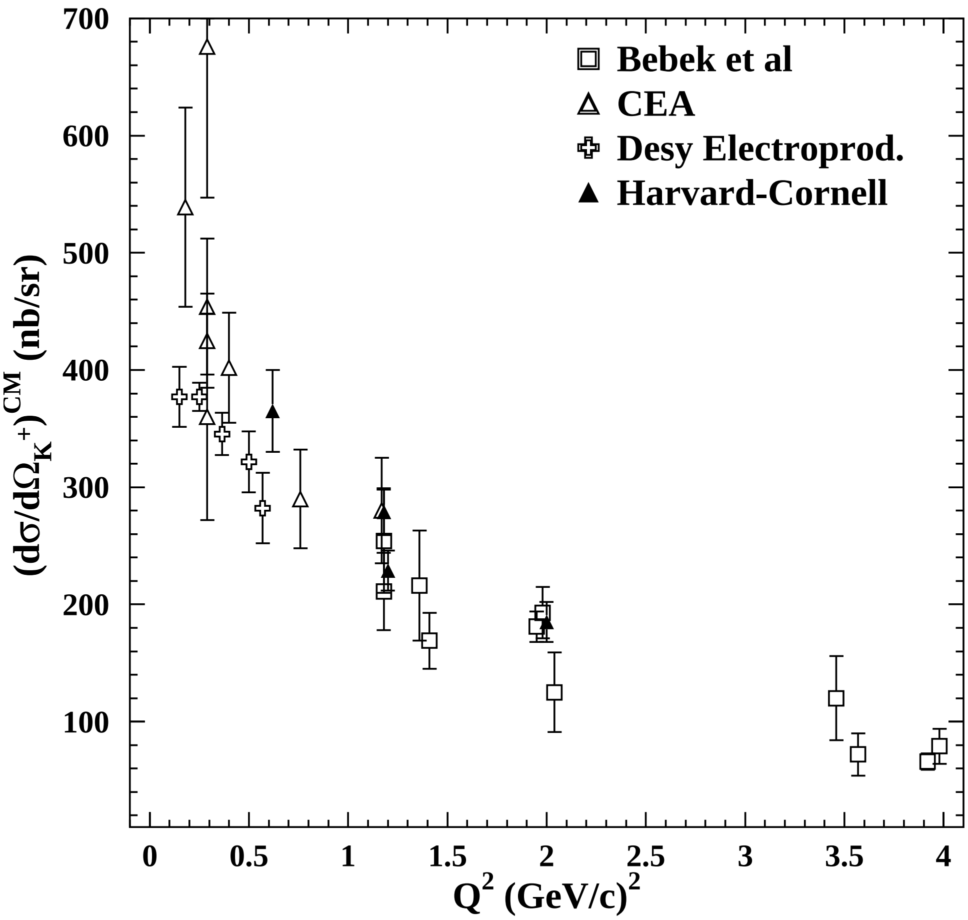

Figure 1.6: Existing world data for the reaction $e + p \rightarrow e' + K^+ + \Lambda$ prior to **E93–018**. All data points are extrapolated to $W = 2.15$ GeV as explained in [2].

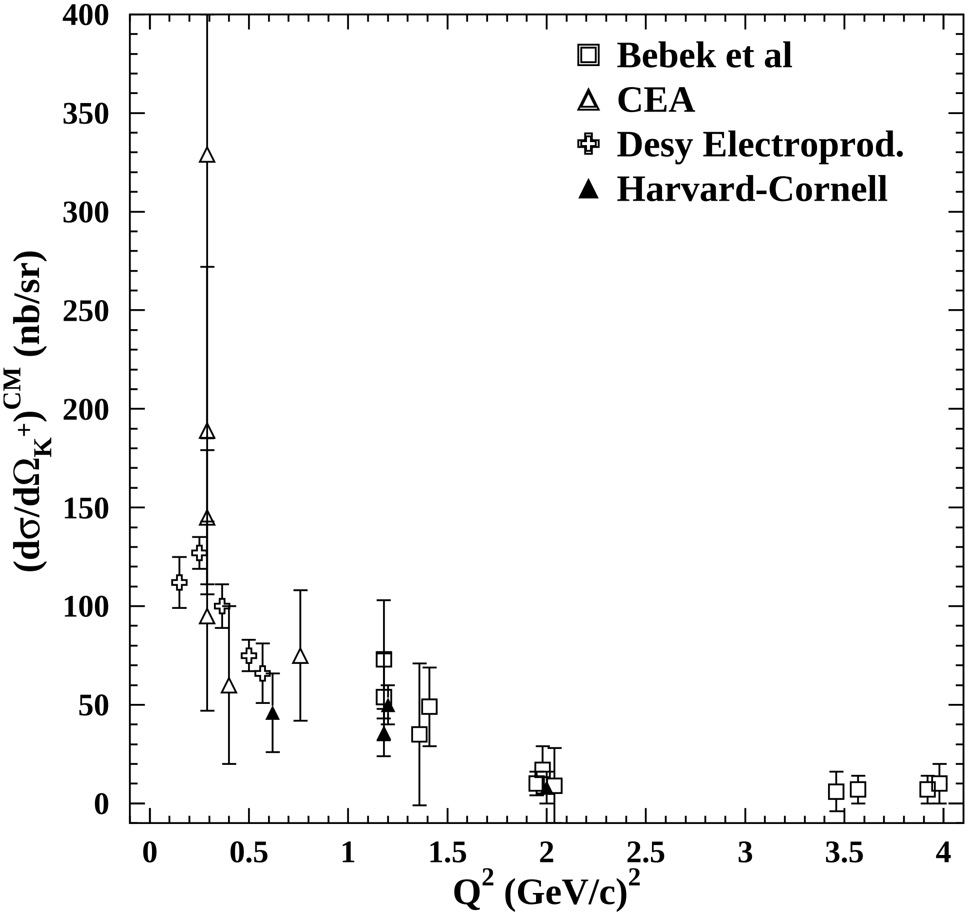

Figure 1.7: Existing world data for the reaction $e + p \rightarrow e' + K^+ + \Sigma^0$ prior to **E93–018**. All data points are extrapolated to $W = 2.15$ GeV as explained in [2].

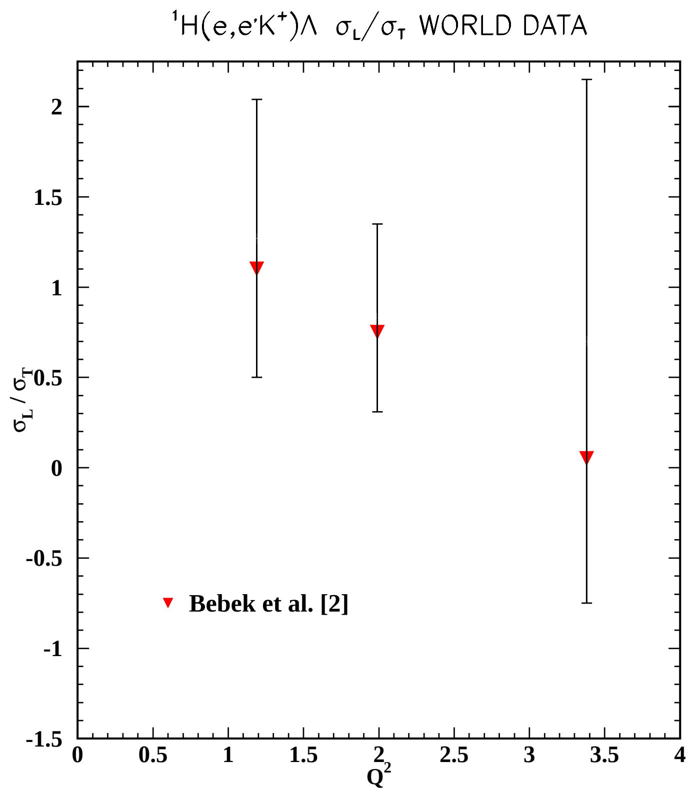

Figure 1.8: Results of the only previous attempt to separate the longitudinal and transverse parts of the cross-section in the $e + p \rightarrow e' + K^+ + \Lambda$ reaction. The quantity plotted is the ratio σ_L/σ_T as a function of the four–momentum transfer, Q^2 (in $(\mathrm{GeV/c})^2$)[2].

Reaction	Observable	Number of experimental Points
$\gamma + p \to K^+ + \Lambda$	Differential cross–section	202
	Total cross–section	21
	Λ polarization	25
	Target polarization	3
$\gamma + p \to K^+ + \Sigma^0$	Differential cross–section	177
	Total cross–section	22
$\gamma + p \to K^0 + \Sigma^+$	Total cross–section	2
$e + p \to e' + K^+ + \Lambda$	Differential cross–section	40
$K^- + p \to \gamma + \Lambda$	Branching ratio $\Gamma(K^- p \to \gamma\Lambda)/\Gamma(K^- p \to \text{all})$	1
$K^- + p \to \gamma + \Sigma^0$	Branching ratio $\Gamma(K^- p \to \gamma\Sigma^0)/\Gamma(K^- p \to \text{all})$	1

Table 1.2: Strangeness electro- and photoproduction data available (up to 1994).

the only direct measurement of the kaon form factor are shown in Fig. 1.9. The data was obtained at CERN [3] by scattering high energy (250 GeV) kaon beams off atomic electrons. The error bars are large, while the range of momentum transfers spanned is extremely small (and extremely close to $Q^2 = 0$).

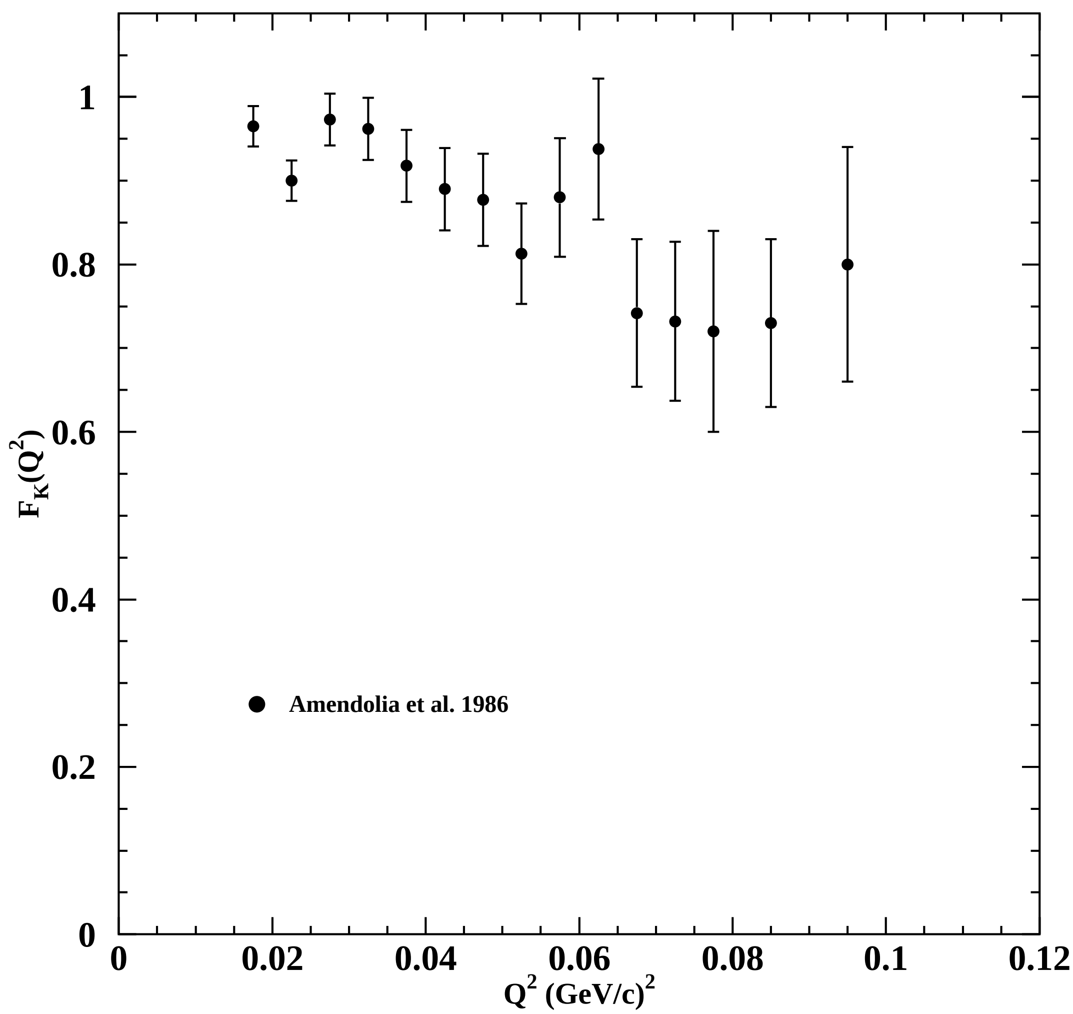

Figure 1.9: Existing world data for the kaon form factor. The measurement involved scattering high energy kaon beams off of atomic electrons [3].

EXPERIMENTAL APPARATUS

2.1 Overview

Jefferson Lab was designed to provide high luminosity, 100% duty factor ("continuous wave",**CW**) electron beams of up to 4 GeV [1] simultaneously to three independently running experimental areas (sometimes referred to as "experimental halls"). Experiment **E93-018** , "L/T Separation in $^{1}H(e,e'K^{+})\Lambda/\Sigma^{0}$", was carried out in the experimental Hall C, the only operational experimental area at that time. The data acquisition phase of the experiment was completed in the fall of 1996.

During **E93-018** the scattered electrons were detected in coincidence with the lepto-produced kaons, detected before their in-flight decay. A 4–cm liquid hydrogen target was used. The yield from a dummy replica of the empty target cell was measured separately for each kinematic setting. A number of single events were recorded also for both the electron and the hadron arm. Elastic scattering off hydrogen (using the same target cell as in the experiment) was measured[2] for calibration purposes.

The experimental equipment used in **E93-018** was the standard equipment available in Hall C. This consisted of [3]:

[1] Upgrades to $6-8$ GeV beam energies and beyond are underway. Starting from the late 1996 delivery of polarized beams is possible also.

[2] At least one elastic setting per beam energy change!

[3] Each system and subsystem comes, of course, with its associated electronics for readout, check-up, remote activation, etc., as appropriate.

- Jefferson Lab 's CEBAF[4] accelerator,
- beam-line (for transporting the electron beam extracted from the accelerator);
- beam-dump (for disposing of the residual beam emerging from the target area);
- target assembly (including the targets themselves);
- a pair of focussing electromagnetic spectrometers, namely:
  - the High Momentum Spectrometer (**HMS**), the electron arm,
  - the Short Orbit Spectrometer (**SOS**), the hadron arm,

    each one of these spectrometers having its own set of detectors comprised of:
    * drift chambers,
    * hodoscopes,
    * Čerenkov counters,
    * shower counters.

In order to address the specific issues related to kaon detection two additional Čerenkov detectors/counters were added to the hadron arm detector stack. All the systems enumerated above will be described in the rest of this chapter.

2.2 Accelerator, Hall C Arc, and Associated Instrumentation

2.2.1 Accelerator

As stated earlier, the CEBAF accelerator is an electron machine, capable of delivering **CW** (100 % duty factor) unpolarized (and polarized) electron beams of up to 4 GeV [5] and

[4]CEBAF stands for **C**ontinuous **E**lectron **B**eam **A**ccelerator **F**acility

[5]Note: The total beam energy is computed, in the first approximation, as number of passes (i.e. number of times the beam passes through both the North and South linacs) times the nominal acceleration/pass plus the injector energy (usually $\sim$ 45 MeV); so the "nominal" 4 GeV beam is actually 4.045 GeV. Of course the energy used in the analysis comes from the more sophisticated beam energy measurement explained later in this chapter.

beam currents of up to 200 μA total current to three experimental halls simultaneously.[6] The microstructure of the beam consists of short (1.67 ps) bursts of beam at 1497 MHz. Each of three experimental halls receives every third of these bursts, for an "effective" frequency of 499 MHz in each hall. Typical beam emittance is 2×10^{-9} mr, with an energy spread $\Delta E/E$ of 10^{-4}. Once beam is established in the accelerator, the relative beam energy can be measured to 10^{-4}. The absolute beam energy is known to 10^{-3}. Technically, CEBAF consists of a pair of recirculating LINACs (The North- and the South- Linac) that each use 160 0.5 m pairs of 5–element niobium cryogenic cavities to accelerate electrons; the beam recirculation is achieved using five pairs of recirculating arcs. The total number of magnets in the beam transport system is around 2200. The electron beam can be extracted and sent to any of the experimental halls after one, two,. . . , five passes through the machine.[7]

The side effects of this setup is that while it is relatively easy and quick to switch between the five available beam energies, it is very time consuming to retune the whole machine in order to alter the "per tune" energy.[8]

The Accelerator Division at Jefferson Lab managed, for the first time to provide such a non-standard beam energy (3.545 GeV) for Experiment **E93-018** . During the data acquisition period of Experiment **E93-018** , Jefferson Lab provided unpolarized, **CW** electron beams with energies in the 2.445-4.045 GeV range, at moderate beam currents (10 to 40 μA).

2.2.2 Hall C Arc

The 41.6 meter Hall C arc beamline transports the beam extracted from the accelerator to the Hall C target. The arc consists of 8 dipoles, 12 quadrupoles, 8 sextupoles, and 8 pairs of beam correctors. Instrumentation for measuring various parameters of the beam

[6]Performance of the accelerator is as per Oct-Nov 1996. Several improvements/upgrades/new features have been implemented since. Several others are projected for the near-, medium-, and long-term future.

[7]These are referred to as one-pass beam, two-pass beam, etc.

[8]Depending on the type of physics experiment, this "granularity" of the beam energy can impose severe limitation in the range of kinematics that can actually be probed and/or on the amount of overhead needed to complete a measurement.

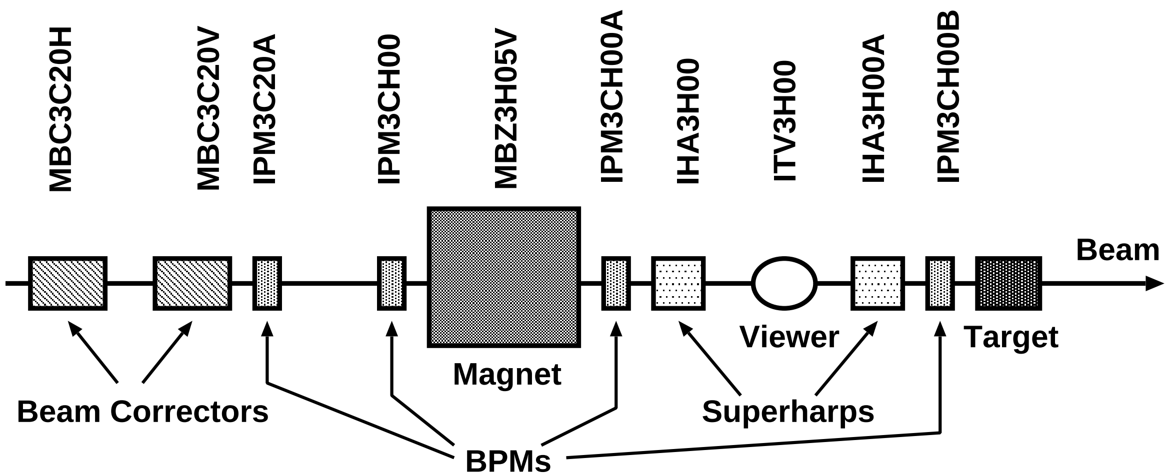

Figure 2.1: Schematic of the Hall C beamline.

(energy, energy spread, current, polarization, etc.) is also present in the arc. Figure 2.1 shows the hardware in the Hall C arc.

2.2.3 Beam Energy Measurements

Proper knowledge of the beam energy (and generally of all important beam parameters) used in a given experiment is one of the most basic requirements for virtually all types of physics analyses. At Jefferson Lab in general and in Hall C in particular the beam energy can be measured in one of the following ways:

- Using the magnet settings in the last arc of the accelerator. As the beam is bent through the last recirculating arc the value of the currents in the arc magnets, combined with the known position of the beam, yields directly the beam energy. Standard Accelerator Division Software is used for this purpose.

- Using the settings in the Hall C arc while measuring the beam position with the superharps (see definition of superharps in the next subsection). This technique involves measuring the beam position in the Hall C arc, thus essentially the actual target and the real position of the beam is used to determine the trajectory, as opposed to the "nominal" position of the arc axis. This method takes advantage of the most precise beam position devices available at Jefferson Lab - the superharps[9]; however the process is destructive for the beam so it cannot occur simultaneously with production running. A variant of this technique uses only the beam position monitors and provides information on the eventual beam energy fluctuations during an extended running period. This technique is less precise but has the advantage of being non-destructive for the primary electron beam - thus it can/was performed parallel to the production running.

- Another way of measuring the beam energy is to take advantage of some very well known physics processes to measure the beam energy. One such technique is the differential recoil method, in which a composite target (in Hall C a BeO target was used) is used to measure elastic scattering on two targets. Indeed, scattering from a nucleus of mass M yields the elastic recoil energy:

$$E_{recoil} = Q^2/2M = 2EE'sin^2(\theta/2)/M \tag{2.1}$$

  For masses M_1 and M_2 one finds for the difference

$$\Delta E_{recoil} = 2Esin^2(\theta/2)(E_1'/M_1 - E_2'/M_2) \approx 2EE'sin^2(\theta/2)(1/M_1 - 1/M_2) \tag{2.2}$$

  So measuring the recoil difference and knowing the spectrometer angle and central momentum allows one to compute the beam energy.

- Another physics-inspired method is to simultaneously measure the cross-section of the ground state and of the first excited state of carbon. The ratio of these two quantities has a very well established minimum around $Q^2 = 0.129$ (GeV/c)^2. Determining the position of this minimum in the data (eventually using a model ratio to fit in the vicinity of the minimum) allows a precise determination of the beam energy. These two methods yield excellent results (absolute knowledge of the beam energy up to 5×10^{-4} for the lower beam energy settings) and were used to calibrate the spectrometers in the commissioning phase of Hall C. However they were of little

[9] See next section for a more in-depth description of these devices.

Pass Number	1	2	3	4	5
"Nominal" Energy (MeV)	845.0	1645.0	2445.0	3245.0	4045.0
Measured Energy (MeV)	845.2	1646.3	2452.8	3245.7	4047.1
Uncertainty (MeV)	±0.8	±1.6	±2.4	±3.2	±4.1
Energy spread ($\times10^{-4}$)	0.81	0.66	1.15	1.40	2.80

Table 2.1: Summary of energy measurements for the 1996 running period.

use for the present analysis (due to the relatively high Λ production threshold the minimum beam energy used during **E93-018** was $E_{beam} = 2.445$ GeV).

- Less precise than the differential recoil and the diffractive minimum methods outlined above, but usable for all beam energies was the measurement of elastic $(e, e'p)$ scattering off hydrogen. These types of measurements were performed at least once per each beam energy used during **E93-018** and were found to provide a $\sim 2 - 3 \times 10^{-3}$ measurement for the beam energy.

The Hall C arc methods, as well as the periodical monitoring of elastic $p(e, e'p)$ scattering were used during **E93-018** to make beam energy measurements. The results are summarized in Table. 2.1. One can see that the accuracy of the absolute measurement is at the 10^{-3} level while the relative energy measurement accuracy is much better ($\sim 10^{-4}$) [25].

2.2.4 Beam Profile Monitors

The "superharp" is an improved CEBAF wire scanner that provides a two-dimensional beam profile measurement with absolute beam position readout using a high precision (18 bit) shaft encoder. Figure 2.2 shows the schematic of a superharp assembly and its associated electronics. The wooden frame of the harp supports three tungsten wires, two of them for measuring the beam profile in the horizontal (X) direction, the third one for measuring in the vertical (Y) direction. The principle of operation of the superharp is very simple: when moving the fork inside the beam (using the stepper motor) each wire will eventually cross the electron beam and secondary emitted electrons will produce a

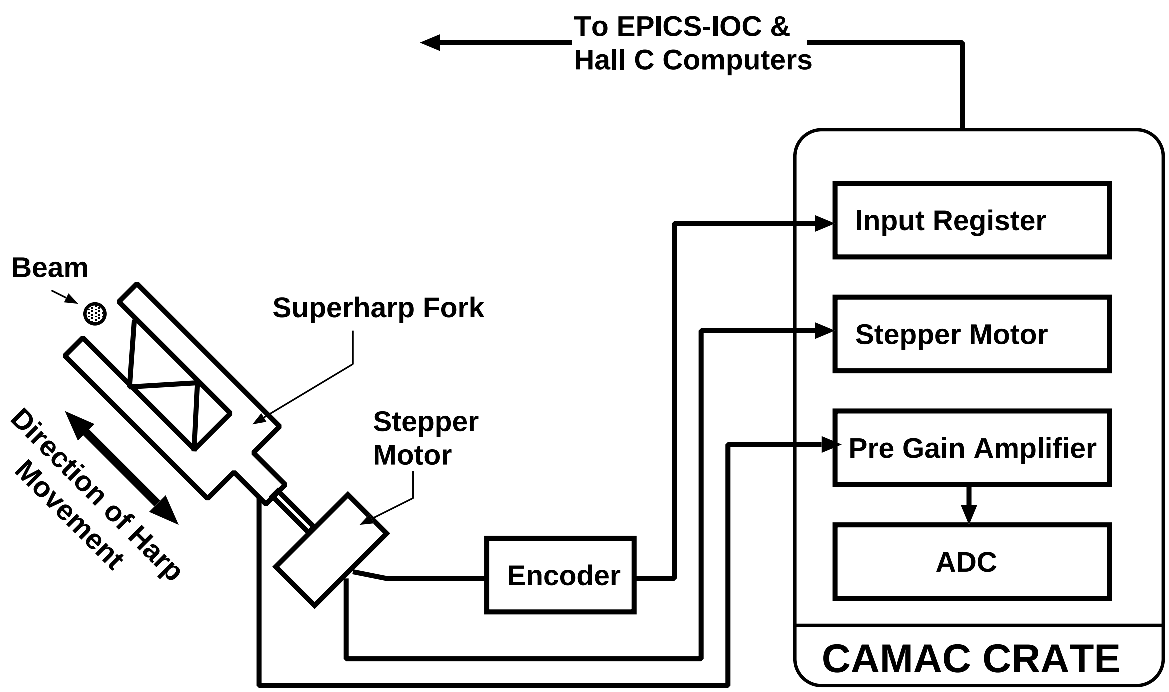

Figure 2.2: Schematic of a Hall C superharp system.

signal that will be detected and amplified. This information, together with the readout of the encoder[10] that drives the stepper motor is stored into a CAMAC ADC module and later transfered into an ASCII file for subsequent analysis. The absolute position is determined using a rotary encoder. The linear movement of the superharp wire is translated into a rotary motion via a threaded rod. The accuracy of the superharp readout is $\sim 10\ \mu$m. This proved to be totally adequate for reconstructing the actual width of the Jefferson Lab beam which is about 100 μm (FWHM) in both directions. Using this code one can extract the beam centroid as well as the widths of the beam in the X and Y directions. Combining the reading of several superharps one can also determine the angle of the beam at the entrance/exit of the Hall C arc. The superharp system used for beam energy measurement includes three pairs of superharps at the beginning, middle, and end of the arc.

[10]Essentially the current position and speed of the moving harp are recorded.

2.2.5 Beam Position Monitors

As shown in Fig. 2.1 the position of the beam in Hall C was monitored using four BPMs. A BPM is a resonant cavity mounted in the beamline such that its axis will coincide with the nominal axis of the beam. The size and shape of the resonant cavity as well as the material from which it is made[11] determine the frequency of the transverse electric and magnetic, TEM, modes possible in the cavity. The mechanical parameters of the cavity can be chosen (or tuned) such that the frequency at which the accelerator operates is also a resonant frequency of the cavity. This will ensure that the electron beam passing through the cavity will excite TEM modes. Some of these modes are sensitive to the position of the beam, or more precisely to the distance of the beam from the nominal center of the cavity. Placing four antennae at 45° intervals inside the BPM allows the collection of these signals. Comparing the signals coming from these four antennae, the relative (X, Y) position of the beam can be determined. As this is only a relative measurement, a comparison with the superharp measurement is needed to calibrate the absolute position of the BPMs. Once the calibration is done one can then use the BPM information as a non-destructive position measurement for the beam position[12]. The final accuracy of the beam position measurement was ± 1.02 mm.

2.2.6 Beam Current Monitors

The beam current in the hall was measured using three cylindrical microwave cavity beam current monitors (BCMs) and a parametric DC current transformer (Unser monitor). The design of the BCMs is somewhat similar to that of the BPMs only that now one is interested in coupling to the TEM modes that are sensitive to the beam current and relatively insensitive (e.g. the TM_{101} mode) to the beam position inside the cavity. Wire loop antennae are used to couple to resonant modes, as in the case of the BPMs. The material and shape of the cavity can be chosen to adjust the quality factor, Q (i.e. the ratio of stored energy to dissipated power, weighted by the resonant frequency,

[11]For a more general discussion of resonant cavities and their suitability for position/charge measurements see [26].

[12]To be on the safe side periodical re-calibration using the superharps might be necessary.

$Q = \omega_0 W/P_d$).

As Q is relatively sensitive to temperature fluctuations and this will directly affect the current measurement, several steps where taken to partially alleviate this problem. The quality factor Q of the BCMs was lowered and all three cavities were thermally insulated from the outside world and provided individually with thermostat controlled heaters (it is much more reliable and cheaper to thermally stabilize a device at a temperature higher than the surrounding medium by heating it). The cavities were kept at a temperature of $\sim 43.3^\circ$ C and the temperature was continuously recorded on a paper strip chart.

The BCMs were calibrated using an parametric DC current transformer (Unser monitor). The advantage of using the Unser monitor is that it has an absolute gain that is extremely stable, measured to 10^{-7}. However, the zero offset of the Unser monitor can have large drifts over relatively short periods of time (hours) so it does not provide a reliable current measurement over extended periods of time. Calibration runs in which the beam was alternately turned off and on over 2 minute intervals at successive beam currents of 10, 20, 30 and 40 μA were taken about once a day. During the beam off periods the offsets of the Unser and cavity monitors could be determined and during the beam on periods, the gains of the cavity monitors could be calibrated against the fixed gain of the Unser. In order to calibrate the gain of the Unser monitor, current from a very precise (10^{-7}) current source is sent through a wire that runs along the beam axis, thus simulating the effect of the electron beam.

2.2.7 Beam Rastering System

The CEBAF accelerator generates a high current beam, small transverse size ($\lesssim 200$ μm FWHM). In Hall C, in order to prevent damage to the target or to the beam dump, two rastering systems that increase the effective size of the beam spot are used.

The slow raster system was located just upstream of the target and was designed to protect the beam dump. As **E93-018** only used low–to–moderate currents (10–40 μA), this system was not used. The fast raster system was situated 25 m upstream of the target and it designed to prevent the melting of the solid targets and to prevent localized boiling in the cryogenic targets. It consisted of two sets of steering electromagnets, one vertical and one horizontal. The current through the magnets was varied sinusoidally[13], at 17.0 kHz (vertical direction), and 24.2 kHz in the horizontal direction. The frequencies were chosen such that the beam motion on the target would not form a stable Lissajoux figure. The typical raster size used in **E93-018** was $\pm$ 0.5 mm in both the horizontal and vertical directions (i.e. a 1 mm X 1 mm box). As the rastering signals were sinusoidal, the beam spent more time at the edges of the box than it does at the center, thus the power was not uniformly distributed over the entire area of the raster pattern. Despite this technical inconvenience, the reduction in power density due to the raster was enough to prevent significant density fluctuations (localized boiling) in the cryogenic target used (see section 4.4.7 for the target boiling correction applied).

2.3 Target

The target assembly used during **E93-018** consisted of two separate target ladders, one for (thin) solid targets and one for the (extended) cryogenic targets. Remotely controlled stepper motors allowed the vertical movement of each ladder (such that the desired target could be positioned in the beam path). Switching from one target ladder to the other was accomplished by first lifting the current ladder to its uppermost position (the nominal "HOME") and then rotating the target ladder around the vertical axis by 90^o. This type of motion was also remotely controlled. All target motion required the electron beam to be removed from Hall C, thus adding to the overhead of the experiment.

2.3.1 Scattering Chamber

The Hall C scattering chamber used in **E93-018** is a large (inner radius $\sim$ 61.6 cm, 150 cm high) cylinder with relatively thick ($\sim$ 6.35 cm) aluminum walls. The main purpose of the scattering chamber was to protect, mechanically and thermally, the delicate

[13]This description of the raster system matches the experimental situation from the fall of 1996 in Hall C. The many improvements/changes in the rastering system that occured since that time are beyond the scope of this work.

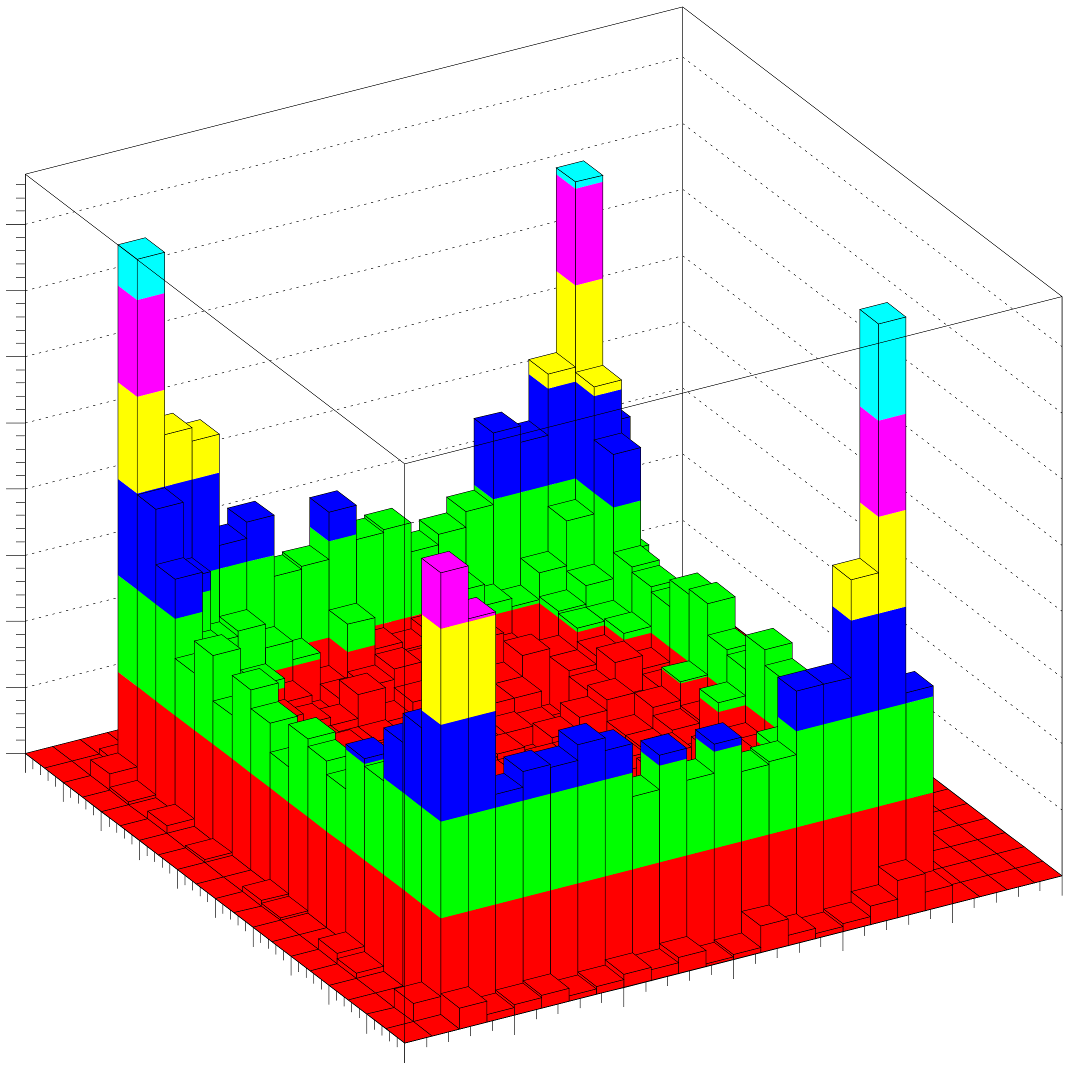

Figure 2.3: x and y fast raster currents (corresponding to the x and y positions of the beam at the target), showing the beam intensity distribution. During **E93-018** the raster size was set to $\pm$ 0.5 mm for both x and y directions.

liquid and solid targets used in physics experiments. The chamber had cutouts large enough to cover the angular acceptance of the two Hall C spectrometers, including the projected (but as of now not implemented) out-of-plane operation of the SOS. Openings for the entrance/exit of the beam were also provided, as was a pumping port (for attaching the vacuum pump(s)) and several "viewing ports" for the visual inspection of the chamber while under vacuum[14]. The beam exit window was made of Titanium foil, approximately 70 mg/cm^2 thick. As the scattering chamber connected directly to the beamline, no entrance window was present. The HMS opening of the scattering chamber was 20.32 cm in height and had a 40.64 μm thick aluminum window. The SOS opening was 12.7 cm in the vertical dimension and its aluminum window was $\sim$ 20.32 μm[15]. The scattering chamber was mounted on a thick plate which is in turn attached on top of the Hall C pivot. The top of the scattering chamber had openings for the cryotarget plumbing and for the target lifting and rotation mechanisms.

2.3.2 Cryotarget

E93-018 used the "standard" Hall C cryogenic ladder, in its 1996 configuration. Figure 2.4 shows the general view of the cryogenic target ladder and an enlarged view of a single target loop. On the ladder there were three target loops, each containing a long ($\sim$ 15 cm) and a short ($\sim$ 4 cm) cell. For measuring the contribution coming from the aluminum walls of the cryotargets a pair of "dummy" targets was also present. These consisted of flat aluminum targets placed at the approximative position of the endcaps of the cryotarget(s) and made of the same type of material as the endcaps themselves. These "dummy" targets were about ten times thicker than the actual cell walls. This not only significantly reduced the amount of time dedicated to the empty target measurements but also has the advantage that the total thickness (in terms of radiation lengths) of the "dummy" target matches almost perfectly the thickness of the "liquid target + endcaps"

[14]A radiation hardened TV camera placed inside the scattering chamber allowed the visual inspection of the target ladders during data taking.

[15]The thickness of the entrance/exit windows represents the balance between safety requirements and the need to minimize unwanted processes like multiple scattering and/or bremsstrahlung.

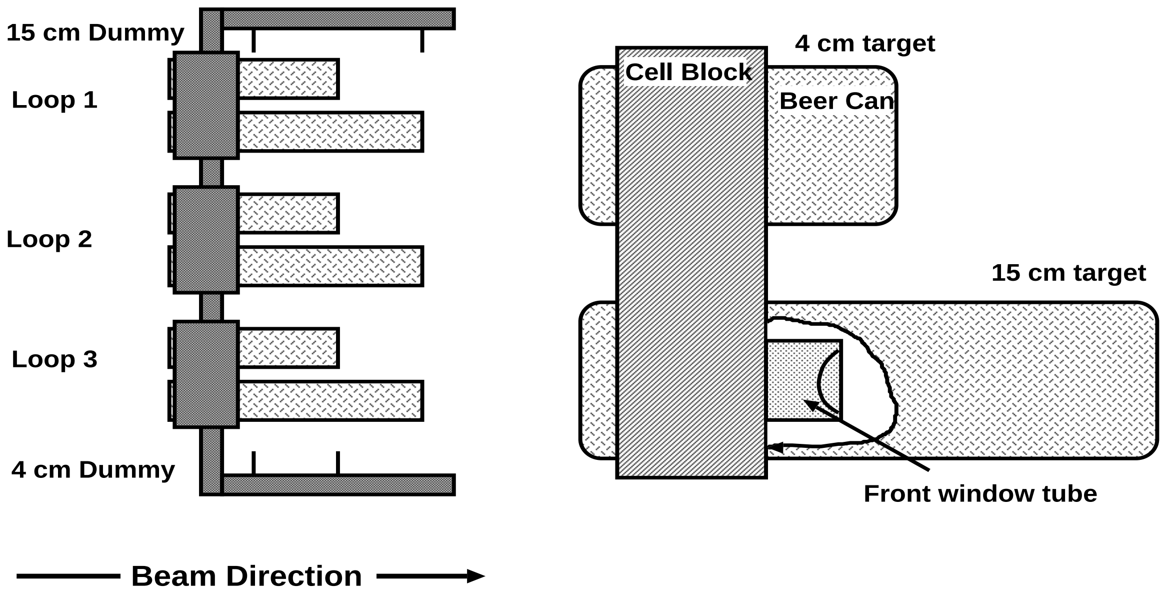

Figure 2.4: Schematic of the Hall C cryotarget ladder and enlarged view of a single target loop.

combination.

The basic 1996 Hall C cryotarget loop consisted of the target block (holding the long and short cells), a circulation fan, a heat exchanger, a low power heater, and a high power heater. The target cells are cylindrical, 6.731 cm in diameter, with $\sim$ 17.78 μm–thick side walls, made out of chemically etched Coors^{TM} beer can blanks. The cells were mounted on a common (thick) aluminum cell block, which was in turn connected to the heat exchanger. The axial fan mounted inside the heat exchanger forces the target liquid to circulate through the cells. As seen in Fig. 2.4 both the entrance and endcap of the target are slightly curved. This means that the actual thickness of the liquid target will vary slightly depending on the position of the beam on target. As any cross-section calculation critically depends on the knowledge of the target thickness, the position of the beam on target was closely monitored during **E93-018** . The beam was centered on the nominal center of the target to within 1 mm (this implies an uncertainty of 0.3 % or less in the target thickness for the 4 cm hydrogen cell used during the experiment)[16].

[16]All known sources of uncertainty, including target-related ones, will be discussed in detail in the

Cold helium gas provided by CEBAF'S End Station Refrigerator (ESR) at about 15 K was used as a cooling agent for the liquid targets. The power rating of these targets was around 200 Watts (i.e. the cooling system can safely dissipate up to 200 W of beam-deposited energy in the target medium), exceeding by a large margin the requirements of **E93-018** where currents were modest ($\leq$ 40 μA) and only the 4 cm target was used[17]. Enough cooling power was available to simultaneously keep all cells at cryogenic temperature.

The loops are kept at constant temperature regardless of the presence/absence of the beam by increasing/decreasing the current on the heaters, keeping the total dissipated power constant. This mode of operation is called "constant heat load" and was the preferred mode for operating the cryotargets. Another possibility would be to actually regulate the amount/flow of cooling agent (using the Joule-Thompson (JT) valves) but that is a slower and less responsive process that was used only when significant long term changes in the temperature/pressure of the cooling agent coming from ESR were observed. In the constant heat load mode of operation the high power heater compensates for the bulk of the heat load, while the low power heater maintains the correct operating temperature, accounting for small variation in the coolant parameters and/or beam intensity.

During **E93-018** , however, only two loops (loops 1 and 3) were operational. One was filled with hydrogen, the other one with liquid deuterium (interspersed with the **E93-018** data taking were periods when the "sister" experiment E91016 ran and needed both H_2 and D_2 targets). The middle loop had a small leak and thus was not used for any measurements. The hydrogen loop pressure was $\sim$ 29 PSIA. Table 2.2 summarizes the normal running parameters for the hydrogen and deuterium loops. As seen in Table 2.2 both targets are operated in a subcooled fashion. This offers a much more stable running conditions, less sensitive to (small) sudden changes in the heat load and/or cooling agent parameters. Each loop contains two Lakeshore Cernox resistors measuring the temperature of the loop to within 50 mK.

---

error analysis chapter.

[17]This set of conditions require less than 50 Watts of cooling power.

Target	Temperature (K)	Density (g/cm^3)	Purity (%)
hydrogen	19.0±0.05	0.072304±0.0003	99.8±0.10
deuterium	22.0±0.05	0.16708±0.0007	99.2±0.13

Table 2.2: Summary of the normal running conditions for the LH2 and LD2 targets

In Table 2.3 and 2.4 lists of materials for the liquid/dummy targets are provided. As these two tables contain extremely relevant information for the cross-section calculation (empty target subtraction) and/or corrections applied to the cross-section (i.e. external bremsstrahlung depends critically on the material "seen" by the incoming/outgoing electron) they will be revisited in the data analysis chapter.

2.3.3 Solid targets

As stated above the standard Hall C equipment includes also a water cooled solid target ladder. The configuration used during **E93-018** allowed for a total of 5 targets, out of which 2 could be thick targets. In addition to the rotation in and out of the beam already explained and the vertical motion that allows different targets to be put in the beam path, the solid target ladder could also be rotated (manually) around its own vertical axis, thus changing the effective incident angle of the beam on target (useful for minimizing straggling in the target material, for example).

As the focus of **E93-018** was exclusively on liquid hydrogen targets, only the thin ^{12}C was used for optics studies. Also the "slanted target", a long, thin ^{12}C target mounted at a $\sim 60^o$ angle with respect to the vertical was used. By moving the target ladder up and down one can change the position of the interaction point along the beam z-axis, to study the effects of an extended target.

2.4 Spectrometers

The standard detection system in Hall C at Jefferson Lab consists of two highly flexible electromagnetic spectrometers that sport medium resolution and relatively large

Item	t (cm)	ρ (g/cm^3)	t$\times\rho$ (g/cm^2)	Xo (g/cm^2)	r.l. (%)
Entrance cap	0.0071	2.700	0.0192	24.01	0.080
Hydrogen (4 cm)	4.38	0.0723	0.3166	61.28	0.516
Hydrogen (15 cm)	15.36	0.0723	1.1106	61.28	1.812
Deuterium (4 cm)	4.20	0.1670	0.7014	122.6	0.572
Deuterium (15 cm)	15.16	0.1670	2.526	122.6	2.060
Target wall	0.0125	2.700	0.0338	24.01	0.141
Exit Cap	0.0125	2.700	0.0338	24.01	0.141
HMS-side window	0.0406	2.700	0.1097	24.01	0.4566
HMS air gap	15.0	0.00121	0.0182	36.66	0.0496
HMS Kevlar entrance	0.0381	0.74	0.0282	55.2	0.0511
HMS Mylar entrance	0.0127	1.39	0.0177	39.95	0.0443
SOS-side window	0.0203	2.70	0.0548	24.01	0.2283
SOS air gap	15.0	0.00121	0.0182	36.66	0.0496
SOS Kevlar entrance	0.0127	0.74	0.0094	55.2	0.0170
SOS Mylar entrance	0.0076	1.39	0.0106	39.95	0.0265

Table 2.3: Material List and Properties for the Target Cell and Scattering Chamber.

Target	Al 4 cm	Al 4 cm	Al 15 cm	Al 15 cm
Al Alloy	5052	3004	5052	3004
Density (g/cm^3)	0.2572	0.2643	0.2570	0.2646
Thickness (cm)	0.09596	0.09667	0.09601	0.09675
X_0 (g/cm^2)	23.6311	23.6396	23.6311	23.6396
Radiation Length	0.0109	0.0112	0.0109	0.0112

Table 2.4: Characteristics of the “dummy” Aluminum Targets.

momentum and angular acceptances. The High Momentum Spectrometer (HMS) has a momentum "bite" $\Delta p/p$ of ± 10 % and is capable of analyzing high-momentum particles (up to 7.5 GeV/c). The Short Orbit Spectrometer has a ± 20 % momentum acceptance but its maximum central momentum is only around 1.7 GeV/c. While the short length of the SOS makes it an ideal choice for detecting short-lived particles (a crucial point that made **E93-018** possible), its detector package provides all of the particle identification (PID) necessary for its use as an electron spectrometer as well.

2.4.1 High Momentum Spectrometer

The HMS is a superconducting spectrometer[18] based on a $Q\overline{Q}QD$ design, with a vertical bend angle of 25 degrees. The magnets, as well as the detector frame are supported by the same carriage, thus fixing the detector frame with respect to the optical axis. To help distribute the weight, the shielding hut that protects the detector hut is supported by a separate carriage. Both carriages can rotate around a rigidly mounted central bearing. In Fig. 2.5 a side view of the HMS spectrometer and the HMS detector hut are shown.

The quadrupoles are cold iron superconducting magnets. Soft iron wrapped around the coils enhances the central field while reducing stray fields. Multipole windings are present for each quadrupole, although these were not used during **E93-018** . For each quadrupole, the power is provided by three water-cooled "Danfysik System 8000" power supplies. These low-voltage, high-current supplies can provide up to 1250 A at 5 V. The corrector coils are powered by three HP power supplies (I_{max} = 100 A at 5 V). The quadrupoles are set by current, based on the measured $\int Bdl$ vs I curve. The optical axis of each quadrupole was determined using the Cotton-Mouton method [27]. Differences of up to 2 mm between the mechanical and optical axis were found. In the final configuration all HMS magnets where aligned (to 0.2 mm) according to their optical axes.

The HMS dipole is a straight-pole face superconducting magnet providing a 25 degree upwards bend for charged particles up to 7.5 GeV/c. This massive device has a bend radius of ~ 12.06 m and a gap width of ~ 42 cm. Its actual length is ~ 6 m, although

[18] As in the case of the target, ESR provides the necessary cooling power as 2 K liquid helium or, more frequently as 15 K cold helium gas.

the effective length is smaller, ~ 5.26 m. Its "Danfysik System 8000" power supply can deliver up to 3000 A at 10 V (although in practice, given the current maximum beam energy of the machine, one needs at most half of that current). The dipole field is set and regulated using a NMR probe. The typical setting/settling time when changing momenta was around 15 minutes during the **E93-018** running. The fields in both the dipole and the quadrupoles are stable at the 10^{-4} level and the reproducibility is somewhat better than 10^{-3}. Tables 2.5 and 2.6 present a summary of the main construction parameters of the HMS magnets, while in Table. 2.7 the final performance of the system (including multiple scattering effects and the finite resolution of the drift chambers) is shown.

	Q1	Q2/Q3
Gradient (G/cm)	605	445
"Good Field" Radius (cm)	22	30
Pole Tip Field (T)	1.50	1.56
Radius to Pole (cm)	25	35
Magnetic Length (cm)	189	210
Stored Energy (10^6 J)	0.25	0.5
Weight (tons)	20.0	30.0

Table 2.5: Design characteristics of the HMS quadrupoles. As Q2 and Q3 are identical, they share a single column in the table.

In its standard operating mode (the mode used during **E93-018**), HMS provides point-to-point focusing in both the dispersive and non-dispersive directions. This tune provides large momentum and angular acceptance, as well as extended target acceptance up to ± 6 cm. In this tune, Q1 and Q3 focus in the dispersive direction and Q2 focuses in the transverse direction.

HEAVYMET (machinable Tungsten alloy, with ~ 10 % CuNi; $\rho \equiv 17$ g/cm^3) collimators (for solid angle determination) and sieve-slits (for optics studies) were placed in a vertical stack ~ 1.26 m from the target in front of the first HMS quadrupole. The thickness of these plates (2 inch) ensures that even the most energetic electrons (based on available Jefferson Lab energies) cannot punch through; this ensures that the size of the collimator aperture precisely determines the solid angle (this statement holds true for

Gap	421 cm
"Good Field" Width	± 30 cm
Bend Angle	25^o
Max. Pole Tip Field	1.66 T (6 GeV/c)
Dynamic Field Range	10:1
Field Uniformity ΔB/B	0.001
Pole Face Rotations	6^o, -6^o
Effective Length	5.26 m
Coil Configuration	$4.1*10^5$ A-turns/pole
Operating Current	6,881 A
Coil Cooling	Thermal Siphon 4.3 K LHe
Weight	470 Tons

Table 2.6: Design characteristics of the HMS Dipole.

both thin and extended targets, although the calculation becomes more involved when using extended targets), and that the events seen at the focal plane actually go through the pattern of holes drilled into the sieve-slit, when doing optics studies.

All of the production **E93-018** data was taken using the so–called "large" collimator. This collimator had an octagonal aperture designed to limit the solid angle as follows: For a δ cut of ±10 %, the solid angle (for a thin target) was around 6.8 msr, with a less than 10 % drop in the acceptance (edges versus center).

2.4.2 Short Orbit Spectrometer

The Short Orbit Spectrometer (SOS) is a $QD\overline{D}$ design, which is based upon the Medium Resolution Spectrometer (MRS) at LAMPF. SOS has a large momentum acceptance, ± 20 %, a large solid angle acceptance, but its extended target acceptance is limited (∼ 2–3 cm). In its standard operating mode the quadrupole focuses in the horizontal (i.e. non-dispersive) direction while the two dipoles bend the incoming particles first upward by 33°, then downward by 15^o, for a total/net bending angle of 18°. The faces of the two dipoles are shaped such that the resulting fringe fields provide some focussing in the dispersive direction. The dipoles share a common yoke.

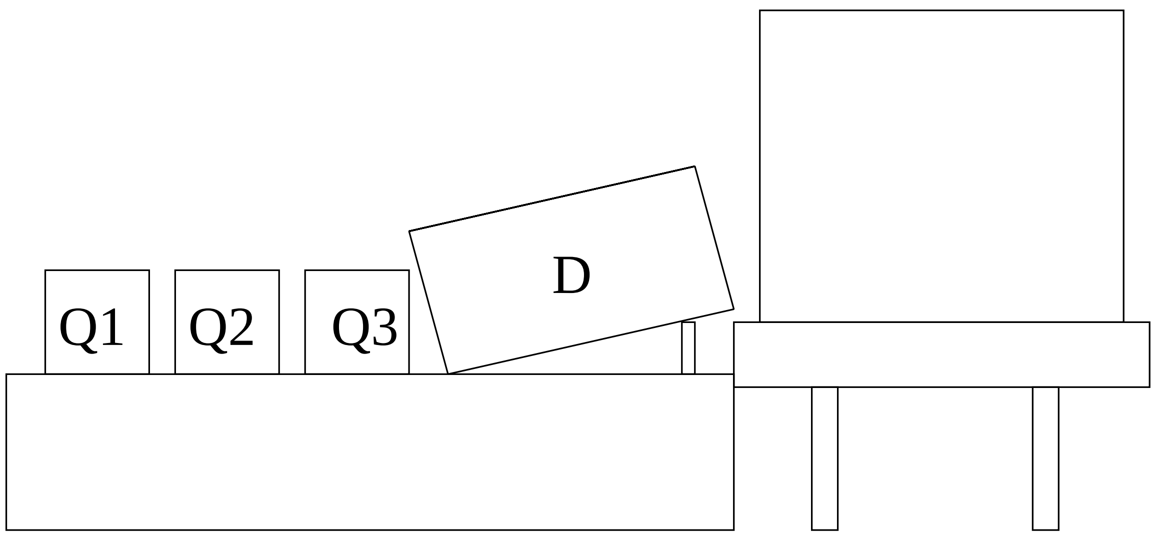

Figure 2.5: Side view of the HMS

Maximum central momentum	7.4 GeV/c (4.4 tested)
Momentum acceptance	$\pm 10\%$
Momentum resolution $[\delta p/p]$	0.04 %
Solid angle (no collimator, thin target)	8.1 msr
In-plane angular acceptance	± 32 mr
Out-of-plane angular acceptance	± 85 mr
In-plane angular reconstruction	0.5 mr
Out-of-plane angular reconstruction	1.0 mr
Extended target acceptance	± 7 cm
Horizontal Vertex reconstruction	$2 - 3$ mm

Table 2.7: Summary of the HMS performance. Multiple scattering effects, as well as the finite resolution of the drift chambers are taken into account.

All magnets, as well as the detector hut, are supported by a common carriage assembly. According to its design specification, SOS should be able to move out-of-plane by up to 20°, aided by hydraulic jacks. While these jacks were in place during **E93–018**, they were not operational. Figure 2.6 shows a side view of the SOS spectrometer, complete with its detector stack. Unlike the HMS case, the optical and mechanical axes of the magnets where found to coincide within 0.1 mm. The final alignment of the magnets was accurate to 0.2 mm. By rotating the entire SOS spectrometer, the magnets can move radially by up to 2 mm; however the positions are reproducible to better than 0.5 mm.

The quadrupole and dipoles are normal conducting magnets, cooled by the Hall C Low Conductivity Water system which provides water at 250 PSI. Remotely controlled InverPower power supplies (one for each magnet) provide the required power. As the polarity of these power supplies can be reversed, SOS can detect either positive or negative particles. While the power supplies for the quadrupole and the second dipole provide up to 1000 A at 160 V, the supply for the first dipole provides 1000 A at 250 V. The highest momentum setting attainable with SOS is ~ 1.75 GeV/c, limited by the current limit on the first dipole. Given the sharp pole edges of the spectrometer, saturation effects can be seen for SOS central momenta as low as 1.5 GeV/c. The highest SOS momentum setting measured during **E93-018** was 1.634 GeV/c, so saturation effects are important in data analysis. Both the quadrupole and the dipoles had Hall probes mounted inside them. These probes measure and regulate the magnet settings.

For **E93-018** the SOS was operated in the "standard" point-to-point tune, with point-like focusing in both the dispersive and non-dispersive directions. Table 2.8 summarizes the SOS performance. As during **E93-018** there were kinematic settings that required a shallow SOS angle combined with a high SOS momentum, the steering of the primary beam by the SOS fringe fields was of certain concern. The movement of the beam on the Hall C beam dump viewer with increasing SOS moment (for some small SOS angles) was plainly visible.

A slit system similar in design with the HMS one was installed in front of the SOS quadrupole (at ~ 1.26 m). The slit box had three HEAVYMET collimators (namely the "large", the "small" and the "sieve-slit" collimators); there was also an empty space.

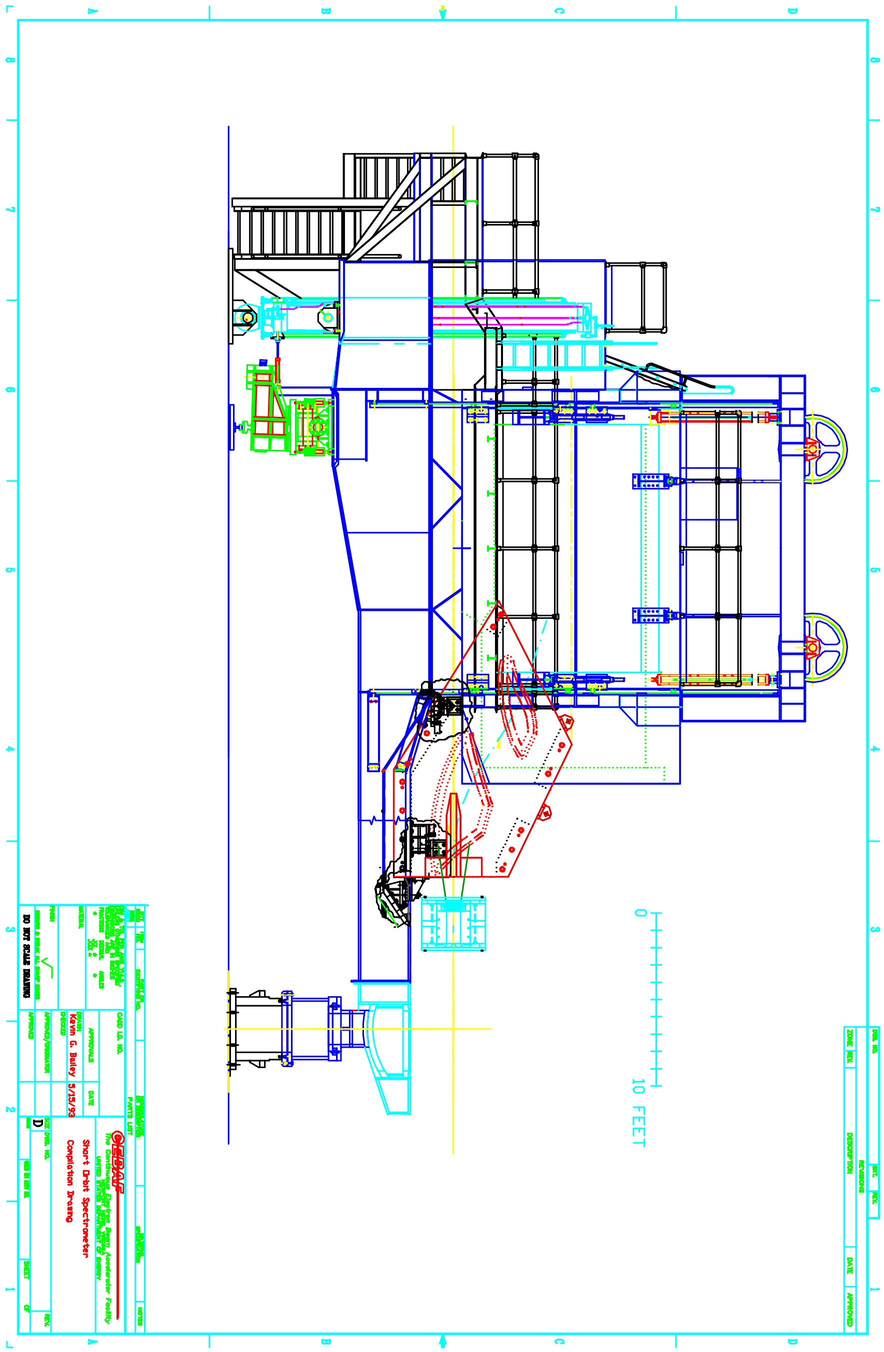

Figure 2.6: Side view of the SOS.

Maximum central momentum	1.75 GeV/c
Momentum Acceptance	$\pm 20\%$
Momentum Resolution [$\delta p/p$]	0.1 %
Solid angle (no collimator, thin target)	$<$ 11 msr
In-plane angular acceptance	± 70 mr
Out-of-plane angular acceptance	± 40 mr
In-plane angular resolution	4 mr
Out-of-plane angular resolution	0.5 mr
Extended target acceptance	$2 - 3$ cm
Horizontal Vertex reconstruction	$1 - 2$ mm

Table 2.8: Summary of the SOS performance. The finite resolution of the SOS drift chambers ($\sim$ 200 μm per plane) is taken into account. No saturation effects are taken into account when computing resolutions, etc.

The SOS sieve-slit had precisely spaced, 0.508 mm diameter holes, that formed a 9x9 lattice pattern. Some holes were missing and acted as a key that uniquely determine the correct orientation of the "reconstructed" slit (i.e. with a perfectly symmetric slit one will never be able to tell "left" from "right", "top" from "bottom"). As in the case of the HMS slit, the central hole has half the diameter of the other holes (with the idea that the best possible angular resolution is in the middle of the spectrometer and the smaller hole should, in principle, give some measure of what that resolution might be). Also, the central three rows of the SOS slit were more closely spaced than the other rows (the ability to separate, or not these closely spaced rows is very telling in the process of evaluating the angular resolution). Both the "large" and the "small" collimators had octagonal apertures that defined the solid angle. Given the thickness of these plates ($\sim$ 6.35 cm) these holes were flared so as to better match the acceptance of the spectrometer. Table 2.9 shows the characteristics of the HMS (SOS) collimators. The "large" SOS collimator was used for all production running during **E93–018**.

Name	Spectrometer	$d\Omega$ (msr)	Central Width (mr)	Central Height (mr)	Shape	Flared (Yes/No)
large	HMS	6.74	± 27.5	± 70.0	Octagonal	yes
small	HMS	3.50	± 20.0	± 50.0	Octagonal	yes
large	SOS	7.55	± 57.5	± 37.5	Octagonal	yes
small	SOS	3.98	± 32.5	± 35.0	Octagonal	yes

Table 2.9: Summary of the size and shape of the HMS and SOS collimators. All figures are for a thin solid target. All solid angles should be smaller for an extended target.

2.4.3 Spectrometer Optics

The magnetic properties (optics) of the HMS and the SOS spectrometers are described in the framework of the COSY INFINITY program [28] for both the analysis program `Engine` and the Monte Carlo simulations (see section 4.3).

The COSY program generates, for each spectrometer, forward transport matrices that allow the calculation of the focal plane quantities (x_{FP}, x'_{FP}, y_{FP}, and y'_{FP}) in terms of the target quantities (x'_{TAR}, y_{TAR}, y'_{TAR}, and $\delta = (p - p_0)/p$), with p_0 being the central momentum of the spectrometer. Each of the focal plane quantities is expressed as:

$$a = \sum_{i,j,k,l} A^a_{i,j,k,l} (x'_{TAR})^i y^j_{TAR} (y'_{TAR})^k \delta^l \quad i,j,k,l \in \boldsymbol{N}, \qquad i,j,k,l \in \Big[0, N\Big] \tag{2.3}$$

$a \in (x_{FP}, x'_{FP}, y_{FP}, y'_{FP})$; where N is the order of the expansion and $A^a_{i,j,k,l}$ is a column of the forward transport matrix. Although COSY allows expansion to arbitrary orders (thus the INFINITY in its complete name), the HMS forward matrix was calculated to 5th order, while for the SOS a 6th order representation was used. In both cases the matrices were sparse.

By inverting the forward transport matrix one obtains the so–called reconstruction matrix which gives the target quantities in terms of the focal plane quantities. Note that as only four quantities are measured at the focal plane, only four independent quantities can be reconstructed at the target. The typical choice is to assume $x_{TAR} = 0$.

For the simulation code(s) used in Hall C, the forward/reconstruction matrices were generated based on theoretical models of the HMS and SOS spectrometers that take into account the positions, fields and lengths of the magnetic elements (quadrupoles and dipoles) of each spectrometer. The code then uses the forward matrices to propagate the tracks produced by the event generator from the target to the focal plane (alternatively events can be propagated to key points inside the spectrometer to check each track against various apertures.), the coordinates of succesfull events are smeared to account for multiple scattering and the finite resolution of the detectors, then the smeared focal plane coordinates are used to reconstruct the event at the target.

While one can use the theoretical (i.e. COSY–generated) matrix elements in the `Engine` [29] for reconstructing target quantities, the recommended method (and the method used in this analysis) is to fit the reconstruction matrix elements from data. The fitting procedure is described in [30] and involves fitting sieve slit data for angle reconstruction/checking, carbon elastic data (i.e. known correlations between angle and momentum) to reconstruct momentum, and sieve slit data from targets at different positions along the beam (i.e. slanted target data) to reconstruct y_{TAR}.

As part of the present **E93-018** analysis (and working together with members of the E91–016 collaboration) new matrix elements were fit for both HMS and SOS. Some of the results are shown below[19]. In Fig. 2.7 the angular reconstruction of the target angles is shown for the new set of HMS matrix elements. The top two panels show respectively the out–of–plane (left) and the in–plane angle (right) reconstruction for a sieve slit run. The bottom panel shows the correlation between the two angles. A thin slanted carbon target was used for this calibration run. The position of the slanted target for this particular run corresponds to $Z_{target} = 0$. In Fig. 2.8 the angular reconstruction for the new SOS matrix elements is shown. The running conditions were similar to those of the HMS plot (i.e. carbon target at $Z_{target} = 0$, sieve slit, etc.). Again, the missing holes act as a key ensuring that the reconstructed angles carry the proper sign. As was the case for HMS, the central hole is smaller in diameter than the other holes and, specific to

[19]Complete sets of plots documenting the HMS and SOS fits (as well as various tests performed with the new sets of matrix elements) are available in the Hall C documentation repository.

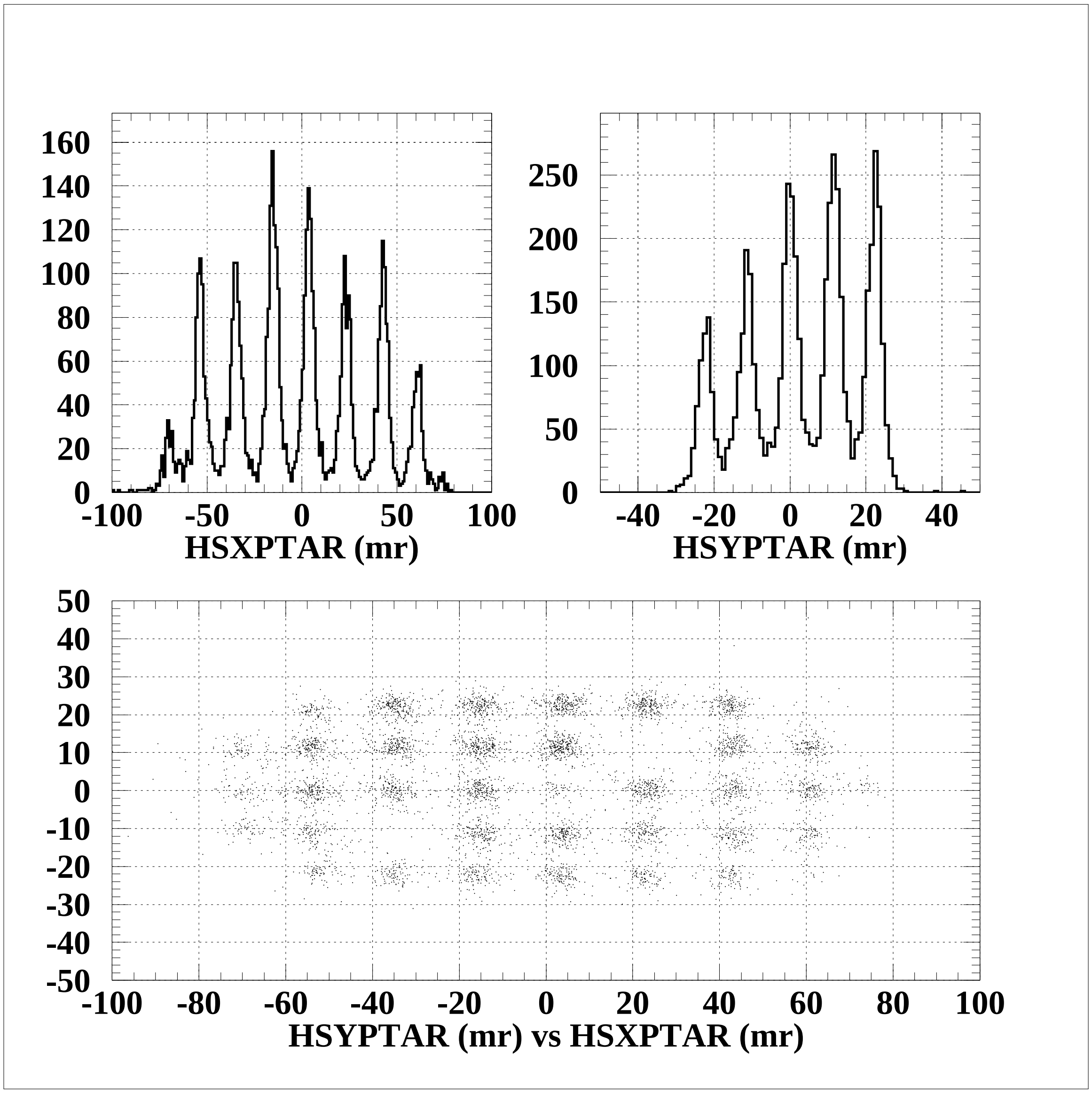

Figure 2.7: HMS out–of–plane (HSXPTAR) (top left) and in–plane (HSYPTAR) (top right) angle reconstruction at the target for a sieve slit run using the new HMS matrix elements. The target used was the slanted carbon target, positioned to intercept the beam at $Z_{target} = 0$. The bottom panel shows the correlation between the two angles. The two missing holes act as a key ensuring the correct sign of the angle reconstruction. The central hole is smaller that the other holes providing an estimate of the angular reconstruction resolution.

the SOS sieve slit. The central three columns (in $SSYPTAR$) are more closely spaced (8.04 mr) than the others (12.07 mr). Figure 2.9 provides a closer look at the HMS angular reconstruction. The quantities shown are the x and y coordinates (in cm) of the reconstructed tracks at the sieve slit position. The sieve slit pattern is reconstructed very accurately, even at the edges of the acceptance. One might also want to note the shift of the central hole from its nominal (0,0) position towards positive values of x (by about 5 mm). This effect was first observed during the fitting of the new HMS matrix elements and was later confirmed, by reconsidering the survey data available (and finding an inaccuracy in the original surveyor's report), as a misalignment of the whole collimator assembly (i.e. the structure that holds both the sive slits and the various collimators). The new HMS and SOS matrix elements were tested using inclusive $p(e,e')$ elastic data (correlations between W^2 and focal plane and target quantities were studied), as well as coincidence $p(e,e'p)$ data (angular–momentum correlations, E_m and p_m (missing energy and missing momentum) as a function of focal plane and target quantities were studied). Also data vs Monte Carlo comparisons (see section 4.3) were performed for the elastic (both inclusive and coincidence) scattering data off hydrogen. As the new HMS and SOS matrix elements were released for the general use of Hall C collaborators, they were extensively tested by several groups working on the Jefferson Lab experiments that ran in 1996. To date, no serious complaints were recorded for neither the HMS, nor the SOS matrix elements.

2.5 Detector Package

The standard HMS and SOS detector packages consisted of two drift chambers, two sets of x-y hodoscope scintillators, a gas Čerenkov detector, and, in the back of the detector stack, a layered lead-glass electromagnetic shower counter detector.

The hodoscope scintillators were used to form the primary trigger. They also provided time-of-flight and dE/dx information. The drift chambers provided tracking information. The gas Čerenkov and the shower counter were used for particle identification (mainly electron-pion discrimination). The layout of the SOS detector package was more compact

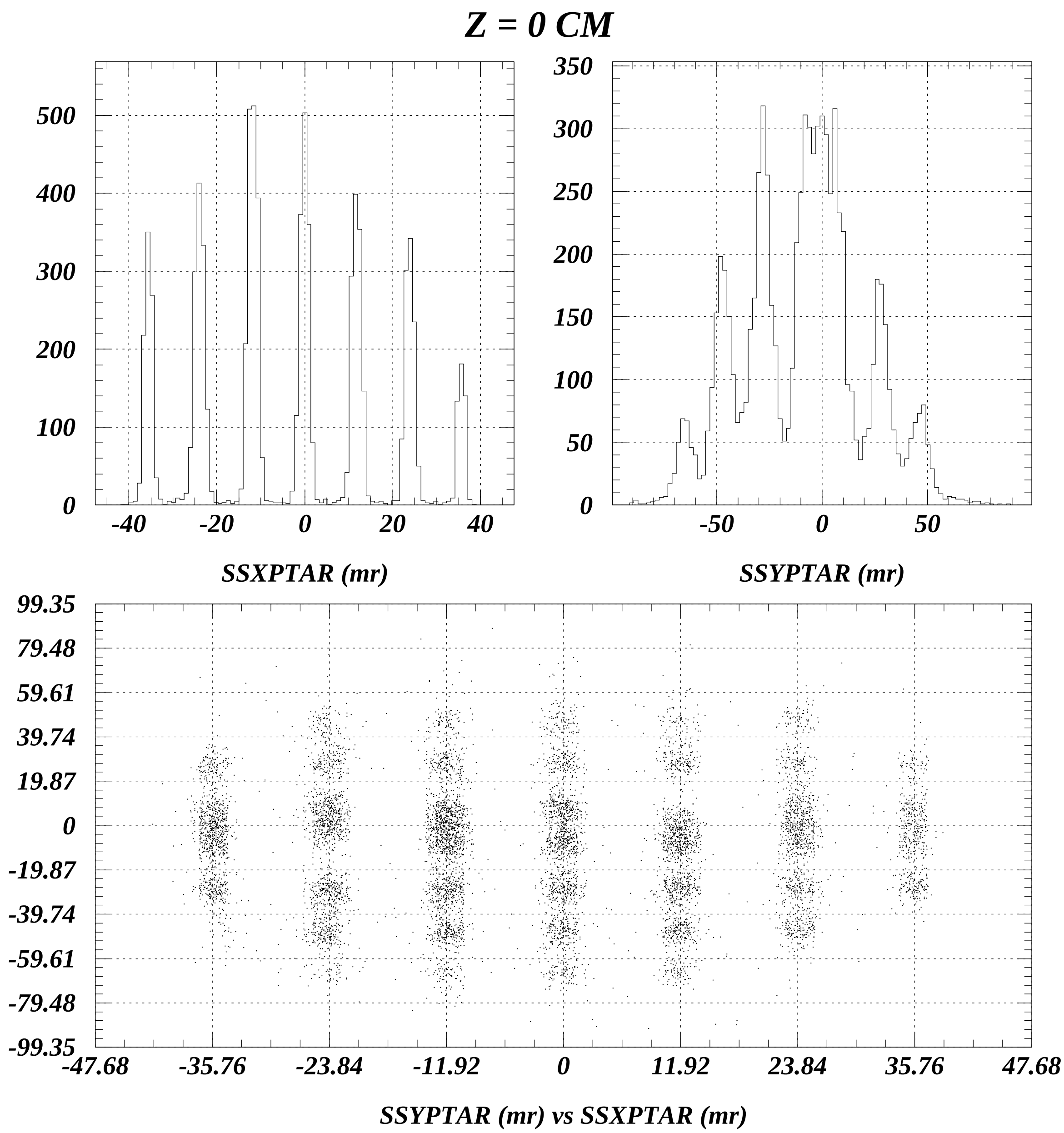

Figure 2.8: SOS out–of–plane (SSXPTAR) (top left) and in–plane (SSYPTAR) (top right) angle reconstruction at the target for a sieve slit run using the new SOS matrix elements. The target used was the slanted carbon target, positioned to intercept the beam at $Z_{target} = 0$. The bottom panel shows the correlation between the two angles. The two missing holes act as a key ensuring the correct sign of the angle reconstruction. The central hole is smaller that the other holes providing an estimate of the angular reconstruction resolution. The central three columns (in $SSYPTAR$) are more closely spaced than the rest.

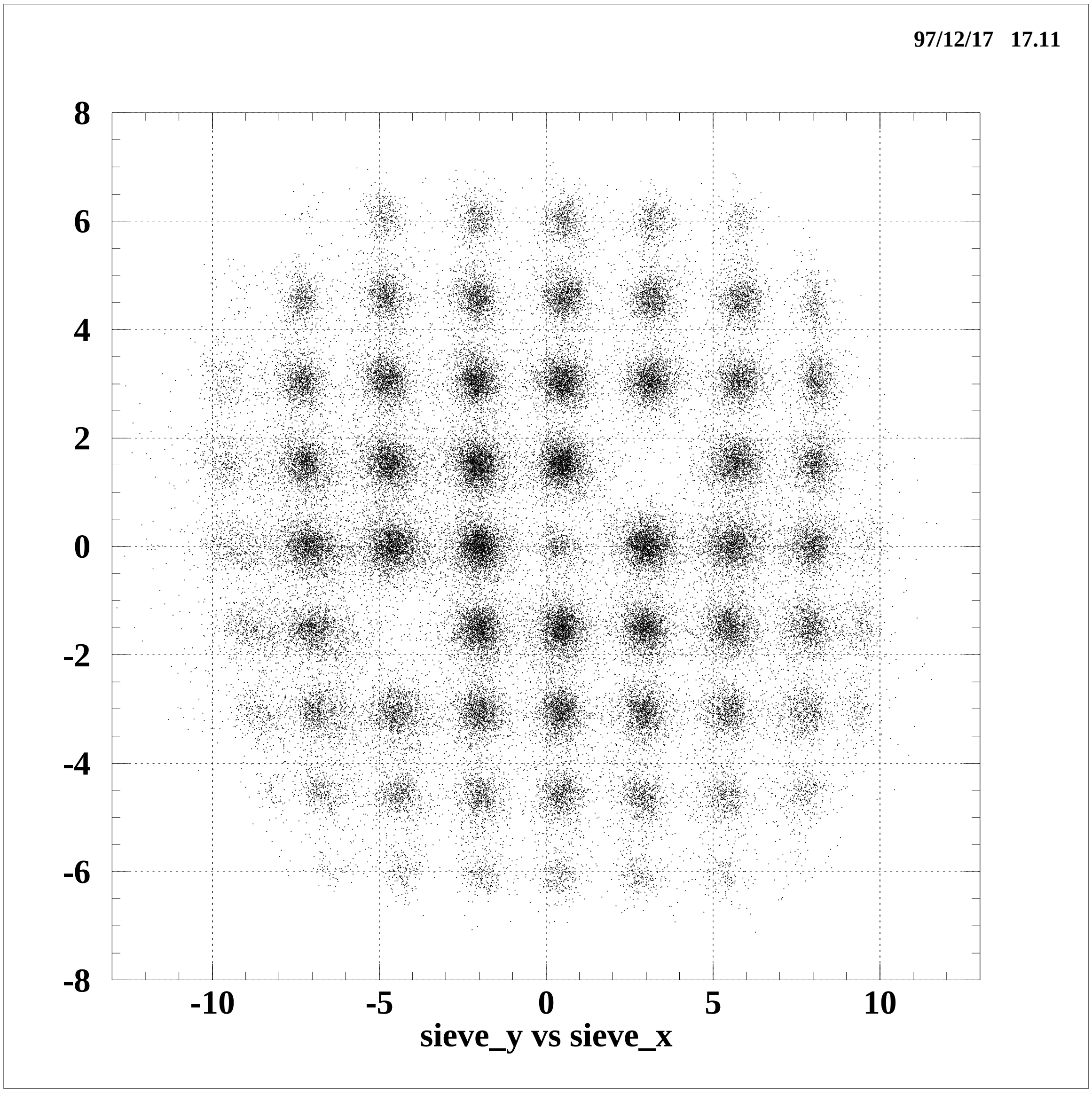

Figure 2.9: x (sieve_x) vs y (sieve_y) coordinate reconstruction at the sieve slit position, using the new HMS matrix elements. The sieve slit pattern is correctly reproduced even at the edges of the acceptance. Also of note is the shift (by ~ 5 mm) of the holes towards positive values of x due to an offset of the entire collimator assembly. All coordinates are in cm.

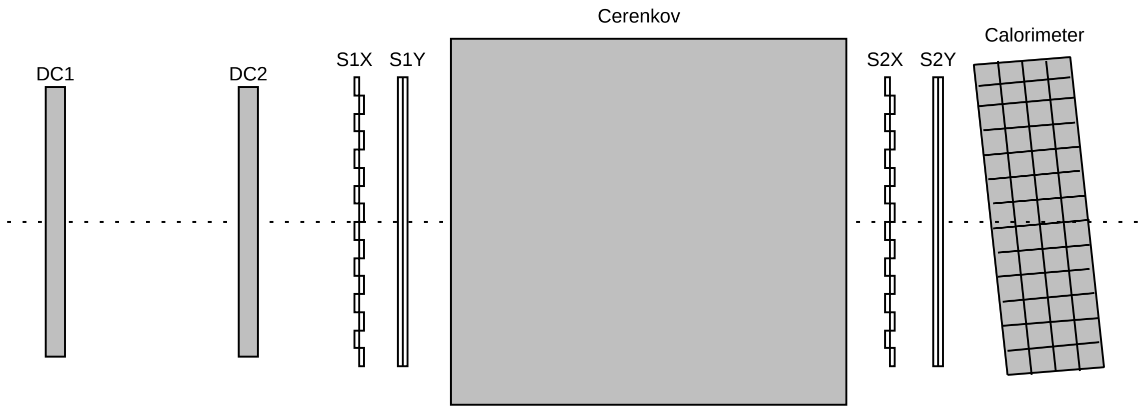

Figure 2.10: Schematic diagram of the HMS detector hut.

(less paddles in the hodoscope planes, smaller drift chambers, etc.), but otherwise nearly identical with the HMS package. For the specific purpose of **E93-018** (and E91016 as well) a silica aerogel (n = 1.034) Čerenkov detector was added to the SOS detector package to help with the K^+/π^+ discrimination (a veto signal coming from this detector could be used in the online trigger, otherwise the information was used only in the off-line analysis). This detector was placed between the last two scintillator planes. Another Čerenkov detector, composed of eight lucite (n = 1.49) paddles was installed in front of the third hodoscope plane. This detector could provide K^+/p discrimination and was used mainly as a online-veto for the limited $^{12}C(e, e'K^+)$ feasibility studies that were performed in parallel with **E93-018** . A schematic of the HMS detector hut is shown in Fig. 2.10, while Fig. 2.11 shows the layout of the SOS detector hut.

2.5.1 Detector Supports

All HMS detectors rested on a unique support frame made out of double-T aluminum beams rigidly mounted on the same carriage that held the spectrometer magnets. The spacing of the detectors allowed reasonably easy access for servicing and repairs. In contrast with the "roomy" HMS hut, the SOS hut was designed to be very compact in order to allow detection (before decay) of short–lived particles. As a result the SOS

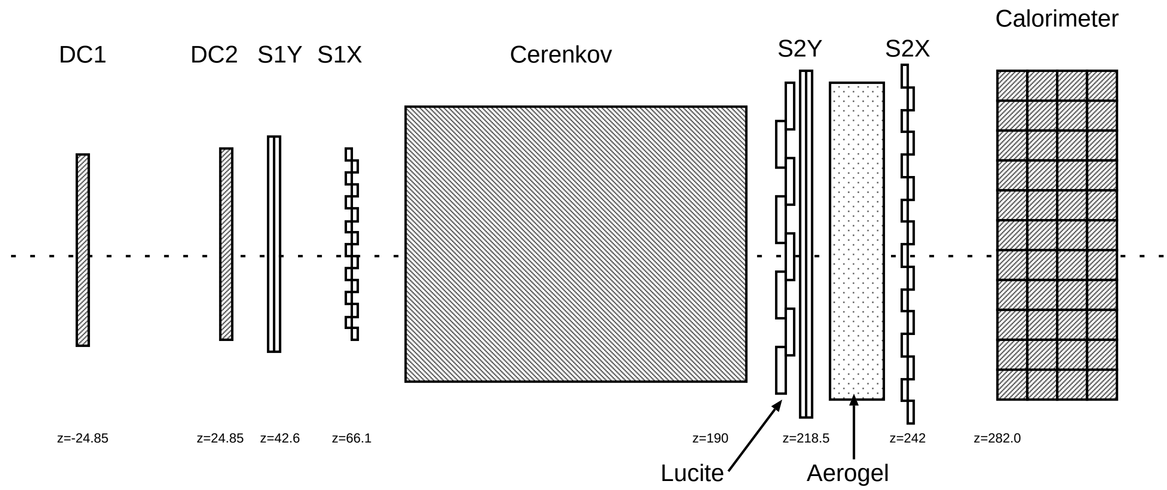

Figure 2.11: "Nearly to scale" schematic diagram of the SOS detector hut (including the aerogel and lucite Čerenkov detectors installed for the specific purpose of kaon identification.

detectors were closely packed together. All of the SOS detectors (less the calorimeter) were mounted on supports that could slide sideways, allowing the detectors to be pulled out of the hut without removing them from their supports. This allowed easy service and repair work on the detectors without disassembly of the support structure, despite the "tight" confines of the SOS detector stack. There were four separate supports for the detectors. The first three were sliding mounts and the last was a fixed support. The drift chambers and the first two hodoscope planes were located on the first support. The second support had the gas Čerenkov mounted on it. The last sliding support held the last two scintillator planes as well as the aerogel and lucite Čerenkov detectors. The lead glass calorimeter was supported by a fixed shelf, mounted to the ceiling and rear wall of the detector hut. Figure 2.12 shows an "artist view" of the SOS detector hut. One can plainly see the layout of the detectors and their supports with respect to the last dipole (also shown). Note that none of the aerogel/lucite detectors are depicted, as they were relatively late (and temporary) additions to the detectors stack.

The drift chamber positions were surveyed by the Jefferson Lab survey group, with respect to fiducial marks present on the last SOS dipole. The final accuracy for the drift

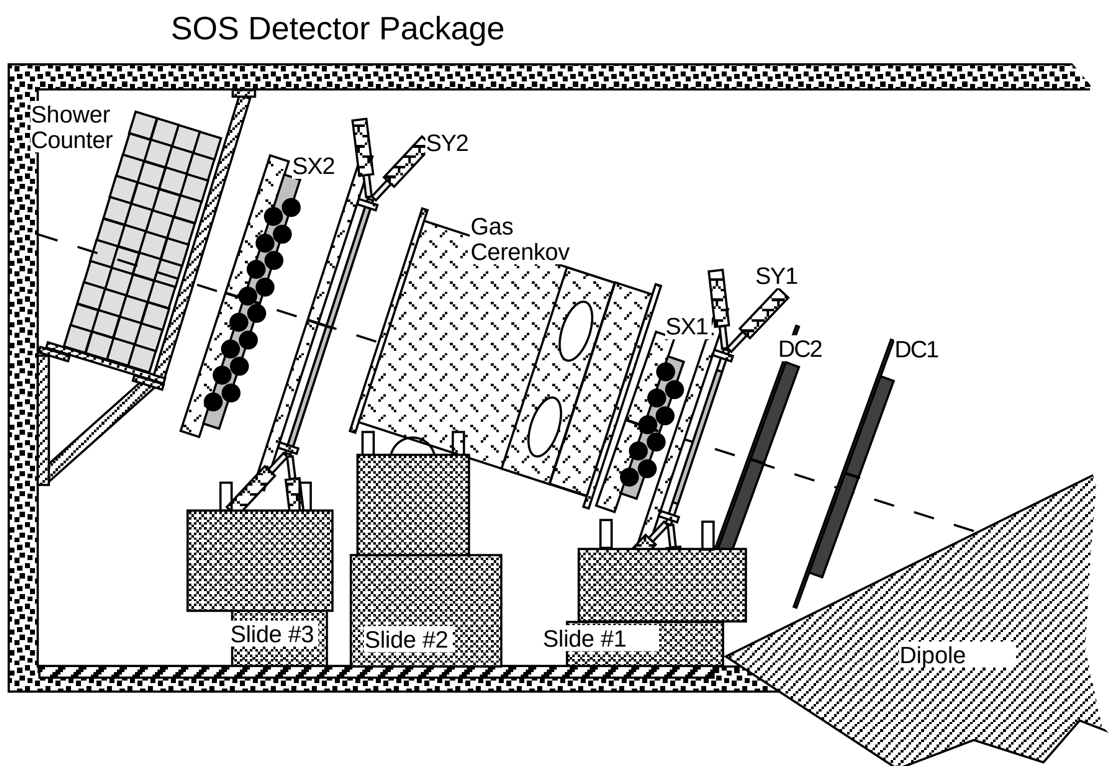

Figure 2.12: Layout of the SOS detectors and supports and their orientation with respect to the last SOS dipole.

chamber positions is 0.4 mm, and is used as such in the tracking software. The positions of the other detectors are known to within few mm from survey measurements of the detector stand positions. Using electron scattering data all detectors were aligned with respect to the drift chambers.

2.5.2 Drift Chambers

As the HMS and SOS drift chambers, while performing similar roles in their respective detector stacks, have different designs, they will be discussed separately below.

HMS Drift Chambers

The HMS drift chambers were designed and built at Jefferson Lab by a Hampton University group, led by Dr. O. K. Baker. While a more in-depth description of the design and performance of these detectors is given in [31] some of the more important parameters will be given here as well. A total of three drift chambers of this design were built; two of them were installed in the HMS detector hut (spaced by 80 cm), the third one was kept as a spare. These devices had large active area (approx. 107x52 cm) and thin aluminized mylar windows. Each chamber consisted of six planes of wires, two measuring in the dispersive (x) direction, two measuring in the non-dispersive (y) direction, and two stereo planes rotated by $\pm 15°$ with respect to the x planes. As seen by incoming particles the planes were ordered x, y, u, v, y', x'. Figure 2.13 shows the front and side views of a HMS drift chamber.

As seen in Fig. 2.13 the x, x' (and same holds true for the y, y') pair of planes were staggered by half a cell to help solve the left-right ambiguity when reconstructing tracks.

The basic HMS drift chamber cell (see Fig. 2.14) was a 3 x 3, 10 mm by 8 mm rectangular lattice with the sense wire in the center surrounded by eight field wires. The sense wires were 25 μm gold–plated tungsten (spring loaded) while the field wires were 200 μm gold–plated Cu-Be (also spring loaded). The tension in the wires was chosen such as to minimize the electrostatic sagging of the wires when the operating high voltage is applied. 200 μm Cu-Be guard planes were installed before the first plane and after the

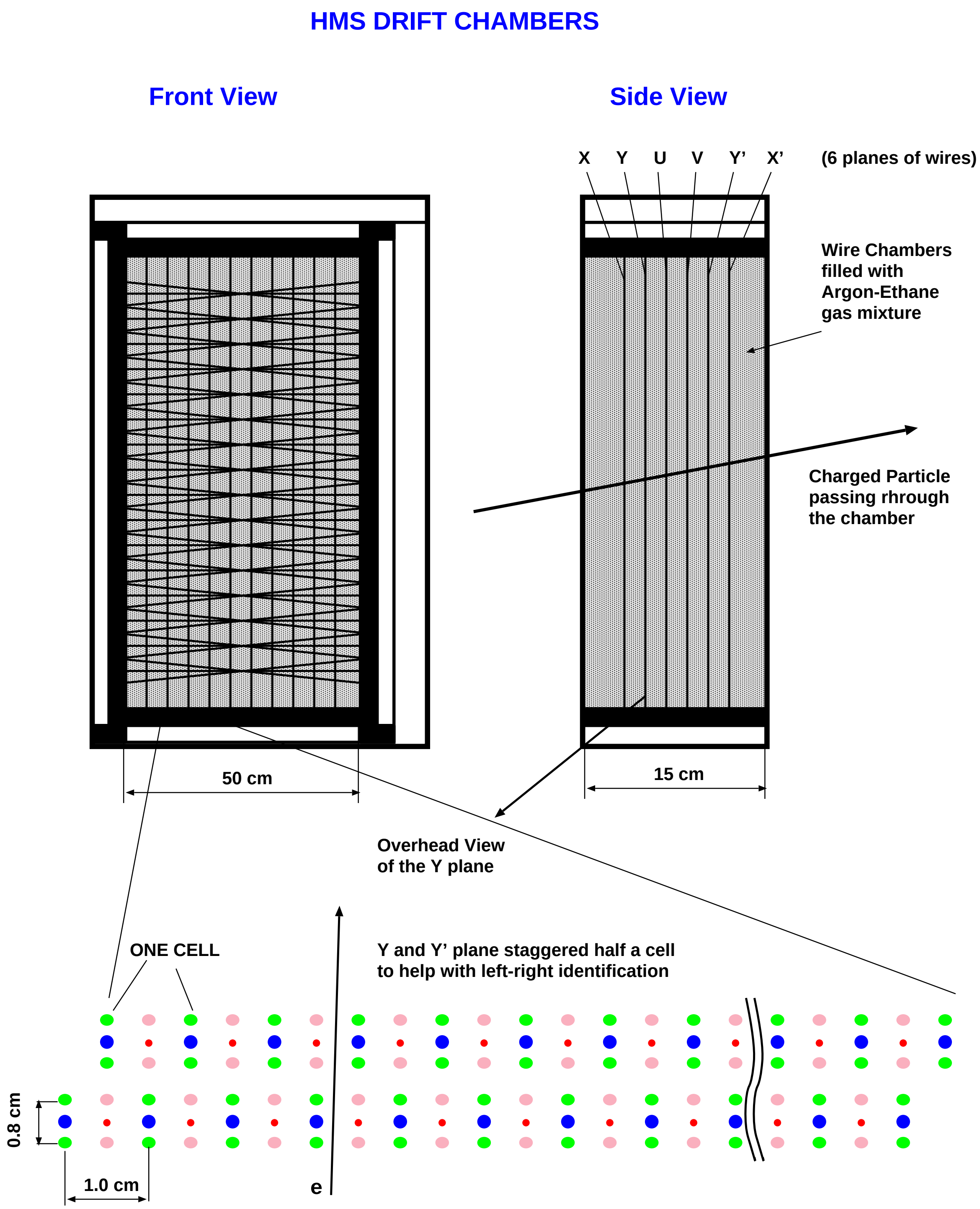

Figure 2.13: Front and side view of an HMS drift chamber. An enlarged view of the y and y' planes is shown at the bottom of the pictures.

HV Card	$V_{\max}$	$I_{\max}$	Detectors
A403	-3000 V	3.0 mA	Hodoscope/Calorimeter
A503	-3000 V	3.0 mA	Hodoscope/Calorimeter
A503P	+3000 V	3.0 mA	Čerenkov Detectors
A505	-3000 V	3.0 μA	Drift Chambers

Table 2.10: CAEN high voltage cards used for the Hall C detectors.

sixth plane in each chamber. As the field inside the cell tends to be asymmetric for the outside cells, all planes had an empty drift cell (i.e. no sense wire) at each end.

The high voltage settings of the eight field wires give the strength and shape of the electric field inside the drift cell. For the HMS drift chambers all wires that were at the same distance from the center of the cell (i.e. same distance from the sense wire) were kept at the same potential. As the cell is a rectangle rather than a square there are three different voltage settings (conventionally called "t == triangle", "s == square" and "c == circle") that needed to be set.

Extensive plateau studies of the HMS drift chambers with and without beam (i.e. cosmic rays) helped to determine the optimal operating point of these devices. The combination 2500/2250/1750 V for the "t-s-c" wires provided the most stable operating point. For these settings the efficiency per plane was greater than 99 % even for the highest particle rates the chambers were supposed to detect ($\geq$ 2.5 kHz/wire/mm). As with all the detectors present in Hall C the high voltage power supplies were CAEN. Table 2.10 lists all CAEN power supply cards used in Hall C, their main characteristics, and the type(s) of detector(s) that used them. The low voltage setting for the discriminator-amplifier cards used to collect/amplify the signal from the wires was also studied intensively. It was found that a setting of 4.5 V offers the optimal choice (i.e. voltage is high enough so that there is no ringing in the chambers but low enough so as to ensure high detection efficiency for minimum ionizing particles).

The gas mixture used in the HMS (and SOS as well) drift chambers was $Ar - C_2H_6$ (50:50 by weight), continuously circulated at a rate of 400-800 cm^3/min (SOS rates were

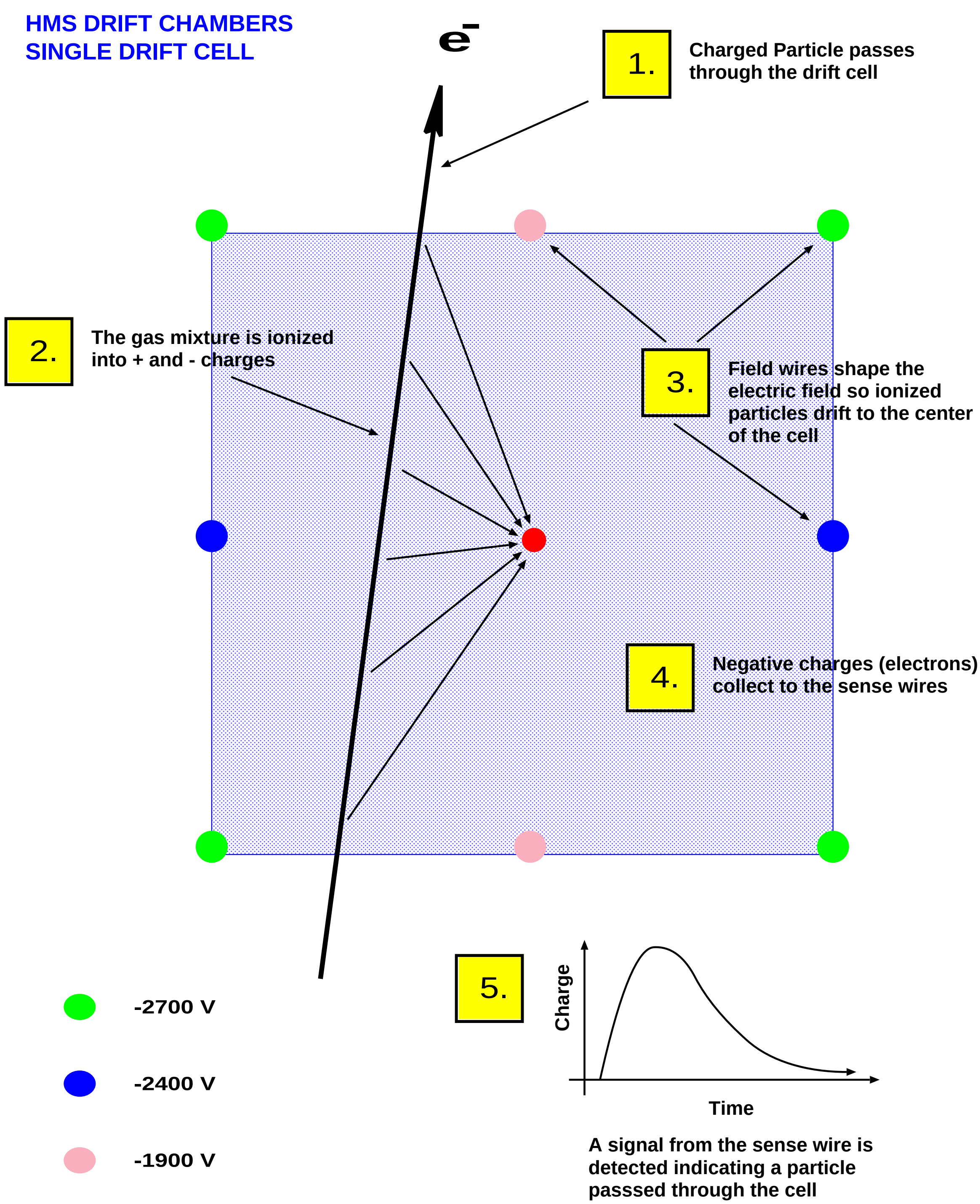

Figure 2.14: Enlarged view of a HMS drift chamber cell. Note that the voltages listed are the maximum settings the chamber can withstand; for the actual operating voltages see text.

lower). Given that the volume of each HMS chamber is $\sim$ 120 l, the lower gas-flow setting (i.e. 0.4 l/min) ensured one complete chamber purging every 5 hours, which is more than adequate for normal running. When "purging" the drift chambers after a longer period of inactivity, temporary higher gas flow rates were acceptable (but not more than 1-1.2 l/min, otherwise the thin mylar windows of the chamber might have burst). Minute amounts of isopropyl alcohol (less than 1 %) were incorporated in the gas mixture by bubbling the mixture through an alcohol-filled jar. The presence of alcohol in the mixture helped quench the electron-ion avalanche that eventually forms at the sense wire when collecting data. In their normal operating mode the HMS drift chambers had a very low leakage current, 0–50 nA/plane.

Each sense wire signal is discriminated/amplified (a combination of LeCroy 2735DC and NanoMaker 277-L cards were used. The two makes were operationally equivalent, although one of the cards carries a much higher price than the other) and then fed into a time-to-digital (TDC) converter, located in a FASTBUS crate inside the hut (to minimize signal distortions and delays). LeCroy 1876(1877) modules were used with either 12 or 13 bit readout (during **E93-018** the upgraded 1877's with 13 bit readout were used) with a sensitivity of 250 ps/channel. The chambers were operated in the so–called "common stop" mode. In this mode each wire signal starts its appropriate TDC channel. The "stop" signal is provided by a delayed signal originating from the hodoscope scintillators (i.e. a delayed trigger). The delay is then removed in the off-line analysis in order to get the proper drift time. The resolution of the HMS drift chambers was 200–300 μm (σ), dominated by multiple scattering.

SOS Drift Chambers

The two SOS drift chambers consisted each of six planes: x, u and v, as shown in Fig. 2.16. There was no y plane. The x and x' planes measured the position in the dispersive direction, the u/u' planes were rotated 60° clockwise from the x plane, and the v/v' planes were rotated 60° counterclockwise from x. As in the case of HMS drift chambers x and x' (as well as u and u'; v and v') are staggered by half a cell to ease the left-right ambiguity problem.

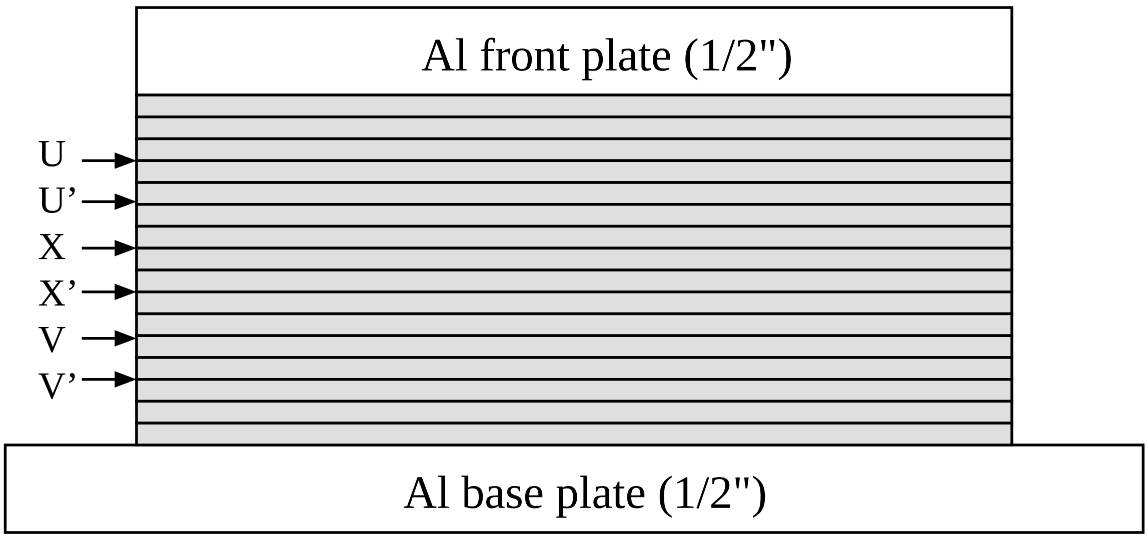

Figure 2.15: Construction details of the SOS drift chambers. The alternating G10 layers holding either cathode foil or wires are shown.

Each chamber was constructed of sixteen layers of 3.175 mm G10 plates, sandwiched between 1.27 cm aluminum plates. The G10 plates holding cathode foils were mounted alternatively to the plates that hold the sense and field wires, as shown in Fig. 2.15. The size of the drift cell, as seen by incoming particles was 1 cm, with the sense wires (30 μm in diameter) alternating with the field wires (60 μm diameter). High voltage provided by CAEN power supplies kept the field wires and cathode foils at a large positive high voltage ($\sim$ 1975 V) providing isolation between the drift cells and minimizing the cross-talk between sense wires. The wire positions were measured during chamber construction and matched the design values within the accuracy limits of the measurement ($\pm$87 μm).

The x and x' planes had 64 wires each while the u and v only held 48. As seen in Fig. 2.16 the active area of the chamber was approximately 63 x 40 cm, with the corners cut-off due to the lack of y information.

The signals from the chamber were read in a similar way as the HMS chamber, using either LeCroy or Nano amplifier/discriminator cards. The discriminator thresholds for all of the cards was provided by single external low voltage supply, remotely adjustable

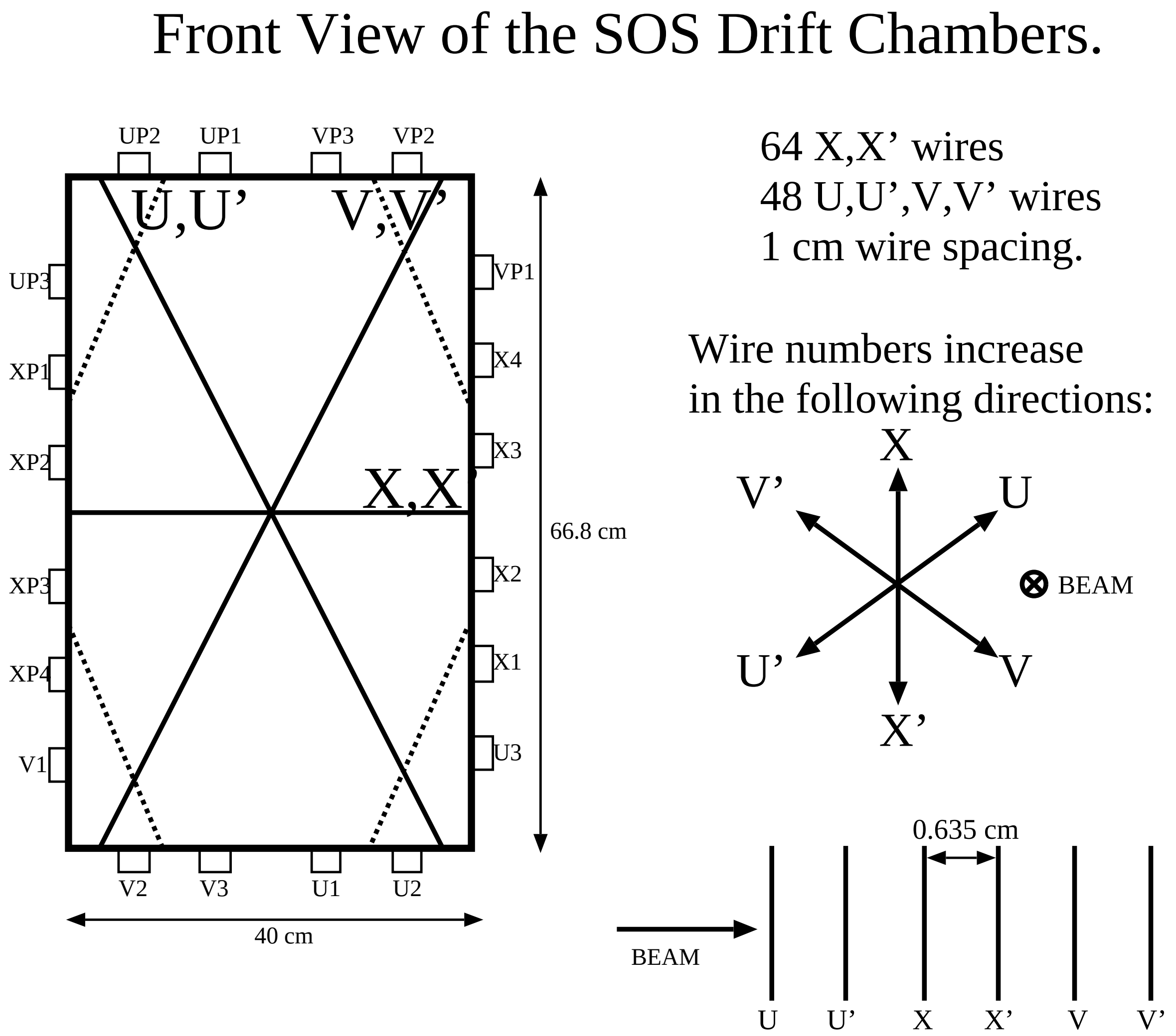

Figure 2.16: Front View of the SOS Drift Chambers showing the orientation of the six planes. The position of the readout cards is indicated on the outside of the chamber. The dotted lines show the approximate extent of the active area of the chambers.

from the counting house. A setting of 1.5 V for the low voltage was used during **E93-018** . The signals from the discriminator cards were fed via twisted pair ribbon cables to the LeCroy multi-hit TDCs (1877). Due to space limitation the FASTBUS rack holding these TDCs was not in the SOS hut but in the electronics shack located just below the detector hut. When a stop from the hodoscope scintillators was received, up to 16 hits per wire could be read and sent into the data stream. The final position resolution was comparable with the performance of the HMS chambers, $\sim$ 200 μm (σ).

SOS drift chambers used the same gas mixture and gas handling equipment as the HMS drift chambers. The volume of a SOS drift chamber being only $\sim$ 13 l, the gas flow through the chamber was much lower (typically 0.2 l/min or less) than for the HMS.

2.5.3 Hodoscopes

The HMS and SOS detector stacks each held four planes of scintillator paddles (two pairs of x-y planes in each spectrometer). The signal coming from these detectors was used to form the primary trigger. In addition, these detectors allowed the measurement of the speed of charged particles by providing time of flight (TOF) information. The HMS and SOS hodoscopes were identical except for the size and number of elements. Each hodoscope plane had 9 to 16 elements[20]. The hodoscope elements were long narrow strips of BC404 scintillator material (Polyvinyltoluene, PVT) with lucite light guides at each end. To ensure light tightness while adding the minimum amount of extra material the scintillators were individually wrapped with one layer of aluminized mylar and two layers of tedlar. The HMS scintillators were all 2.12 cm thick and 8 cm wide. The x elements were 75.5 cm long (16 elements/plane) while the y elements were 120.5 cm long (10 elements/plane). There was an $\sim$ 0.5 cm overlap between elements in the same plane in order to avoid missing particles. The total active area for HMS was thus 120.5 x 75.5 cm and the spacing between the front and the back scintillator planes was 230 cm. In the SOS the front two planes are smaller than their back counterparts. The front x plane (S1X)

[20] In general more segmentation is desired in the dispersive direction so (x) hodoscope planes will have more elements than their (y) counterparts. Also, the HMS hut is larger than the SOS hut so more scintillators were needed in HMS than in SOS.

had 9 elements (36.5 x 7.5 x 1.0 cm in size) while the front y plane had also 9 elements, 63.5 x 4.5 x 1.0 cm; for a total active area of 63.5 x 36.5 cm. The rear x plane (S2X) had 16 elements (36.5 x 7.5 x 1.0 cm) while S2Y had 9 elements, 112.5 x 4.5 x 1.0 cm in size, for a total active area of 112.5 x 36.5 cm. The spacing between the front and the back planes in SOS was 180 cm.

Each scintillator was readout by two Philips XP2282B photomultiplier tubes (PMTs), one at each end, nominally operated at 2500 V. The high voltage was subsequently fine-tuned/calibrated by gain matching the tubes with a ^{60}Co gamma ray source. The voltages were set such that the Compton edge from the gamma rays gave a pulse height of 500 mV at the output of the base. Planned but not used during **E93-018** (as it was in its early construction stages) was a laser pulser gain monitoring system that would provide active gain matching of the tubes. "Time walk" corrections due to pulse height variations (some of which might be particle-dependent) and offsets between individual elements were fitted offline using data accumulated during the actual production running.

The output from the tubes was sent via a patch panel present in the detector hut and a combination of RG58 and RG8 cables to the counting house. A splitter then fed a third of each signal, through $\sim$ 400 ns of RG58 cable delay to the ADCs; the rest of the signals went to PS7105 Discriminators. One set of outputs from these discriminators was fed via logic delay modules to TDCs and VME scalers. The other set of outputs was sent to a LeCroy 4654 logic module. This module generated the OR of all tubes on one side of a given plane. The trigger logic used the "AND" of the sets of tubes on each side of a plane (a condition somewhat more relaxed than requiring both ends of a given paddle to fire) as well as the "OR" of the front (and back) pairs of planes (e.g. S1 = S1X + S1Y). Figure 2.17 shows a diagram of the electronics for the hodoscopes.

2.5.4 Čerenkov Detectors

In this section the principle of operation for Čerenkov detectors is reviewed briefly. The two (slightly different) actual designs used in HMS and SOS as threshold Čerenkov counters are described. The construction and operation of the silica aerogel and lu-

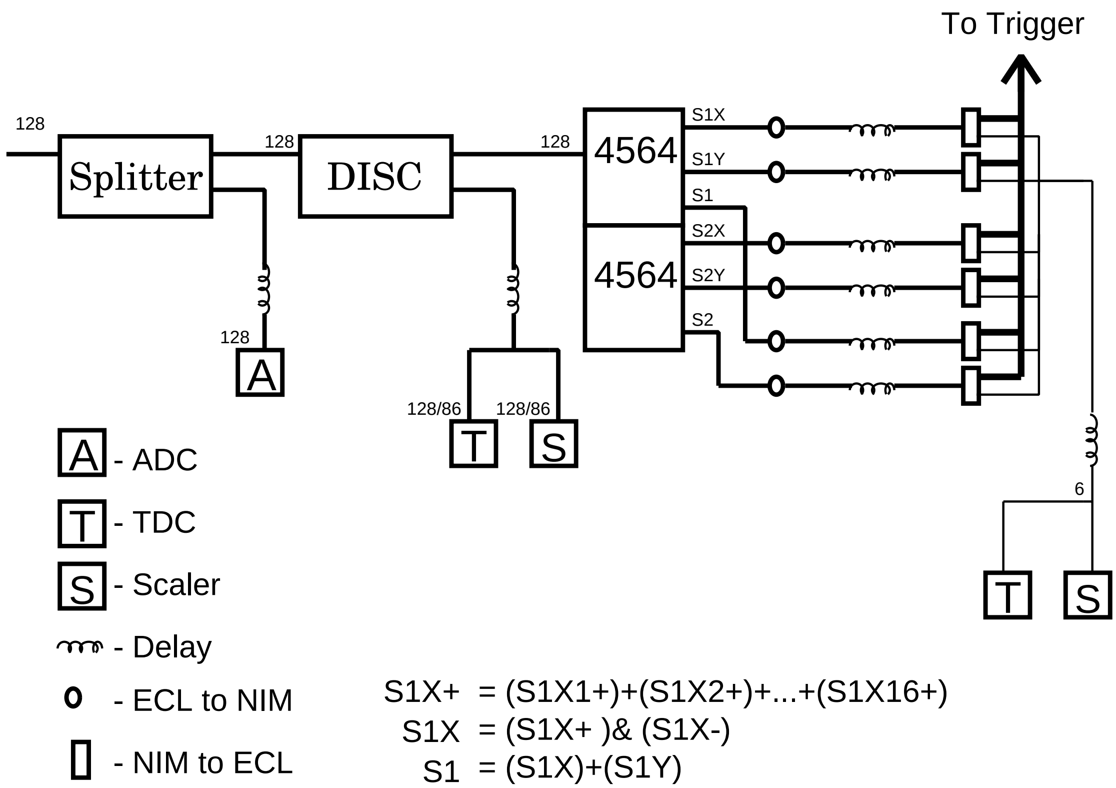

Figure 2.17: Generic HMS/SOS Hodoscope electronics. The numbers indicate the number of inputs coming the HMS/SOS spectrometer.

cite Čerenkov counters, installed in the hadron arm for the specific purpose of kaon identification, will also be reviewed.

Overview

A charged particle moving in a medium with a velocity larger than the speed of light in that particular material will emit Čerenkov radiation along a conical wavefront. The angle of emission θ of the radiation of a given wavelength, λ, can be related to the velocity of the particle, β, and the refractive index of the medium as follows:

$$cos\ \theta = \frac{1}{\beta\ n} \tag{2.4}$$

The number of Čerenkov photons, N_γ, emitted per unit length, l, is given by:

$$\frac{d\ N_\gamma}{d\ l} = 2\pi\alpha Z^2 \int_{\lambda_1}^{\lambda_2} (1 - \frac{1}{\beta^2 n^2}) \frac{d\lambda}{\lambda^2} \tag{2.5}$$

where α is the fine structure constant, Z is the charge of the particle, and λ_1 and λ_2 define the spectral range of the detected radiation [32].

A threshold Čerenkov counter detects particles having sufficient velocity to produce Čerenkov light in the radiator. By carefully choosing the index of refraction n, one can fix the threshold velocity so that it can discriminate between particle types. For the particular purposes of Hall C related experiments it is necessary (most of the time, at least) to discriminate between electrons and heavier particles. Therefore the Hall C gas Čerenkov detectors were designed to produce copious amounts of Čerenkov radiation for electrons but not for pions/muons and all other heavier particles.

HMS gas Čerenkov

The HMS Čerenkov counter was a threshold Čerenkov counter designed and built by the University of Virginia. It consisted of a large cylindrical tank, with a diameter of 150 cm and a length of 152 cm, positioned between the front and back pair of hodoscope scintillators. The ends of the tank had thin (0.1 mm) 2024-T3 aluminum windows allowing the passage of charged particles emerging from the HMS spectrometer. Inside the tank the

Čerenkov light was focussed by two mirrors onto two 12.7 cm (i.e. 5–inch) Burle 8854 photomultiplier tubes. The detector was designed to operate at or very slightly above atmospheric pressure. Although several other filling options were available, including various freons, CFCs, etc; the use of such expensive and environmentally unfriendly gases was deemed unnecessary for the requirements of the present experiments. Therefore during **E93-018** the detector was filled with CO_2 at atmospheric pressure and room temperature. In these conditions the threshold momentum is 17.9 MeV/c for electrons and 4.9 GeV/c for pions. As a consequence the detector was fully sensitive for electrons, yet unsensitive for pions (and heavier particles) for all kinematic settings. The expected number of photons produced by an electron in ~ 1.5 m of CO_2, according to eq. 2.5, was $N_\gamma \approx 60$.

SOS gas Čerenkov

The SOS gas Čerenkov was designed and built at the University of Colorado. While a complete description of the detector can be found in the "CEBAF SOS Čerenkov Detector Handbook"[33] the most important characteristics will be given here as well.

The SOS Čerenkov detector was an aluminum box, approximately 1 cubic meter in volume, 99 cm high, 73.7 cm wide, and 111 cm long. The walls were 1.3 cm thick. The entrance and exit windows were a composite of one layer of 0.254 mm lexan graphics film (for gas tightness) and one layer of 0.05 mm tedlar film (for light tightness). The total thickness for these lexan/tedlar windows was 39 mg/cm. Inside the detector the light was reflected by four overlapping spherical mirrors onto their respective photomultiplier tube. The detector box had four ports for photomultiplier tubes (PMTs). As in the case of the HMS Čerenkov, Burle 5–inch 8854 PMTs were used. Each of these PMTs was magnetically shielded. Inside the detector box, Winston cones (reflective cones around the phototube front face) were used to increase the effective solid angle of each tube. The system was designed to operate at or near atmospheric pressure. Special precautions (including operating the system slightly below atmospheric pressure, etc.) needed to be taken if freon (or other CFC gas) was to be used. A system of solenoid valves and a retention bladder as well as monitoring equipment were provided for this purpose (i.e.

the SOS Čerenkov gas handling mechanism). During **E93-018** the system was filled with CO_2 and monitored so as not to exceed ± 0.05 PSID with respect to atmospheric pressure.

SOS Aerogel Čerenkov

For the specific purpose of separating pions from heavier/slower hadrons (including kaons) the SOS detector stack contained a silica aerogel Čerenkov detector. The aerogel material ($n(SiO_2)+2n(H_2O)$) had a measured index of refraction of 1.034±0.001, giving a pion threshold of 531.4 MeV/c and a kaon threshold of 1873.7 MeV/c. The design of this detector was very simple (see Fig. 2.18): the aerogel material was closely packed in an aluminum tray in the front of the detector. Charged particles entered this tray and produced Čerenkov light (provided their speed is high enough). The light is then reflected several times, eventually making its way in the diffusion box situated at the back of the detector. The photons were collected by the photomultipliers placed on the sides of the diffusion box.

Specifically the aerogel material came in 25 x 25 x 3 cm tiles. These were packed together three-layer deep and positioned to form a compact 100 x 40 x 9 cm block. This entire block was then wrapped in one layer of Millipore filter paper (96-98% reflection). Two layers of aluminized mylar were wrapped on all sides except the top of the block. The block was placed, uncovered side up, in an aluminum tray, held in place by thin steel brackets. Thin wires were strung across the open face of the material . The diffusion box was also lined with reflective Millipore paper. On each side of the box there were seven ports circular ports. In each port a 5–inch Burle 8854 photomultiplier tube was mounted. ADC signals from each individual PMT were recorded in the data stream (a simple hardware summation scheme enabling the use of the aerogel signal as a veto in the online trigger will be discussed in the electronics setup section). In addition to the above the diffusion box had two gas feedthroughs, allowing the circulation of dry nitrogen gas in the diffusion box (as the aerogel material is extremely hygroscopic, and the humidity in the Jefferson Lab area of the US is rather high, maintaining the detector in a clean, dry, environment helps extend its life) and two light fiber feedthroughs which were to be

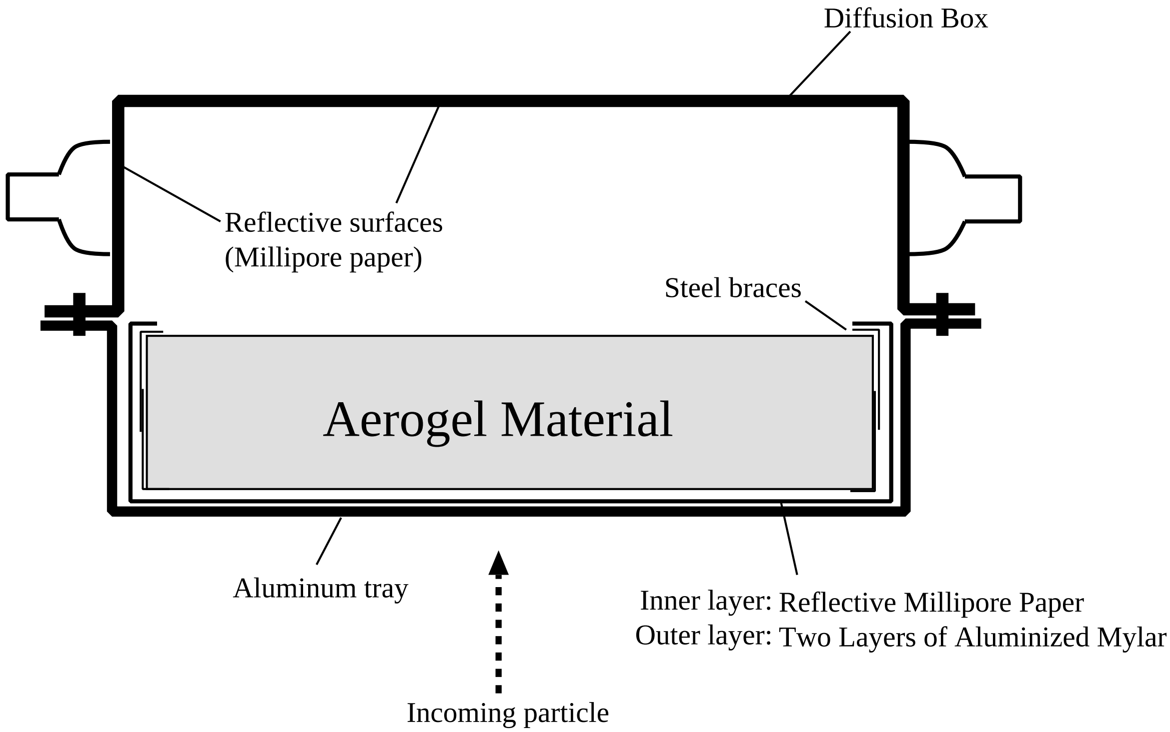

Figure 2.18: Schematic of the SOS silica aerogel detector.

used by the the online laser pulser gain monitoring system, planned for Hall C.

2.5.5 Lead Glass Calorimeter

Both the HMS and SOS had lead-glass calorimeters/shower counters at the back of their detector stacks, used primarily for particle identification (e/π separation). The principle of operation and construction of these shower-counter detectors will be reviewed in this section.

High energy electrons and photons interact with matter mainly through bremsstrahlung and pair production, respectively. Both these processes create photons and electrons (positrons) which will have similar interactions, thus producing a shower (cascade) of secondary particles. If the medium through which this shower propagates has high enough refractive index, n, the relativistic charged particles produce Čerenkov radiation which can, in principle be collected with PMT tubes. As the total pathlength of the particles in the shower is proportional to the energy of the incident particle so the total Čerenkov light is proportional to the energy of the showering particle. Pions or, more generally, hadrons, have to interact strongly with nuclei in order to produce the so-called "hadronic showers". The dynamics of a hadron shower is rather complex and will not be covered here. For the purposes of the **E93-018** analysis it is important to note that, in a hadronic shower about half of the available energy is used for multiparticle production while the remainder is shared by a few highly energetic secondary particles. The resulting cascade is mostly composed of pions and nucleons. Several of the dominant processes inside a hadronic cascade do not lead to secondaries producing Čerenkov light. Also since the mean free path for hadrons is much longer than for electrons, a hadron shower will have a different spatial evolution than an electromagnetic shower. The thickness of the shower counter can be chosen such that the electromagnetic cascade is completely contained in the detector while allowing only for a fraction of the hadrons' energy to be deposited in the detector. These differences between electromagnetic and hadronic showers makes possible the electron/pion identification [34, 35].

The HMS and SOS calorimeters were of identical design and construction except for their total size/number of blocks. 10 x 10 x 70 cm blocks of TF-1-000 lead–glass blocks were used for both detectors. Lead glass is a transparent glass composed primarily of lead oxide and silicon dioxide (51.2 % PbO, 41.3 % SiO_2, 7 % Na_2O). The main properties of this type of lead glass are: density, ρ= 3.86 g/cm^3, radiation length 2.5 cm, index of refraction, n=1.67.

The HMS shower counter had the blocks stacked four layer deep, each layer containing 13 blocks (the total thickness along the central ray was 16 radiation lengths). The SOS shower counter also had four lead block layers, but each layer had only 11 blocks. To account for the asymmetric flaring of the SOS acceptance six of the blocks were positioned above the nominal position of the central ray through the spectrometer and only five blocks were positioned below it. To avoid losses through the cracks between the layers the shower counters were rotated by $\sim 5^\circ$ with respect to the optical axis of the spectrometer (see figure 2.10). Each module was individually wrapped first with 25 μm aluminized mylar (to maximize internal reflection) and then with $\sim 40\ \mu$m tedlar–type opaque film (to ensure light tightness of the block). Silicone grease (n=1.46) mounted Phillips XP3462B PMTs (8-stage, 5 inch diameter) were used to read, at one end only, each individual module/block signal. These signals were recorded in the data stream for offline analysis. In addition, a simple hardware summing scheme enabled the shower counter signal to be used as a veto in the online trigger. Each photomultiplier was magnetically shielded with μ-metal foil. As in the case of other HMS/SOS detectors the (negative) high voltage was provided by CAEN power supplies.

The attenuation (light loss) in the blocks and the gain of the phototubes were extensively studied, and, to minimize the signal variation across the shower counter, the best lead glass blocks were paired with the worst PMTs. The operating voltages were set to match the gains of individual modules[21]. A program for the off-line (limited) gain matching will be described in the calibration section. A detailed description of the calorimeter design and performance will be published in the future [36].

2.6 Trigger

The HMS and SOS had separate trigger systems, providing triggers for events in each spectrometer. Hodoscope signals produced when a charged particle passed through the active area of the scintillators provided the first part of the trigger. In the electron arm signals coming from the gas Čerenkov detector and/or the calorimeter were used to determine if a particular event came from an electron or a pion. Typically if an event had either a gas Čerenkov signal or a large shower counter signal, it was labeled as an electron. Triggers with no Čerenkov signal were labeled as pions. For the purposes of **E93-018** all electron events were considered when forming the coincidence trigger while only prescaled pion events were recorded as part of the HMS singles events. For the hadron arm the sum of the signals coming from the aerogel Čerenkov provided a veto that could be (and was) used to discriminate between "pion" events and kaon/proton

[21]The online pulsed-laser gain matching scheme described for the hodoscopes is to be implemented for the shower counters as well; however this was not operational during **E93-018** .

events. This signal eliminated 80-90 % of the pion events in the SOS, thus dramatically reducing the pion background. While most of the **E93-018** data (except for kinematic settings where the SOS momentum was high enough such that part of the detected kaons were actually above the aerogel threshold) was acquired using the aerogel veto in the online trigger, for each kinematic setting at least an hour of running was done without the aerogel in the trigger, to check for any kaon losses the aerogel veto might induce. No significant differences were found between the runs with and the runs without the aerogel in the trigger. Similarly the sum of the lucite Čerenkov signals could be used as a veto, discriminating between protons and kaons, and pions; however this feature was not used in the **E93-018** production data. After the raw spectrometer trigger (i.e. the "pretrigger") was formed, additional logic provided the final trigger for the trigger supervisor (TS), ADC gates, and start/stop signals for each event. The full trigger logic for the single spectrometer trigger is shown in Fig. 2.19 and will be described below.

2.6.1 Hodoscope Trigger

As stated previously, each hodoscope plane had between 9 and 16 scintillator paddles (depending on the type of plane (x/y) and also on the spectrometer), each one being read-out at both ends (conventionally labeled the "positive"/"negative" side). After being discriminated the signals from either side on each plane were OR-ed together, resulting in eight signals for each spectrometer:

$$S1X+, S1X-, S1Y+, S1Y-, S2X+, S2X-, S2Y+, S2Y- \tag{2.6}$$

(in reality these labels also had a leading "H" or "S" to distinguish between HMS/SOS signals). A hit in a given plane, say 1X, was defined as a coincidence between the corresponding "plus" and "minus" signals (i.e. $S1X = S1X + .AND.S1X-$, etc.). This definition was less restrictive than the condition requiring both ends of a given element to fire. This setup was more robust than a simple AND-ing of the signals from each individual paddle, required much less electronic modules to implement, and the amount of random signals introduced was found to be insignificant. Using the set of signals (2.6) two primary scintillator triggers were formed:

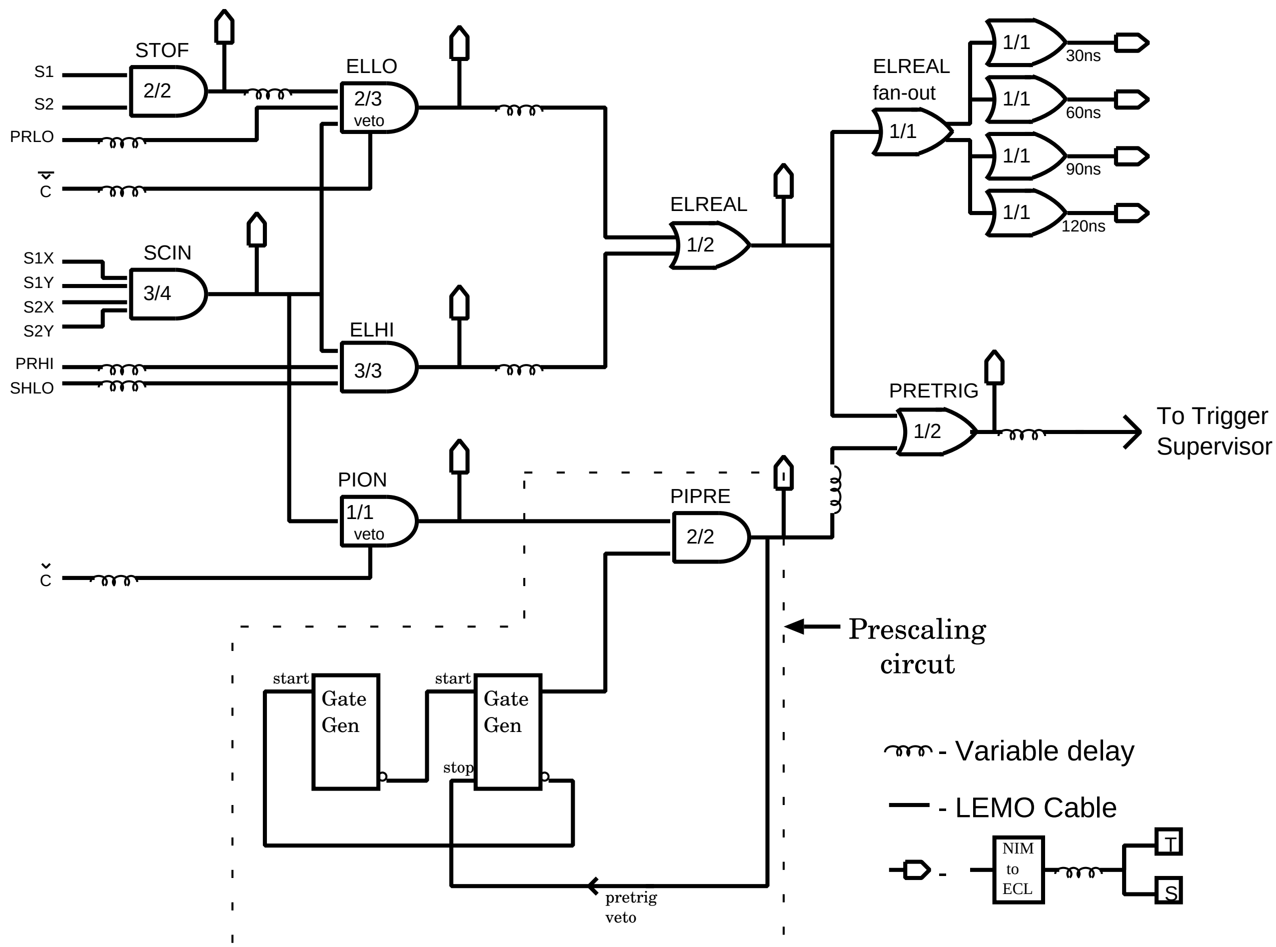

Figure 2.19: HMS/SOS single arm trigger electronics.

1. "STOF" was defined as the coincidence of one of the front planes and one of the back planes. This was the minimal/least restrictive condition that would still ensure enough information was available such as to have a good TOF measurement in the scintillators.

2. "SCIN" was defined as the coincidence between any three out of the four planes in the hodoscope. This was known as the 3/4 (three-out-of-four) and will be referred as such below. Note that "SCIN" was a subset of "STOF", i.e. every time "SCIN" was true then "STOF" was also true, while a true "STOF" does not guarantee a valid "SCIN".

For all **E93-018** data the "SCIN" signal was used for both the electron and the hadron arms.

2.6.2 Electron Trigger

The experimental requirements of **E93-018** called for a high efficiency for electron detection in the HMS. In order to be accepted as valid electron triggers, events had to either fire the gas Čerenkov OR to produce a signal in the HMS calorimeter above a certain threshold. This ensured a very robust running condition, less sensitive to inefficiencies in either of the two detectors. Of course, having an OR instead of an AND between the signals limited somewhat the hardware pion rejection efficiency to $\sim 100:1$, but that was not a problem for the **E93-018** running. Having a relatively tight coincidence window, as it will be explained below, certainly helped cut down the rates.

Signals from the two HMS gas Čerenkov PMTs were summed and fed into a discriminator whose level was set just over the one photoelectron limit. This defined the "CER" signal. Using the shower counter information two logic signal were formed. First the total (hardware) sum of all blocks was discriminated to provide the "SHSUM" signal. Separately the sum of all blocks in the first layer was discriminated to form the preradiator,"PRSUM", signal. The total energy signal had one discriminated output, "SHLO", while the preradiator had two outputs, "PRHI" and "PRLO" (set using a high and a low discriminator threshold setting). The final electron trigger, "ELREAL" was the OR of two conditions. "ELHI" required a high calorimeter signal, but no Čerenkov signal, while "ELLO" required a Čerenkov signal, but not a calorimeter signal. "ELHI" was defined as the coincidence of the "SCIN", "PRHI", and "SHLO" signals (i.e. the tight scintillator cut and both a high preradiator sum and total energy sum from the calorimeter). "ELLO" required the Čerenkov signal (by being vetoed by the "$\overline{CER}$" signal) as well as either a tight hodoscope condition ("SCIN") or a less restrictive hodoscope condition ("STOF") and a shower counter signal ("PRLO").

2.6.3 Pion Trigger (using the gas Čerenkov signal)

A pion trigger was provided for the study of single arm pion backgrounds[22]. The raw "PION" signal was defined by the "SCIN" signal, vetoed by the "CER" signal (N.B.:this is not mutually exclusive with the electron trigger). This "PION" trigger was prescaled using a dynamic prescaling circuit, and the prescaled pion triggers, "PIPRE", was combined with the "ELREAL" signal to give the final HMS (SOS) singles trigger.

2.6.4 Aerogel and Lucite Trigger

As a background reducing measure, a trigger signal formed using the aerogel (and lucite) information was provided for the hadron (SOS) arm. As was the case with all hodoscope, shower counter, etc. signals, the signals from the silica aerogel (lucite) detectors traveled from the detector hut to the counting house through $\sim$ 30 feet of RG58 cable followed by$\sim$ 450 feet of RG8 cable. In the counting house the signals were fed into a 50–50 splitter. One of the outputs of the splitter was delayed by 360 ns RG58 delay cables and then was fed via LeCroy 1881M ADC modules into the data stream. The other output of the aerogel (lucite) detectors went into a custom made (University of Maryland) amplifier module. The amplified signals, as well as the summed output went via delay cables into the same ADC. Sums for the seven PMT tubes on either side of the aerogel detectors were provided (for the lucite a straight summation of all signals was performed). The

[22]This feature, although present, was not used in the **E93-018** whose interest was in coincidence rather than single arm studies.

signal from either side of the aerogel was discriminated at about the three photoelectron level, and then the NAND (i.e. the .NOT..AND. of the signals) of the two sides was provided as VETO signal for the "SCIN"/"STOF" signals described above. This way one avoided the loss of the events for which one side of the detector gives an anomalously high signal (as the size of the aerogel detector was slightly smaller than the envelope of the particles emerging into the SOS hut there was a small, but noticeable probability of a "direct hit" of a particle on one of the aerogel PMTs, resulting in an anomalously high signal).

2.6.5 Trigger Supervisor

The trigger supervisor (TS) provided the interface between the trigger hardware and the computer data acquisition system. The Hall C TS was built locally at Jefferson Lab and was designed to work in conjunction with the CODA (Cebaf On-line Data Acquisition system), also developed locally at Jefferson Lab . Based on the run state the TS made all of the "decisions" about how to process and respond to the triggers it receives. As Jefferson Lab provides high intensity CW beam, which in turn translates to high data rates, all measures increasing the rate at which the events can be processed need to be taken. In that spirit the use of the sparsification feature of the ADCs and TDCs helped reduce the event size. The TDCs normally operated in sparsified mode, not giving an event for a channel if no stop signal was received after some preset time. For each channel of the LeCroy 1881M ADCs a threshold could be set individually and the module could be programmed to ignore all channels that have a signal smaller than the threshold. Using this sparsification technique meant that there were no pedestal values recorded for each channel during normal data acquisition. To alleviate this problem, at the beginning of each run a fixed number of events (typically a thousand) were generated by a random trigger while data sparsification was disabled. This allowed the measurement of the pedestal values for the ADCs. After these events, sparsification was enabled and only the real triggers were taken. The data acquisition mode was controlled using the TS status outputs. The outputs from the TS that determined how events would be processed. The TS “GO” signal was active at all times when a run was in progress. The TS “EN1” signal indicated that a run was in progress and normal data taking was enabled. Finally, the TS “BUSY” signal was active whenever the TS was busy processing an event. During a normal run, the following sequence of events occured: first, the TS “GO” signal turned on, and the pedestal triggers were recorded. After the preset number of pedestal events the ADCs changed to sparsified mode and the TS set the “EN1” signal, enabling the physics triggers and blocking the pedestal triggers. The “BUSY” signal was enabled/disabled as needed.

While the TS provided all of the control signals, an 'external' record of the logic that went into processing the event, the blocking of trigger due to the status of the run and/or the TS was kept in external logic and the intermediate steps were sent to scalers and TDCs to be recorded. The trigger signals (HMS, SOS, and PED triggers) and the TS control signals (GO, EN1, and BUSY) were fed into an 8LM programmable logic module (LeCroy 2365). The 8LM has eight outputs. Four of these were used for the HMS, SOS, COIN, and PED pretriggers. A pretrigger was generated by each incoming pretrigger during the appropriate part of the run, even if the TS was busy (i.e. PED pretriggers were passed during the beginning of the run, and the physics pretriggers were passed, and coincidence triggers generated, during the normal running). The other four outputs were the HMS, SOS, COIN, and PED triggers. These were identical to the pretriggers except that they required that there was no BUSY signal. These triggers were fed directly to the TS, and each one would cause an event to be read out. In Table 2.11 the programming of the 8LM is summarized.

Once the trigger types to be processed were determined, the trigger supervisor needed to determine, for each trigger type, what hardware needed to be read out. Once a trigger arrived at the TS, the latter waited 10 ns before latching all of the enabled trigger types into a data word. A lookup table was used to determine what event type (if any) the trigger corresponded to and what gates needed to be generated for data readout. The Hall C TS had four defined event types, HMS, SOS, COIN, and PED events. These did not exactly match the incoming trigger types because, if multiple triggers came in at the same time, the TS had to decide what kind of trigger the given combination corresponded

Table 2.11: 8LM Trigger Logic

output signal		definition
HMS PRETRG	=	$(HMS)\&(EN1)$
SOS PRETRG	=	$(SOS)\&(EN1)$
COIN PRETRG	=	$(COIN)\&(EN1)$
PED PRETRG	=	$(PED)\&(GO)\&(\overline{EN1})$
HMS TRIG	=	$(HMS)\&(EN1)\&(\overline{BUSY})$
SOS TRIG	=	$(SOS)\&(EN1)\&(\overline{BUSY})$
COIN TRIG	=	$(COIN)\&(EN1)\&(\overline{BUSY})$
PED TRIG	=	$(PED)\&(GO)\&(\overline{EN1})\&(\overline{BUSY})$

to. For example, if both the HMS and SOS triggers arrived (or the COIN with anything else), the TS treated the event as a coincidence event. In standard operating mode, there would be no ambiguity. PED triggers could come at the same time as any of the physics triggers. The coincidence window in the 8LM was larger than the 10 ns the TS waits for triggers, so any HMS and SOS overlap in the TS would also form a COIN trigger in the 8LM, and all the singles triggers were delayed so that the COIN trigger would always reach the TS first. For PED and COIN triggers, gates were generated for all of the FASTBUS modules (HMS, SOS, and beamline information), while for the singles triggers, only the appropriate spectrometer and beamline FASTBUS modules received gates and starts.

After the TS sent out the gates, each spectrometer re-timed the gates it received with respect to the single arm trigger for that spectrometer. This was necessary for coincidences because the ADC gates must come at a fixed time with respect to the time the particle passed through the detector. The trigger for that spectrometer comes at a nearly fixed time with respect to the detected particle, but a coincidence trigger has its timing set by the later of the two spectrometers. Therefore, if the HMS came first, the timing of its ADC gates would be set by the SOS trigger for coincidence events, and the ADC might fail to integrate the signal properly. The gates from the TS are then delayed and have their widths fixed so that they are timed properly for use as ADC gates and

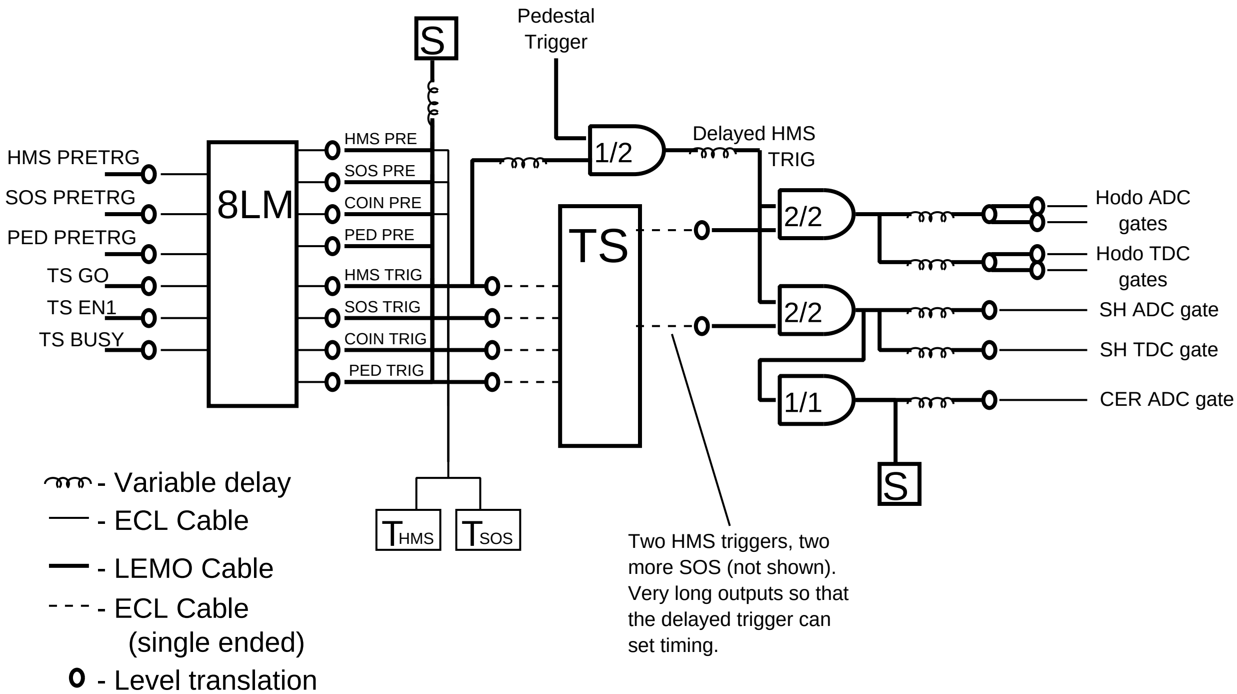

Figure 2.20: Simplified scheme of the Hall C Trigger Supervisor Electronics.

TDC starts. Figure 2.20 shows the trigger supervisor related electronics.

2.6.6 Other Signals

Besides providing signals for the trigger, all of the intermediate signals were sent to scalers and TDCs. All the scaler information was recorded in the data stream. In addition, a set of visual scalers was provided for the easy on-line monitoring of the data acquisition system. The TDCs were used mainly as latches, showing which signals were present when the trigger was taken. This allowed the determination of the event types that formed a particular trigger. The (visual) scalers allowed for quick detection of certain types of electronics problems in the intermediate steps of trigger formation. The scalers were also used to measure computer and electronics dead time.

2.6.7 Data Rates

The maximum data acquisition rate was limited by the FASTBUS conversion time and the data readout time. In basic data acquisition mode, the total time to process an event was just under 1 ms. This interval was broken up as follows: $\sim 100\mu$s for FASTBUS data conversion, 400 μs for FASTBUS readout, and 400 μs for transporting the FASTBUS information through the VME readout. In this mode the data acquisition rate was limited to $\sim$ 1 kHz and the computer dead times were large even for modest data rates. As the high current, high duty factor of the Jefferson Lab CEBAF machine have the potential of providing very high raw data rates, several steps were taken to increase the data acquisition rate and/or to minimize the dead time.

Modifications in the VME CPU made possible the processing of events asynchronously, the so-called "parallel mode", thus eliminating the 400 μs dedicated to VME processing. Optimization of the FASTBUS readout and utilization of the multi-block read feature of the ADCs reduced the FASTBUS processing time to 300 μs, giving a total processing time/event of only $\sim 400\mu$s and a trigger rate limit of slightly higher than 2 kHz. This mode, while clearly better than the previous one, still had large dead times for the higher data rates.

The fraction of the time the computer was busy, which gives the fraction of events missed, was roughly equal to the rate of events taken over the maximum allowable rate (2-2.5 kHz). So even a "modest" 500 Hz data acquisition rate will sport a $\sim$ 20-25 % computer dead time. As this was deemed too high for the precision experiments (including **E93-018**) in Hall C, further improvements were required. In addition to the benefits of the "parallel" mode explained above, the ability of the FASTBUS modules of buffering eight (or more) events was exploited, the "buffered" mode. This allowed the TS to accept new triggers immediately after the FASTBUS conversion was done, without waiting for the readout time. While this procedure did not improve total rate limit, the processing time/event still being $\sim$ 400 μs, the computer dead time was cut down by a factor of $\sim$ 4, as fewer events were missed for rates lower than the maximum. Figure 2.21 shows the data acquisition rate versus the raw trigger rate for the basic, parallel,

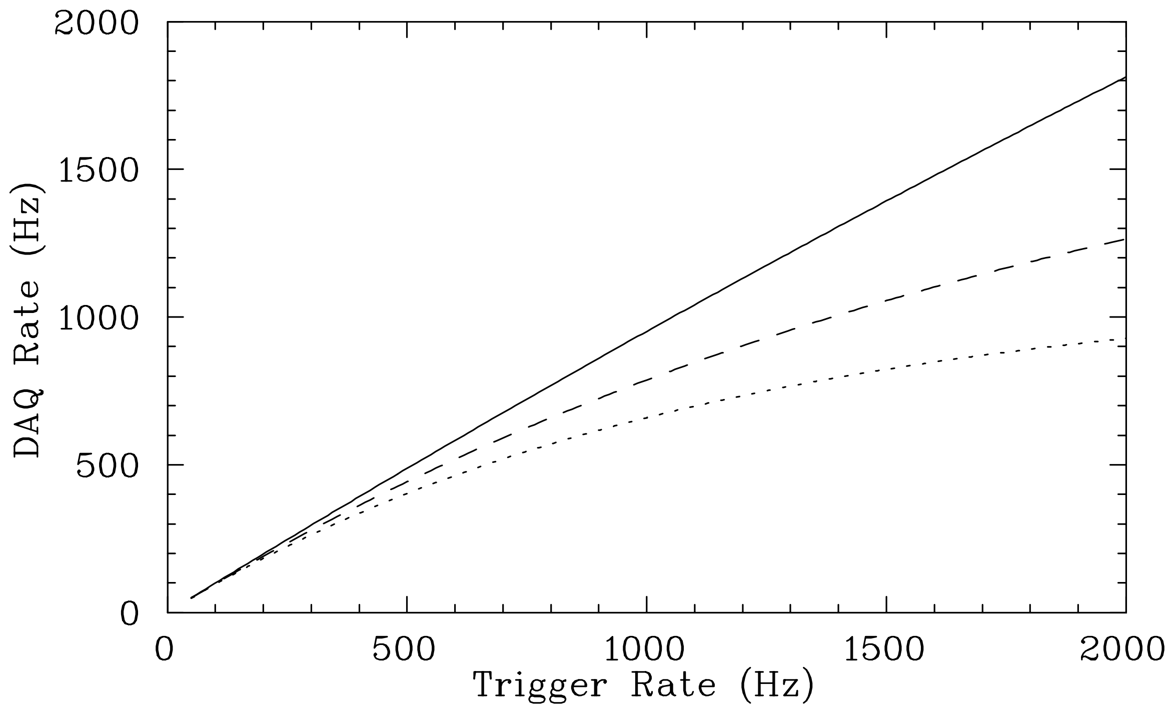

Figure 2.21: Data acquisition rates versus the raw trigger rate for basic/standard (dotted), parallel (dashed), and parallel-buffered(solid) run types.

and parallel-buffered modes.

During **E93-018** all coincidence events, as well as (heavily) prescaled HMS and SOS singles were recorded. The width of the coincidence window was $\sim$ 30 ns, and the relative delays between the two spectrometers was such as to prevent the lower energy protons for producing a coincidence event, while still keeping the coincident electron-kaon peak in the middle of the coincidence window. The data acquisition rates varied between 20 and 1000 Hz (dominated, of course by the extremely high proton and pion background), highly dependent upon the kinematic setting, while the dead time was always kept below 10 %. The preferred data acquisition mode of running during **E93-018** was the "COIN_PRE_PAR_BUFF" mode, thus taking advantage of all the improvements described above.

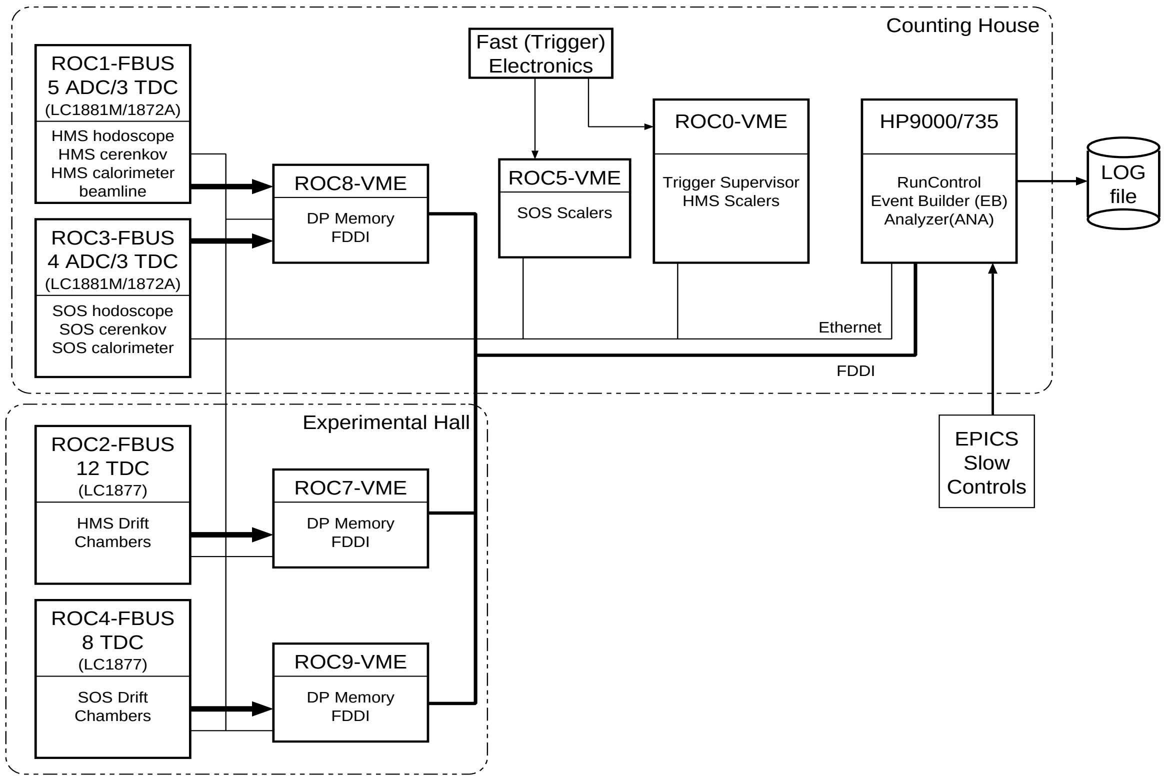

Figure 2.22: Simplified Schematic of the CODA Data Acquisition System as implemented in Hall C.

2.7 Data Acquisition

The system used for data acquisition throughout **E93-018** was CODA (the CEBAF Online Data Acquisition system), developed by the data acquisition group at Jefferson Lab (formerly CEBAF, thus the “C” in CODA). This system allowed for both event information and slow controls readout to be acquired and stored in data files. General information on CODA and RunControl (a graphical user interface, GUI, to CODA) can be found in [37, 38]. In Fig. 2.22 a simplified schematic of the system implemented for Hall C experiments is shown; a more in-depth description of the system is provided in [39]. In this section only the main features of the Hall C CODA system will be reviewed.

2.7.1 CODA - Physics Events

CODA provided the user interface and managed the DAQ sub-systems. Its main two components are the event builder (EB) and the event analyzer (ANA). To improve performance the event builder and the event analyzer were fused into one program, suggestively called "CODA_EBANA".

The Hall C data acquisition system was a heterogeneous assembly of FASTBUS and VME crates, each of them housing various ADCs and/or TDCs. An intermediate level of abstraction, called "Readout Controller" or ROC, was introduced. This not only helped the event builder cope with the differences between the FASTBUS and the VME calling conventions but also offered enough flexibility to accommodate (relatively quickly) changes in the physical layout/population of various physical FASTBUS and/or VME crates.

Data fragments from various ROCs were combined together by the event builder. The EB then added the header information (i.e. length of the event, packing information, etc.). The raw data event, including the header were then saved into the event file. In addition, the data could be sent through an analyzer subsystem to allow full or selective/partial online analysis of the data, possibly enabling the preprocessing of the events before they were recorded to tape. As the data analysis process was relatively time-consuming, the default analysis subroutine was just an empty/dummy subroutine, thus ensuring the maximum possible raw DAQ rate. As no online data integrity checks were performed, the whole task of ensuring that detectors worked properly, spectrometers were in focus, etc., was left for the so-called "just-offline" analysis, a tuned-down version of the full "offline analysis" code. Figure 2.23 shows the typical software flow diagram.

For **E93-018** , coincidence physics events as well as prescaled singles events coming from either spectrometers were recorded. The TDC readout was sparsified, so that only channels with starts were read out. Taking advantage of the programmable thresholds for each channel the readout of the LeCroy 1881M ADCs was sparsified as well. The thresholds were typically set to be 15 channels above the pedestal. At the beginning of each run one thousand random triggers were generated with sparsification disabled in order to

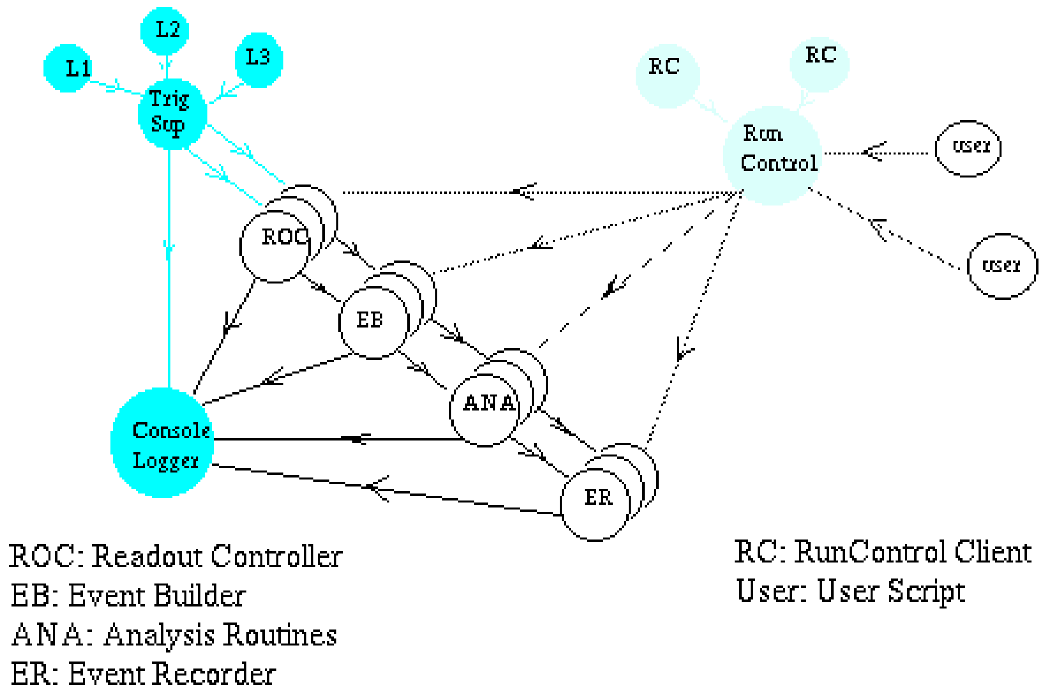

Figure 2.23: CODA software flow chart. Only the level one trigger (L1 in figure) was used during **E93–018**.

measure the centroids and widths of the pedestals. Some beam related quantities were also recorded on an event-by-event basis. Beam position monitors, beam loss monitors, and beam raster read-back values were recorded for each event. The typical event size for the Hall C DAQ was $\sim$ 500 kB/event/spectrometer (or $\sim$ 1 megabyte/second/coincidence event), which limited the total data rate (coincidences plus singles) to about 2 KHz.

2.7.2 EPICS - Slow Control Events

In addition to the physics event, other event types could be defined in CODA, allowing readout of hardware scalers and/or execution of user scripts (i.e. pieces of code written in CODA that were treated as events, allowing the periodic execution of certain processes). During **E93-018** the hardware HMS, SOS and Coincidence scalers were read out by a script triggered by an asynchronous process every two seconds. This procedure included the readout of the BCM monitors as well. Every 30 s a script triggered by CODA readout various slow controls variables from the Jefferson Lab EPICS database and sent them into the Hall C data stream. Spectrometer magnet settings, accelerator settings, and target status variables (temperatures, pressures, coolant flow, etc.) were accessed and logged this way.

DATA ANALYSIS TOOLS AND CALIBRATIONS

3.1 Overview

In this chapter the tools and techniques used for data analysis will be described in detail. The general framework of the Hall C analysis software will be layed out, together with the various calibration and data checking procedures available for each detector. The tracking procedure as well as a review of the raw PID signals and their reliability (for both the electron and the kaon arms) will be explained. In the remainder of this section the general philosophy of the Hall C analysis software is outlined.

The analysis of the Hall C raw data files was accomplished using the Hall C analysis software called `ENGINE`. The `ENGINE` was conceived as a general framework/shell for the analysis of both single-arm and coincidence experiments. The program has interfaces with CODA (raw event readout/decoding) and CERN's CERNLIB/GEANT libraries (histograms/ntuples, etc.); also CTP (CEBAF Test Package) was used for dynamic allocation of histograms/tests, etc. To ensure readability by all members of the Hall C collaboration the `Engine` was written almost entirely ($\sim$ 55000 lines of code) in FORTRAN77, except for the CTP package ($\sim$ 15000 lines of C) and the interface to CODA (written for the CODA parser which in turn produced C code). The experiment-specific parts of the code were grouped in just a handful of "physics" subroutines that could easily be customized and maintained by the users to reflect the configuration/needs of each particular experiment. For these physics routines the “standard” `ENGINE` provided only skeletal code.

The detector calibrations were done using separate pieces of code and their results were stored in ASCII files which were then used as input to the `ENGINE` for the second-pass analysis of the data.

In practice the `ENGINE` read the raw CODA/EPICS events, decoded the detector hits, generated/reconstructed tracks and particle information for each event. The `ENGINE` also kept track of hardware and software scalers (it actually generated software scalers, based on the recorded information) for each run. A rather intricate, yet logical, array of ASCII files was used as input by the `ENGINE` to decide which way a particular analysis task was to be carried-out. Anything from names/locations of the raw data files to flags specifying which events (HMS/SOS/COIN or combination thereof) were to be processed, to the frequency with which histograms were to be saved on disk could be set using these configuration files. The `ENGINE` output information in three different formats:

1. ASCII report file(s) containing both hardware and software scalers, as well as calculated detector efficiencies.

2. Histogram file(s) containing a “standard” set of histograms, in CERNLIB’s HBOOK format, used to check the detector performance and monitor the integrity of the data. These were mostly used for the on-line analysis (actually the “just-offline” analysis).

3. Ntuple file(s), also in HBOOK format, containing event-by-event information. As these tended to be large, they were mostly reserved for the final physics analysis.

3.2 CEBAF Test Package

The CEBAF Test Package (CTP) software library provided a flexible way to store and modify histogram, test, and scalar definitions and other analysis parameters. CTP was loosely modeled on LAMPF’s Q system [40] and was written at Jefferson Lab in the

C programming language. As the bulk of the "standard" Hall C software was written in FORTRAN77 (this ensured that all members of the Hall C collaboration could read/understand the analysis code) an interface mechanism was devised that allowed CTP the "sharing" of variables with the FORTRAN code. According to this procedure all fortran variables that were to be "seen" by CTP first had to be included into a common block, then "registered" using appropriate calls to CTP C routines. At compilation time the CTP parser read all defined *.cmn files (i.e. files where the various FORTRAN common blocks were defined) and produced the source code that automatically performed the CTP registration of all variables that appeared in common blocks. These variables then became accessible from both the fortran code and from CTP (via RPC - remote procedure calls); they could be examined and/or changed without having to recompile the code. In addition, variables which were not part of the FORTRAN portion of the `ENGINE` could be defined and used to create tests/histograms.

CTP procedures were used by `ENGINE` to access both the input parameters/flags that control the analysis, and to define histograms, tests, and scalers to be output. All parameter as well as histogram and test definitions were stored in ASCII files that were read and parsed by CTP at the beginning of the analysis; then the histograms were created, booked, etc. By changing the appropriate ASCII files one could change the number/characteristics of the histograms/tests the `ENGINE` produced/used, without having to recompile the code. This offered much more flexibility than the "standard" FORTRAN77 code that didn't allow any kind/form of dynamic allocation of structures. The defined CTP tests were evaluated at the end of each physics event, then the histograms were filled (tests could be used to selectively fill some/all of the histograms) and the software scalers were incremented (any/all CTP tests functioned as software scalers as well).

In addition to the functions described above CTP allowed the user to make effective use of the stand-alone event display code. This code, called "one_event_display", was based on CERN's GEANT package and allowed the visualization of individual events, tracks, and/or detector hits. It was possible for the event display code to define/modify/exchange CTP variables/tests and then exchange them, via RPCs, with the `ENGINE`. This ability to setup and use tests for selecting certain classes of events made the event display a very useful debugging tool. Given that the event display inherited all the graphical capabilities of GEANT/CERNLIB, it could also be used as a presentation tool.

3.3 Hall C `Engine`

In Fig. 3.1 the schematic flowchart of the Hall C `ENGINE` is shown. The main components of this code will be described below.

3.3.1 Initialization

The `ENGINE` started by reading in the main configuration file, usually called "REPLAY.PARM" (the name itself is stored in an environment variable and can be set to suit ones needs/taste). In this file several pieces of information governing the behavior of the `ENGINE` program were set. First a series of filenames were specified. These included:

- name of the raw data file,
- name of the main parameter file (location and calibrations of various detector elements),
- name of the file containing histogram definitions,
- name of the file containing test definitions,
- name of the kinematics file (i.e. file containing beam energies, spectrometer momenta and/or angles, etc.),
- name of the MAP file (i.e. mapping between ADC/TDC channels and physical detectors),
- names of the templates to be used as model for producing scaler reports,
- names for the scaler reports to be produced,
- names for the histogram and Ntuple file(s) to be produced,

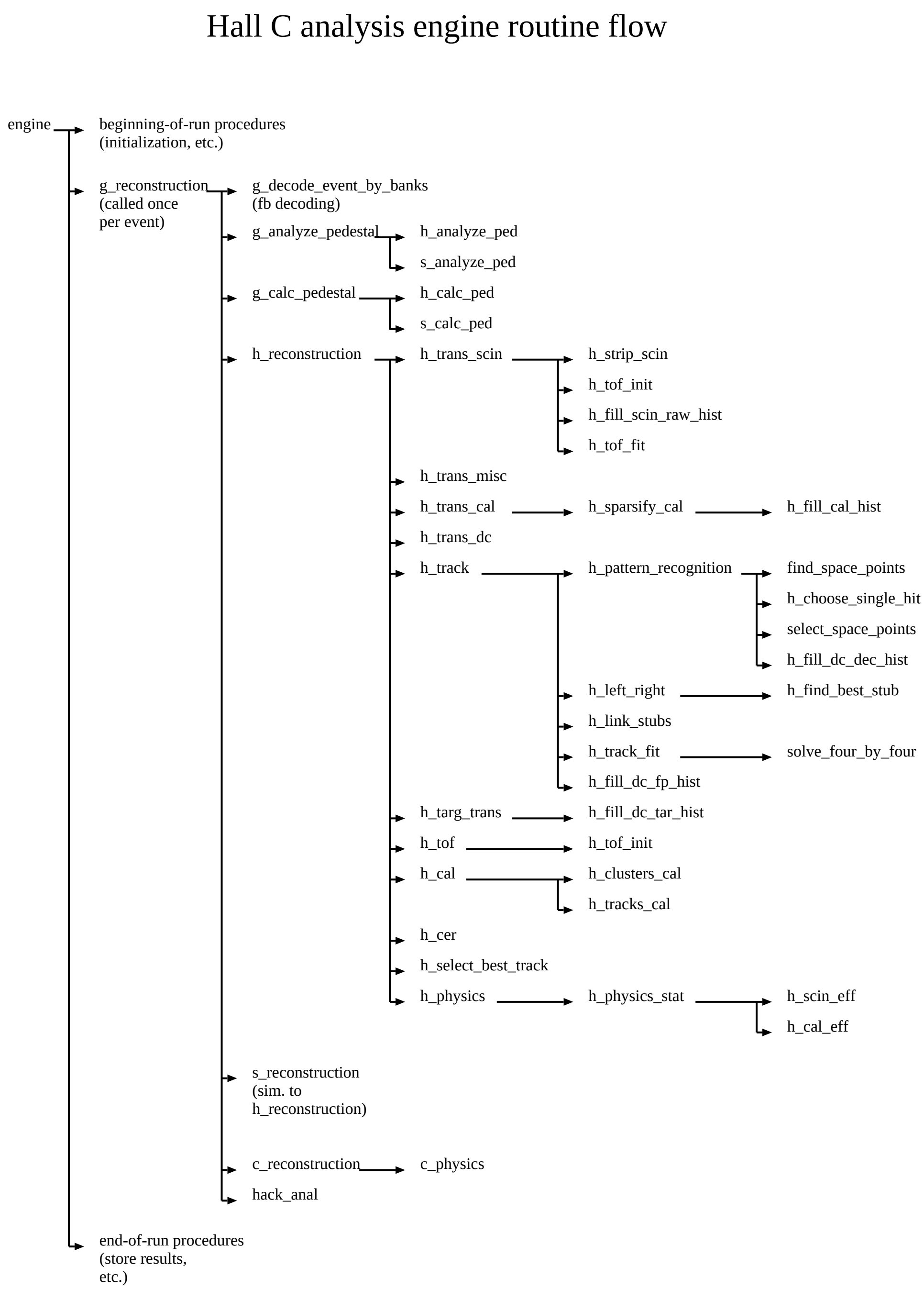

Figure 3.1: Flow diagram of the Hall C analysis software, `Engine`.

- name for the preprocessed run (see below) to be produced,
- ...

The filenames specified in REPLAY.PARM may have contained the required information themselves or they might have pointed to an even larger collection of filenames (i.e. the histogram file was typically just a collection of "#include" statements which would point one towards the appropriate HMS/SOS, etc. histogram files). Some of these filenames might have included the C-inspired "%d" token which would, at runtime, be replaced by the current run number, according to the Hall C numbering scheme.

Additionally, in REPLAY.PARM a series of flags that turn on/off various parts/aspects of the analysis code were set. These included:

- HMS on/off flag. This flag controled whether or not HMS singles events were to be analyzed;
- SOS on/off flag. Same as above only for SOS singles;
- COIN (coincidence) on/off flag. Turn on/off the analysis of HMS/SOS coincidence events. Invariably set to 1=="on" for the **E93-018** analysis;
- PEDS (pedestals) flag;
- RPC on/off flag. Setting this flag forced the `ENGINE` to wait for RPC requests from other processes. Useful when used in conjunction with the one_event_display.

After all the run parameters were defined, the code performed the initialization of the defined histograms and/or ntuples, then proceeded to open the raw data file. The beginning of run information events included read-back values for the ADCs (i.e. pedestal events) and TDCs, as well as settings for various kinematic variables (such as beam energy, spectrometer central momenta and angles, etc.). Lastly the `ENGINE` decoded the (eventual) command line options that may have been given (any CTP variable can be specified/initialized via a command line option). For variables initialized in more than one place (i.e. beam energy might be read from the kinematics database, might be present as a beginning of run parameter, and also can be specified in a command line statement), the priority order was as follows: command line, then beginning of run, then database/parameter files. After processing all initialization events and performing all related tasks, the main event loop began.

3.3.2 Main Event Loop

The main event loop read and processed events according to their type. The types of events relevant to the present analysis will be listed below:

1. scalar events - decoded and incremented all hardware scalers. This included the time and the charge since the last scalar event. The total (running) time and the total accumulated charge were computed.

2. EPICS (slow control) events - these events monitored the status of the cryotarget, magnetic settings and coolant levels/parameters for the spectrometer magnets, beamline diagnostics (beam position monitor readings, settings of various arc magnets), etc. Once decoded, this information was typically stored in ASCII files, to be further analyzed by specific, stand-alone programs (such as the beam current calibration code).

3. physics events - these could be further broken down into four sub-types: pedestal events, HMS, SOS, and COIN events. As explained earlier the pedestal events were just a convenient way of obtaining a measurement of the ADC pedestal at the beginning of each run. The HMS, SOS, and COIN event types could only be generated by real spectrometer triggers. The raw detector hits for each event were read, decoded, and passed to the main reconstruction routine for the HMS and/or SOS. After an event was successfully reconstructed, the appropriate particle identification information was computed and saved for each spectrometer. The *h_physics, s_physics,* and *c_physics* routines were called, allowing the calculation of all defined single arm and/or coincidence physics quantities.

3.3.3 Event Reconstruction

Following the general philosophy outlined in [41] the HMS and SOS analysis codes were nearly identical both at the data structure and at the subroutine level. Only the names of the variables (leading "h" for all HMS variables, leading "s" for SOS variables) and actual number (i.e. SOS hodoscope planes held fewer paddles than HMS hodoscope planes) and values of the parameters differed between the two spectrometers. The only other noticeable difference was the presence of the code relating to the two Čerenkov detectors specifically installed in the hadron arm for the purpose of kaon identification. Figure 3.2 shows the flow diagram for the SOS reconstruction (as used in **E93-018**); the HMS schematic is identical except for the bits that relate to the aerogel and lucite analysis.

As seen in Fig. 3.2 for each event the hodoscope hits were translated from raw ADC and TDC values/channels to times and pulse heights. After timing corrections due to pulse height variations and cable length offsets were applied, all events outside of a large (user defined) timing window were discarded to eliminate random hits. The remaining signals were used to determine the velocity of the particle and the time at which the particle passed through the drift chambers. This later information was subsequently used as the start time (in reality the stop time, as the wire chambers are operated in the common stop mode) for the drift time calculation. After the hodoscope information had been decoded, the information from all other detectors (drift chambers, calorimeter, Čerenkov detectors, etc.) was decoded and track independent quantities (such as total calorimeter energy, total number of photoelectrons from a Čerenkov detector, etc.) were calculated[1].

After finishing the calculation and saving all track independent variables, the program called the tracking routine. The basic strategy here was to use the information from the drift chambers (and the start time from the hodoscopes) to reconstruct the trajectories of charged particles that passed through the active area of the detector array. Each wire

[1]Note that for some segmented detectors one can compute both track-dependent and track-independent quantities (i.e. total energy deposited in the calorimeter versus the total energy deposited along a given track in the calorimeter).

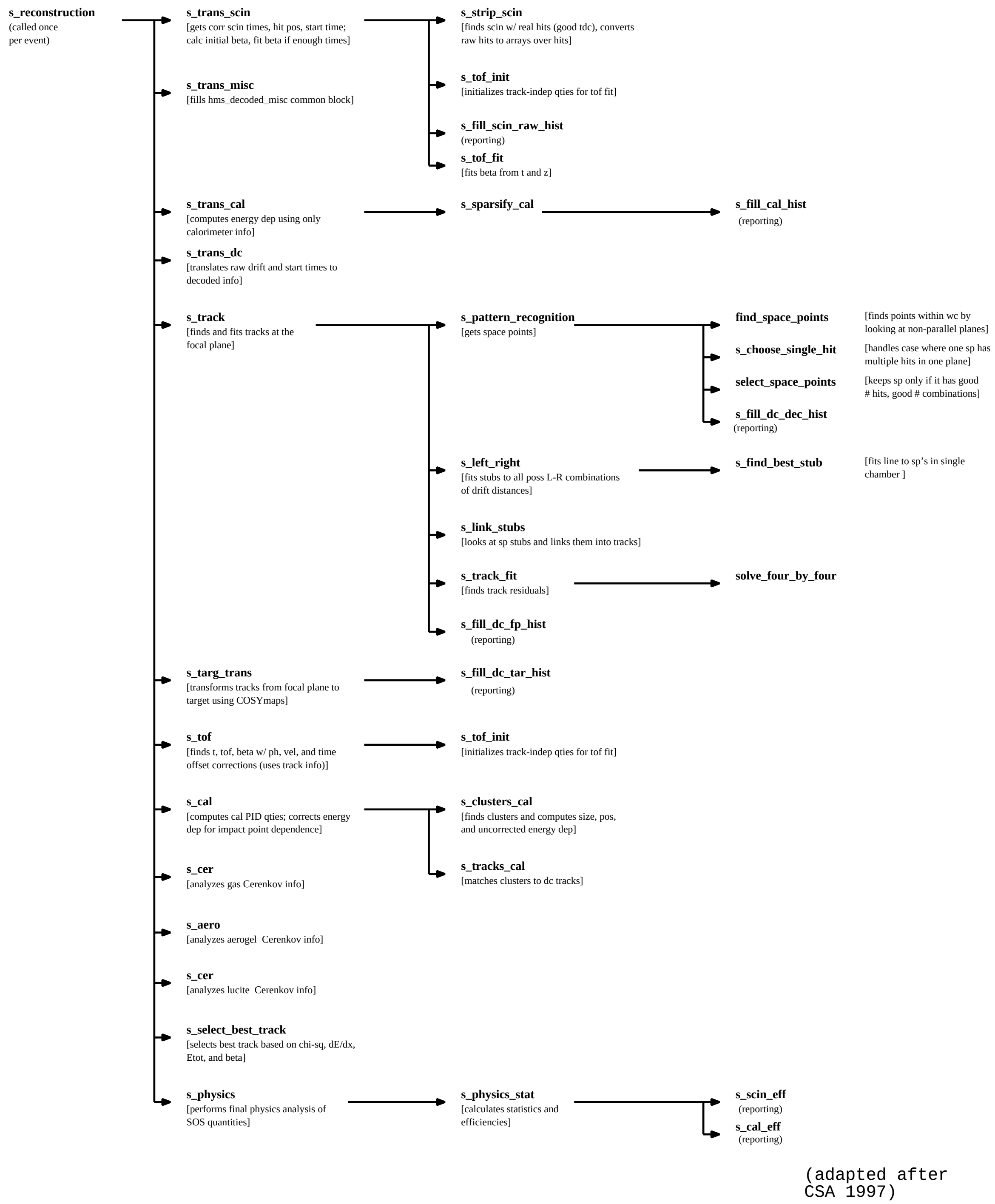

Figure 3.2: Flow–Chart of the SOS event reconstruction software (as used in **E93-018**). The HMS Flow–Chart is similar, except for the aerogel and lucite portions of the code.

that fired/gave a signal for a given event provided two essential pieces of information: the position of the wire itself and, using the start time from the hodoscope, the drift time of the electron-ion pairs produced by the charged particle inside the gas mixture of the chamber. Knowing the drift time and also the drift velocity of electron-ion pairs in the particular gas mixture used in the chamber allowed the calculation of the drift distance (i.e. the distance from the wire at which the event occurred). However this information could not resolve if the particle passed to the left or to the right of a given wire (this is the so-called left/right uncertainty). So effectively for each wire hit one got two space points where the particle could have passed. Combining the information from all planes of a chamber one had $\sim 2^6$ possibilities that needed to be tested (in reality the number was somewhat larger as soft delta rays, cross-talk between wires, etc. add a certain amount of noise for each track). Reconstructing a track then was just a matter of fitting a trajectory (to a line, as there was no magnetic field inside the detector hut) for each of the combinations mentioned above and then choosing the trajectory with the lowest χ^2.

This brute force method for track reconstruction is very robust and provided accurate results even when significant noise was present and/or when information was partially missing; however the method was very time consuming and that can be a long term problem when analyzing a huge volume of data. To reduce the tracking time the so-called small angle approximation was used. This approximation takes advantage of the fact that planes measuring the same coordinate of a track (say the x and x' planes) are staggered by half a cell. If the two planes are physically close together inside the chamber and the incoming particles come almost perpendicular to the chamber, then one can choose the left/right combination that will make the particle go between the wires that fired. This approximation worked very well for SOS where the ordering of the planes was (x, x', u, u', v, v'), effectively lowering the number of combinations to be tested from 2^6 to 2^3. For HMS this procedure could be applied only for the y and y' pair (the x planes are too far apart and the stereo planes are not parallel), still providing a factor of four reduction in the number of possible combinations. Keeping true to the general philosophy of the Hall C `ENGINE` the use of the small angle approximation could be turned on/off by appropriately setting a pair of variables (one for each spectrometer).

The last part of the tracking algorithm involved checking if the tracks reconstructed in the front and back drift chambers were consistent with each other (as between the front and the back drift chambers the particles travel through air, the matching conditions needed to be somewhat relaxed, to account for multiple scattering.) Of course this statement was energy dependent and also particle dependent. For each full track the χ^2 of the fit was recorded and, using the known optics properties of the spectrometer, the track was back-propagated through the spectrometer to the target yielding the position along the beam direction, the angles in both the dispersive and non-dispersive directions, as well as the fractional difference between the momentum of the track and the central momentum of the spectrometer.

Once the best track was selected, track-dependent variables were calculated (effectively as a subset of the more general track-independent quantities).

Lastly the single arm and (if appropriate) the coincidence physics quantities were computed, all defined tests were evaluated, the corresponding software scalers were incremented, and all the appropriate histograms were filled. If the saving of Ntuples was enabled, these were also filled at this time.

3.3.4 Output

Periodically during the course of the analysis (typically every 10000 events), and also when the end of run event was encountered, or when the physical end-of-file was found, if the CODA data acquisition system ended ungracefully (read "crashed"), the `ENGINE` dumped the output files, flushing all existing buffers to disk.

This involved writing the scalar report files containing the final values for both the hardware and software scalers, measured detector efficiencies, beam current and integrated charge, as well as electronics and computer dead times.

The histogram file(s) primarily contained 1D and 2D detector summary histograms, used for online monitoring or the detector performance and also for the subsequent offline calibration checks.

The Ntuple files contained event-by-event information. As the final space occupied by an Ntuple depends on the product $N_{events}\times$ $N_{variables}\times$ Average Variable Size (assuming the default Hall C Row-Wise Ntuples for which no compression is available), and taking into account that the number of raw events for **E93-018** was high, the number of variables saved in the Ntuple was kept to a minimum. The minimal list of coincidence variables saved in the Ntuples can be found in Appendix B and contains tracking information (both focal plane and target), particle ID information (including TOF information) for both the electron and hadron arms, raw and corrected coincidence time between the spectrometer, and average energy loss for each arm and for the beam.

One will note the absence of all "physics" information from the Ntuple. This was a carefully thought out analysis decision based on the following rationale: **E93-018** is an experiment for which the raw background–to–real ratio is rather high (typically one finds one coincident kaon event for 500-1000 raw coincidence triggers), so computing physics quantities for events that will anyway be rejected by PID, etc. cuts would have been an exercise in futility. Instead the decision was made to save both analysis time and disk space and rely on COMIS[2] functions to compute all meaningful physics quantities only for the subset of identified kaon events for the first pass analysis. A logical flowchart for both the offline and the online analysis is shown in Fig. 3.3. To speed up the analysis, the runtime compilation option of COMIS was used, as well as relying on sets of Ntuple masks to save and recall the most common PID cuts applied.

3.4 Calibration Procedures

Calibrations of the various detectors installed in the HMS and SOS detector huts were necessary in order to achieve the best possible performance. These calibrations included hardware benchmark tests and checks, accomplished well before the actual running of **E93-018** , during the designing and building of the detectors, hardware tests and calibration runs accomplished in the initial setup/check-up phase of **E93-018** , and, finally, software calibrations carried out in the analysis phase of the experiment. In this section

[2]COMIS is the CERNLIB FORTRAN interpreter.

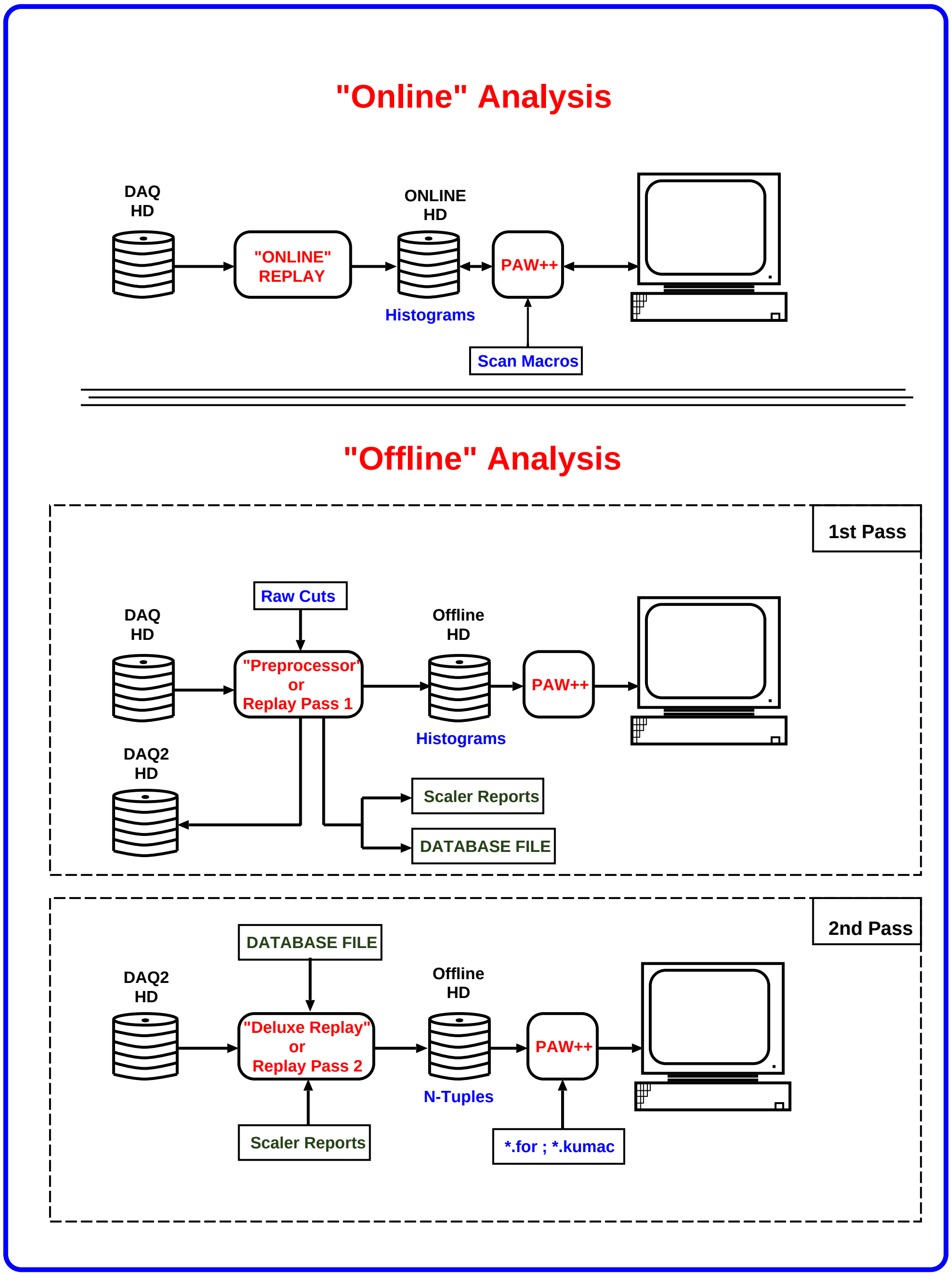

Figure 3.3: Flowchart illustrating the online and offline analysis philosophy for the present **E93-018** analysis.

these various calibration procedures are described.

3.4.1 Calibration of Gas, Aerogel, and Lucite Čerenkov Detectors

As the number of ADC channels for the gas, aerogel, and lucite Čerenkov counters was relatively small (from 2 channels for the HMS gas Čerenkov up to 14 channels for the SOS aerogel detectors) the final gains were calculated directly, without the use of dedicated software. The pedestal values were subtracted from the ADC signals and then the gain was determined for each PMT tube by finding the one photoelectron peak and/or by comparing the mean and widths of the signal in the central region with the expected (Poisson statistics) result. For each PMT only one parameter was needed, the number of channels per photoelectron. Adjustment of the high voltage on some of the phototubes was necessary in some cases, to ensure that the PMTs of a given detector are as closely gain matched as possible. As with the other parameters of the experiment, these gains were closely monitored both on- and offline.

3.4.2 Hodoscope Timing Calibrations and Corrections

Bench testing of the scintillators to be used in both the HMS and the SOS hodoscopes indicated a mean time resolution of $\sim$70-100 ps. However, several timing corrections had to be carefully studied/fit, applied, and continuously monitored in order to achieve a final resolution of the "as built" hodoscope close to the "ideal" limit quoted above.

First the TDC scale and nonlinearities were studied. The TDC scale (i.e. ps/channel) was initially determined by testing all TDCs (including the spare modules) using a Time Interval Generator (Phillips Model 7120). The precise RF signal of the accelerator (499 MHz) was used to double check the time scale, using the prescaled RF as the TDC start, and the raw RF as the TDC stop. The modules altogether had time scale variations of $\pm$6%; however the variations within a module were smaller, at the 1-2% level.

The fitting procedure of the TDCs allows for an arbitrary offset that could account for most of the variations described above. The only error due to channel–to–channel variations that remained was the variation over the range of TDC values in each channel. Typically, a TDC value for a single signal would vary over a range of 100 channels or less, so the time variation corresponding to a 2% variation in scale would be ± 1 channel, or ± 25 ps. The TDC scale for each set of hodoscopes was set to the average of the TDC channels being used, and no channel–to–channel correction was applied.

In addition to the scale calibration of the TDCs, corrections had to be made to account for the timing variations with pulse height, propagation time of the signal inside the scintillator/light guide, as well as an overall timing offset between individual signals (i.e. differences in cable lengths, etc.). These software calibrations involved running the `ENGINE` to analyze real data, dumping (typically into ASCII files) hit information for many events, and then fitting for some/all the corrections using stand alone fitting code(s).

Because in the entire Hall C data acquisition electronics fixed threshold discriminators were used, the time at which a given signal would exceed its set threshold depended on the height of the signal. Thus, large signals would fire the discriminator earlier, relative to the signal maximum, than small signals. As these corrections could amount to hundreds of picoseconds, they would have a significant effect on the resolution of the scintillators. To better study this problem one needed to separate it from the other competing effects listed in the previous paragraph. One could start by observing that limiting the hits to a small region of one of the scintillators (by imposing a tight drift chamber cut for example), the corrections due to light propagation in the scintillator were minimized. Imposing this cut and comparing the time (relative to start time) of an individual scintillator to the average time of all scintillator hits, one could clearly see the timing variation with respect to the pulse height (see Fig. 3.5). However, this effect was still diluted by the fact that the averaged time varied due to pulse height walk in the other scintillators as well. To fit the correction, crossed pairs of scintillators (i.e. one scintillator paddle in an x plane and the other in a y plane) were taken in order to limit the region of the scintillator that was hit and the mean times of the elements (one might want to recall that each scintillator paddle had PMT read outs at each end) were compared. The use of this mean time eliminated the dependence on position along the scintillator, leaving only the pulse height walk correction and an overall offset. After the application of a rough correction on the pulse height walk on three of the four PMTs of a given crossed scintillator pair, the remaining dependence on the ADC value gave the form of the pulse height variations for the uncorrected tube. This procedure is illustrated (for the SOS) in Fig. 3.4 where the pulse height correction is plotted, for each of the four hodoscope planes, as a function of the paddle number. For the present analysis the correction of the form used for fitting was:

$$\Delta t = PHC * \sqrt{max(0,(ADC/PHOFF - 1))} + t_0 \tag{3.1}$$

where ADC is the raw ADC value, and PHC (pulse height correction), PHOFF (pulse height offset) are the timing correction parameters, and t_0 is an arbitrary offset between the two scintillators.

Once the pulse height correction was determined, the velocity of light propagation in the scintillator paddles could be measured by taking the time difference of the PMTs on the opposite ends of each scintillator element. A plot of this time difference versus the position along the scintillator yields the velocity of propagation of the signal (i.e. the slope). Note that the velocity determined by this procedure is not the speed of light in the plastic scintillator, but rather the "effective" speed of the photons propagating in the scintillator (typically photons will reflect several times off the sides of the scintillator before being collected by the PMT). This velocity correction was strongly dependent on both the index of refraction and the geometry of the scintillator. Taking advantage of the fact that the scintillators that form a given plane were geometrically identical, the average velocity was measured (and subsequently used) on a per plane rather than per scintillator paddle basis.

Finally, for each tube an offset was provided to account for variations in cable length and/or different response times of the PMTs. These offsets were fit in the same way as the pulse height corrections. Velocity and pulse height corrected mean times were generated for a pair of scintillators. The offsets were then adjusted in order to make the velocity of the particle as measured by the TOF between scintillator hits agree with the

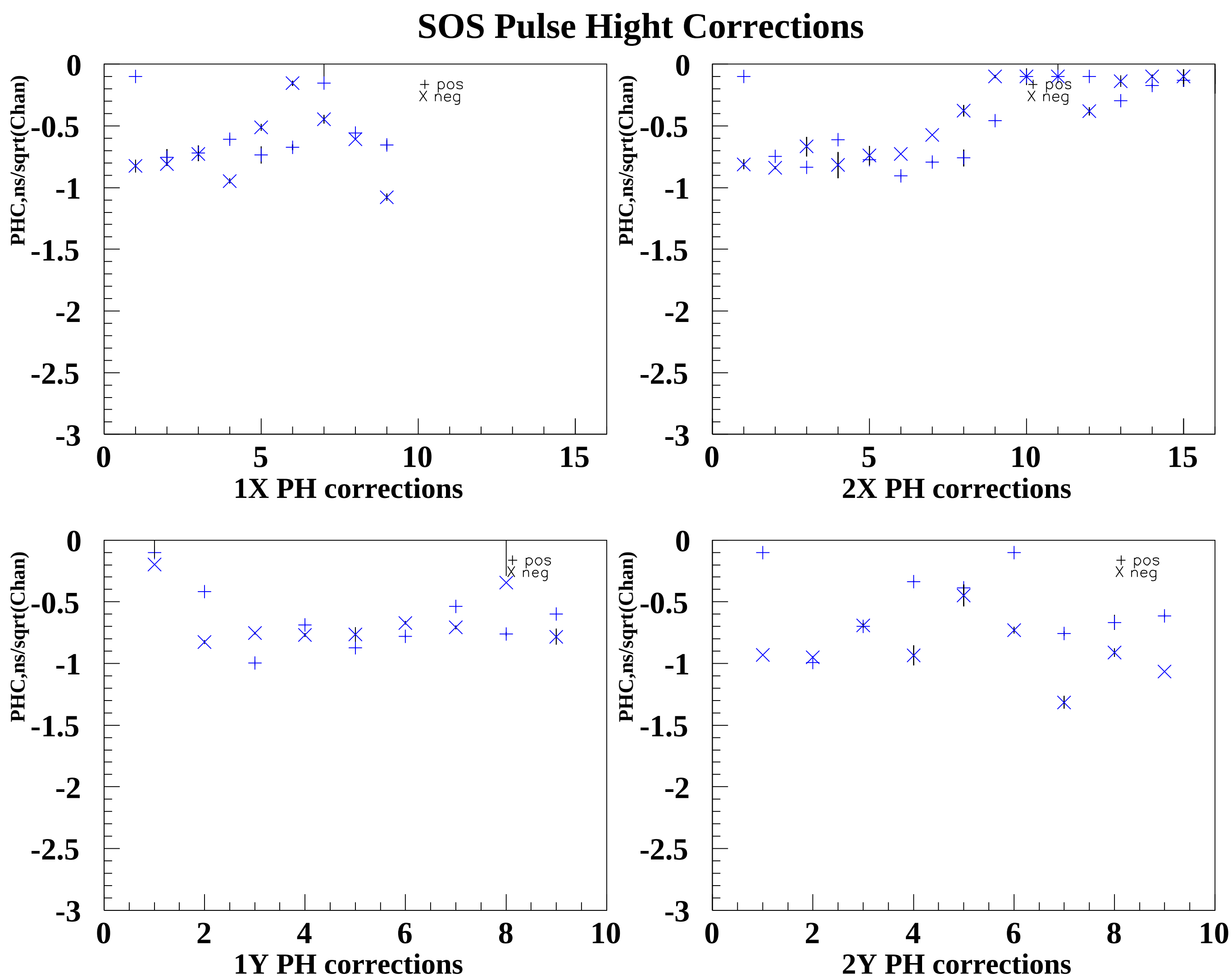

Figure 3.4: Pulse height corrections versus the paddle number for the SOS hodoscopes. Each of the panels corresponds to one of the four scintillator planes.

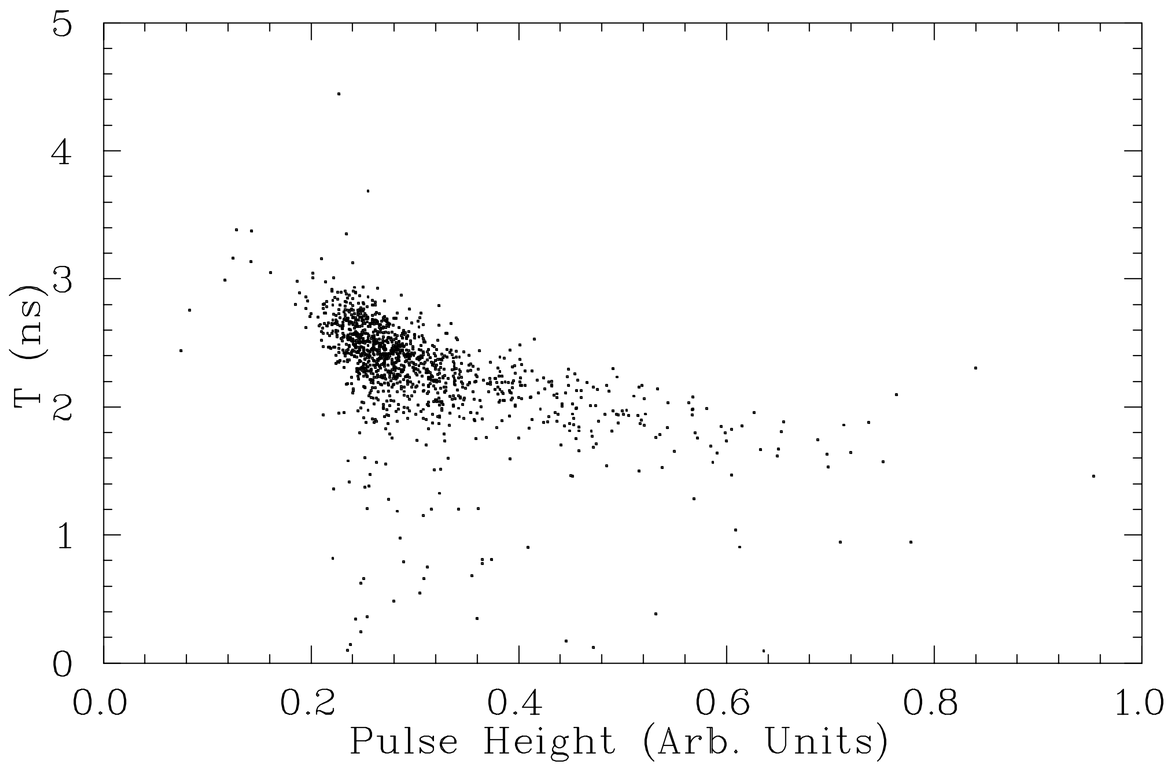

Figure 3.5: Time (relative to start time) versus pulse height (as determined from the ADC) for events in a small region of the scintillator.

known velocity of the calibration particle (β=1 for electrons, and β as determined from the momentum of the particle for hadrons).

The mean time was generated for a pair of scintillators, after the velocity and pulse height walk corrections were made. The offsets were adjusted in order to make the time between the scintillator hits agree with the known velocity of the particle (β=1 for electrons, or β as determined from the momentum of the particle for hadrons). For the current **E93-018** analysis all these software calibrations were carried out for both the electron and the hadron arm for every kinematic point, and checked for consistency for each run. In Fig. 3.6 the typical output of the HMS TOF fitting program is shown while Fig. 3.7 shows an SOS calibration. Numbers consistent with the 110–130 ps timing resolution advertised earlier are seen for the standard deviation of the TOF measurements.

Lastly note that since many of these calibration procedures require large amounts of data (typically a hundred thousand counts or so - many more than all our available kaon data at any given kinematic point), for the hadron arm pion and proton samples were used for the TOF calibrations.

3.4.3 Lead Glass Calorimeter Calibrations

The main purpose of the electromagnetic calorimeter/shower counter was to measure the energy deposited by electrons in the lead glass blocks. In order to accomplish this task the gain of each lead-glass–PMT module must be determined, and the ADC values measured by the module needed to be converted into deposited energy.

The main problems that needed to be solved by the calibration procedure were the light attenuation in the lead glass blocks and the gain (mis)matching between different blocks/layers.

Attenuation in the lead-glass detectors gave a variation of the signal with the distance from the PMTs. As each lead-glass block was only read at one end[3] information external to the calorimeter (i.e. hodoscope or drift chamber position information) was necessary for this correction. A multiplicative position dependent correction factor was used to account for the light attenuation in each block. To check the validity of this assumption the measured energy distribution as a function of the distance from the PMTs was used. Note that the conversion from ADC channels to energy deposition was determined for a hit in the central region of the blocks, rather than raising the signal everywhere to remove the attenuation altogether.

In addition to the attenuation correction, it was necessary also to account for the gain variation between individual modules. During the hardware setup of the **E93-018** experiment electron data samples were collected and the high voltages for the calorimeter PMTs were adjusted so that blocks in the same layer (i.e. all blocks that are at the same z value along the central ray through the spectrometer) would give identical ADC signals (to ∼10 % accuracy). This output signal matching condition meant that in the dispersive

[3]Since the completion of **E93–018**, a program to implement the read-out of the lead-glass blocks at both ends was started.

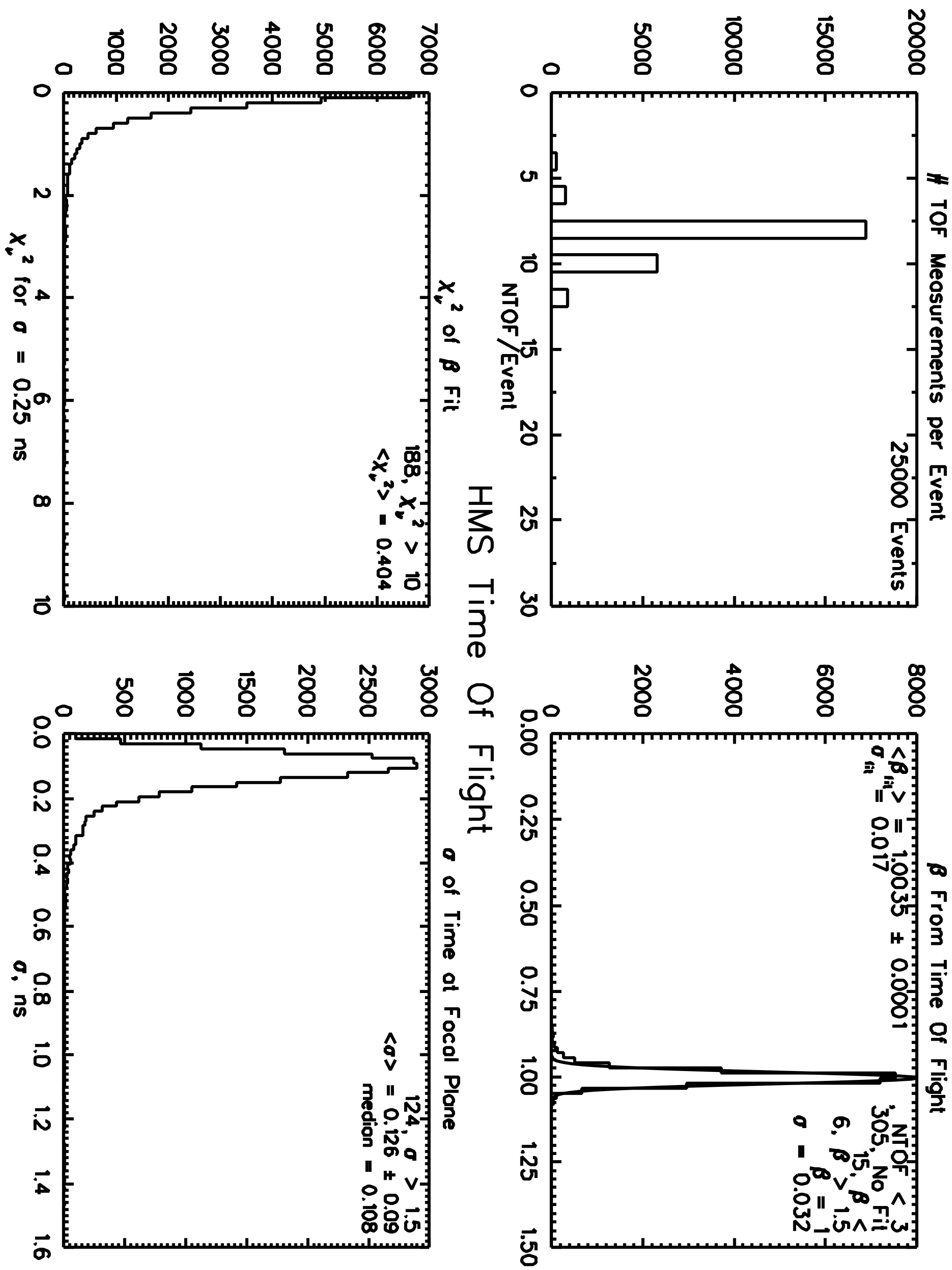

Figure 3.6: Typical output of the stand alone code used for HMS TOF calibration showing the number of independent TOF measurements per event, the distribution of measured velocity $\beta = \frac{v}{c}$ for the calibration sample, the χ^2 distribution, and the standard deviation (σ) of the measurement. A clean sample of electrons was used for this calibration.

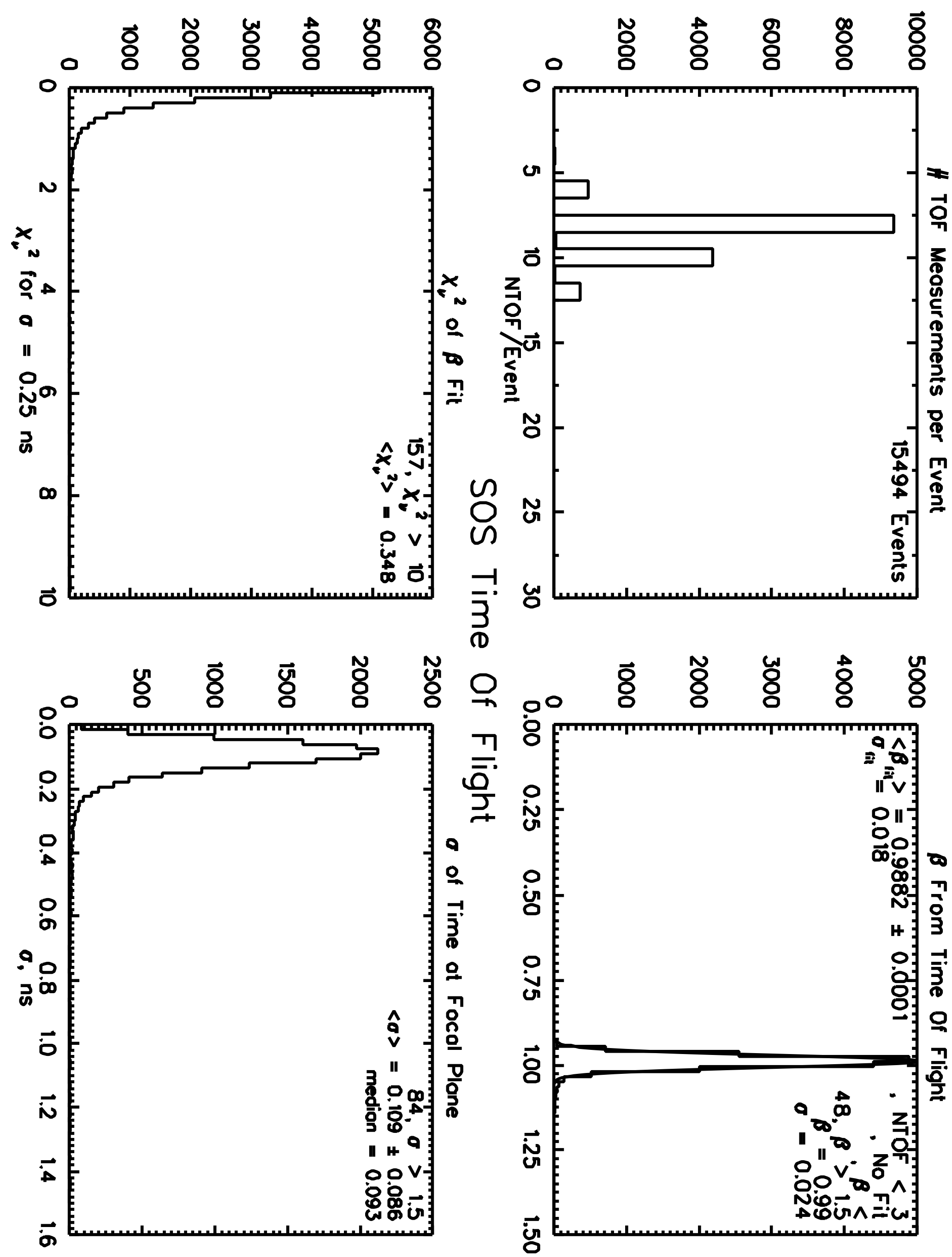

Figure 3.7: Typical output of the stand alone SOS TOF code. Definition of variables is identical to the HMS plot. Note that a clean sample of pions was used for this particular calibration.

direction one imposed gain variations of the same order of magnitude as the momentum acceptance of the spectrometer (20 % for HMS, 40 % for SOS). The advantage of this method versus the straight gain matching condition was that it ensured a more uniform calorimeter trigger efficiency over the whole active area of calorimeter. Note that this last condition was very important for the **E93-018** analysis since all our data was acquired using the "ELLO" trigger (see section 2.6).

During the software calibration of the detectors the above conditions could be further improved (to a few percent level) to account for the eventual gain variations over extended periods of time.[4] In order to fit these gain differences "good" electron events were selected using a Čerenkov cut, and the pedestal subtracted ADC values for each lead-glass block were recorded, together with the energy of the electron as determined from track reconstruction (i.e. we used the reconstructed momentum of the track). A stand alone code would then vary (within reasonable limits) the gain correction for each block, in order to minimize the difference between the true energy of the electron and the energy of the electron as measured from energy deposition in the calorimeter. As the electrons tend to deposit almost all their energy in the first two to three layers of the calorimeter, this procedure becomes unreliable for calibrating the last layer of the calorimeter. For this last layer one could use once again a Čerenkov cut to select a clean pion sample and use that, and the knowledge that pions will tend to deposit equal amounts of energy (~60 MeV) in each layer to calibrate the last calorimeter layer.

The energy resolution $\delta E/E$, after applying all the above corrections, was $\sim 5.6\%/\sqrt{E}$ for SOS and 6-8%/$\sqrt{E}$ for HMS (for E in units of GeV).

3.4.4 Drift Chamber Calibrations

For both the HMS and SOS drift chambers several calibration procedures had to be carried out in order to ensure that the optimum performance of these devices was reached. These included both hardware calibrations done during the commissioning of the Hall C spectrometers and re–checked in the setup phase of **E93–018**, as well as software calibra-

[4] To successfully carry out this procedure large numbers of electrons/pions are needed. Also, for lower central momenta of the spectrometer the reliability of the procedure becomes problematic.

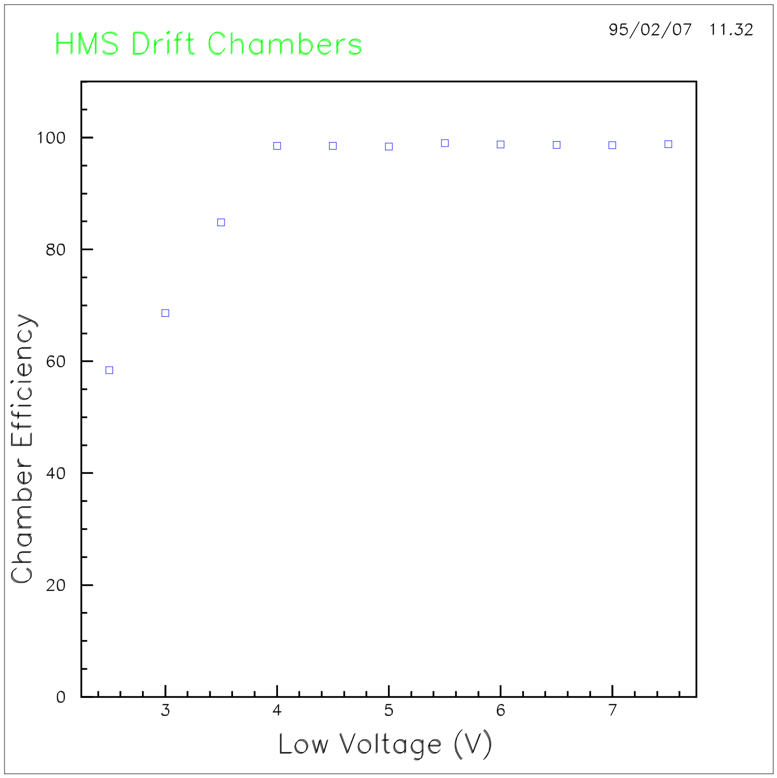

Figure 3.8: HMS Drift Chamber calibration plot as obtained in early 1995 during the commissioning of the Hall C spectrometers. The chamber efficiency (in %) is shown versus the voltage applied on the amplifier-discriminator cards. The nominal operating voltage of the HMS drift chamber threshold was 4.5 V.

tions performed and monitored for each kinematic point during the actual experiment.

The hardware calibrations and initial performances of the HMS drift chambers are described in detail in [31] and here we will only state the main results of that study. In Fig. 3.8 the efficiency of the HMS drift chamber is plotted versus the voltage on the amplifier-discriminator cards. Based on this study the operating voltage for these chambers was chosen to be 4.5 V (a similar study for the SOS chambers helped fixed their running point at ~1.5 V). As explained earlier the main function of the drift chambers was to provide accurate position information. For each event the drift chambers provided a list of wire hits and a TDC value for each hit. Using the timing information from the hodoscopes (so the hodoscope calibrations have to be carried out first) one could determine the time at which the charged particle passed through the active area of the chamber. Combining this information with the TDC value recorded for each hit, one could then determine how far from the sense wire a given event occured. To determine this distance the following procedure was followed: For a reasonably large number of events (typically 100K+ events) the difference between the TDC value recorded by the chamber and the time at the focal plane (as measured by the scintillators) was plotted. This is the raw drift time distribution. The main assumption is that the cell would be uniformly illuminated[5] averaging a large number of events over all the cells in a given plane; even though for (every) individual cell the distribution could be highly non-uniform. A loose cut was then applied to reject all random "noise" hits (drift chambers are sensitive for minimum ionizing particle so they might fire even for spurious delta electrons) and the remaining time spectrum was integrated. The actual drift distance is then:

$$d = d_{max} \frac{\int_{t_min}^{T} F(t)dt}{\int_{t_min}^{t_max} F(t)dt} \tag{3.2}$$

Where t_{min} and t_{max} are the limits of the time interval to be included in the fit (typically -25 to 250 ns), T is the time value as recorded by the chamber TDC (after the scintillator time at focal plane and an offset accounting for the difference in cable lengths are subtracted), d_{max} is the maximum drift distance, equal to half of the drift cell size, i.e. five mm. Following this procedure one effectively maps (thus the "time-to-distance" map name) the drift chamber TDC values into distances from the sense wires at which the event occured, which can in turn be used by the fitting algorithm to perform track reconstruction. Incidentally one can readily see that the width of the time distribution is $\sim$100 ns which is consistent with the maximum drift distance of 5 mm and the known drift velocity of 50 μm/ns for electrons in the 50:50 argon-ethane gas mixture used to fill the drift chambers (i.e. 100 ns $\times$ 50 μm/ns = 5000 μm = 5 mm). While the results are certainly consistent with the gas mixture and size of the drift cell, as well as the applied voltage, the conformal mapping procedure outlined above was very robust and relatively

[5]Single arm $p(e, e')$ scattering data above the resonance region ($W > 2$ GeV) was used during **E93-018** for these types of calibrations.

insensitive to (small) variations in temperature, pressure, and/or gas composition. For the **E93-018** analysis a time-to-distance map was generated for each kinematic point for both HMS and SOS chambers. The performance of the chambers was closely monitored both online and offline. A new time-to-distance map was generated whenever the fit of the drift distance distribution with a constant function in the central region (to avoid edge effects the first and last bins were discarded in the fit) yielded a χ^2/degree of freedom bigger than 2 for **any** plane. Figures 3.9 to 3.12 extensively illustrate this calibration procedure for all HMS and SOS drift chamber planes.

The final resolution for the drift chambers was 200-250μ (σ) for the HMS and 150-180μ (σ) for the SOS, as exemplified in Fig. 3.13 where typical residuals (i.e. difference between the drift chamber position and the fitted track), summed over all the cells in a given plane, are shown for both HMS and SOS, together with a Gaussian fit for each distribution.

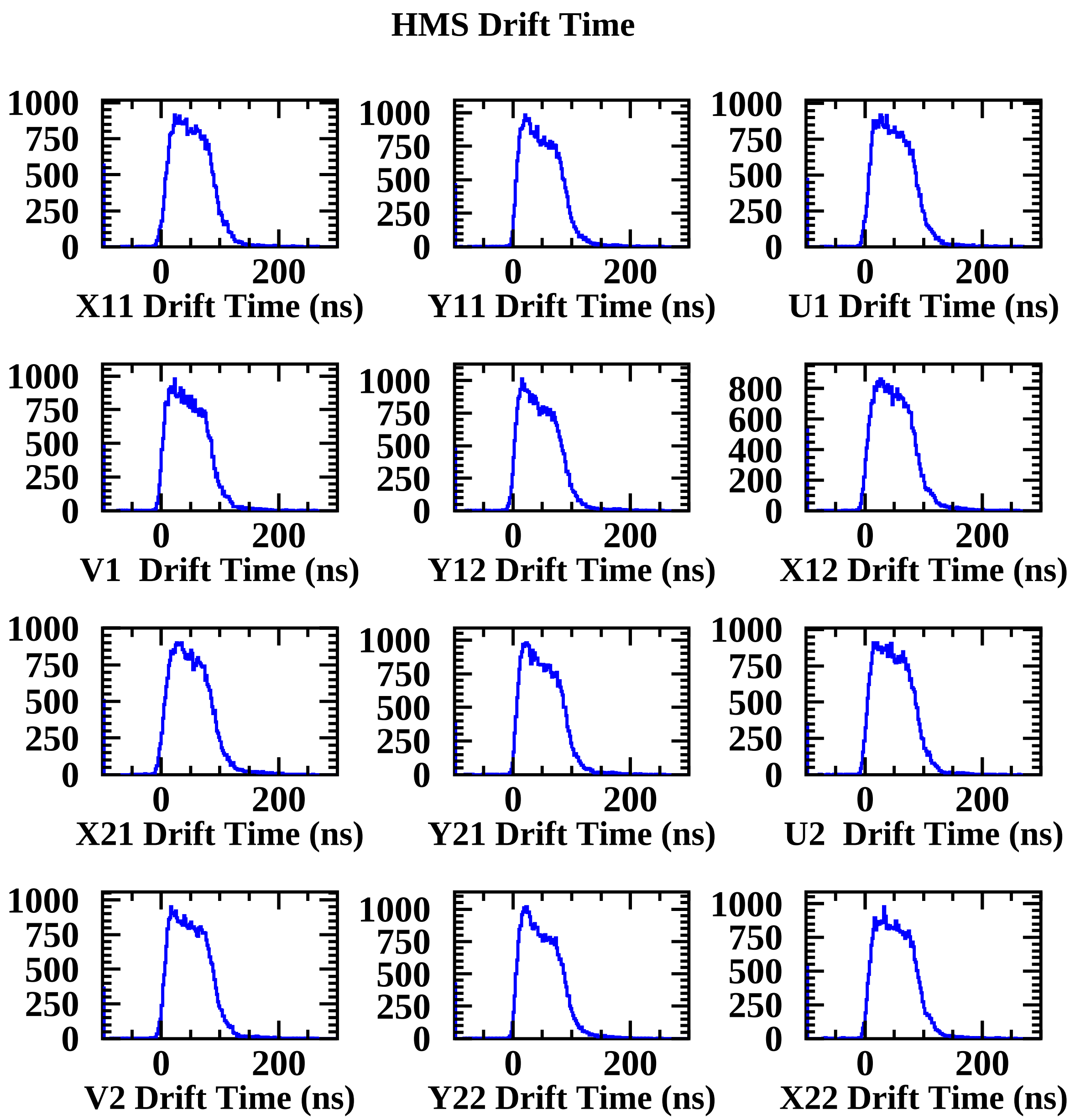

Figure 3.9: Drift Time distributions for HMS drift chamber planes. The first six plots correspond to the first drift chamber while the last six plots are for the second drift chamber.

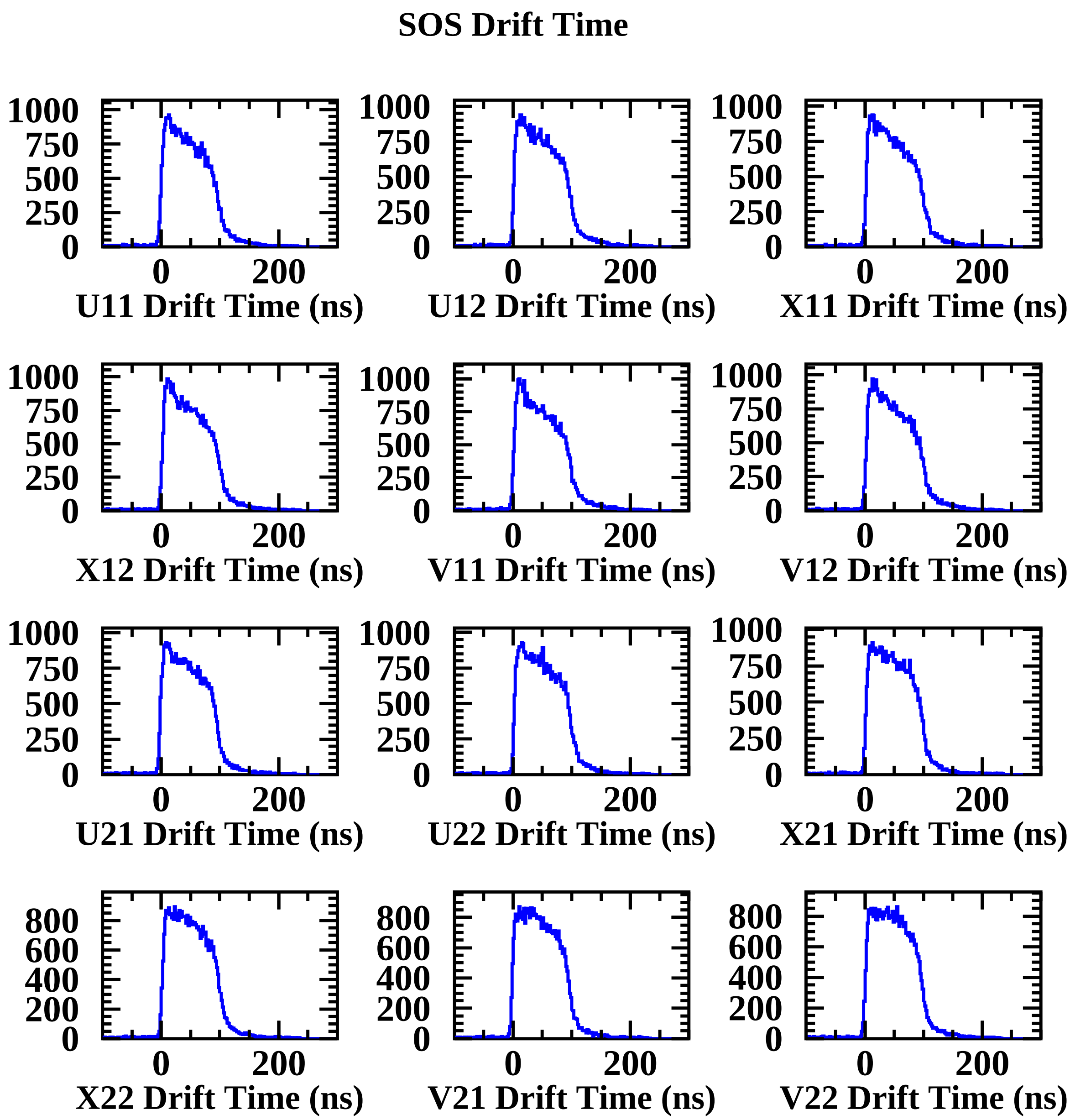

Figure 3.10: Drift Time distributions for SOS drift chamber planes. The first six plots correspond to the first drift chamber while the last six plots are for the second drift chamber.

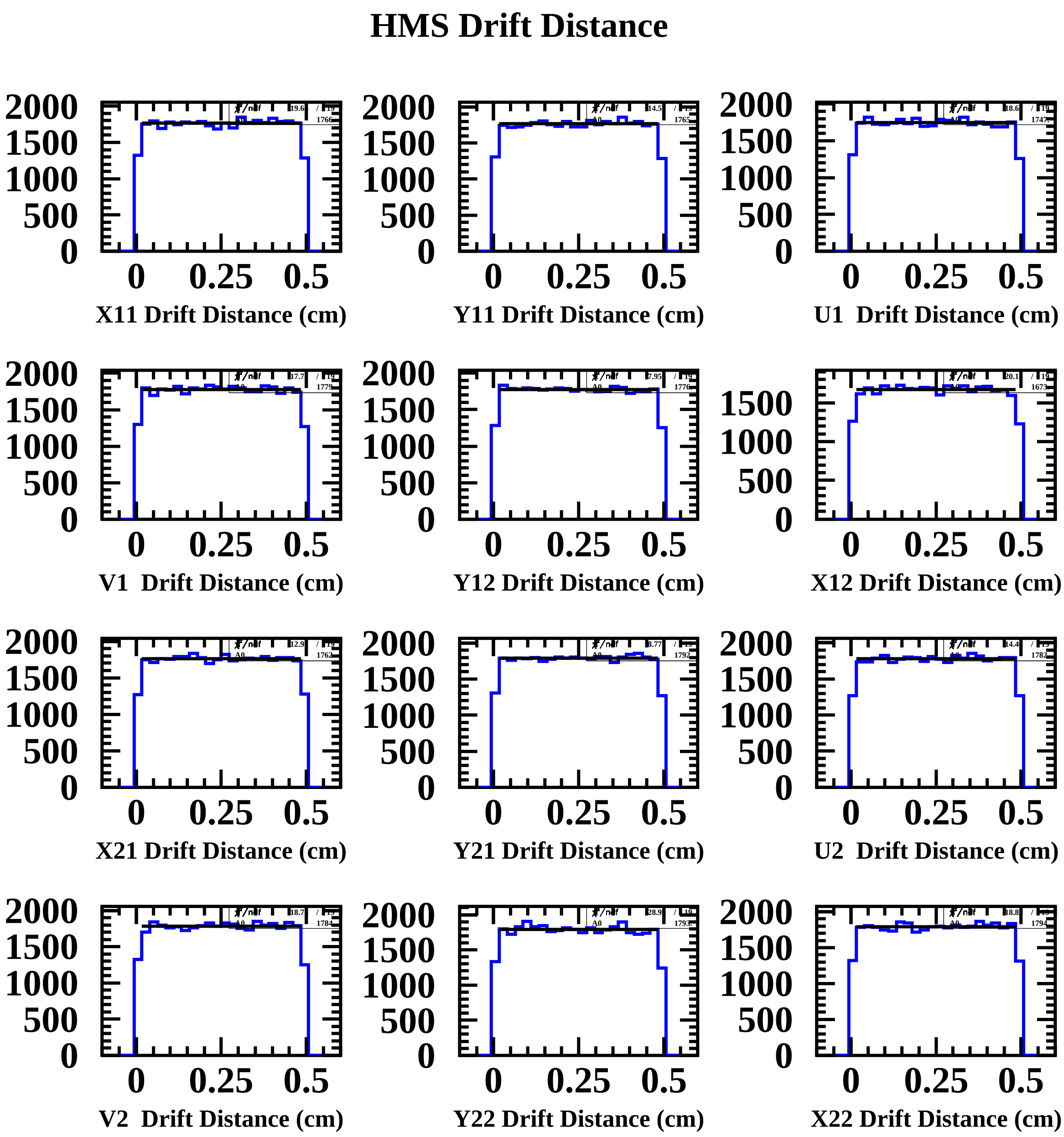

Figure 3.11: Drift Distance distributions for HMS drift chamber planes after the time-to-distance map calibration has been carried out. The plane/chamber ordering is the same as in the drift time plot. The $\chi^2/D.F.$ for the constant fit applied is below 2 for all 12 distributions shown.

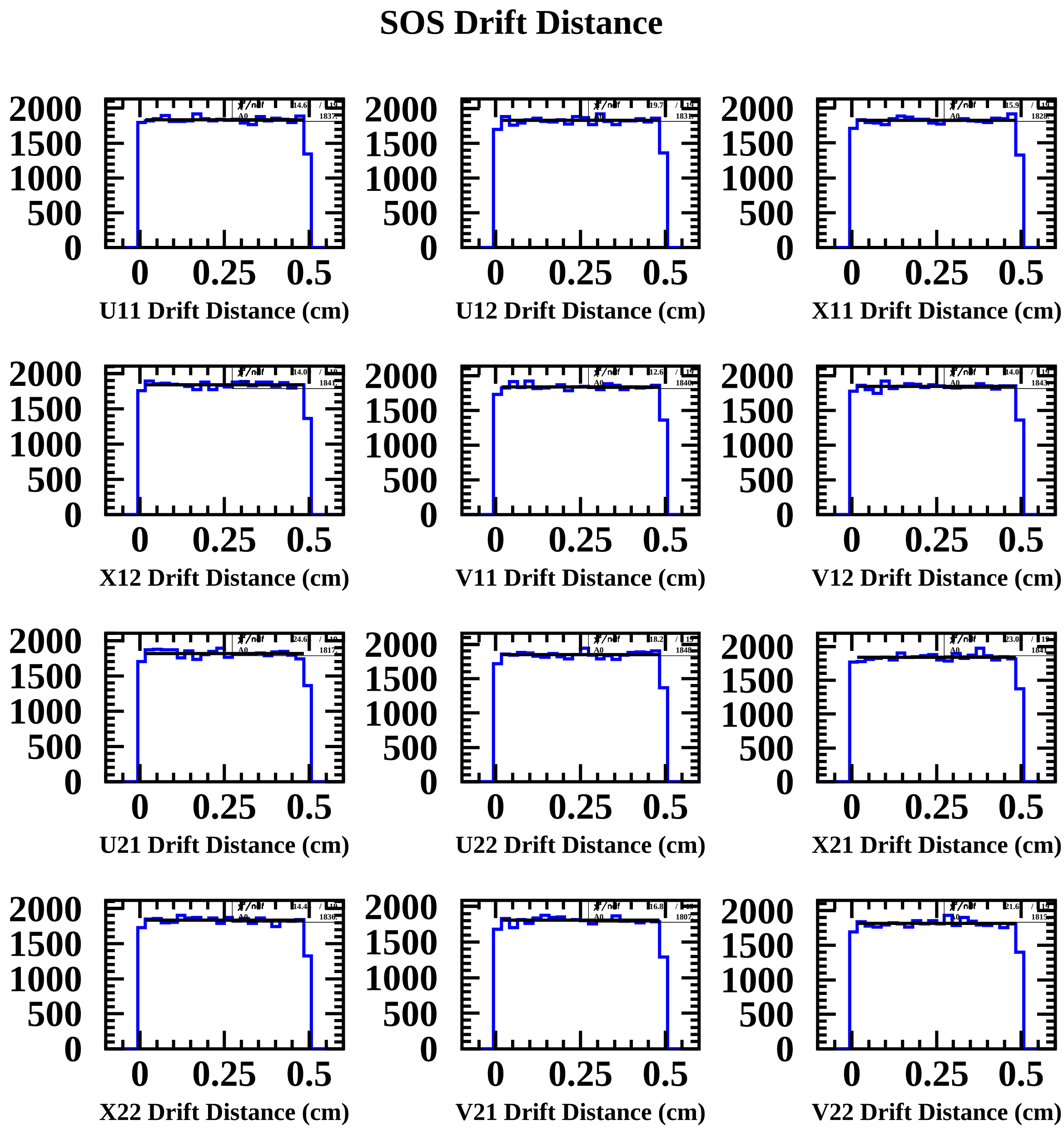

Figure 3.12: Drift Distance distributions for SOS drift chamber planes after the time-to-distance map calibration has been carried out. The plane/chamber ordering is the same as in the drift time plot.

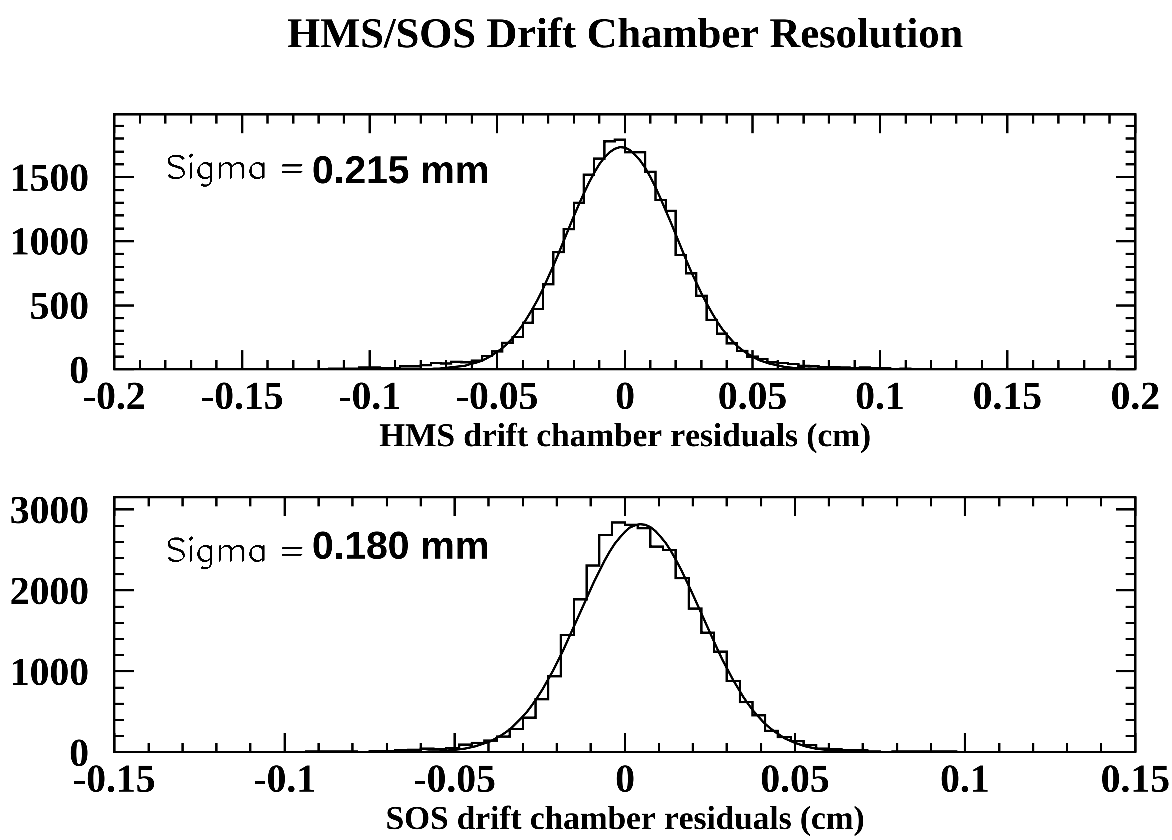

Figure 3.13: Typical residual (difference between the measured and the fitted coordinate) distributions for HMS (top plot) and SOS (bottom plot). The width of these distributions is indicative of the position resolution of the drift chambers. The standard deviation from a simple Gaussian fit to the distribution is shown for reference.

PHYSICS ANALYSIS

The goal of the present **E93-018** analysis is to separate the longitudinal and transverse parts of the cross-section for the $H(e, e'K^+)\Lambda$ reaction. To achieve this goal one needs to correctly identify a clean sample of coincident electrons and kaons, measure accurately the integrated charge, and determine the size and shape of the acceptance of the apparatus corresponding to the chosen $(e, e'K^+)$ sample, among other things. As with any electroproduction experiment, the magnitude of the radiative corrections and their influence upon the final result needs to be carefully evaluated. The shape and magnitude of the spectrometer acceptance needs to be well understood via extensive Monte Carlo studies and compared with optics studies. Last but not least, (in)efficiencies and dead times of the various tools (i.e. detectors) used during the experiment need to be measured/evaluated and their influence removed (corrected for) in the final answer. Once all of the above points are successfully addressed one can then proceed to extract the kaon electroproduction cross–section and then, considering all three ε points measured for each Q^2 setting, perform a (series of) Rosenbluth separation(s) to obtain the transverse and the longitudinal parts of the cross–section. All these analysis steps shall be described in detail in the remainder of this chapter.

4.1 Tracking Cuts

As explained previously, the tracking algorithm of the `Engine` used the available position information (primarily drift chamber wire hits and drift distances) to reconstruct the trajectories of charged particles passing through the active area of the detector hut. For any given successfully reconstructed track two coordinates, x and y, and two slopes, x' and y' were measured. The spectrometer coordinate system used here had $\hat{z}$ parallel to the central ray, $\hat{x}$ pointing downwards (i.e. in the dispersive direction for vertically bending spectrometers such as HMS and SOS), and $\hat{y}$ oriented such as to form a right–handed Cartesian reference system. Of course the pair of x and y coordinates could be evaluated at any point along the z axis in the hut (and, in the absence of magnetic field, the two slopes should be, modulo small changes due to multiple scattering, the same regardless of the z position in the hut). However in order to ensure consistency, the tracking code returned the so–called "nominal focal plane" coordinates, usually labeled by the FP subscript (such as in x_{FP}, x'_{FP}, etc.). While the "true" or optical focal planes of the Hall C spectrometers were relatively complicated surfaces (as an example the HMS "true" focal plane was not only a curved surface but also it intersected the central ray at an angle of only $\sim 6°$), the "nominal" focal plane was a conventional, plane surface, normal to the z axis of the spectrometer. The position of the "nominal" focal plane (along the z axis) was chosen to correspond to the intersection between the central ray through the spectrometer and the "real" focal plane: this meant that the "nominal" focal plane was positioned roughly mid–way between the two drift chambers for HMS, while for SOS the FP was located ~ 6.25 cm before the first drift chamber. The "nominal" focal plane also represented a convenient, stable reference point where other, non–optical properties of reconstructed tracks (such as timing information) coould be expressed. After the focal plane coordinates for a track were found, the `Engine` used these coordinates to reconstruct the coordinates of the event at the target, via the set of matrix elements characterizing the optical properties of the spectrometer. As only four quantities were measured at the focal plane, one could reconstruct only four independent quantities at the target. Assuming x_{TAR} = constant (and typically equal to zero), the variables reconstructed at the target were δ, y_{TAR}, x'_{TAR}, and y'_{TAR}; where x_{TAR} is the vertical position at the target, y_{TAR} is the horizontal position at the target (measured in the horizontal direction perpendicular to the central ray), y'_{TAR} and x'_{TAR} are the slopes of the tracks at the target (albeit slopes, these quantities are often referred to as the in–plane and the out–of–plane angles respectively), and δ is the percentile difference between the central momentum of the spectrometer and the current momentum.

In order to reject the events that scattered back inside the spectrometer acceptance (via lucky "bounces" off the collimators, various apertures in the spectrometer, etc.) a set of loose cuts was applied on the reconstructed target in–plane and out–of–plane angles. As the event reconstruction had finite resolution (caused by the drift chamber resolution, multiple scattering in the spectrometer windows/detectors, the uncertainty in the optics matrix elements, etc.), these cuts were kept large enough to avoid rejecting real events. The size of the cuts is shown in Table 4.1. The number of events rejected by these cuts was typically 0.4–0.5% for HMS and 0.2–0.5% for SOS. No correction was applied to the final cross–section for these rejected events. Note that additionally a cut was imposed on the reconstructed momentum of the particles for both HMS and SOS, thus avoiding the region of the momentum acceptance where the optics of the spectrometers was less well understood. For the analysis of the $(e, e'K^+)$ events another cut is imposed on the fiducial region of the aerogel detector. The focal plane positions and angles were used to project back each SOS track at the approximate z position of the aerogel and the resulting coordinates were compared with the known (up to a preset tolerance that accounts for multiple scattering, uncertainties in the reconstructed track, etc.) dimensions of the aerogel box, rejecting the events that passed outside the active area of the detector. To keep everything consistent a similar cut was implemented and used in the Monte Carlo simulation of the SOS spectrometer (to be discussed below).

4.2 Particle Identification (PID) Cuts

The goal of the present **E93-018** analysis was to study kaon electroproduction in the $^1H(e, e'K^+)\Lambda$ reaction. Therefore one of the most basic requirements was to correctly

HMS	SOS
$\vert x'_{TAR}\vert \leq 100$ mrad	$\vert x'_{TAR}\vert \leq 50$ mrad
$\vert y'_{TAR}\vert \leq 60$ mrad	$\vert y'_{TAR}\vert \leq 100$ mrad
$\vert\delta \leq 8\%$	$\vert\delta\vert \leq 15\%$

Table 4.1: Size of the cuts imposed on the reconstructed (target) quantities for both HMS and SOS.

identify the outgoing electron and kaon. Of course one needed to be concerned not only with how efficient a given cut or another was at eliminating pions and/or protons but also how many real kaons were lost by applying the same cut. In addition one needed to impose a cut in the missing mass distribution to discriminate between the Λ and Σ^0 channels (the **E93-018** kinematics were below the threshold for producing hyperons with masses higher than the Σ^0).

4.2.1 Electron Identification

In addition to electrons, the HMS, the nominal "electron arm" in this experiment, was sensitive to all negatively charged particles (mostly π^-). To correctly identify the electrons one used a combination of gas Čerenkov and shower counter information (Both e and π^- are highly relativistic for all **E93-018** kinematics, thus impossible to separate using TOF measurements over the limited flight path available). The efficiency of this procedure was studied in great detail in [42] over a wide range of spectrometer momenta and angles. For the present analysis an "electron" was any HMS track producing a signal greater (or equal) to three photoelectrons in the gas Čerenkov and yielding an energy deposition greater (or equal) to 70% of the central momentum setting of the spectrometer in the lead–glass calorimeter. These two requirements combined to give an extremely efficient electron identification ($\sim$ 99.8%) [43] while keeping the pion mis-identification to a minimum. In Fig. 4.1 the number of photoelectrons for the gas Čerenkov is shown versus the fractional energy deposition in the lead–glass calorimeter.

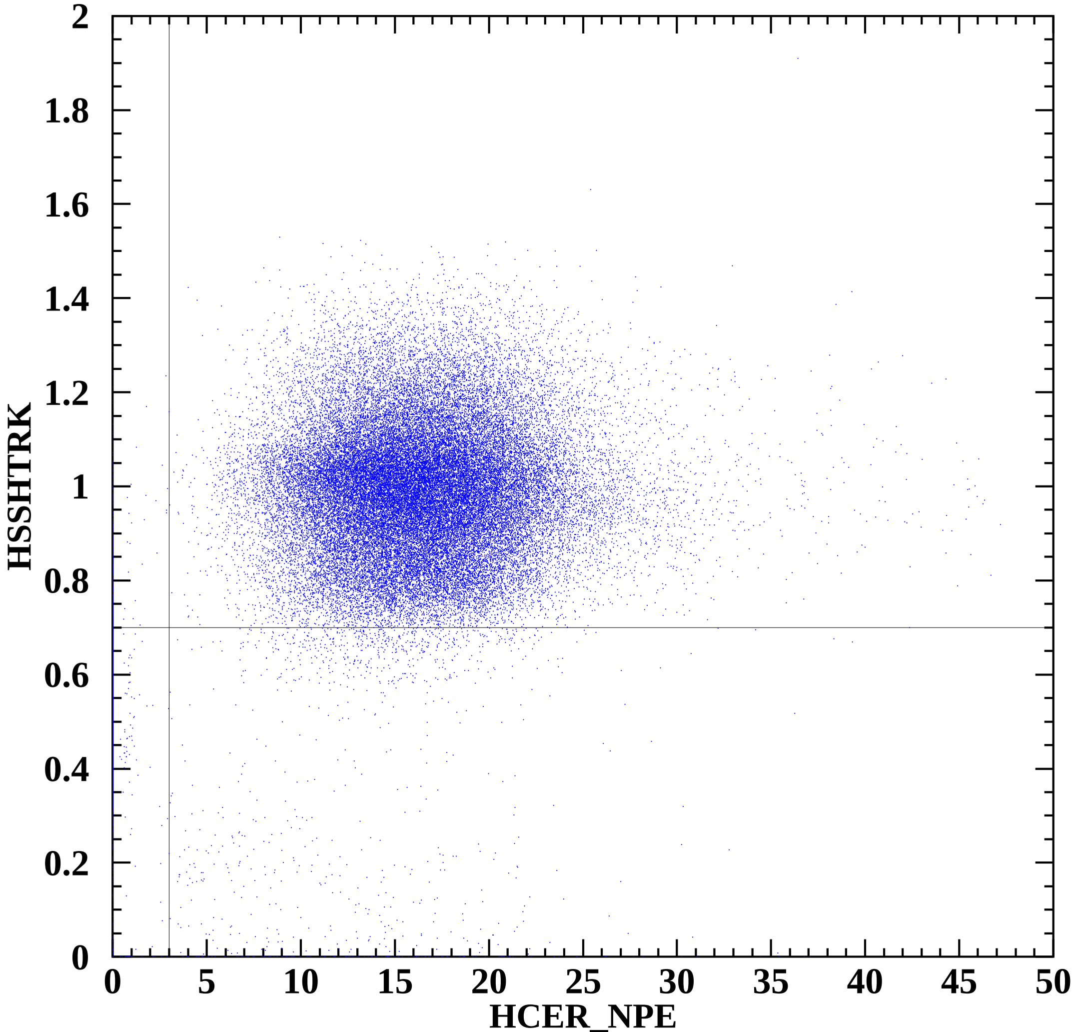

Figure 4.1: The fractional energy deposition in the HMS lead–glass (HSSHTRK) versus the number of photoelectrons in the HMS gas Čerenkov (HCER_NPE).

4.2.2 Kaon Identification

Along with kaons, the hadron arm used in the **E93-018** experiment, the SOS spectrometer, also recorded positive pions and protons. As the cross-sections for pion production and for inelastic proton scattering were far greater than the kaon electroproduction cross-section, the correct identification of the kaon sample became very difficult (i.e. one had to overcome the huge tails the proton and pion distribution project over the much smaller kaon distribution). In Fig. 4.2 the "raw" velocity distribution of the particles detected in the SOS is shown. One can plainly distinguish large proton and pion peaks and, perhaps, a smaller kaon "shoulder". Note that the pion peak in this figure is already suppressed (by a factor of about 5) due to the inclusion of the aerogel signal in the online trigger. In order to "clean-up" the distribution shown in Fig. 4.2 several steps had to be taken:

Aerogel Čerenkov Cuts

First a tighter aerogel cut had to be applied in software. From previous chapters one might recall that the online trigger had only a very loose cut applied on the number of photoelectrons in the aerogel Čerenkov. After careful calibration off-line one could use a tighter cut in order to achieve a better pion rejection. In Table 4.2 the measured number of photoelectrons yielded by the aerogel detector is shown versus the central momentum of a pion sample measured during the one of **E93-018** calibration runs.

Note that for $\beta = 1.0$ particles one expects, for a 9 cm thick aerogel layer with n=1.034, about 20 photoelectrons. Also one will note that the threshold velocity of $\beta = 0.967$ is reached for kaons having a momentum of 1.879 GeV/c, well above not only all the kinematic settings measured during **E93-018** but also above the maximum central momentum allowed for the SOS spectrometer itself ($\sim$ 1.75 GeV/c). For this analysis the off-line aerogel cut was set typically to 5 photoelectrons, resulting in a pion rejection of 800:1. Figure 4.3 shows again the velocity distribution of particles in SOS, this time versus the number of photoelectrons in the aerogel detectors. As one can see, a cut at $\sim$5 photoelectrons will reject almost all pions, while keeping the kaon sample unchanged: The events for which the measured velocities corresponded to a kaon while

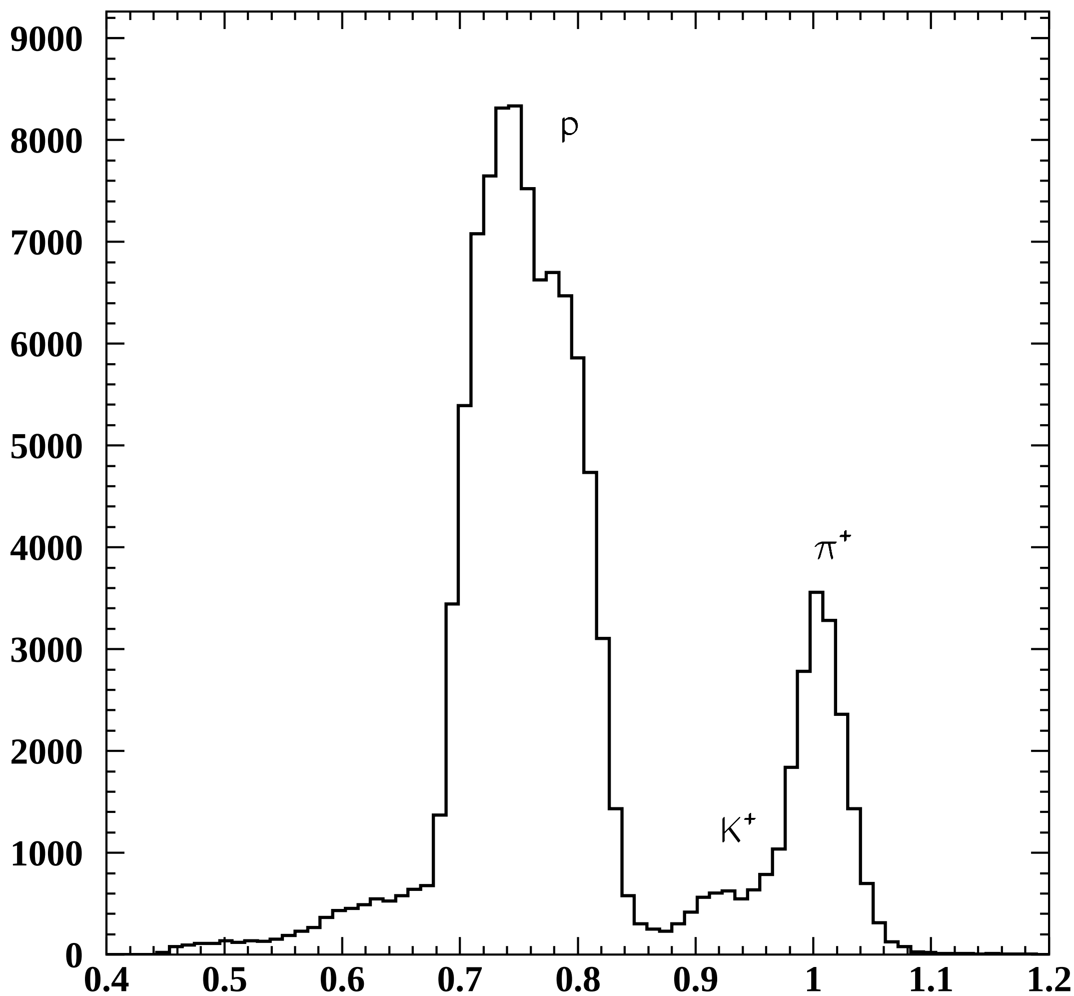

Figure 4.2: The velocity $\beta = v/c$ distribution for all particles detected in the hadron arm (SOS). The pion peak shown here is already reduced by a factor of 2–3 due to a loose aerogel cut applied online.

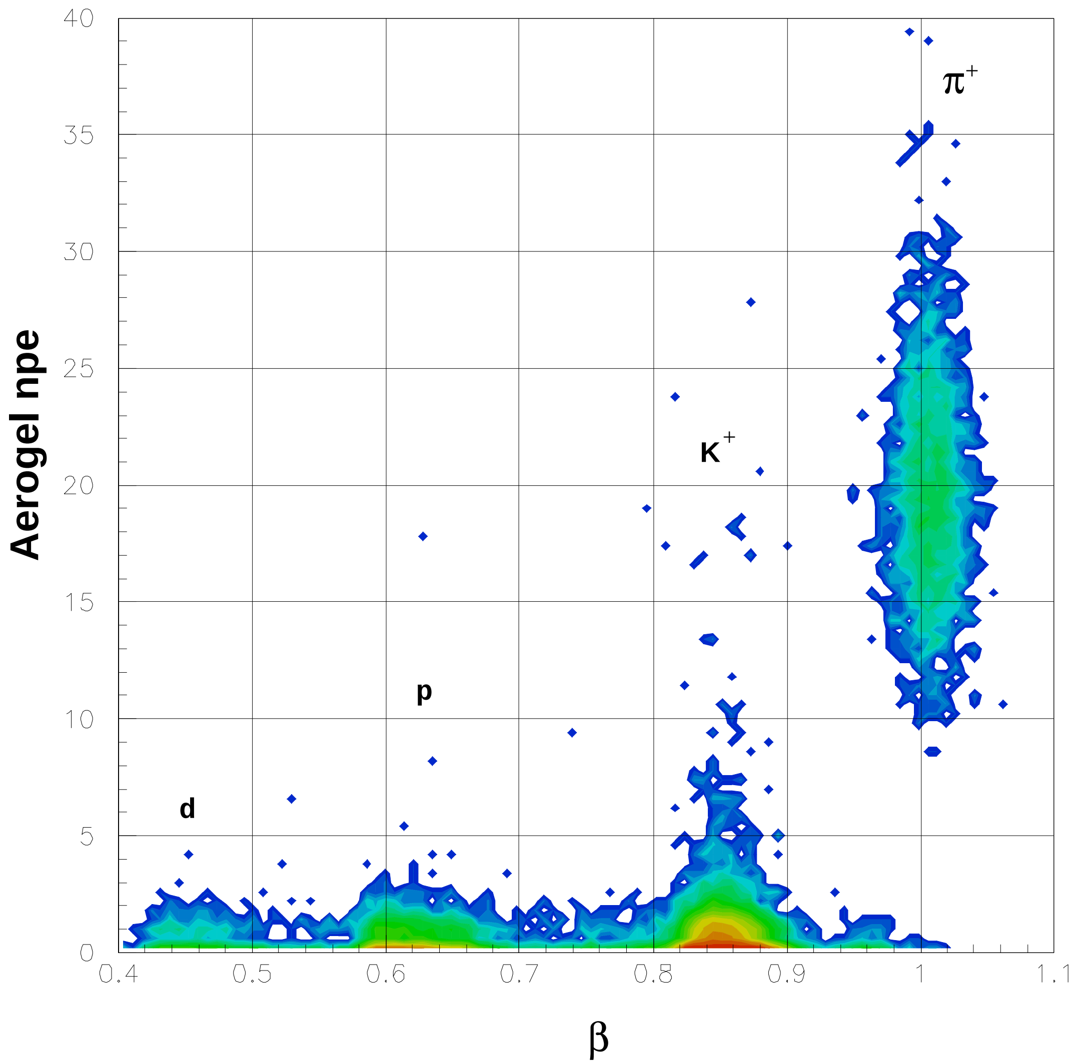

Figure 4.3: Velocity $\beta = v/c$ distribution in SOS versus the number of photoelectrons detected in the aerogel Čerenkov. The central SOS momentum for this test run was 800 MeV/c.

P (GeV/c)	β	npe
0.530	0.967	0.00
0.557	0.970	1.45
0.613	0.975	4.71
0.687	0.980	7.92
0.797	0.985	11.08
0.980	0.990	14.19
1.391	0.995	17.26
2.000	0.998	19.07
∞	1.000	20.27

Table 4.2: Average number of photoelectrons (npe) yielded by the aerogel Čerenkov versus momentum for various pion velocities.

the signal in the aerogel detector was still large were due mainly to proton knock-on events and, to a lesser extent, to events in which a kaon decayed very close in front of the last scintillator planes (i.e. the TOF determination of β was consistent with a kaon but the event was, at least when passing though the aerogel, a muon or a pion, thus the high signal in the aerogel detector).

Lucite Čerenkov Cuts

While the aerogel detector helped with K^+/π^+ discrimination, an array of lucite paddles provided (some) p/K^+ discrimination at all but the highest SOS momenta sampled during **E93-018** . The lucite had a high index of refraction, n=1.43, resulting in a threshold velocity, β of about 0.836. This in turn meant that protons with momenta smaller than $\sim$1.431 GeV/c would be below the threshold velocity (thus emitting no Čerenkov light), while similar momentum (i.e. in the 1 GeV/c range) kaons would be above threshold, thus emitting Čerenkov light. Two parallel and equally important checks were carried out to test this lucite detector. Using narrow β cuts one could focus on either the proton distribution or the pion+kaon distribution. Using the proton distribution one could study the proton rejection as a function of the cutoff number of photoelectrons

Lucite npe	Proton Rejection (%)	π^+ and K^+ Losses (%)
1	3.50	7.e-4
2	36.30	4.e-3
3	68.25	7.e-3
4	82.45	1.5
5	88.93	2.5
6	92.34	4.3
7	94.08	7.0
8	95.00	11.0
9	95.81	15.5
10	96.38	20.3
11	96.75	25.3
12	97.13	30.6

Table 4.3: Proton rejection and pion and kaon losses as a function of the npe cutoff for the SOS lucite detector.

(npe), while the pion+kaon distribution was used to study the number of pions and kaons lost versus the npe cutoff. The results of these studies are shown in Table 4.3. The focus here was not only on the fraction of protons rejected but also on the number of kaons that one might lose by applying a given npe cutoff. One could choose the npe cutoff such as to maximize the function $f_{\text{cutoff}}(\text{npe}) = f_p(1 - f_{\pi^+})$ with f_p the fraction of protons lost (rejected) and f_{π^+} the fraction of pions/kaons lost. This procedure yielded the optimal npe cutoff that offered the largest reduction in the proton background while keeping the correction for the pion/kaon losses at an acceptable level. In the present analysis, however, the lucite Čerenkov was not the only mean available for proton/kaon identification (TOF could/was also used) so the npe cutoff was chosen such as to keep the kaon losses to a minimum. The practical value used throughout this analysis was $npe = 3$ which kept the kaon losses well below 1% while still providing a significant reduction in the proton background, especially during the initial "preprocessing" of the raw data. The remaining protons as well as pions that survived these aerogel and lucite cuts were further discriminated using the two TOF techniques illustrated below.

Time–Of–Flight (TOF) Cuts

As shown in the previous chapters the SOS scintillators had an intrinsic resolution of ∼100 ps/plane, resulting in a velocity resolution of about $\delta\beta = 0.018$ (for $\beta = 1$ particles). The momentum resolution, $\Delta p/p_0$, of the SOS spectrometer was of the order of 10^{-3}. One could then combine these two types of measurements to gain yet another way of performing particle identification in the hadron arm. The technique used in this analysis was to compare the β as measured from TOF with a β value obtained by taking the measured momentum of a particle and then using the known kaon mass to compute β according to $\beta_{momentum} = p/\sqrt{p^2 + m_K^2}$. From a plot of the distribution of the difference between these two β measurements, the so–called $\Delta\beta$, one expects to see a peak centered around zero for the particles for which the mass was correctly assigned (i.e. kaons) and lateral peaks for the particles for which the mass was incorrectly assigned (i.e. protons and pions). One could then apply a cut on this distribution around the region of interest corresponding to the known TOF and momentum resolution of SOS. In order to be on the safe side and avoid clipping the "tails" of the kaon distribution, the size of the cut used in this analysis was computed based on much worse resolution than the actual performance of the SOS detectors (i.e. ∼200 ps for the TOF resolution and 1-2 % for the momentum resolution). This technique is illustrated in Fig. 4.4 where the distribution of the $\Delta\beta = \beta_{TOF} - \beta_{momentum}$ is shown. The region of interest (i.e. the kaon region) is delimited by the two vertical lines. One can easily see that this cut removes the bulk of the proton and pion backgrounds, and, of course, this technique is independent of the aerogel and lucite cuts explained above and can be used in conjunction with those cuts.

Coincidence Time Cuts

The goal of the **E93-018** experiment and therefore of this present analysis was to study kaon electroproduction in coincidence with the scattered electron (i.e. we study an exclusive reaction as opposed to just kaon inclusive data). One can take advantage of this requirement and use the coincidence time (i.e. the time difference between the electron and the hadron arms) as yet another handle to help clean-up the hadron arm

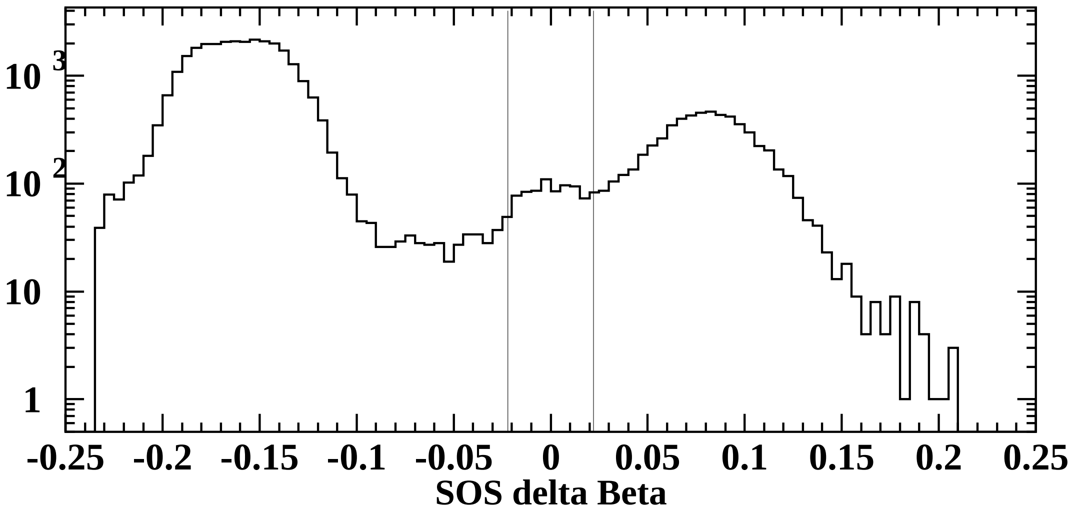

Figure 4.4: The $\Delta\beta = \beta_{TOF} - \beta_{momentum}$ distribution in the hadron arm of experiment **E93-018** . One can clearly distinguish the kaon peak (centered around zero), while the proton (pion) peaks are located at negative (positive) values of $\Delta\beta$.

particle identification. As shown in previous chapters, the CEBAF accelerator provided very narrow current peaks (∼2 ps) roughly 2 ns apart (i.e. corresponding to a third of the "nominal" accelerator frequency of 1497 MHz). If one were to detect only one species of hadrons in coincidence with the scattered electron, from a plot of the time difference between the two arms, the so–called coincidence time, one would expect to reproduce this microstructure of the beam, provided the coincidence time intrinsic resolution was good enough. In order to achieve the best possible resolution one needed, for each spectrometer, to correct each individual ray for the difference in pathlength between the central ray though the spectrometer and the current ray. This procedure yielded the so–called "corrected coincidence time" which, for the Hall C setup, had a resolution better than 500 ps (typical values found in this analysis are around 350 ps). A more in–depth discussion about the pathlength correction, including all the relevant details, etc., can be found in [44] while in Appendix A the parameterizations of the pathlengths, as used in the `Engine`, are given for both HMS and SOS. When more than one type of particle was detected in the hadron arm (as is the case in **E93-018**) one had a superposition of several (one for each type of particle detected in the hadron arm) of these ∼2 ns patterns, with various offsets between them. In Fig. 4.5 the corrected coincidence time is shown versus the velocity in the hadron arm. One can clearly distinguish the "real" or in–time coincident kaon peak from the random peaks, spaced ∼2 ns apart. Real and random peaks can also be seen for both protons and pions as well (as the mass used to evaluate the pathlength corrections was the mass of a kaon, these proton/pion distributions show characteristic slopes). As seen in Fig. 4.5 one could then place accurate cuts around the coincident kaon peak as well as over several (to improve statistics) random peaks (for later subtraction of the random coincidences contribution in the "real" peak). Due to the offsets mentioned above the "real" kaon peak is clearly separated with respect to the proton/pion coincident peaks, as are (at least some of) the random kaon peaks.

PID Tests For The Hadron Arm

As shown in the previous paragraphs, several techniques could be used simultaneously to obtain an as clear as possible a "real" (and random as well) sample. Figure 4.6 illustrates the additive effect of the cuts discussed. From top to bottom, the corrected coincident time is plotted with no PID cuts for the hadron arm[1], with an aerogel cut (i.e. aerogel npe < 3), an aerogel and a lucite cut (npe > 3 for the lucite), and finally with the aerogel, lucite, and a TOF (i.e. the $\Delta\beta$ cut explained above). One can easily see the dramatic reduction of the proton and pion backgrounds. In the end one is left with a very clean "real" kaon peak, as well as several kaon random peaks, consistent with the expected 2 ns microstructure of the CEBAF electron beam. There might be some remnant in–time pions in the peak around cointime = -2.5 ns, therefore that random peak was not used for random contribution subtraction. The difference between the integrated number of counts in the "real" kaon peak shown in the fourth plot and the number of counts in a similar region from the first three plots (using adjacent regions to estimate and subtract the backgrounds for the first three distributions) is consistent, within the statistical uncertainties, with no kaon losses due to the cuts applied.

[1]Electron arm PID cuts are applied for all four plots.

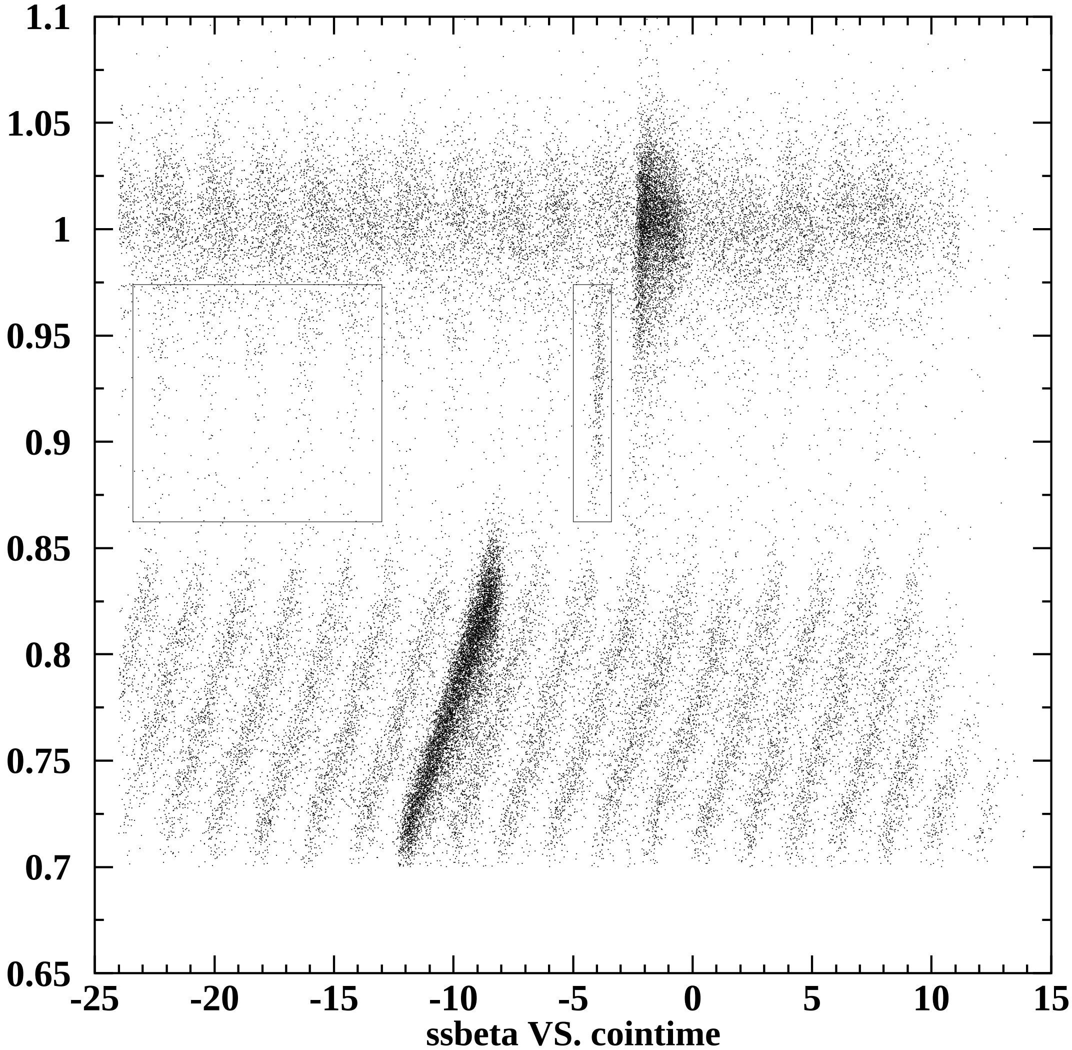

Figure 4.5: Corrected coincidence time versus the velocity in the hadron arm of experiment **E93–018**. The boxes show the in–time kaon peak (center of the plot), and five random kaon coincidence peaks (left side of the picture).

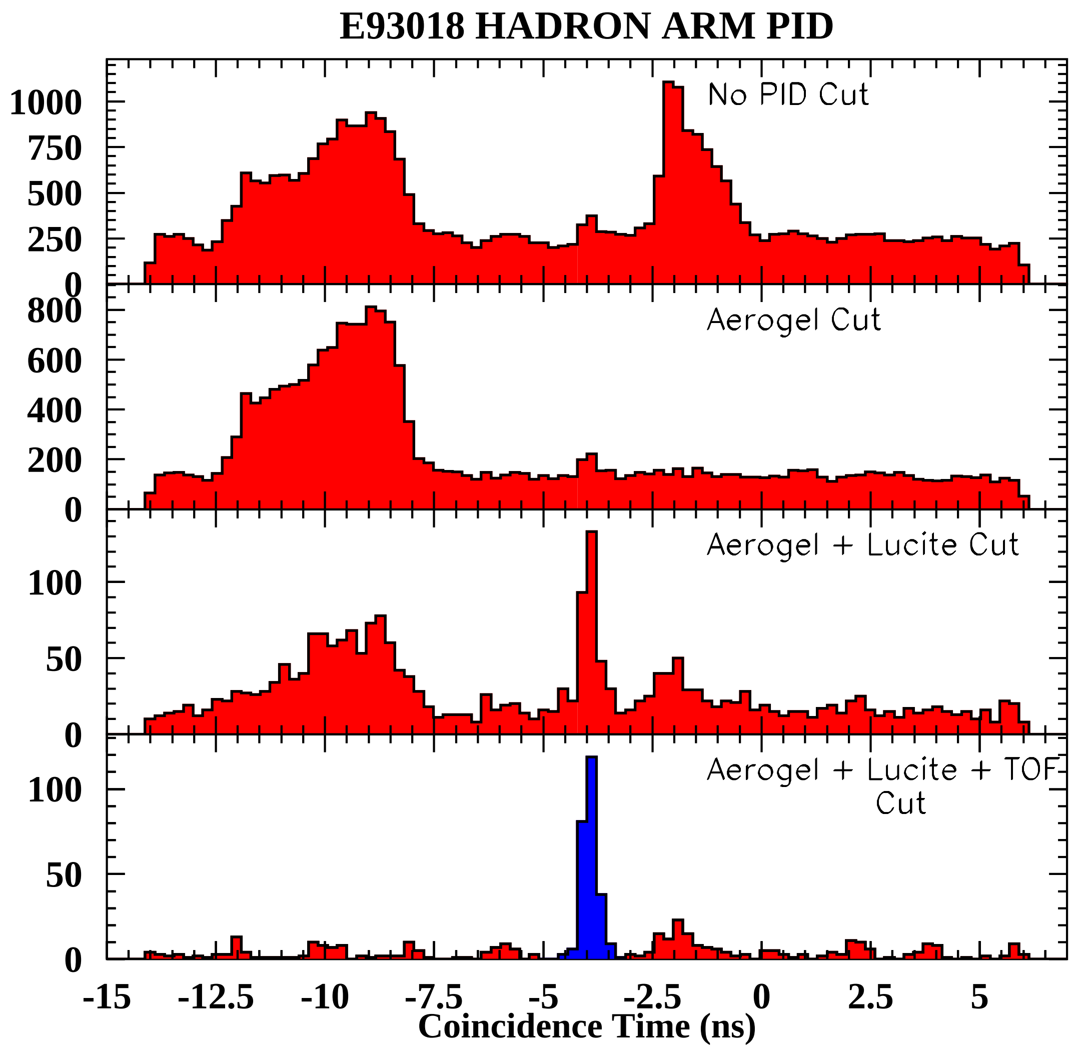

Figure 4.6: Influence of increasingly more restrictive PID cuts on the corrected coincidence time between the electron and the hadron arms as measured during experiment **E93–018**.

While it is of course encouraging to find that the various PID cuts applied in the hadron arm did not induce any losses in the original kaon sample, there was another question that remained to be answered: How many protons and/or pions still remained in our kaon sample? A possible answer to this question might be found by examining the missing mass distribution produced from the coincident electron–kaon sample considered. Figure 4.7 shows the missing mass distribution for a typical **E93-018** electron–kaon coincidence sample, after the random coincidence and target walls contributions have been removed. One can clearly distinguish the prominent Λ and Σ^0 peaks corresponding to the two hyperons that could be produced with **E93-018** kinematics, as well as characteristic radiative tails projecting from each peak towards higher missing mass regions. Now consider the region below the Λ threshold (i.e. 1.115 GeV/c^2) in Fig. 4.7. As this region is below threshold for hyperon production (and our target is hydrogen) no real electron–kaon coincidence event can produce counts in this region. Therefore whatever counts are to be found below threshold must come from random pion and/or proton events mimicking a real kaon. As one can see from Fig. 4.8 the number of counts below the Λ threshold represented less than one percent of the number of counts in the Λ peak (most values are in the 0.1 to 0.5 % range). This fraction was recorded and corrected for in all kinematical settings. As a summary of the hadron arm particle identification procedure (one of the more daunting tasks of this analysis) it can be stated that the various PID cuts do not seem to alter the original kaon sample, while removing all but a small fraction (taken into account in the analysis) of the pion and proton backgrounds, yielding in the end a very clean coincident kaon sample[2]. From the missing mass of the unidentified hyperon, appropriate cuts were applied to select either the Λ or the Σ^0 channels.

[2]The hadron arm PID procedure described in this section is coincidence experiments specific, due to the use of the corrected coincidence time for PID. Should anyone need it, the single arm kaon identification, which must rely solely on aerogel, lucite, and TOF, is not as impressive.

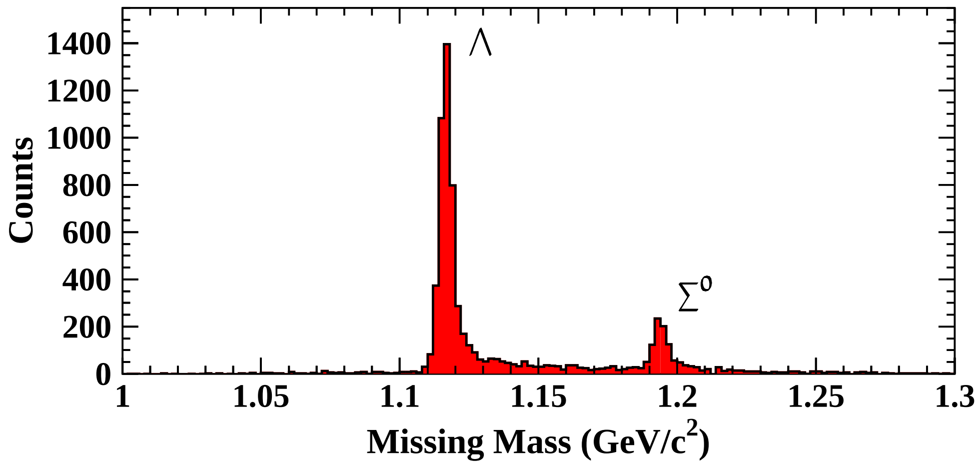

Figure 4.7: Typical missing mass spectrum for electron–kaon coincidences, as measured during **E93-018** . The random coincidences as well as the target wall contributions have been subtracted. Note the two prominent Λ and Σ^0 peaks. No radiative corrections have been applied.

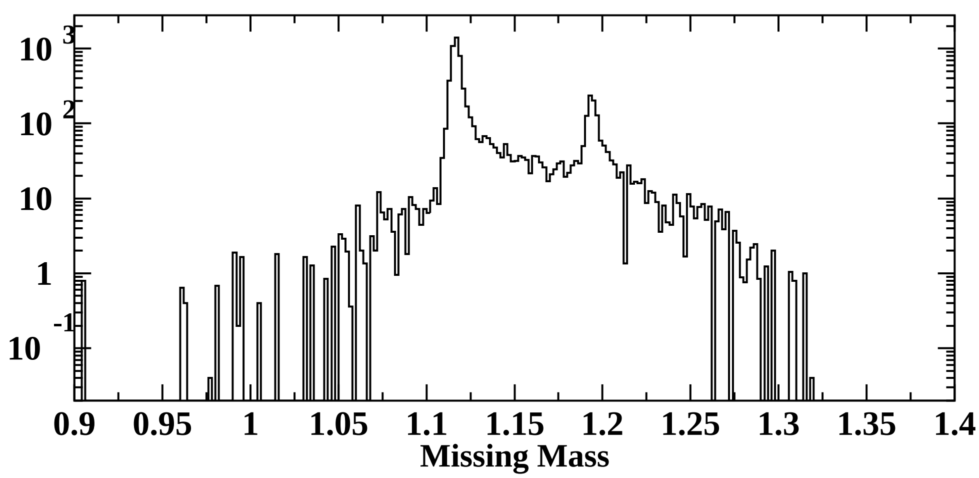

Figure 4.8: Missing mass spectrum as measured during **E93–018**, plotted on a log scale to show the number of background events present below the Λ threshold, relative to the number of counts in the Λ peak itself.

4.3 Monte Carlo Simulations. Phase Space. Radiative Corrections

A good simulation of the appropriate experimental setup is an essential condition for any modern day physics experiment. Quite often, extensive Monte Carlo simulations are performed even before the experiment takes place, in order to identify and solve beforehand if possible, potential problems that might affect one's expected results. Due to the limited amount of resources available, one needs to have a reasonable estimate of the time needed to complete a certain measurement, given the desired statistical uncertainty. These estimates are also obtained through Monte Carlo simulations.

Several simulations were carried out in the planning phase, during the actual running, and in the data analysis phase of experiment **E93–018**.

4.3.1 Rate estimation. Kinematics Determination

A simple Monte Carlo program was written (mostly by our Bucharest University collaborators) to estimate the number of $(e, e'K^+)$ counts per unit time and unit beam current. A full description of this program and its features, as well as tables with results can be found in [45] while its characteristics are given below. The program included only limited knowledge of the HMS/SOS spectrometers (i.e. only generic limits for the angular and momentum "bites"); however it had a full–fledged 3–body event generator coupled to a very simple, yet effective model for the cross–section (as the purpose of this code was only to give count rate estimates, up to a factor of $\sim$2, the accuracy of the cross-section model was not critical) for both the Λ and the Σ channels. Estimates for the quasielastic kaon electroproduction off light nuclei were also possible (via a set of approximations). The code incorporated decay corrections for the kaon arm and, given the beam current and the size of the online and/or offline coincidence window, could provide estimates for the singles counting rates in the electron/kaon arm, coincidence rates, as well as expected accidental–to–true (A/T) ratios. This program was used in the optimization phase of the experiment and also, during the actual experiment, in order to adjust some of the kinematical settings in order to avoid physical and/or administrative limitations of the

Hall C setup. For example, due to limitations in the minimum spectrometer angle the $Q^2 = 0.50$ (GeV/c)^2 kinematics had to be modified so in practice data was taken for $Q^2 = 0.52$ (GeV/c)^2.

4.3.2 Standard Hall C Monte Carlo, SIMC

The "official" Monte Carlo code for the Hall C HMS/SOS setup is called SIMC. The program is based on the original code SIMULATE written for the SLAC experiment NE18, adapted to the experimental conditions and spectrometers in Hall C. A complete description of the original SLAC code can be found in [46]. As was the case with its predecessor, SIMC incorporates extensive knowledge of the optics of the two spectrometers (HMS and SOS), via forward and backward COSY maps, as well as comprehensive lists of the size/shape of all relevant apertures (and materials) inside the spectrometer. The two detector huts (size, positions, materials) are modeled as well. Multiple scattering effects as well as Coulomb and straggling corrections in the target are also present in the code.

Additionally, SIMC includes a PWIA calculation for $(e, e'p)$ off hydrogen, deuterium, and, given the appropriate spectral functions, off heavier nuclei. Radiative corrections are also incorporated in the code, as described in [46].

Our understanding of the spectrometer models (i.e. the optics model of the spectrometer) and also the basic physics assumptions made in the code (radiative correction prescription, multiple scattering, etc.) were extensively tested by measuring with both spectrometers physical processes considered well known, such as (e, e') and/or $(e, e'p)$ elastic scattering off hydrogen. The model used in SIMC for elastic scattering includes a dipole parameterization for the electric form factor and a Gary–Krümpelmann [47] parameterization for the magnetic form factor. The cross–sections computed under these assumptions are known to agree with the world's measurements within a few percent, in the range of kinematics accessible during **E93–018**. So, using the real electron beam, several elastic scattering calibration runs were measured for both HMS and SOS. Then, the same kinematical settings were simulated, with SIMC, using the same normalization (i.e. total integrated charge, efficiencies, etc.) as in the data. A comparison of the focal plane distributions (i.e. two coordinates, x and y, and two angles, x' and y') are shown in Fig. 4.9 for the case when the scattered electrons were detected in HMS. In all four panels the data are represented by the solid lines while the Monte Carlo results are shown with dashed lines. A similar plot can be obtained for inclusive elastic scattering in SOS (i.e. the scattered electrons are detected in the SOS). These results are shown in Fig. 4.10, using the same notations as for the HMS. In both of these figures one can see a good agreement between the data and the simulation. This not only shows a reasonably good understanding (and accuracy in modeling) of the two spectrometer' optical properties but also validates our overall normalization.

4.3.3 SIMC and Meson Electroproduction

The last logical step towards obtaining a comprehensive Monte Carlo package was to combine the features of the two programs described above. While keeping all its original capabilities, the SIMC code was adapted to simulate kaon (or more generally, meson) electroproduction: the kinematic conditions specific to meson electroproduction were added as a natural extension to the existing event generator, as were subroutines that assigned cross–sections to successful events. For the early stages of the program the simple cross–section parameterization described in [45], as well as a version of the WJC were implemented [48]. All these added features were controlled by a relatively small number of runtime flags. Also the robust radiative correction procedure already present in SIMC had to be extended to cover kaon electroproduction diagrams as well. Lastly, a new set of variables had to be defined to allow simulation of particle decays in the spectrometers and in the detector stacks. These included the total physical length of each spectrometer, the mass of the particle detected in each spectrometer (i.e. by default SIMC only expects electrons in the electron arm and protons in the hadron arm), the decay constant for the expected particle in each arm (negative values for this variable flags stable particles), various counters, etc. For the specific purpose of the present experiment all kaon decay modes with branching fractions larger than 1 % were implemented in the

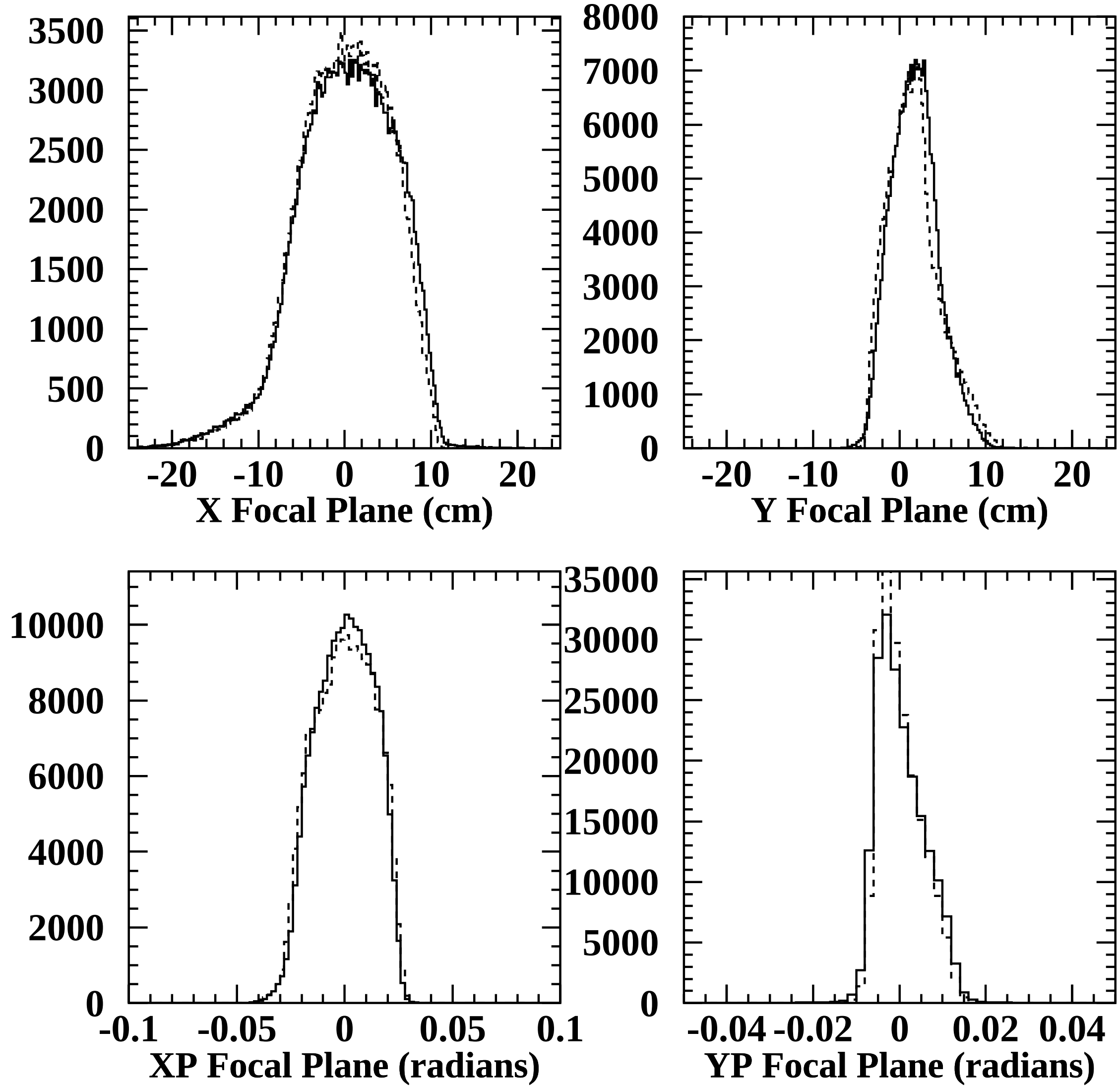

Figure 4.9: Comparison between the measured (solid line) and the Monte Carlo simulated (dashed line) focal plane distributions for inclusive elastic scattering off hydrogen in the HMS. X and Y are the two coordinates measured at the focal plane (top two panels), while XP and YP are the angles measured in the dispersive and the non–dispersive directions (bottom panels), respectively.

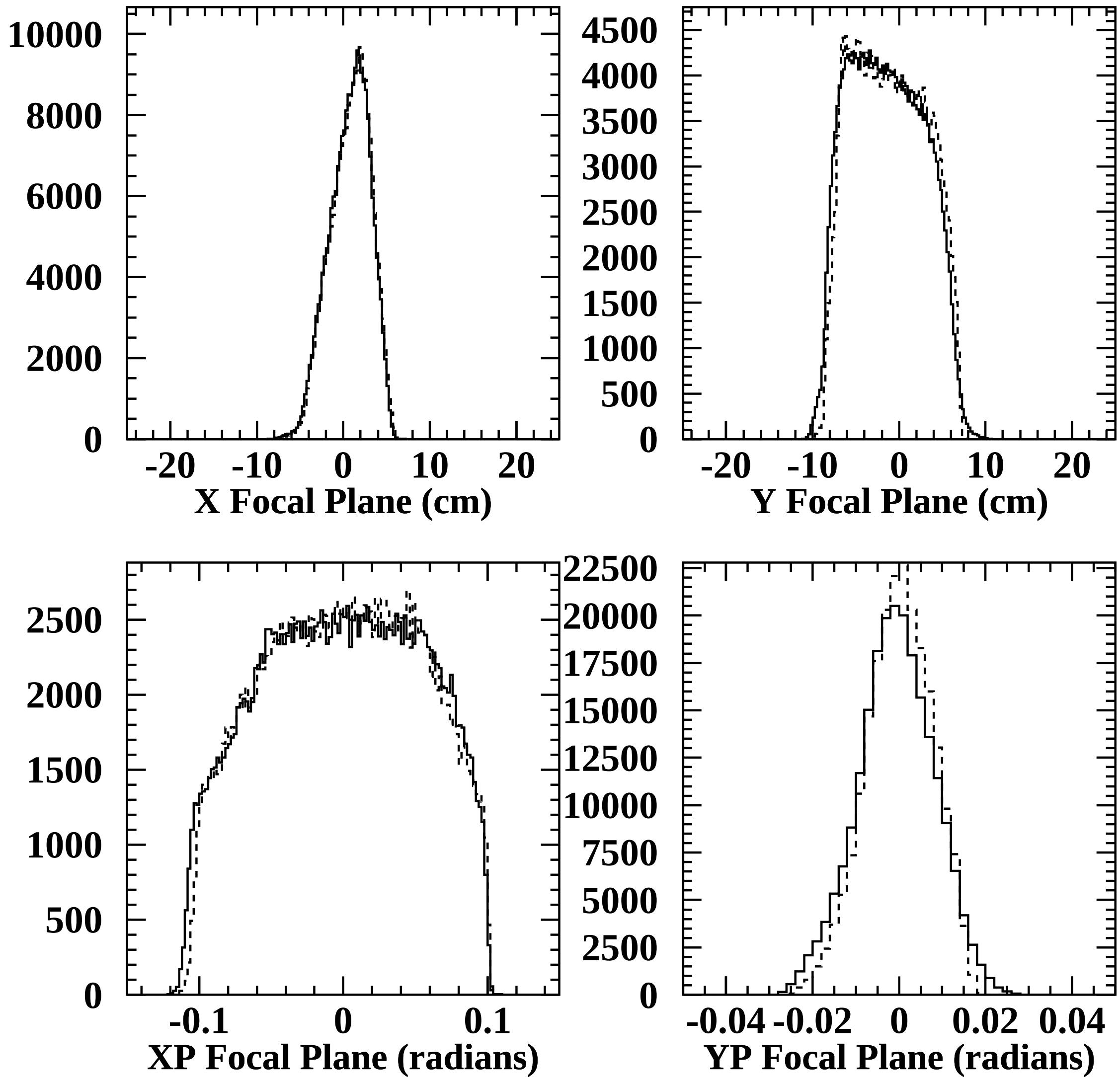

Figure 4.10: Comparison between the measured and the Monte Carlo simulated focal plane distributions for inclusive elastic scattering off hydrogen in the SOS. Notations are the same as in Fig. 4.9

code as well. This enhanced version of SIMC was called SIMC_EEK. In Fig. 4.11 a missing mass distribution, as measured during **E93-018** , is shown. Overlaid one can see the result of SIMC_EEK, using the same total charge, efficiencies, etc., as measured in the experiment[3]. There is a good agreement between the simulation and the measured spectrum. Specifically one might wish to note that the experimental width (multiple scattering, radiative effects) of the Λ peak is reproduced well, as is the (long) radiative tail (more on this in the next section).

4.3.4 Radiative Corrections

The size and correct application of the radiative corrections is one of the important steps in any electron scattering–type experiment. This section outlines how this correction was carried out in the present **E93-018** analysis.

Two coincidence experiments, **A** and **B**, measuring identical sets of observables, $a_1, a_2, .., a_n$ and $b_1, b_2, .., b_3$ can compare results only if the radiative corrections are carried out in a similar fashion in both experiments[4]. A complete calculation, even at the lowest order in α, requires, at the very least, some previous knowledge of the structure of the nucleon, i.e. structure functions. While in principle any (reasonable) choice can be made, what is important is to be consistent. The strong and electromagnetic parts of the interactions do not decouple completely[49], thus one has to use prior knowledge for, at least, the structure of the nucleon. In doing so one has restricted oneself to comparing results only with experiments that use the same approach to radiative corrections.

Generally, when implementing radiative correction procedures one has the choice of either "deradiating the data" in which case one applies a set of radiative correction factors (based on a simple model of the cross–section) to the data in an attempt to obtain a "radiation free" spectrum, then iterating until the model cross–section matches the deradiated data; or "radiate a theory" in which all radiative corrections are applied

[3]Note that, for clarity, only the Λ peak is simulated

[4]Improvements over time of the radiative correction prescriptions are of course desired and expected; however the core assumptions that enter ones radiative correction code cannot be fundamentally changed unless one is willing to do so for all available data sets.

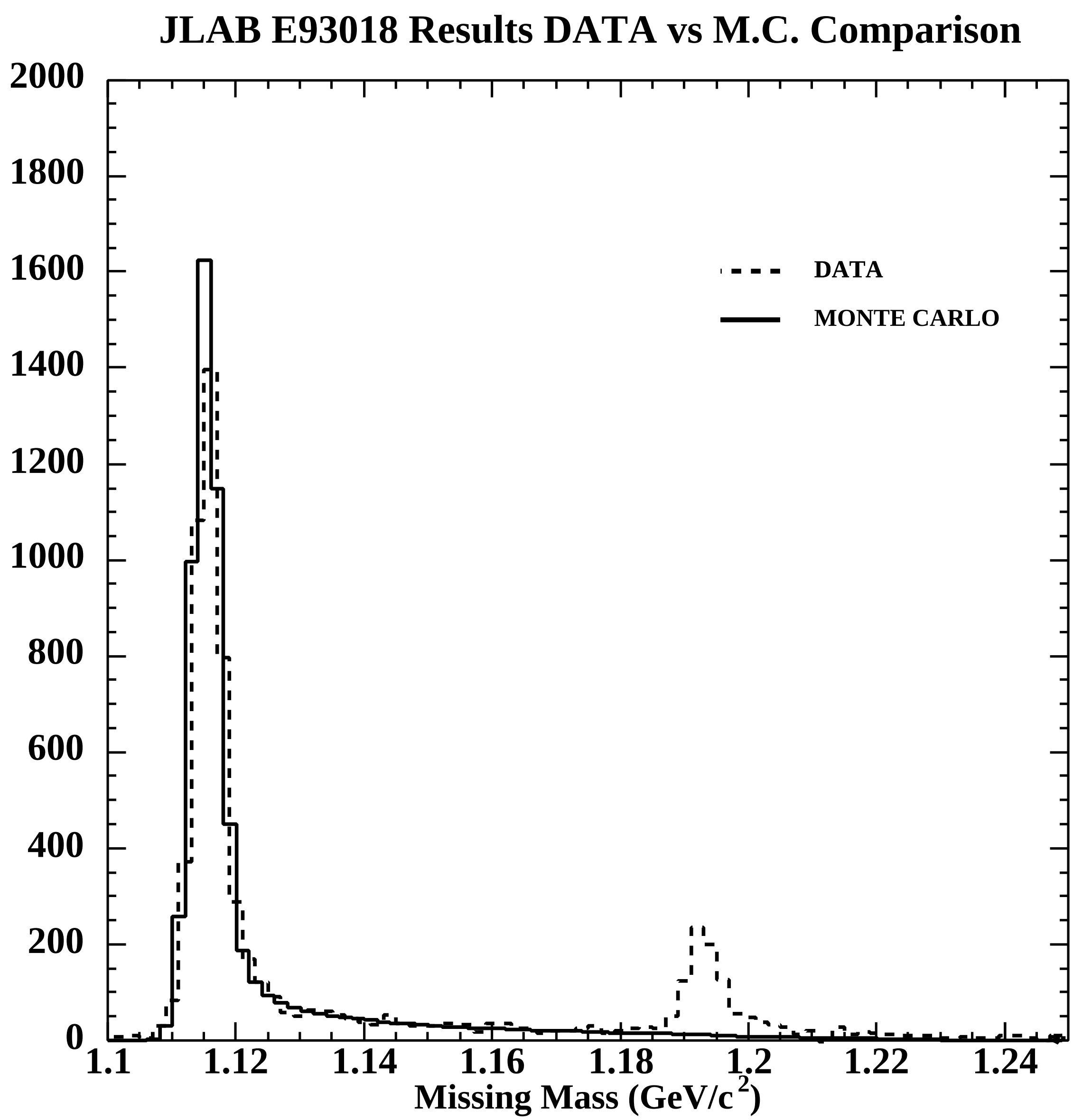

Figure 4.11: Comparison between measured (dashed line) and Monte Carlo simulated (solid line) $^1H(e,e'K^+)$ missing mass spectra. For clarity only the Λ channel was simulated whereas the data show both the Λ and Σ^0 peaks.

to a model cross–section, leaving the raw data unchanged (in this case one also has to iterate the radiative correction procedure until it matches the data).

As explained in the previous subsection the radiative corrections were carried out in the Monte Carlo simulation program, SIMC (or its "meson–friendly" variant), thus we chose to radiate a theory rather than to deradiate the data. To justify, at least partially, this choice one might want to note that, given the hydrogen target used in this experiment (so no Fermi motion for the target nuclei), and also given that the known widths of the Λ and Σ^0 hyperons are extremely small compared with the expected resolution of the HMS–SOS system, unfolding the experimental data (assuming an absolutely accurate unfolding procedure were to be available) would just yield delta-type functions, smeared by the finite resolution of the system.

As implemented in SIMC, the radiative correction prescription is based on the work of Mo and Tsai [50], modified to accommodate exclusive and semi–exclusive reactions. For an in–depth description of the radiative correction procedure one is again referred to [46], whereas only the most important assumptions will be listed below, together with the **E93-018** –specific modifications.

Throughout the present analysis the so-called "soft photon approximation" was used (i.e. the energy of the emitted photons is very small compared with both the incident and the emergent electron energies). For the angular distribution of the emitted photons the "peaking approximation" was used (i.e. the photons are emitted either in the direction of the incident or in the direction of the scattered electron).

These two assumptions imply that the effect of the radiation on the central kinematics is negligible (i.e. ε is computed from the nominal kinematic values without any correction, as are the $\theta_{\gamma K}$ and ϕ angles, etc.).

In extending the radiative correction procedure to cover meson electroproduction histograms Gary-Krümpelmann type parameterizations [47] (dipole) of the form factors were used for both the proton and the kaon. The parameterization of the form factors together with the built-in dependences of the cross-section on kinematic variables Q^2, W and t did represent, of course, an Ansatz on how σ_T and σ_L should behave but then, again, this would have been true for any Mo and Tsai–inspired radiative correction prescription.

Q^2 (GeV/c)^2	F_{RC}
0.52	1.320
0.75	1.305
1.00	1.295
2.00	1.281

Table 4.4: Radiative correction factors used in the analysis.

Within this framework, for every bin in $E_{e'}$, $\Omega_{e'}$, Ω_{K^+} one then writes the "true" cross-section as:

$$\left(\frac{d^5\sigma}{d^5V}\right)_{true} = F_{RC}\left(\frac{d^5\sigma}{d^5V}\right)_{meas} \tag{4.1}$$

where F_{RC} is the radiative correction factor and $\left(\frac{d^5\sigma}{d^5V}\right)_{meas}$ is the measured cross-section (calculated as explained in section 4.5). For the Λ channel typical values for F_{RC} would be in the 1.2–1.4 range, fairly insensitive[5] to the virtual photon polarization for a given Q^2. In Table 4.4 the correction factors used in the present analysis are shown. The insensitivity of the radiative corrections to ε seen in the present analysis is consistent with the earlier observations of [51] (L/T separation in $p(e,e'\pi^+)$, form factor extraction) and [24] (exclusive pion and kaon electroproduction, L/T separation (π^+ only)).

In estimating the uncertainties associated with the radiative correction factors given by (4.1), we compared the data and the Monte Carlo yields for several missing mass cuts, both as a function of Q^2 and, more importantly for the Ronsenbluth separation, between different ε points at the same value of the four–momentum–transfer. In Table 4.5 the results of this study are shown. The first column specifies the kinematic point (i.e. the four–momentum transfer, Q^2), the second column shows the missing mass (in (GeV/c)^2) cut used, $\varepsilon_{1\ldots3}$ denote the low, middle, and high ε points, while the DATA and the M.C. columns show the yields from data, respectively, from SIMC_EEK[6], while the last column, within each ε point, shows the ratio between the real/measured and the

[5]At least as long as the missing mass cut applied for the Λ identification is not too tight.

[6]Note that in practice a huge number of events (successes) were generated for each setting, then weighted appropriately (charge, decay, etc.) to give the simulated number of counts.

Q^2	M_x cut	ε_1			ε_2			ε_3		
		Data	M.C.	Ratio (%)	Data	M.C.	Ratio (%)	Data	M.C.	Ratio (%)
0.52	1.10-1.13	4795	4965	96.58	7218	7465	96.69	10480	10910	96.06
0.52	1.10-1.14	5084	5206	97.65	7679	7828	98.09	11120	11420	97.37
0.75	1.10-1.13	4118	4386	93.89	10740	11130	96.50	15210	15770	96.45
0.75	1.10-1.14	4405	4591	95.95	11380	11700	97.26	16100	16540	97.34
1.00	1.10-1.13	3563	3706	96.14	5127	5416	94.66	18750	19680	95.27
1.00	1.10-1.14	3802	3894	97.63	5460	5697	95.84	19930	20620	96.65
2.00	1.10-1.13	1591	1650	96.42	2242	2327	96.33	3621	3785	95.66
2.00	1.10-1.14	1738	1785	97.37	2405	2473	97.25	3960	4081	97.03

Table 4.5: Data vs Monte Carlo radiative corrections checks in the **E93-018** $p(e, e'K^+)\Lambda$ analysis. Description of the notations used in the table is provided in the text.

simulated yields. Based on the results from Table 4.5, a 0.5 % point–to–point uncertainty was assigned. Additionally, a 2 % overall (i.e. scale/normalization) uncertainty was assigned to the whole radiative correction procedure. Also the model dependence of the radiative correction factors was studied by switching between the two models available in the simulation code but the differences found were negligible.

For reference, in Figures 4.12 to 4.14 missing mass distributions for the Λ region are shown for all ε points measured at Q^2=0.75 (GeV/c)^2 (experimental data are the symbols/stars, while the SIMC_EEK result is shown as a histogram) [7].

4.3.5 Acceptance Corrections

The probability for a given spectrometer to accept/reject events that are produced in a given region of the target, with a given initial momentum and angle is typically expressed as the so–called spectrometer acceptance.

If one were to simulate all the coordinates that completely define a track at the target (i.e. three coordinates, polar and azimuthal angles, and also the initial momentum of the particle) then the acceptance will either be one (i.e. the particle is accepted in the spectrometer), or zero (i.e. the particle is not accepted in the spectrometer). However,

[7] Similar plots are of course available for all measured kinematics but because of space considerations were omitted.

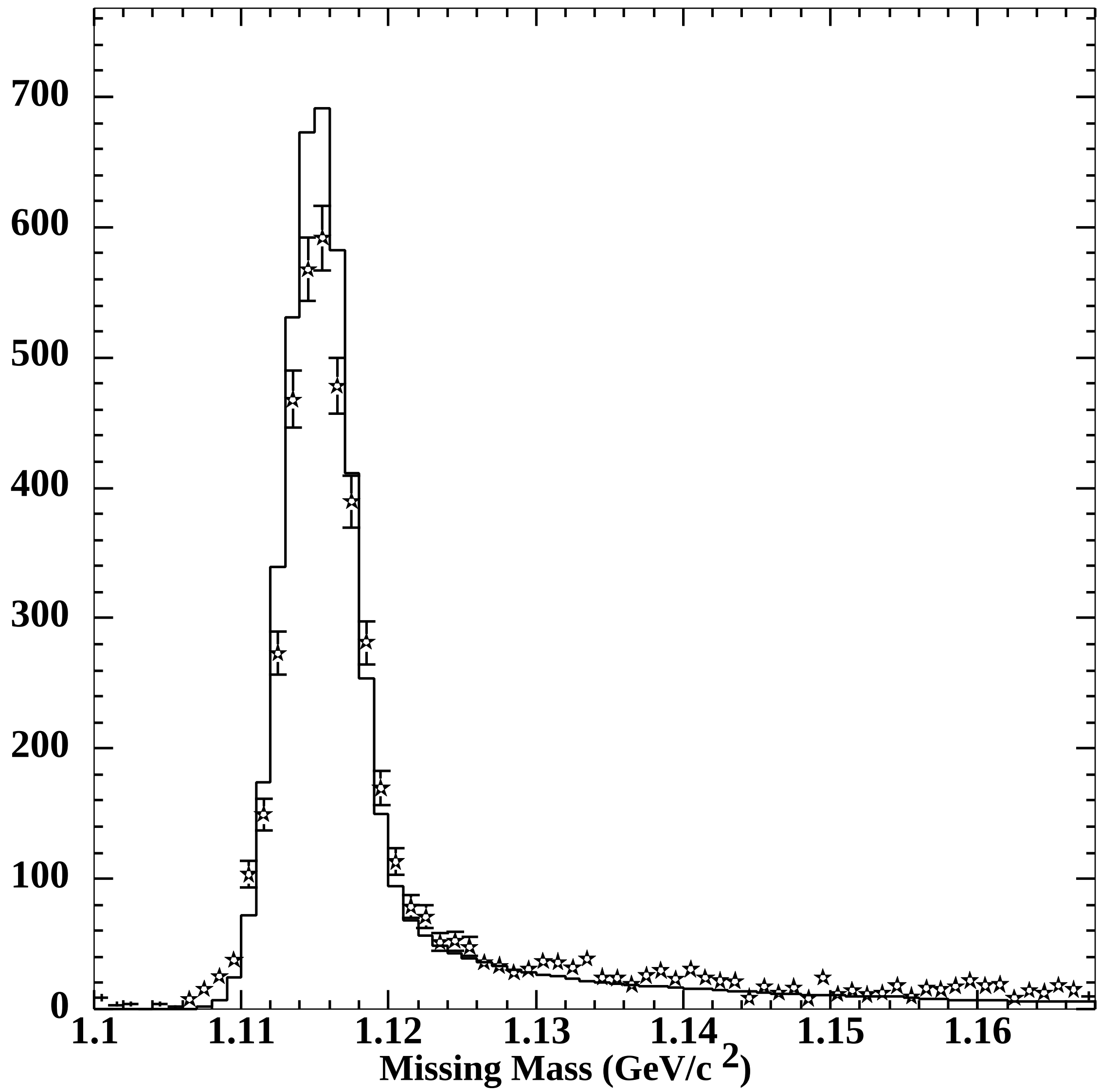

Figure 4.12: Missing Mass (GeV/c^2) plot for the Λ region showing both data (symbols) and Monte Carlo (solid line) distributions for the lowest ε point measured at Q^2=0.75 (GeV/c)^2.

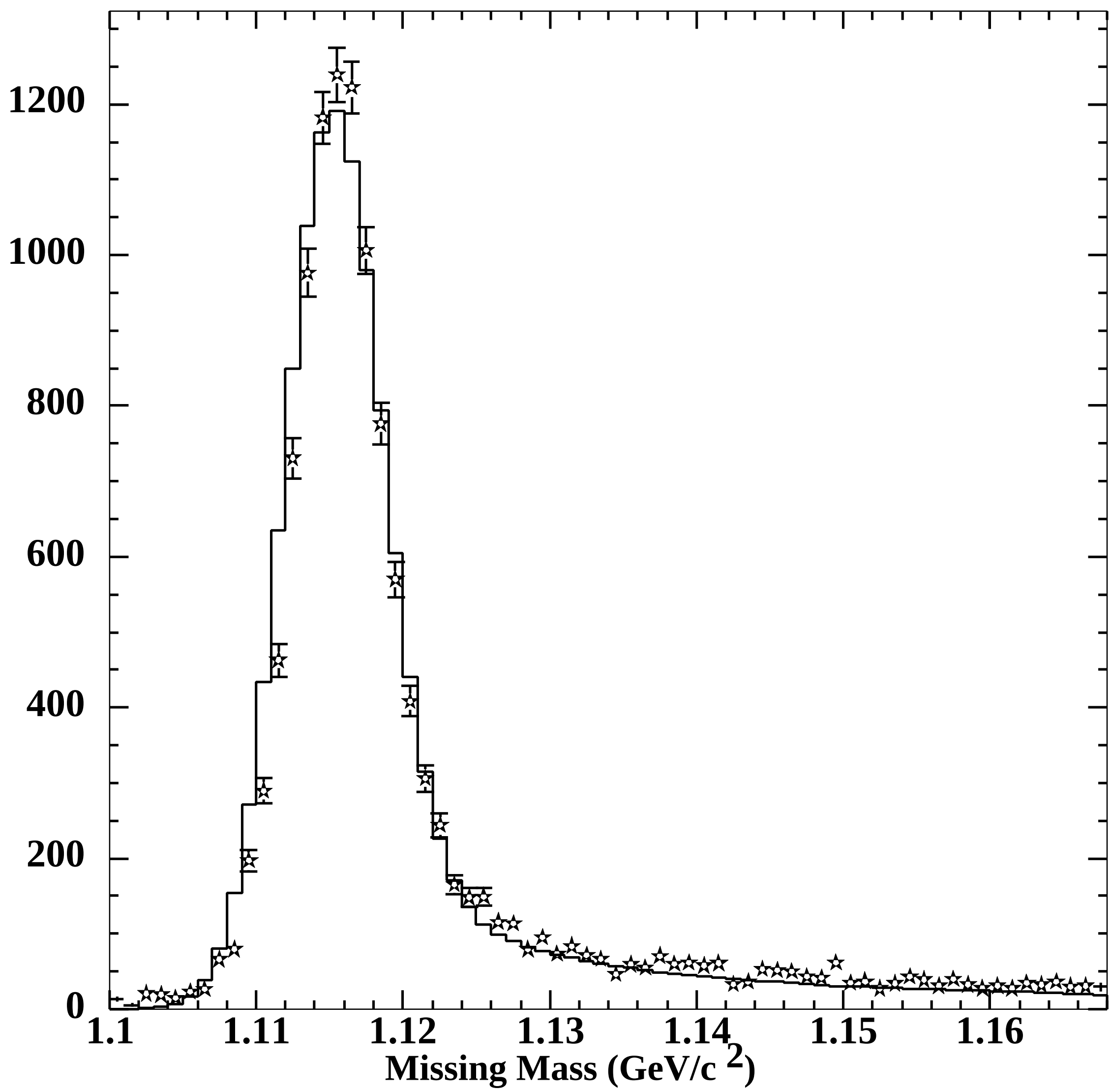

Figure 4.13: Missing Mass (GeV/c^2) plot for the Λ region showing both data (symbols) and Monte Carlo (solid line) distributions for the middle ε point measured at $Q^2 = 0.75$ (GeV/c)^2.

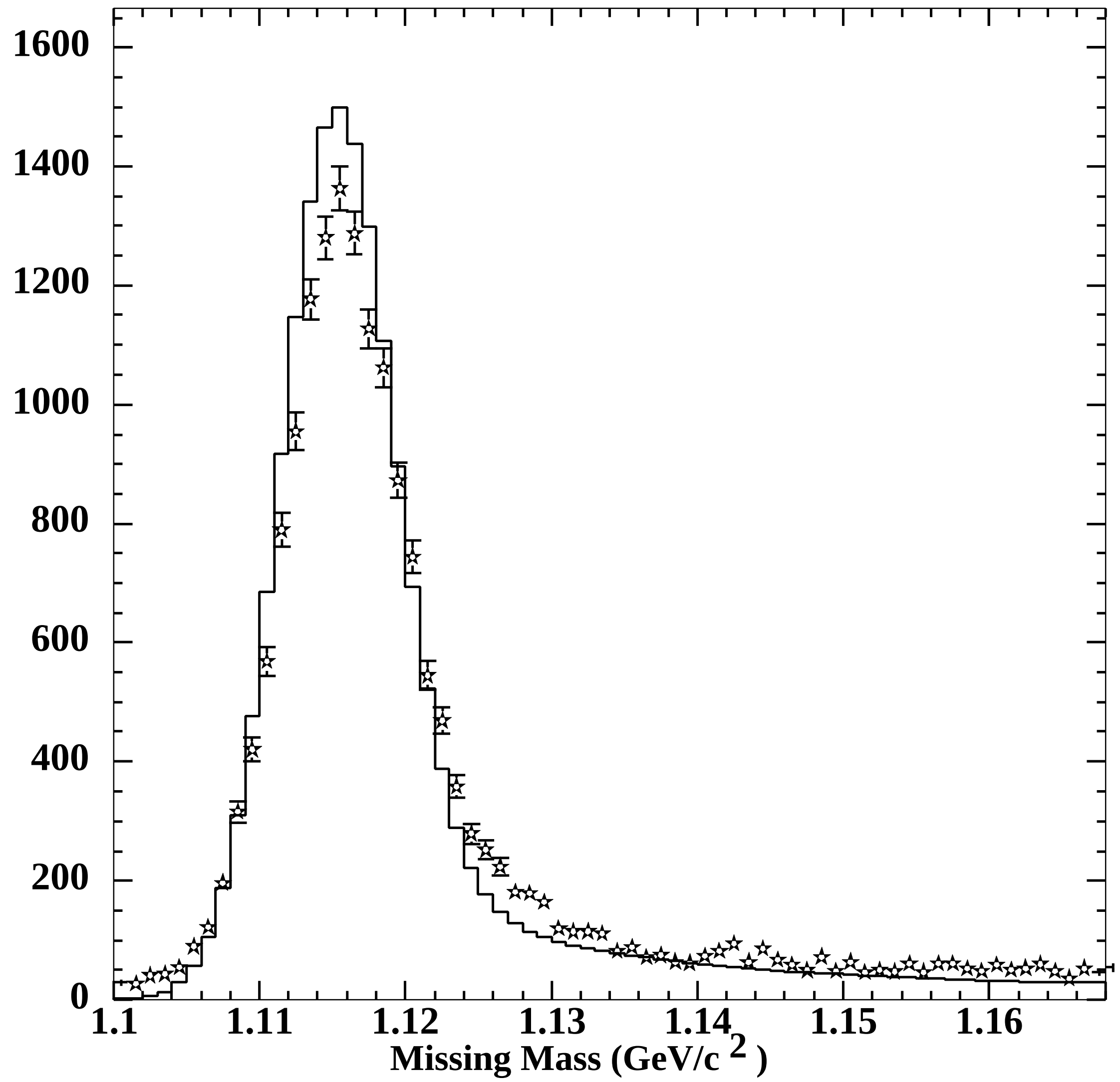

Figure 4.14: Missing Mass (GeV/c^2) plot for the Λ region showing both data (symbols) and Monte Carlo (solid line) distributions for the highest ε point measured at $Q^2 = 0.75$ (GeV/c)^2.

most of the time one wishes to integrate over all coordinates that are not relevant for the physics analysis. In such case one can truly interpret the acceptance as a probability distribution (i.e. the probability of an event with given in–plane, out–of–plane angles, and momentum to be accepted in the spectrometer). The approach taken in this **E93-018** analysis was to model each of the spectrometers separately using the available single arm Monte Carlo programs. Effectively one factorizes the total acceptance $A(V)$ into its HMS and SOS parts:

$$A(V) = A_{SOS}A_{HMS}. \tag{4.2}$$

Recall that the spectrometer acceptance is a property of the optical system. Therefore one should refrain from introducing into the acceptance correlations that do not belong in there (i.e. any type of correlation related to the particular reaction studied does not belong in the spectrometer acceptance).

At the beginning of the analysis several attempts were made to obtain an analytical representation for the acceptance. An analytical form of the acceptance would have simplified further calculations (namely the cross–section calculation). Several classes of functions were considered for this representation, including cubic splines [52] with various numbers of knots and multiquadric functions [53]. However, this approach failed (see e.g. Fig. 4.15– Fig. 4.17), mainly because both classes of functions used tend to introduce "features" not present in the original distribution. Also the number of parameters tended to increase rapidly as a function of the number of knots and number of dimensions of the fit for spline functions. The multiquadric approach tries to keep the number of parameter to reasonable values (although the typical 200+ parameters is by no means a small number) but the computation time is greatly increased (i.e. $\sim$ 8-12 hours for one kinematic setting, one spectrometer for 3×3 mr^2 steps in XPTAR and YPTAR and 10 MeV steps in momentum - for a medium loaded HP workstation). Given all the problems associated with analytic representation(s) for the acceptance function the solution adopted in this analysis was to just bin the Monte–Carlo–generated acceptance n-tuple in XPTAR, YPTAR and δ in bins compatible with the known resolutions in these variables and use the resulting three-dimensional structure as a look-up table for the the

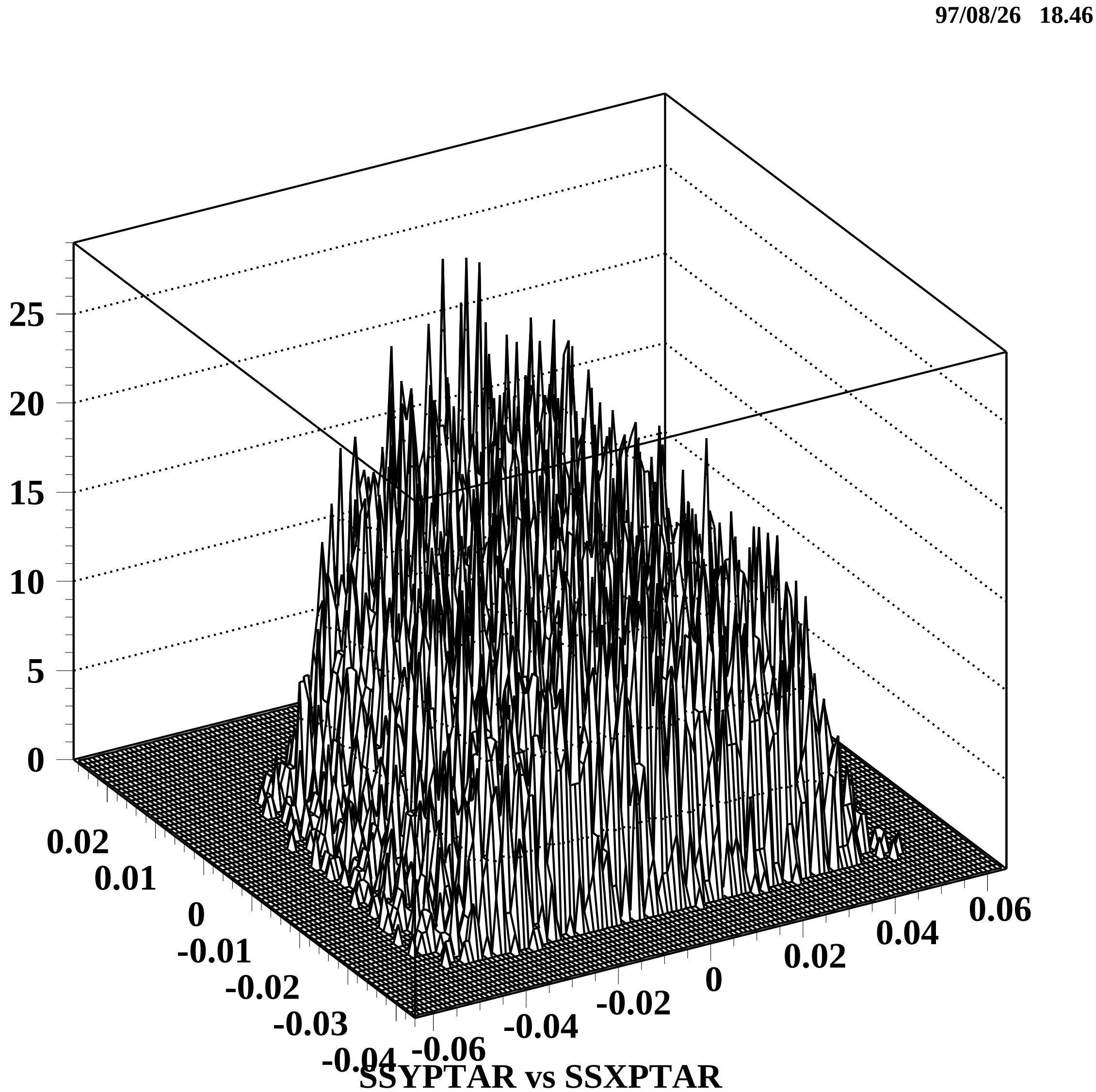

Figure 4.15: XPTAR vs YPTAR distribution in the SOS for a given 10 MeV slice in momentum. This is the raw/starting Monte Carlo distribution. A total of 4 million events were simulated.

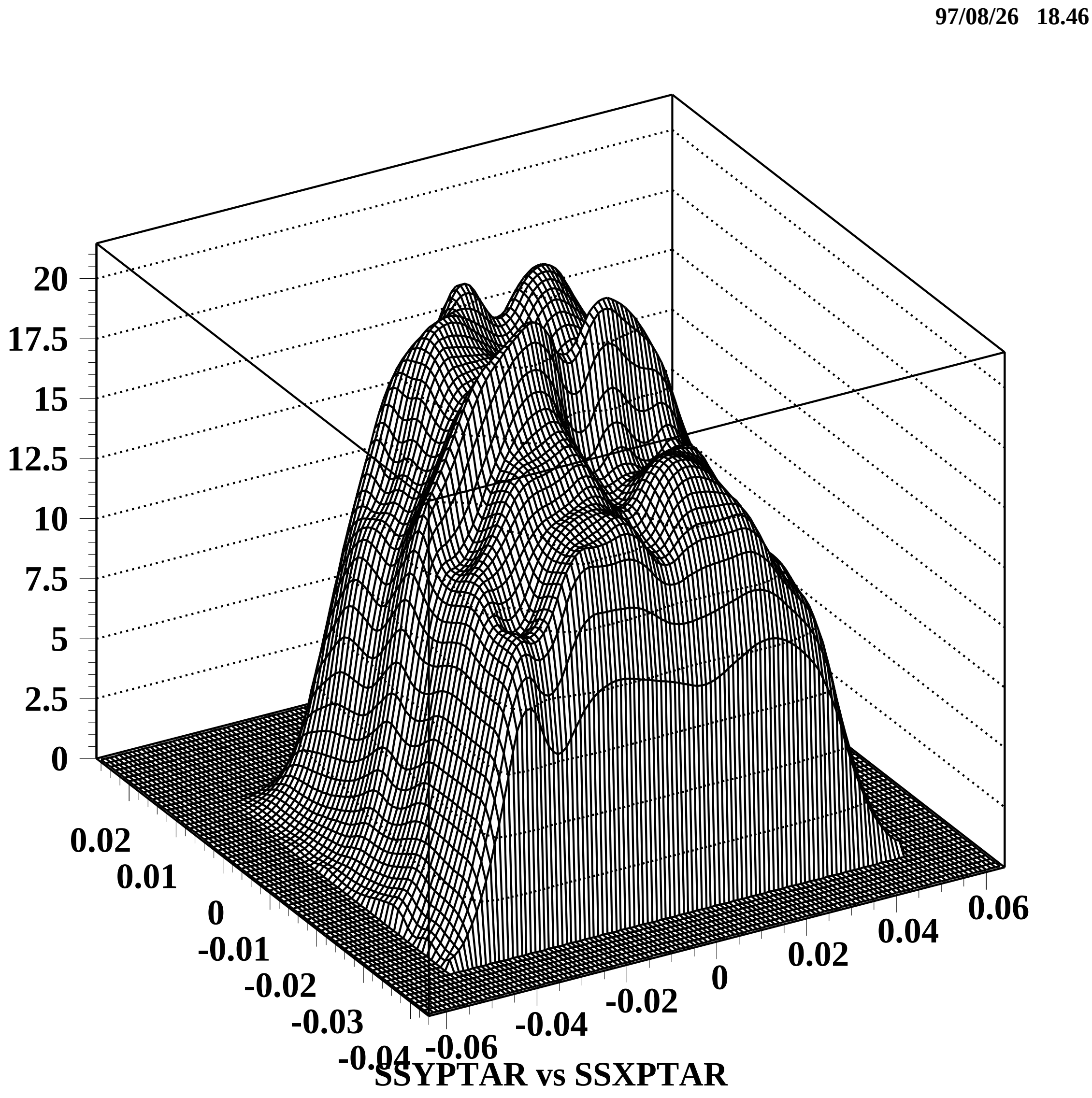

Figure 4.16: XPTAR vs YPTAR distribution in the SOS for a given 10 MeV/c slice in momentum. The fitting functions used were cubic splines with 12 knots.

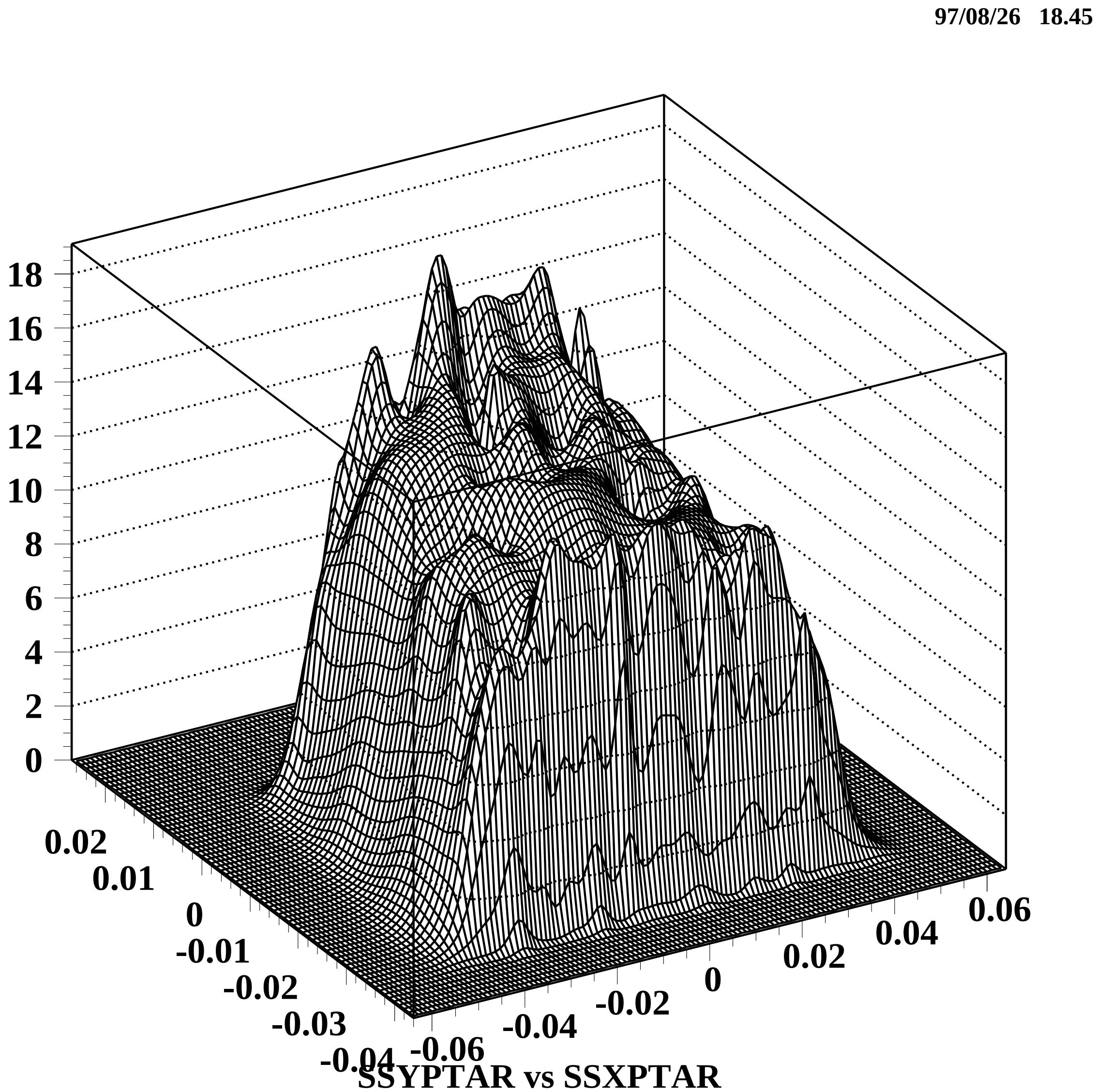

Figure 4.17: XPTAR vs YPTAR the distribution in SOS for a given 10 MeV/c slice in momentum. Multiquadrics were used for the fit.

acceptance function. One still needed a way of "smoothing"-out the inherent statistical fluctuations associated with the limited number of events generated in each acceptance bin. As a reminder, for three dimensions, with n bins in each dimension one has n^3 bins. If one now wishes to populate the bins such as to have 1% statistical uncertainty in each bin, one ends up with a VERY big number. If one then makes the argument that the contribution from a small bin in the final product (i.e. cross-section) will be small, therefore more modest statistics are needed in the Monte Carlo, then one ends up with a picture similar to Fig. 4.15, with all the problems associated with bin-to-bin normalization implied by it. The solution adopted in this analysis was to use ideograms rather than histograms when building the look-up table. Thus, for each accepted Monte Carlo event several (typically 27) events were actually booked in the n-tuple but with fractionary weight (such that the sum of the weights equals one); these events were spread in the three directions by randomly sampling on a hyper-gaussian curve with widths given by the angular and momentum resolutions. In Fig. 4.18 and Fig. 4.19 one can clearly see the effect of this procedure. When using acceptance functions one needs to apply some cutoff value (i.e. discard any events for which the acceptance correction would be too large). In this present analysis a cutoff value of 70 % was used (all events for which the acceptance correction would be larger than 70 % were discarded). This choice represents only a modest drop in the available number of events (not more than 10-15 %) while limiting the uncertainty introduced by the use of the acceptance function. An added benefit was that the "blur" of the edges introduced when using ideograms was completely removed from the analysis.

In order to evaluate the uncertainty associated with the acceptance correction and also to test the influence of the acceptance cuts used in the analysis the following procedure was devised: For each spectrometer, for every target quantity of interest (i.e. in–plane angle, YPTAR, out–of–plane angle, XPTAR, momentum $\delta = (p - p_0)/p_0$), for each Q^2 setting, for every ε point measured, the ratio of data to Monte Carlo (SIMC_EEK) yields was studied for several cut sizes. The data and Monte Carlo yields were cross–normalized for the nominal value of each cut (see Table 4.1 for a list of the nominal cuts), then the cuts were varied by ± 20 % around the nominal value, each time recording the ratio of

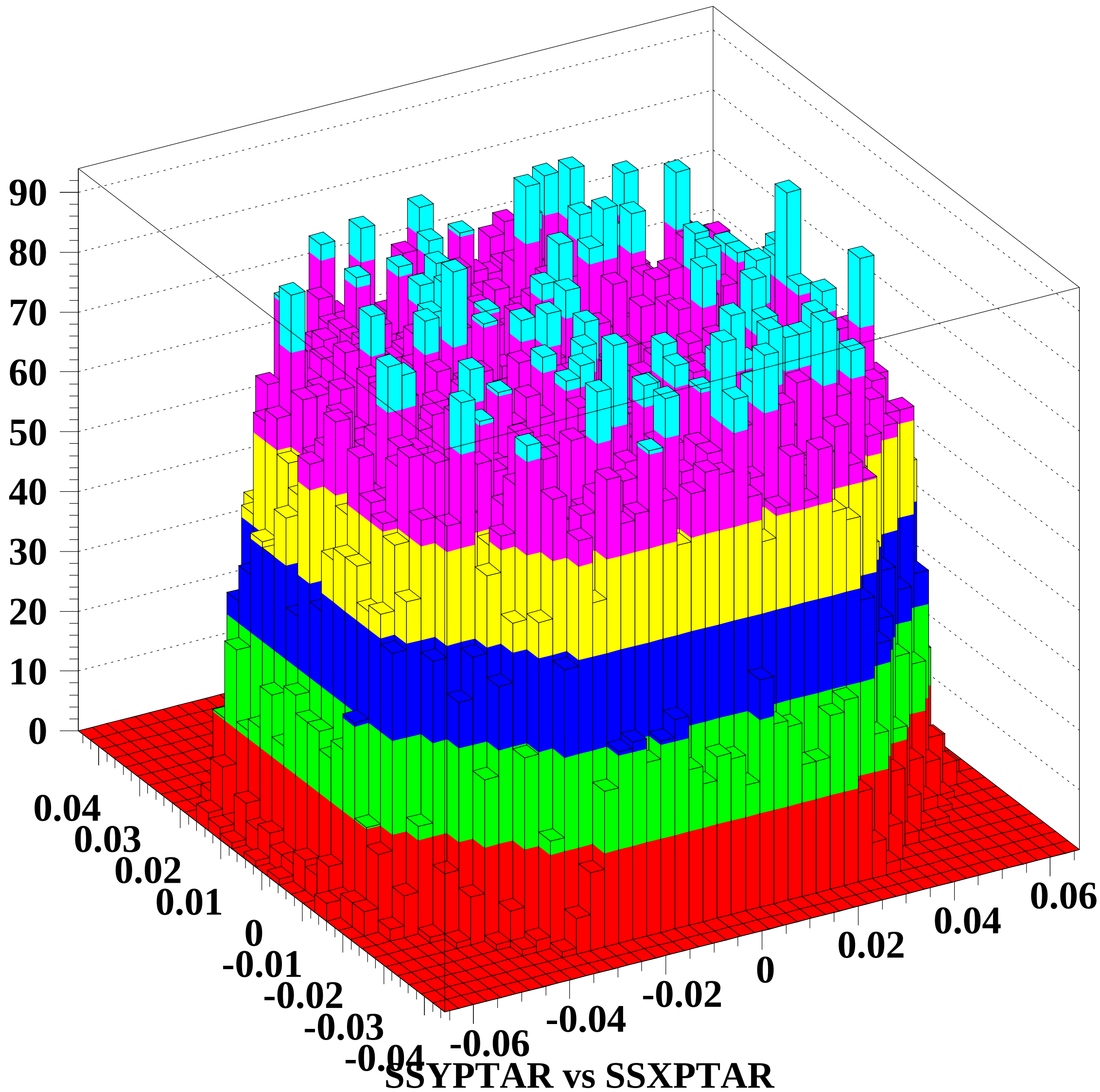

Figure 4.18: XPTAR vs YPTAR distribution in the SOS for a given 10 MeV slice in momentum. This is the conventional/raw histogram.

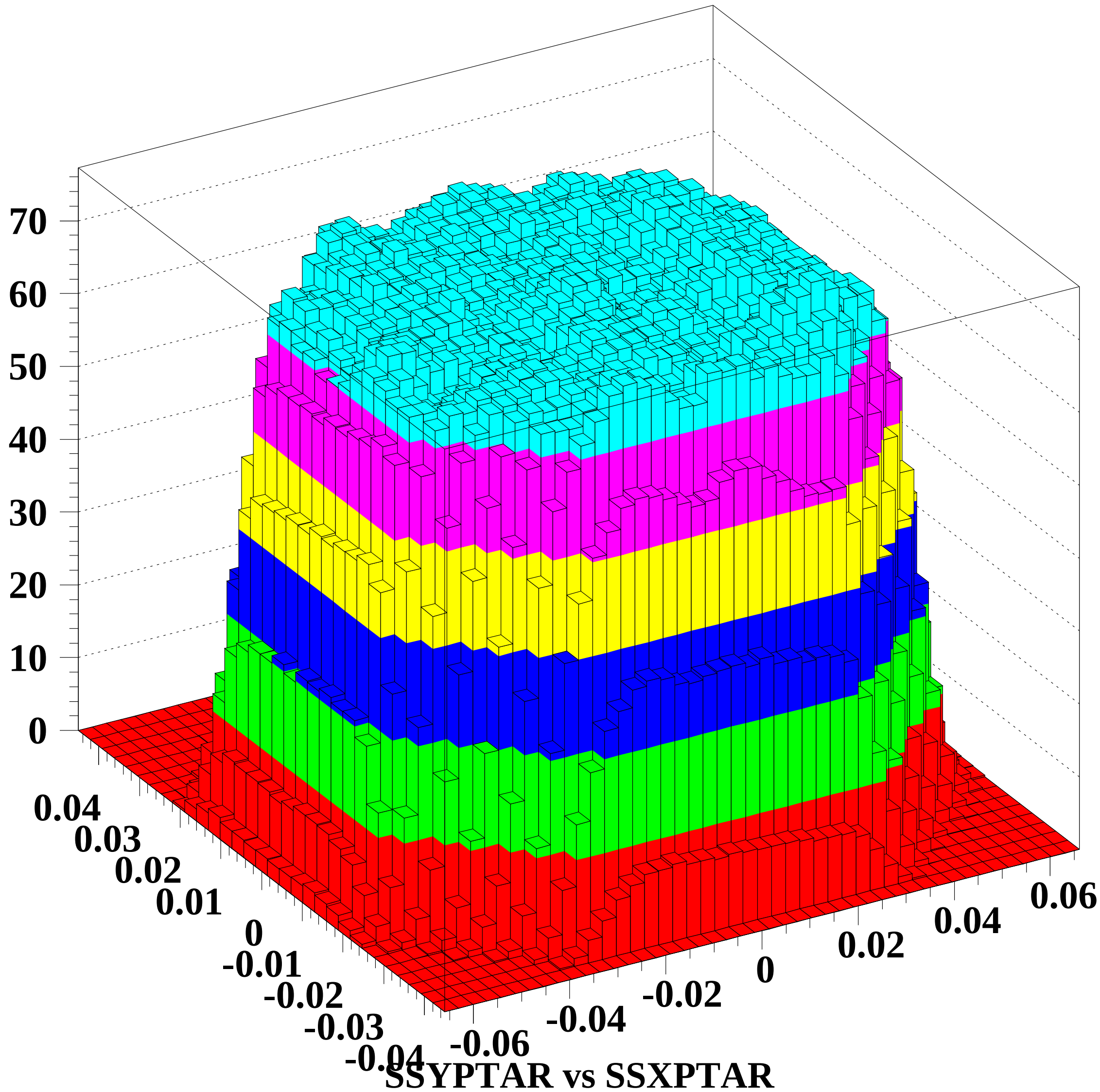

Figure 4.19: XPTAR vs YPTAR distribution in the SOS for a given 10 MeV slice in momentum. This is an ideogram obtained as described in the text with the same number of equivalent events as in the previous figure.

the data versus Monte Carlo yields. In Fig. 4.20 the result of such a study is shown for the $Q^2 = 0.52$ (GeV/c)^2 setting[8]. The three types of symbols (circle, square, and star) correspond to the three ε points measured. The first three panels show the results for the HMS spectrometer while the last three panels show the SOS values. Based on this study of the acceptance cuts it was concluded that the nominal cuts from Table 4.1 represent a reasonable choice for the present analysis (i.e. the results are stable with respect to the variation of the cuts). The point–to–point uncertainty associated with the acceptance correction was between 1.6 and 2.4 % (depending on the Q^2 setting). In addition, an overall uncertainty of one percent (scale type) was assigned to the entire acceptance correction procedure.

[8]Similar plots are available for all kinematic settings, however they are omitted here due to space constraints.

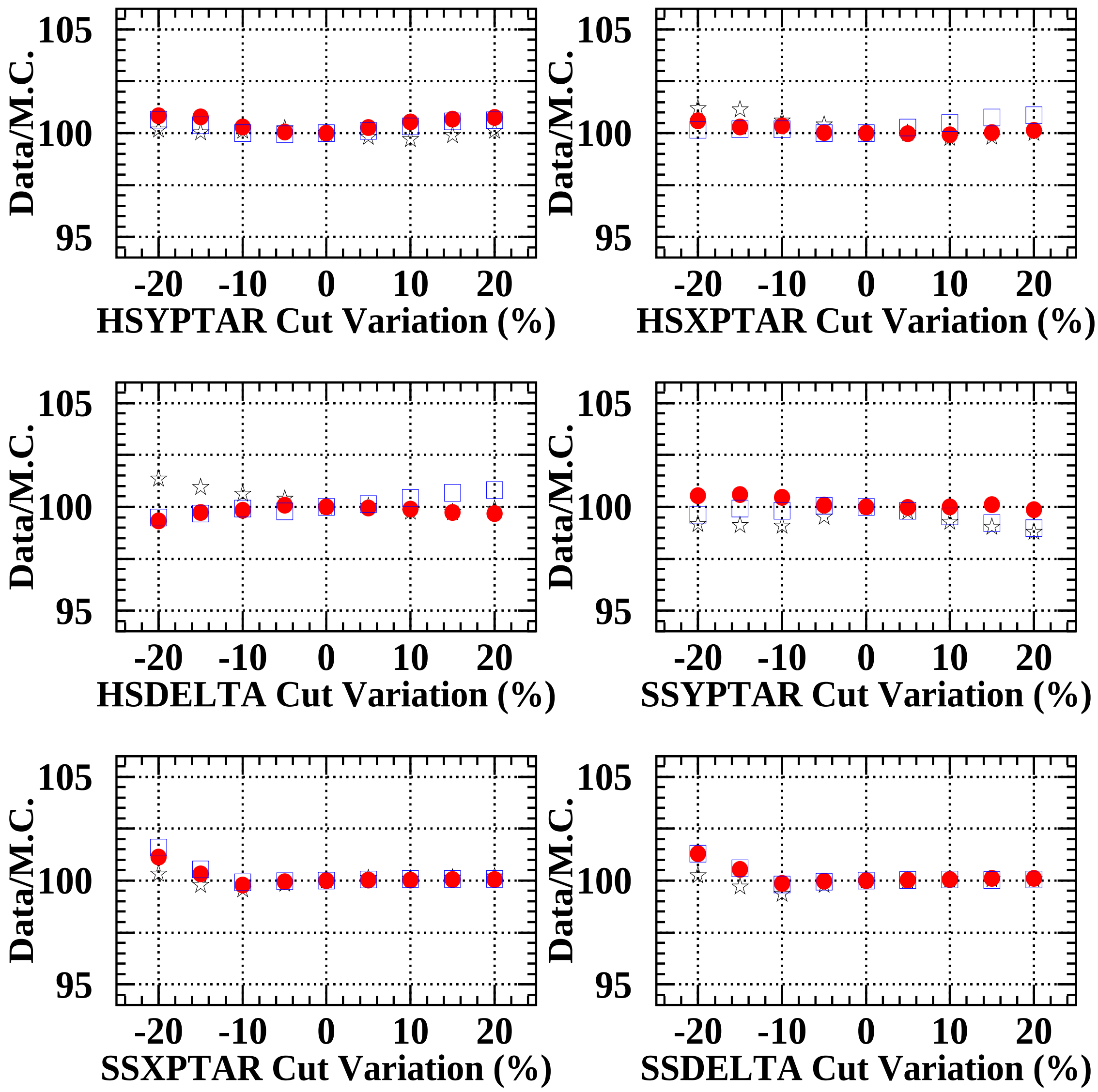

Figure 4.20: Systematic study of the acceptance cut influence for the $Q^2 = 0.52$ (GeV/c)^2 setting. Data to Monte Carlo ratios (in %) are shown for variations of the nominal HMS/SOS cuts of up to 20 %. The in–plane, YPTAR , out–of–plane, XPTAR, and momentum deviation, DELTA (%) are shown for the HMS (panels 1–3) and the SOS (panels 4–6).

4.4 Correction Factors

In the previous sections it was shown how the sample of coincident electron–kaon events can be correctly identified and how, using missing mass cuts one can isolate the $p(e, e'K^+)\Lambda$ channel. The size and shape of the spectrometer acceptance was obtained via Monte Carlo techniques. Also a prescription for evaluating the magnitude of the radiative corrections was given.

In addition to the above ingredients, in order to extract the kaon electroproduction cross–section one needs a series of corrections in order to account for inefficiencies of various detectors, decay losses, etc. In this subsection all these corrections shall be discussed, as well as ways to estimate/test them.

4.4.1 Hodoscope Trigger Efficiency

As shown in section 2.6 the requirement that three out of four scintillators fire is an essential condition in defining a trigger for both the HMS and the SOS spectrometers. Using the reconstructed tracks one can project in z to select the scintillator paddles that should have fired. Measuring how often these elements actually fire, one can determine the efficiency of all scintillator paddles. In implementing this procedure the overlap region between adjacent scintillator paddles (i.e. 2.00 cm for HMS and 1.25 cm for SOS) is excluded to avoid ambiguities. Due to multiple scattering this procedure is less precise in estimating the efficiency of the back two planes (problem tends to be bigger for the narrower SOS hodoscopes than for the HMS hodoscopes). To avoid problems one will either have to use only the efficiency of the front two scintillator planes for estimating the overall efficiency or artificially increase in software the "effective" size of the scintillators (thus relaxing somewhat the "matching" condition between the center of the paddle and a given track).

Once the scintillator efficiencies are known one can calculate the probability of missing a trigger due to hodoscope inefficiency and apply an appropriate correction. Because all the **E93-018** data required only 3–out–of–4 planes, the hodoscope trigger efficiency was expected to be (and actually was) high, $\geq 99.5\%$ for both the HMS and SOS. In Fig. 4.21

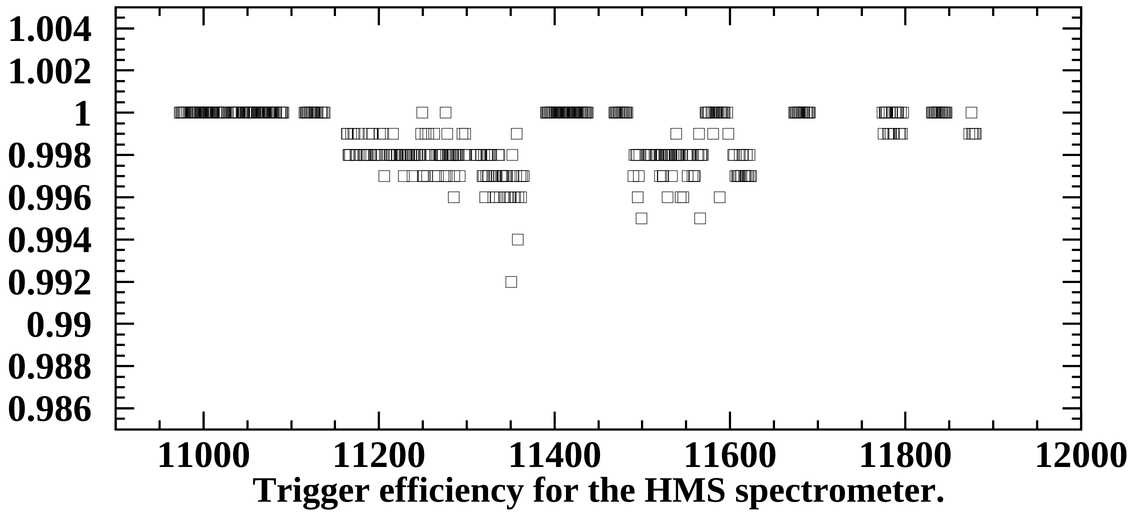

Figure 4.21: Hodoscope trigger efficiency for HMS.

the HMS hodoscope efficiency is shown as a function of time (i.e. run number). These hodoscope efficiency values are used to correct the data on a run by run basis, while the spread of the data can be used as a measure of the uncertainty due to this correction.

4.4.2 Tracking Efficiency

After a trigger was formed for one spectrometer, the data acquisition system polled all detectors in the spectrometer for information which was then embedded in the data stream and stored on disk. Later, in the data analysis stage of the experiment, the drift chamber information was used to reconstruct the trajectory of the particle that produced the original trigger. The tracking efficiency measured the fraction of the events for which a trajectory could not be found (or at least not in a reliable way). The main reason for which the tracking algorithm would fail to find tracks was when, for a given event, too little or too much drift chamber information was recorded. If the number of wires that fire/event was below a certain limit (i.e. dead or less efficient wires), then the left–right ambiguity could not be removed and a track was not fit. If too many wires fire/event then the chance of including a "noise" hit in the track increased, not to mention the exponential increase in the CPU time consumed.

The tracking efficiency was defined, in the current analysis, as the number of events for which a track was found, divided by the number of "good" events (i.e. the number of events for which a track was expected to be found). An event was defined as being "good" and therefore track-able if a trigger for the spectrometer was formed (otherwise the event wouldn't even exist), the time of flight determined, before tracking, that it was a forward–going particle (as opposed to a cosmic ray)[9], and one of the drift chambers had less than a prescribed number of hits (the limit used in this analysis was 15 hits). It was assumed that events for which both chambers have more than 15 hits each are caused by particles scraping the edge of one magnet, causing a shower of particles. As these kind of events fell outside the nominal acceptance of the spectrometer, they were not considered when evaluating the tracking efficiency.

The tracking efficiency described above was calculated, for each run, separately for several classes of events: all events, events passing particle identification cuts, events within a fiducial region as defined by the hodoscopes, and events that pass both the PID and fiducial cuts. These increasingly more restrictive cuts on the event sample used to determine the tracking efficiency were needed because the efficiency calculated for all events included the tracking efficiency for both real and background events, thus it was, at best, a statement on the overall performance of the chambers. For example, consider the electron arm. For the purpose of this analysis one was interested in finding the tracking efficiency for electrons; however the raw data sample, even with some PID in the trigger, might have still contained significant numbers of negative pions, which would alter our tracking efficiency measurement. Imposing a tight PID cut, one removed this inconvenience. For the hadron arm separate tracking efficiencies were computed separately for protons, positive pions, and kaons. Of course the kaon–only tracking efficiency would be statistics dominated. However, observing that the tracking efficiency

[9]For these upward–bending spectrometers the cosmic rays would tend to travel from the back of the detector hut towards the front so, after accounting for all cable delays, any track for which the time at the back two scintillator planes is earlier than the time at the front two planes would flag a cosmic ray. This observation was particularly important for the kinematic settings where the overall rates were low, as in the $Q^2 = 2.0$ $(\mathrm{GeV/c})^2$ setting, comparable with the 2–4 counts/sec one expects from cosmic rays for the HMS/SOS.

was similar (i.e. within 0.2 %) for protons and pions, one could then argue that the tracking efficiency for kaons should be the same. In this present analysis the tracking efficiency for kaons was taken as the average of the proton and pion tracking efficiencies, thus avoiding the larger errors associated with the shorter runs for which one only had a handful of kaons.

In addition to the PID cuts explained above a fiducial cut was imposed. This was achieved by considering, for tracking efficiency determination purposes, only the events for which the central paddles of the scintillator hodoscope fired. This condition effectively removed from the efficiency calculation all events that might have been subject to scrapping off the apertures. In particular, for the hadron arm, this cut removed from the tracking efficiency calculation, all events (pions, kaons) for which the original particle decays in the spectrometer hut and the daughter particles emerged at a wide enough angle (thus missing the back scintillator planes). Requiring only one (either) chamber to have less than 15 hits was a somewhat looser condition than requiring both chambers to have each less than 15 hits. In particular it allowed for tracks that had a clear track through the detector stack plus some noise (possibly a delta electron and/or electronics noise) to be reconstructed.

In the present analysis the data was corrected, on a run–by–run basis, for the efficiency calculated using only events passing both the PID and fiducial cuts (for "historic" reasons this is called "fiducial efficiency"). The electron arm (HMS) tracking efficiency was typically 93–97 % while the hadron arm (SOS) tracking efficiency was sensibly lower, 82–95 %, mainly due to the much higher rates in the hadron arm.

Even though the HMS/SOS drift chambers were designed to work at rates of up to a few kHz/wire, a small but noticeable deterioration of chamber' performance (i.e. decrease of the tracking efficiency) was observed with increasing total event rate in the spectrometer. In particular this meant that there would be variations in tracking efficiency between different kinematic settings (i.e. for the electron arm the Mott cross–section changes considerably from setting to setting, etc.) and also, within the same kinematic setting, there would be variations due to beam current changes (i.e. higher luminosity produces higher rates). In Fig. 4.22 the HMS fiducial efficiency is shown as a function of the total HMS

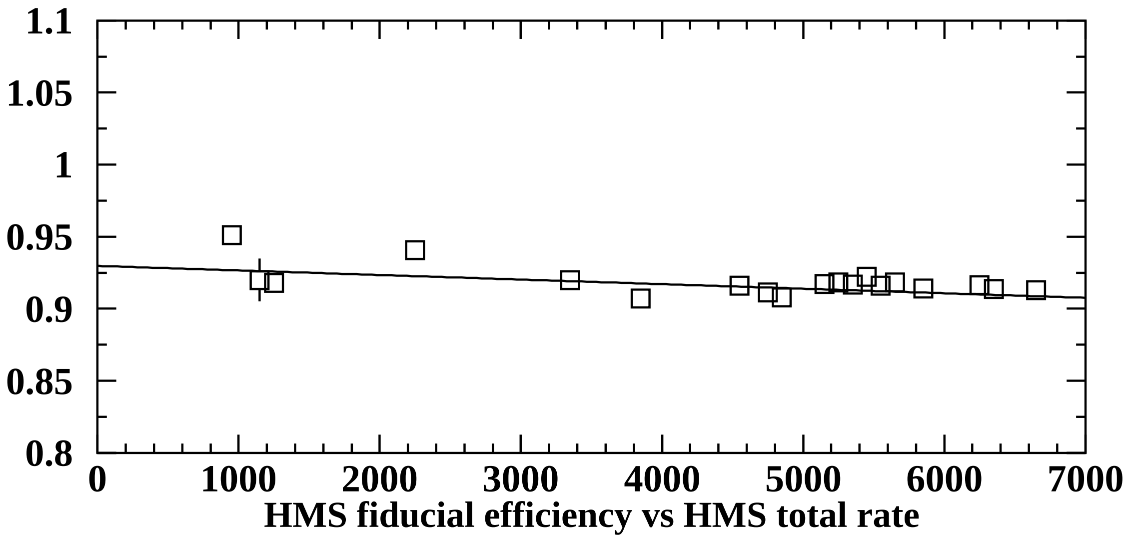

Figure 4.22: **E93-018** electron arm (HMS) fiducial efficiency as a function of the total HMS rate (Hz).

rate (in Hz). Similarly, Fig. 4.23 shows the SOS fiducial efficiency as a function of the SOS rate. In both figures the line represents a first order polynomial fit through the data. Taking into account this rate dependence of the fiducial tracking efficiency it is estimated that the uncertainty associated with the tracking efficiency was below 0.5 % for both the electron and the hadron arms. A variation of 0.5 % (or lower) in tracking efficiency was also observed when comparing runs that are taken in the same conditions (i.e. same kinematic, same current). Taken into account the above two observations, a 0.5 % uncertainty was assigned to the fiducial tracking efficiency for both the HMS and the SOS.

4.4.3 Electronic and Computer Deadtime

Electronic Deadtime

Whenever a logic gate wan the trigger is opened (i.e. activated) the output signal stayed "high" for a fixed period of time. If a subsequent event tried to activate the same gate during the same period of time, it was ignored. This mechanism is generally called

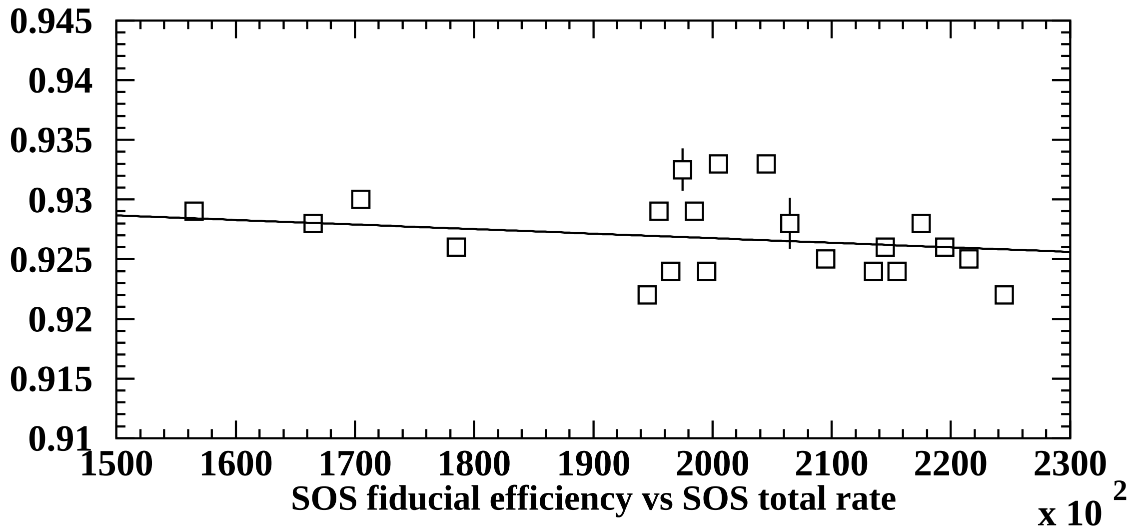

Figure 4.23: **E93-018** hadron arm (SOS) fiducial efficiency as a function of the total SOS rate (Hz).

electronic deadtime and in principle all measured counts need to be corrected for it. For a mean event rate R, the probability of finding n counts over a time period t is given, in terms of Poisson distribution, by:

$$P(n) = \frac{(Rt)^n e^{-Rt}}{n}, \tag{4.3}$$

while the probability distribution for the mean time between events is

$$P(t) = Re^{-Rt} \tag{4.4}$$

For a gate width of Δt, any event arriving within a time Δt of an event accepted by the gate will be missed by the DAQ. For small deadtimes this probability is nearly identical to the probability of an event occurring within a time Δt of the previous event (regardless if the first event triggered or not the logic gate). So, for small deadtimes, the fraction of measured events is given by the probability that the time between events will be greater than the width of the gate, Δt:

$$\frac{N_{meas.}}{N_{total}} = \int_{\Delta t}^{\infty} Re^{-Rt} dt = e^{-R\Delta t} \tag{4.5}$$

Now, the width of all logic gates used in Hall C (at least during **E93-018**) was 30 ns, with the exception of the gates for the hodoscope discriminators. The width of the hodoscope gates was 50 ns, in order to eliminate the potential double pulsing/ringing of the discriminators arising from the very low threshold used for these devices. The hodoscope discriminators were not, however, dead, even when their outputs were active. A new signal arriving while the discriminator output was high would cause the output signal to be extended to 60 ns after the latest hit. Given this observation one could safely assume that $\Delta t = 30$ ns for electronic deadtime evaluation purposes. Throughout **E93-018** the live time was very high, close to 100 %, so it could be approximated by $e^{-R\Delta t} \approx 1 - R\Delta t$. To estimate the deadtime correction, four versions of the final trigger were produced, each with a different gate width (30, 60,90, and 120 ns). Using these measurements one could extrapolate to zero deadtime in order to determine the number of real triggers lost. The electronic deadtime was measured and corrected for on a run–by–run basis. The correction was small for all kinematic settings, typically 1.0 % or less.

Computer Deadtime

The computer deadtime describes the situation when events are lost because a hardware trigger is formed during the time that the DAQ is busy processing the previous event. This was a far more significant source of dead time than the electronics deadtime explained earlier. As shown in section 2.7 the total processing time for an event was $\sim$300–400 μs. Running in buffered mode reduced this problem because now the DAQ could accept a new event even before the previous event was fully processed. Thus the time for which the DAQ was dead was reduced to only $\sim$100 μs, equal to the time needed to perform the FASTBUS conversion. These figures were valid for operating the Hall C DAQ in its single arm mode. For coincidences the size of the event was roughly twice the size of a single arm event (neglecting the small amount of overhead relating to coincidence signals, etc.), thus the processing time of a coincidence event took two times longer than for a single arm event. The computer dead time (actually the computer live time) was obtained by taking the ratio of events actually processed by the Trigger Supervisor versus the total number of triggers formed. The computer dead time was calculated for each run, and the data was corrected for lost triggers on a run–by–run basis. The computer dead time during **E93-018** was between one and ten percent, strongly dependent on the kinematic setting and on the beam current.

Assuming that the event size stayed more or less the same for all coincidence events, then the dead time would only be a function of the total data acquisition rate. Studying the dependence of the computer deadtime on the total coincidence rate one could then estimate the uncertainty associated with this correction. In Fig. 4.24 the computer dead time, as measured in the SOS detector stack, is plotted versus the total coincidence rate (in Hz). The line shows the expected/theoretical dead time (based on a $\sim$200 μs conversion time). The width of of the residuals distribution (i.e. differences between the experimentally measured and the expected value for the dead time) was used as an estimate of the uncertainty for this correction. The value obtained from Fig. 4.24 and used in the data analysis was 0.2 %. During **E93-018** two independent measurements of the computer dead time were performed, one using the HMS electronics (i.e. TDCs), one using the SOS electronics. These redundant measurements provided an independent check on the value quoted above. In Fig. 4.25 (left panel) the computer dead time measured in the SOS (electronics) is plotted versus the computer dead time as measured in the HMS. The line corresponding to the first diagonal (i.e. perfect correlation between the two measurements) is also shown. In the right panel of Fig. 4.25 a Gaussian fit for the difference between the two measurements is shown, indicating that indeed the correlation between the two independent measurements was almost perfect. Lastly, in Fig. 4.26 one can observe the clear difference between running in buffered (lower line) versus non–buffered mode (upper line). For the particular kinematic setting shown (Q^2 = 1.00 (GeV/c)^2, lower ε point), the SOS FASTBUS crate controller was repeatedly failing and, in an attempt to temporarily alleviate the problem (while the support group was looking to identify, "borrow", and install a replacement controller), the DAQ was intermittently switched between its buffered and non–buffered modes. For this particular case the dead time is roughly four times greater in the non–buffered mode than in the buffered mode.

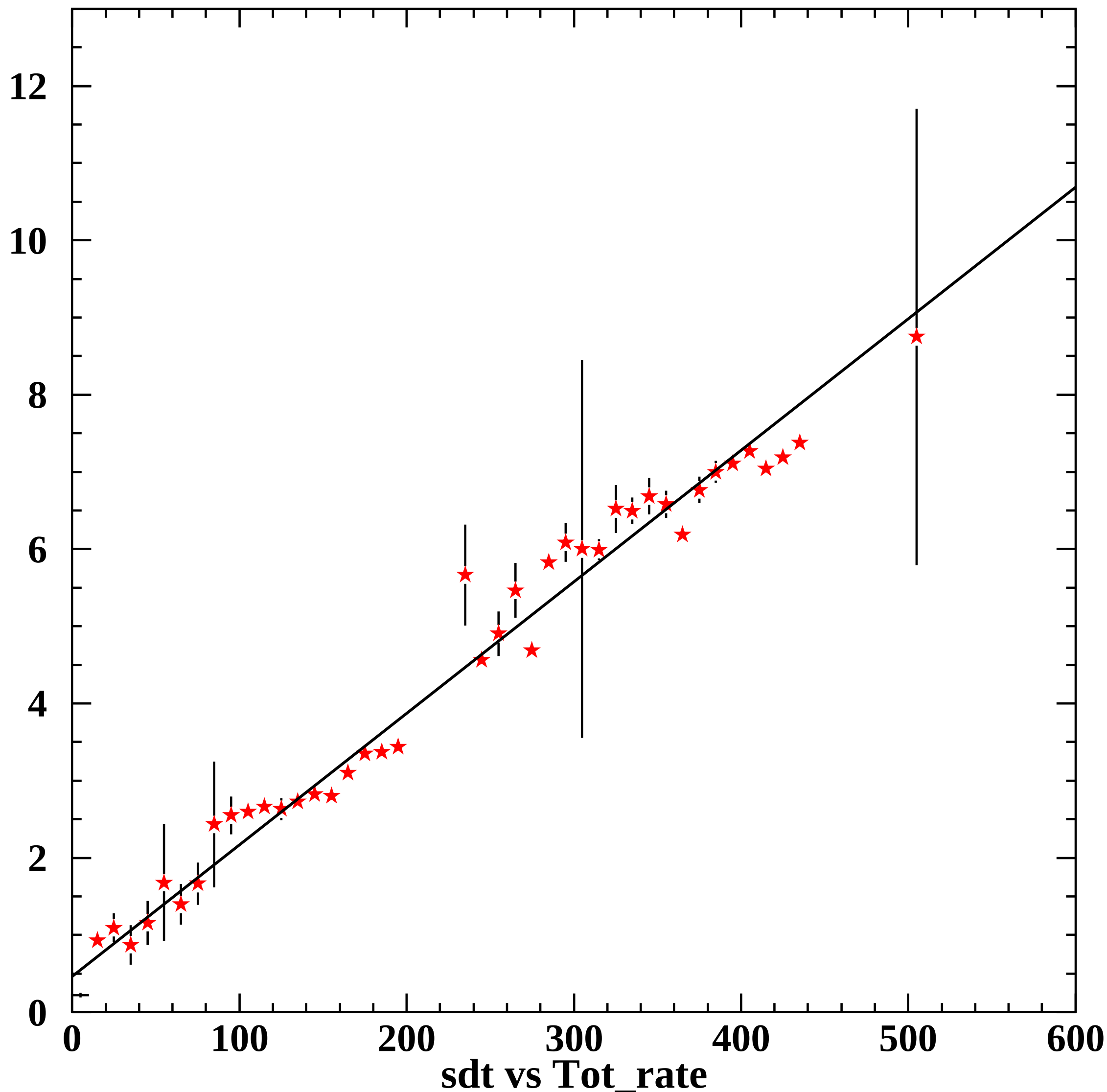

Figure 4.24: **E93-018** computer dead time (%), as measured in the SOS electronics stack, *sdt*, versus the total coincidence rate ,*Tot_rate* (Hz).

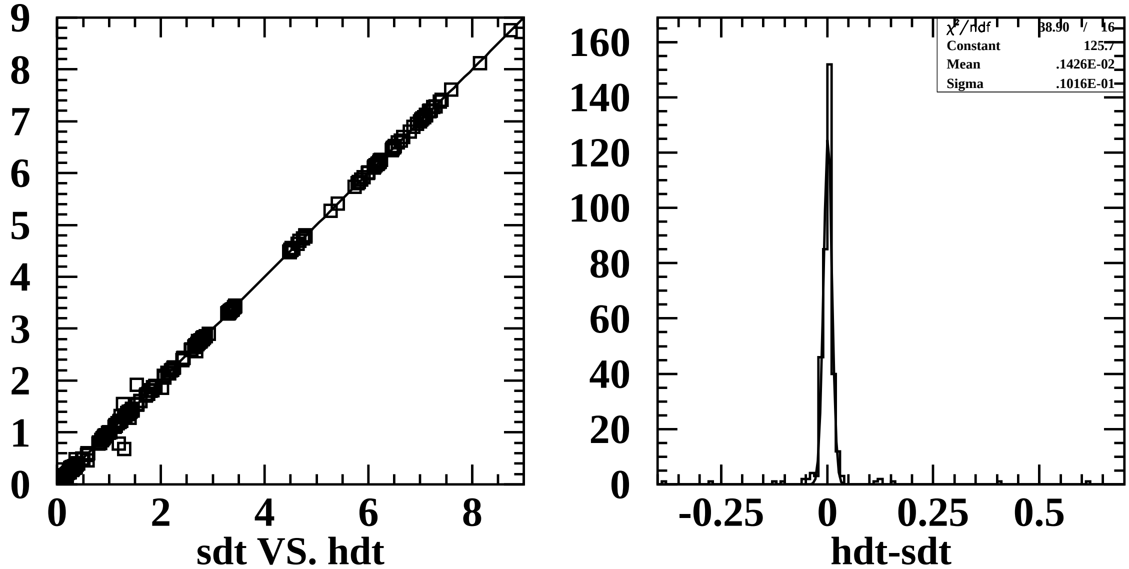

Figure 4.25: Left panel: Correlation between the computer dead time measurement in the SOS (sdt) and HMS (hdt). Both quantities are in percent. Right panel: Gaussian fit for the difference between the SOS/HMS measurements of the computer dead time.

Coincidence Blocking

Yet another source of dead time is the so–called coincidence blocking. This type of dead time occurs when a SOS single event arrives within the TS latching time (in other words a real coincidence event trigger is formed but an extra SOS single arrives in the same coincidence window). This in turn will cause mistiming in the ADC gates and TDC stops for the *next* coincidence event. Instead of arriving somewhere within the set coincidence window, the next coincidence event will apparently be several hundred ns away from it. In Fig. 4.27 a typical raw coincidence spectrum is shown. One can see that the events for which the coincidence blocking is in effect (the unhatched distribution) are clustered several hundreds of TDC channels away from the "good" coincidence events (the hatched distribution). The ratio of the blocked coincidences over the total number of coincidences gives the correction that needs to be applied to the data. As one applies cuts on the coincidence timing distribution as an important part of the particle identification process, the coincidence blocking correction needs to be evaluated before any PID cut is applied.

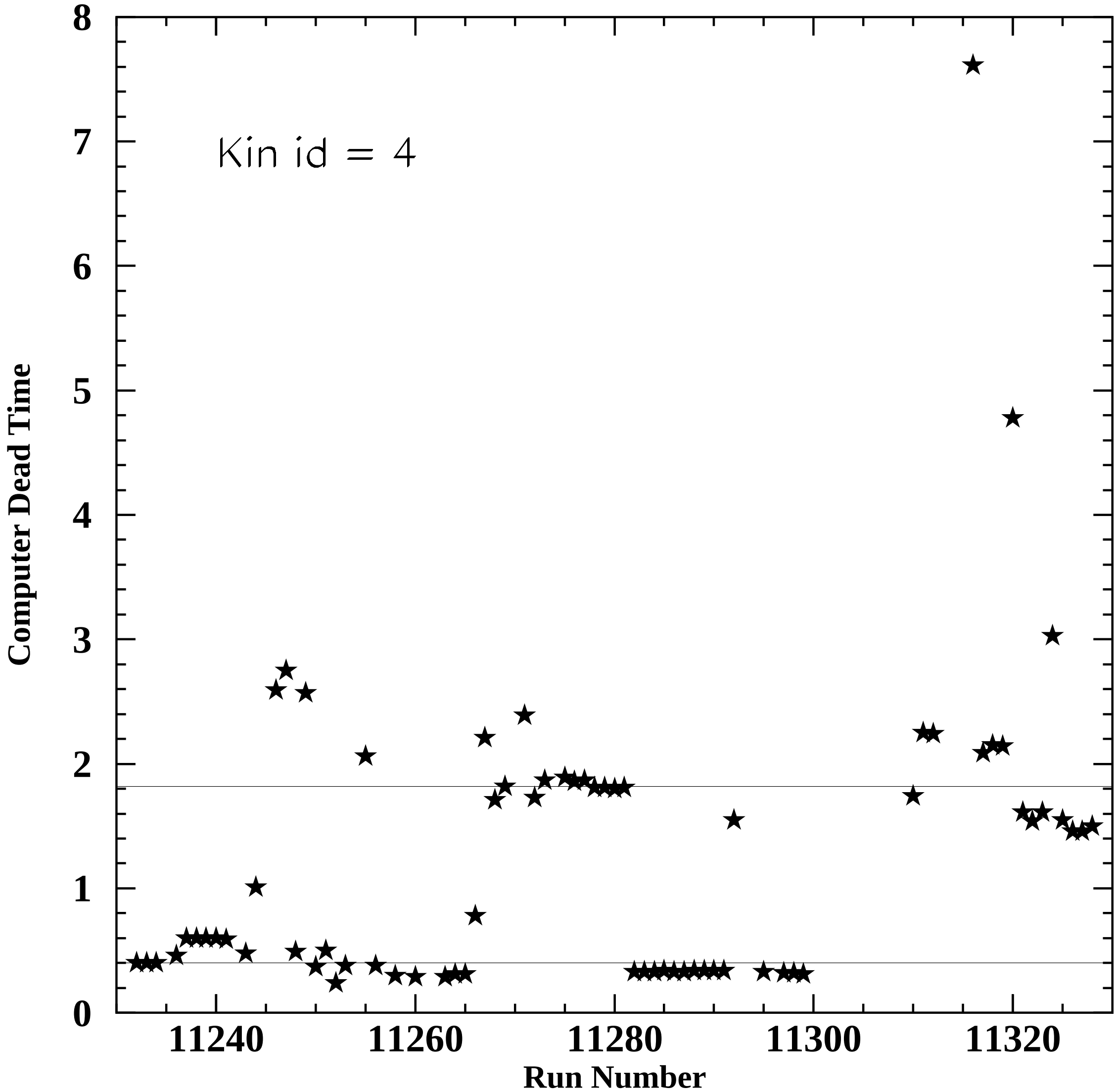

Figure 4.26: Computer dead time [%] differences between running in buffered (lower horizontal line) versus non–buffered mode (upper line) as observed during **E93–018**. All runs are at the same kinematics and beam current.

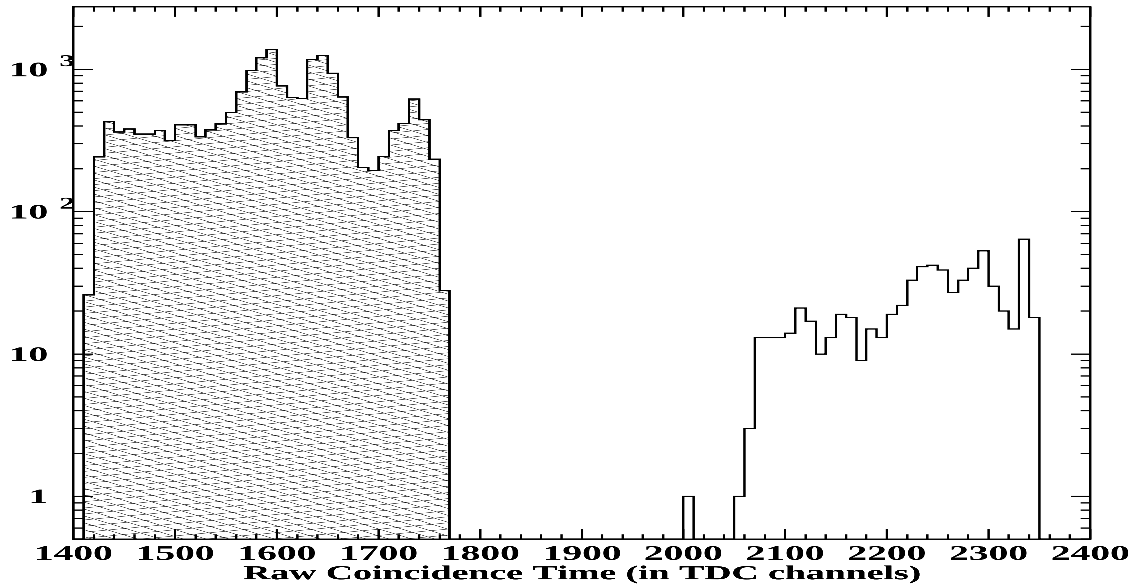

Figure 4.27: Raw coincidence distribution as measured during **E93–018**. The time difference between events unaffected by coincidence blocking (hatched part of the plot) and events for which the coincidence blocking is in effect (unhatched distribution) is clearly visible.

Let R_{SOS} be the trigger rate in SOS, and let τ be the time window in which coincidence blocking can occur. Then the probability of having coincidence blocking is given by:

$$\int_0^\tau R_{SOS}e^{-R_{SOS}t}dt = 1 - e^{-R_{SOS}\tau} \tag{4.6}$$

Further approximations of eq. 4.6 can be obtained for $R_{SOS}\tau \ll 1$, i.e. $1 - e^{-R_{SOS}\tau} \approx R_{SOS}\tau$. During **E93-018** the SOS singles rates varied anywhere from a few KHz to $\sim$ 600 KHz. Correspondingly, the observed coincidence blocking was between 1 and 10 percent, as shown in Fig. 4.28. A procedure similar to the one outlined above for the computer dead time was used to evaluate the uncertainty associated with this coincidence blocking correction. Taking the residuals (differences) between the measured and computed quantities in Fig. 4.28, resulted in 0.4 % as an upper estimate for the uncertainty. This value was used in subsequent calculations.

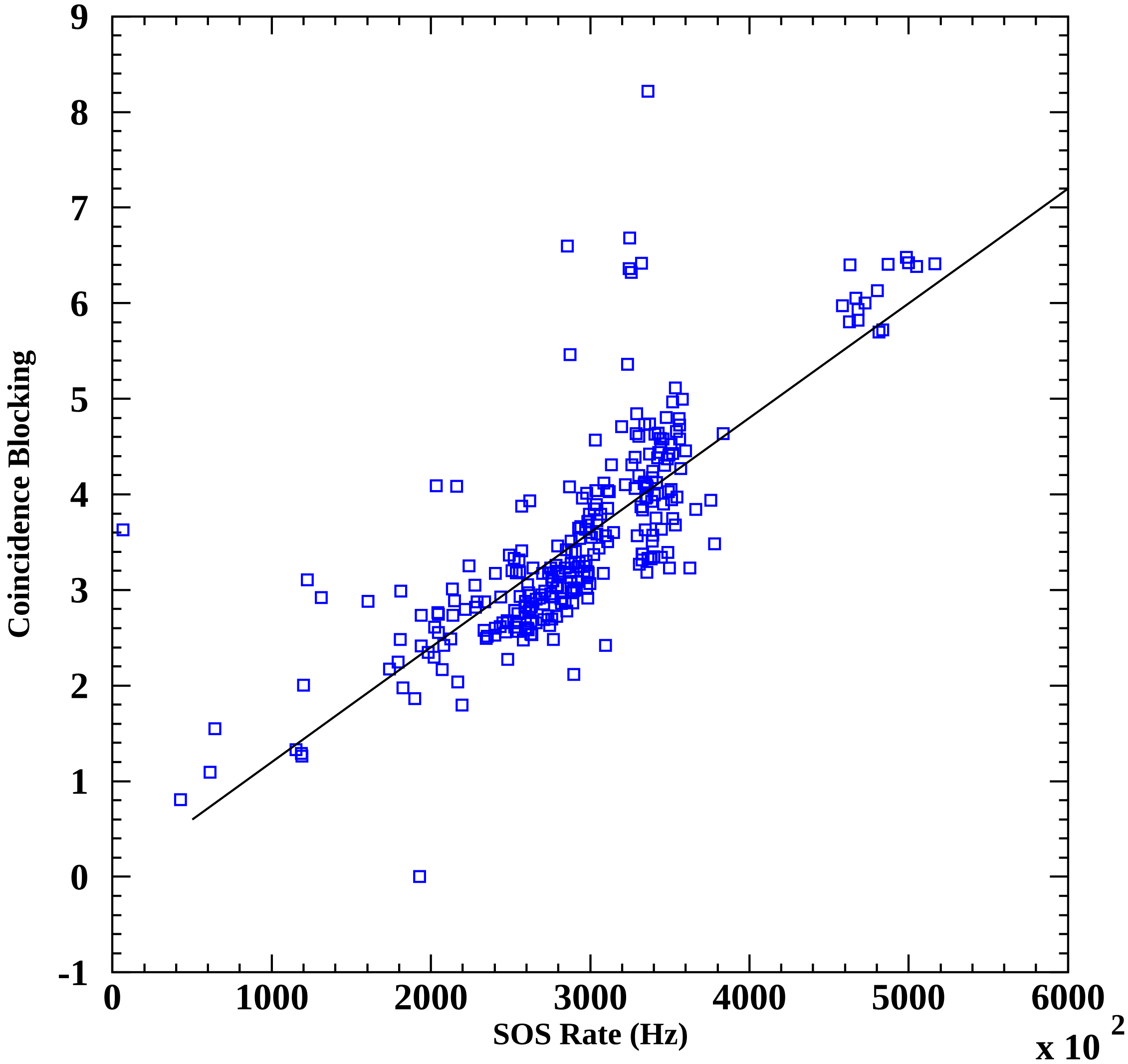

Figure 4.28: Coincidence blocking correction (in percent) as a function of the total SOS trigger rate (Hz). The curve shown is the theoretical prediction, computed from eq. 4.6.

4.4.4 Kaon Decay Corrections

In experiment **E93-018** scattered electrons were detected in coincidence with the leptoproduced kaons. The K^+ meson is an unstable particle, with a mean life time of $\tau = (1.2371 \pm 0.0029) \times 10^{-8} s$; or in a more useful form $c\tau = 3.709$ m. Therefore all measurements based on kaon observation needed to be corrected for decays, the size of the correction increasing as the distance from the target to the place where the kaon was detected increases.

All discussion about decay corrections should start with a definition of a "kaon". In the present analysis a good (i.e. coincident) "kaon" was defined as:

- a particle that produced a trigger in SOS in coincidence with an electron in HMS (electrons are identified by a combination of Čerenkov and shower counter cuts) and,
- a particle for which a track could be reconstructed in SOS (based on drift chamber information) and,
- a particle that had a velocity, β (computed from TOF information) compatible with the velocity of a kaon at the same momentum (i.e. $|\beta_{TOF}$ - $\beta_p| < \delta_\beta$ where δ_β was taken between 0.05 and 0.1) and,
- a particle for which the aerogel signal was below a certain level (typically 3 photo-electrons).

Based on the above criteria the decay correction is evaluated at the position of the last scintillator plane. One could argue that the trigger used was 3/4 scintillators so there could be some cases in which the last scintillator may not fire and still have a valid trigger so those cases should be treated separately. However, the number of events that passed the 3/4 check and failed the 4/4 check was fairly small and, evaluating the decay correction at the third and fourth scintillator plane position, the difference in the decay correction was found to be 0.4 % or less[10].

[10] Whereas the total size of the correction, as shall be shown below, was quite large.

In the first approximation the decay correction is given by the well–known survival probability law:

$$P(x_0) = e^{-Mx_0\Gamma/|\vec{p}|} \tag{4.7}$$

where:

- $P(x_0)$ is the probability for a particle not to decay after traveling a distance x_0 or greater;
- M is the mass of the particle;
- x_0 is the distance traveled;
- $\Gamma = 1/\tau$ is the inverse of the proper lifetime;
- $\vec{p}$ is the momentum of the particle.

Taking into account that the position of the fourth scintillator plane was $\sim$ 10.23 m away from the target and that the momenta of the kaons detected in **E93-018** were $\sim$ 1.2 GeV, the typical survival probability would be $\sim$ 33 %. This value implies that quite a sizeable decay correction ($\sim$ 300 % or so) needed to be applied to the data. Given the size of the decay correction one needed an extremely good knowledge of all factors that influence the survival probability, in order to keep the uncertainty at acceptable levels. Additionally, one needed an accurate estimate of the fraction of kaon events for which the decay product(s) were still able to mimic a kaon trigger, in order to avoid double–counting (i.e. eq. (4.7) overcorrects for the fraction of kaon events whose decay products would still mimic a valid kaon trigger). Examining the known decay modes for a kaon one finds that the most likely decay channels are:

- $K^+ \rightarrow \mu^+ + \nu_\mu \qquad \Gamma_j/\Gamma = 63.51$ %
- $K^+ \rightarrow \pi^+ + \pi^0 \qquad \Gamma_j/\Gamma = 21.17$ %
- $K^+ \rightarrow \pi^+ + \pi^+ + \pi^- \qquad \Gamma_j/\Gamma = 5.59$ %
- $K^+ \rightarrow \pi^+ + \pi^0 + \pi^0 \qquad \Gamma_j/\Gamma = 1.73$ %

- $K^+ \to \pi^0 + \mu^+ + \nu_\mu \qquad \Gamma_j/\Gamma = 3.18$ %
- $K^+ \to \pi^0 + e^+ + \nu_e \qquad \Gamma_j/\Gamma = 4.82$ %
- ... many other with less than 10^{-3} branching ratio.

From the decay products the positive pions and the muons had the potential of mimicking a kaon (in terms of velocity β) if their energy was low enough.

As explained earlier the Monte Carlo simulation code was enhanced to allow for the decay (and subsequent tracking of decay products) of unstable particles (kaons for the purpose of this experiment) both inside the magnetic spectrometer[11] as well as in the detector hut[12]. All kaon decay modes with branching ratios above 1 % were implemented in the code (the decay products were assumed to be isotropically produced in the rest frame of the decaying particle).

Running the simulation code for all kinematical settings measured during **E93-018** it became apparent that no decay product that could potentially mimic a kaon trigger in terms of velocity could ever emerge the spectrometer without taking at least one (in general more) "lucky bounces" off the quadrupole/dipoles and be then subsequently rejected by our fiducial cuts. This conclusion is not so surprising if one considers the mass difference between a K^+ meson and its decay products (compare $M_K \sim 494$ MeV with $M_\pi \sim 140$ MeV or $M_\mu \sim 106$ MeV). This means that, in order to have had the same velocity as a kaon with a momentum in the 1 GeV/c (and up) range (thus potentially failing our aerogel and TOF cuts), the momentum of the decay product needed to be very small (a few hundred MeV/c). Now, a particle with such a low momentum, placed in a spectrometer whose central momentum is at least 1.126 GeV/c (i.e. our lowest SOS setting), would be deflected so much by the magnetic field of the spectrometer so that it will most likely be lost in the yoke of the magnet.

After verifying that all decays occurring in the magnetic elements of SOS could be discarded as kaon double–counting sources, one could concentrate solely on the kaon

[11] The incremental SOS maps were used to track decay products originating inside the spectrometer.

[12] As usual the coding was done in general terms so decay in HMS could be simulated as well, although that was not needed in this experiment.

Decay mode	Correction (%)
$K^+ \to \mu^+ + \nu_\mu$	2.5
$K^+ \to \pi^+ + \pi^0$	1.3
$K^+ \to \pi^+ + \pi^+\pi^-$	1.6
all other	<0.5
Total	<6.0

Table 4.6: Summary of the double–counting corrections (%) for the central SOS momentum of 1.126 GeV/c.

decays occurring inside the SOS hut. Given that the distance from the target to the exit of the last SOS dipole was $\sim$ 7.2 m one had only a decay correction of only $\sim$ 20 % (even allowing for decay in the last meter of the SOS) instead of the original 300 % correction to worry about. For those events that decayed in the SOS hut the same cuts (aerogel, TOF) that were applied to the data were simulated in the Monte Carlo code. In particular a simulated velocity distribution, β, was produced, using the position where the kaon decayed and smeared by the measured time resolution of the scintillator paddles. Poisson statistics were used to estimate the number of decay products that would give a number of photoelectrons above/below the cut used in the data analysis. Table 4.6 summarizes the results of our simulation of the double–counting correction for the lowest momentum setting of SOS (i.e. the setting where we have the largest double–counting correction). The estimated overall uncertainty arising from the use of the total and double–counting corrections was at the $\sim$ 2 % level (mainly due to the uncertainty in the total physical path of particles through the spectrometer). Additionally the change of the decay correction as a function of the virtual photon polarization, ε, was studied. As the decay correction strongly depended (eq. (4.7)) upon the pathlengths, which in turn were parameterized in terms of the focal plane quantities, the number of kaons detected in a fixed box at the focal plane, divided by the total number of kaons detected, was studied for all ε points measured at each Q^2 setting. The ratio of events in the box (for a given tight cut in momentum) to the total number of events is sensitive to the point–to–point uncertainties associated with the decay corrections. In Fig. 4.29 to Fig. 4.31 the total number of events at the focal plane (top panel) and the number of events inside the box (bottom panel) are shown for all ε points at $Q^2 = 0.52$ (GeV/c)^2. Based on this study it was concluded that the point–to–point uncertainty in the decay correction was at the 0.5 % level.

4.4.5 Kaon Absorption Correction

As they travel from the target, through the magnetic spectrometer, and into the detector hut, a number of hadrons will be lost to elastic/inelastic scattering off the materials encountered. The correction factor that was used to counter this effect is generally called absorption correction.

For the specific conditions of **E93-018** kaons produced at the target had to travel some 10.23 m before being detected in the SOS hut. While most of this distance particles travel through vacuum (so no absorption), there were a number of vacuum windows, portions of detectors (as kaon detection becomes complete only at the back of the detector stack, the front detectors must be considered as potential kaon absorbers), even a part of the liquid target itself.

Assuming n_0 particles enter a layer of material of density ρ and thickness t. Then, the number of particles absorbed in that layer will be:

$$n = n_0 \frac{N_A \rho}{A} t \sigma_0 \tag{4.8}$$

where $N_A = 6.022 \times 10^{23}$ mol^{-1} is Avogadro's number, A is the atomic number of the material[13], and σ_0 is the absorption cross–section.

In Table 4.7 a list of the properties of the materials [54] encountered by a particle traveling from the Hall C target through the SOS spectrometer (and its associated detector stack) is presented[14].

For absorption cross–sections two different parameterizations were used. First a $K-N$ scattering calculation [55] based on the multiple scattering theory of Kerman, McManus

[13] For composite materials ρ, σ_0, and A are averages.

[14] In some cases the exact properties of the material used were not known so estimates based on known properties of similar materials had to be quoted instead.

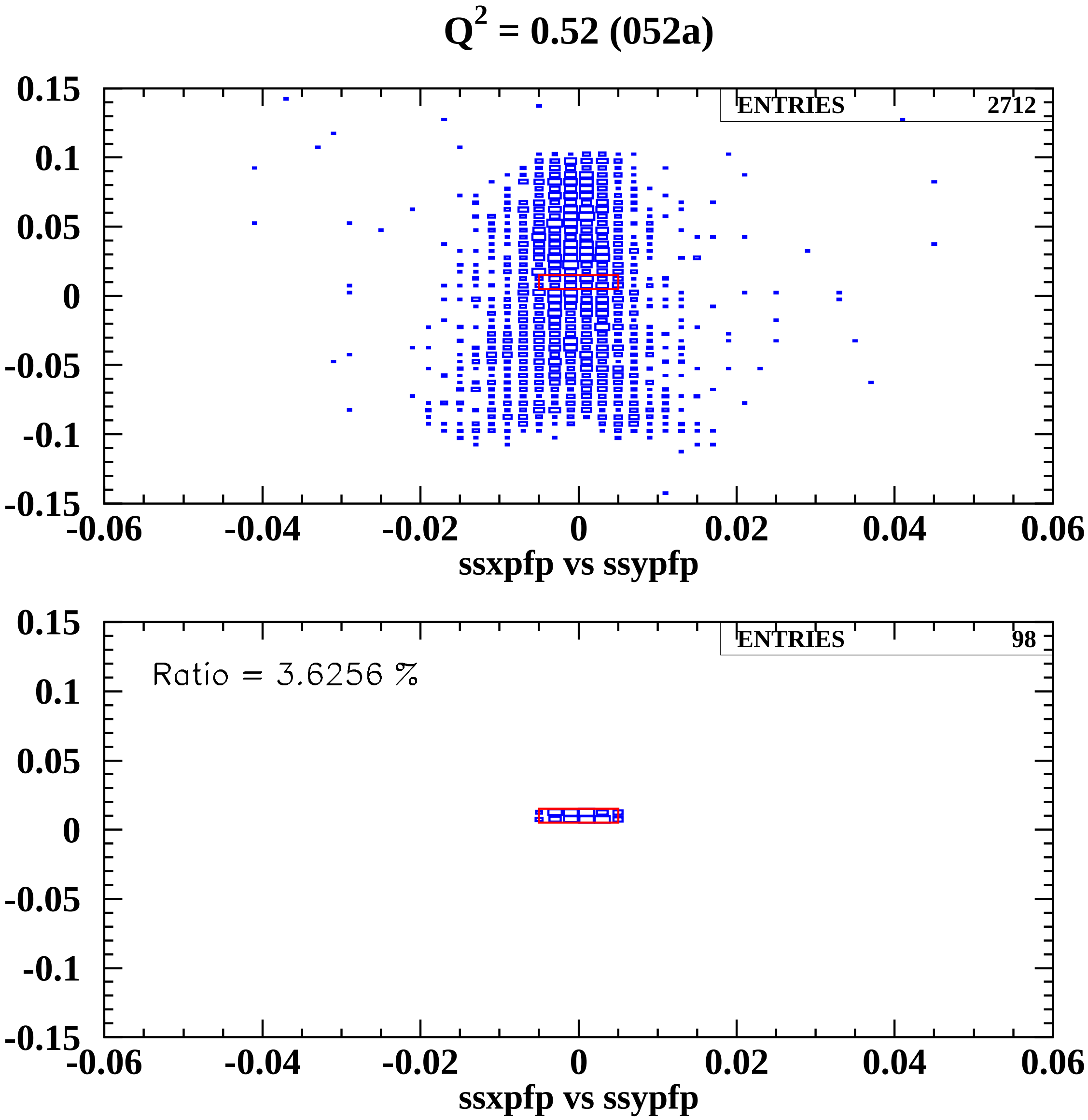

Figure 4.29: Ratio of total number of detected kaons (top panel) versus the number of kaons detected in a predetermined focal plane area (bottom panel) for the lowest ε point at $Q^2 = 0.52$ (GeV/c)^2.

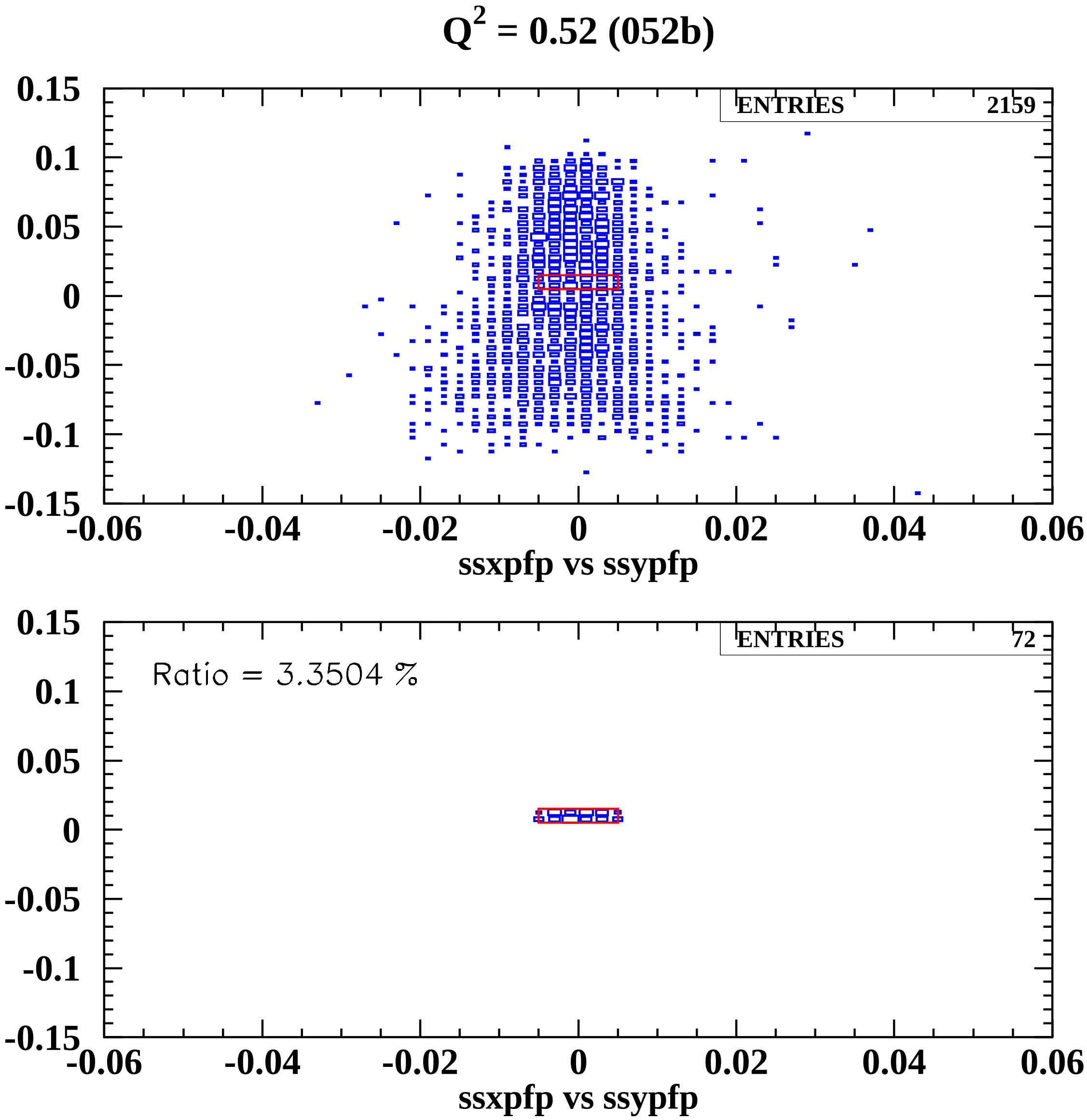

Figure 4.30: Ratio of total number of detected kaons (top panel) versus the number of kaons detected in a predetermined focal plane area (bottom panel) for the middle ε point at $Q^2 = 0.52$ (GeV/c)^2.

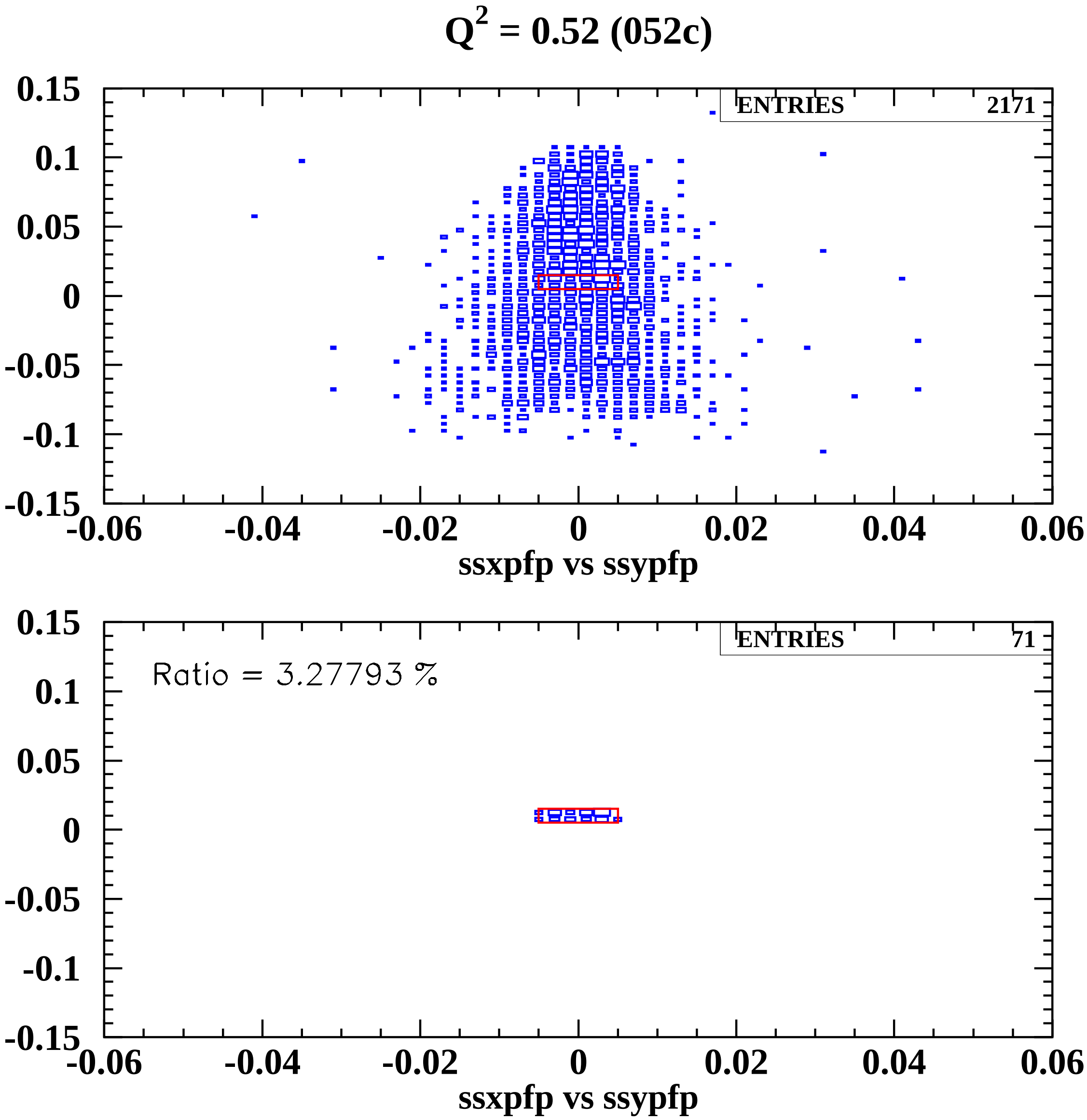

Figure 4.31: Ratio of total number of detected kaons (top panel) versus the number of kaons detected in a predetermined focal plane area (bottom panel) for the highest ε point at $Q^2 = 0.52$ (GeV/c)^2.

Absorber	Density (g/cm^3)	Thickness (cm)	$\bar{\lambda}$ (g/cm^2)	X (g/cm^2)	$X/\bar{\lambda}(10^{-3})$
3.37cm LH	0.0708	3.37	47.3	0.239	5.04
5 mil Al target window	2.70	0.0127	88	0.0343	0.39
8 mil Al chamber window	2.70	0.0203	88	0.0548	0.62
Air (no vac. coupling)	0.00121	~ 15	75	0.0182	0.24
Kevlar	0.74	0.0127	~ 70	0.0094	0.13
Mylar	1.39	0.0076	72	0.0106	0.15
Kevlar	0.74	0.0381	~ 70	0.0282	0.40
Mylar	1.39	0.0127	72	0.0177	0.25
Air (DC 1 through S2)	0.00121	~ 149	75	0.180	2.40
Mylar cathode	1.39	7(0.00125)	72	0.0122	0.17
Wire (effective) W $6 \times 30\mu m + 6 \times 60\mu m$	19.3	12(0.0002)	147.7	0.00469	0.03
Ar/Ethane (50/50 weight)	0.00154	6(0.6178)	~ 70	0.00571	0.08
Mylar cathode	1.39	7(0.00125)	72	0.0122	0.17
Wire (effective) W $6 \times 30\mu m + 6 \times 60\mu m$	19.3	12(0.0002)	147.7	0.00469	0.03
Ar/Ethane (50/50 weight)	0.00154	6(0.6178)	~ 70	0.00571	0.08
Poltysty. (1.04 overlap)	1.03	2(1.04)(1.0)	70	2.142	30.61
Čerenkov windows (2mil tedlar,10mil lexan)	~ 1.39	2(0.030)	~ 70	2(0.042)	1.21
CO_2 (1atm)	0.001977	100	76	0.753	9.91
Mirror (rohacell, mylar, carbon)	-	-	~ 70	0.45	6.43
Poltysty. (1.10 overlap)	1.03	0.25(1.10)(1.0)	70	0.283	4.05
Total	-	-	-	-	62.4

Table 4.7: List of SOS materials and their properties.

and Thaler [56] was used. In this approach the absorption cross–section is written as:

$$\sigma_0 = 21.065 p^{-0.99} A^{0.79} \tag{4.9}$$

whereas the momentum of the kaon, p, is in GeV/c, and the resulting cross–section in mbarn.

The second formula, based on eikonal approximation of W.Weise [57] reads:

$$\sigma_0 = A\sigma_{KN}\Big(1 - \frac{3}{8}\frac{1}{\pi r_0^2}\Big)(1-\beta^2)A^{1/3} \tag{4.10}$$

where σ_{KN} is the kaon–nucleon cross–section, $r_0^2 = (1.2fm)^2$, and β the ratio of the imaginary and real parts of the forward K+ N scattering amplitude. Using published K^+–^{12}C [58] and K^+–p [54] scattering data one can parameterize β as: $\beta = 0.82119 - 0.11274 * p$ (same units for p as above).

While the two approaches gave results that differed by up to 3 % for higher momentum settings (i.e. around 2 GeV/c or so)[59], for kaon momenta in the 1–1.2 GeV/c (where most of the **E93-018** data was taken) range the difference between the two formulas was minimal. In practice, equation 4.9 was used to correct for absorption losses, on an event–by–event basis. Typical size of the correction was around 5 % (of course, with a small momentum dependence). The uncertainty associated with this correction was estimated to be below 0.5 %.

4.4.6 Bin Centering Correction

More often than not the analysis of nuclear physics experiments involves accumulating/integrating counts over some region in phase space. A general assumption made is that, over the size of the chosen bin, the cross–section of the process studied doesn't change. Thus, in the end, the measured observables are given for the center of each bin. However, this approximation breaks down when the size of the bins is large and/or when the relevant cross–section exhibits large variations over a small range in phase space. Indeed, let $f(x)$ be the function of interest (say an experimental cross–section), and let $[x_1, x_2]$ be the interval of interest (which, of course, can be multidimensional). While the mean value theorem (MVT) theorem guarantees the existence of a point $c \in [x_1, x_2]$ such as $\int_{x_1}^{x_2} f(x)dx = f(c)(x_2 - x_1)$, this point c will be different from that in the middle of the (x_1, x_2) interval $(x_2 - x_1)/2$ (except for the very particular case of a purely linear $f(x)$). The bin centering correction tries to account for this effect.

The kaon electroproduction cross-section is expected to be relatively smooth over the range of kinematics considered, however, the bins considered are large, so a bin centering correction was needed. In practice, the weight $\frac{\sigma_0}{\sigma_{ev}}$ was used to correct each event. Here σ_0 is the model cross–section at the center of the bin and σ_{ev} is the model cross–section for the current event kinematics. In terms of the general case f function discussed above one effectively has:

$$\int_{x_1}^{x_2} f(x)dx = \int_{x_1}^{x_2} f(x)\frac{f_{\text{model}}(x_0)}{f_{\text{model}}(x)}dx \tag{4.11}$$

where $x_0 = (x_2 - x_1)/2$. Equation 4.11 will reduce to $f(x_0)(x_2 - x_1)$ if the model function f_{model} has the same x behavior as the function f one tries to measure.

In the present **E93-018** analysis the laboratory frame (i.e. five–fold $\frac{d^5\sigma}{dE_{e'}d\Omega_{e'}d\Omega_{K^+}}$) model cross–section was used to perform the bin centering. The corrections observed were at the few percent level (up to 8 %). The two models available in SIMC_EEK were used separately to evaluate this correction. The difference between the models ($\sim$ 2 %) was assigned as the uncertainty for this correction.

4.4.7 Target Boiling Correction.

As the beam passes through the target a certain amount of energy will be deposited in the target as heat. If this heat is not dissipated quickly enough, then local variations (even boiling if one is talking about cryogenic liquid targets) might occur. In practice this problem is (partially) alleviated by "rastering" the electron beam (artificially increasing, just before the target, the transverse size of the beam spot with a pair of deflecting magnets). In practice one needs to keep the beam spot quite small (otherwise the systematic errors in the scattering angle, etc. will be unacceptable) so a small amount of localized boiling might still be present. For the present analysis we used a value of 0.04 %/μA/mm–raster to correct for the density variations of the target. This value was obtained from the high luminosity scans performed since the beginning of Hall C operations [60]. During these tests the beam current in the Hall was varied (essentially from zero to the maximum allowable beam intensity), monitoring the counting rate in reference scintillators in both the HMS and the SOS, and then repeating for different raster sizes. Given the range in beam intensity observed during **E93-018** a 0.6 % point–to–point uncertainty was assigned to the target boiling correction. Additionally a 0.5 % scale type uncertainty was assigned to account for the target purity (<0.2 % impurities for the hydrogen target), uncertainty in the equation of state of liquid hydrogen (i.e. differences between the ortho- and para- states), uncertainty in the target temperature due to the finite resolution of the Cernox resistors, etc.

4.5 Cross Section Extraction.

The accurate extraction of the experimental cross–section out of the raw data is a prerequisite (condition "sine qua non") of any successful Rosenbluth separation. This section outlines the approach taken in the **E93-018** , highlighting the most important steps.

4.5.1 Extraction of $d^5\sigma/d\Omega_{e'}/d\Omega_{K^+}/dE'$.

Generally the number of events/the yield from a given region of phase-space (for a given electron-scattering experiment) is:

$$N(\Delta V) = N_e N_T \overline{\Big(\frac{d^n\sigma}{d^nV}\Big)} \Delta V \tag{4.12}$$

where:

- N_e is the number of incident electrons ($N_e = Q/e$);
- $Q = \int_t I(t)dt$ is the total charge;
- e is the electron charge;
- $N_T = \rho x / N_A$ is the number of target nuclei per unit surface;
- ρ is the density of the target;
- x is the length of the target;
- N_A is Avogadro's number;
- $\overline{(\frac{d^n\sigma}{d^nV})}$ is the average differential cross-section for the process studied;
- ΔV is the phase-space volume.

Depending on the specific process studied, and on the conditions in which the measurement is performed (i.e. the number of independent observables measured during the experiment) ΔV will have a certain dimension, denoted here by n.

Let us assume for now that the calculation of $\frac{d^n\sigma}{d^nV}$ is the ultimate goal of our analysis (alternatively one might consider it the beginning of the "theoretical" discussion...). Knowing the total charge, Q, the geometry of the target and its composition, and of course the size of the phase-space volume and the yield associated with it, eq. (4.12) can then be used to compute the cross-section.

For real detection systems, however, the relation (4.12) needs several corrections. Let us rewrite eq. (4.12) as:

$$N(\Delta V) = N_e N_T \varepsilon_1 \int_{\Delta V} \frac{d^n\sigma}{d^nV} \varepsilon_2(V) d^nV \tag{4.13}$$

Here ε_1 is a correction factor that takes into account the overall inefficiency of the detector system (i.e. all the correction factors discussed in previous sections) while $\varepsilon_2(V)$ accounts for the efficiency correction(s) that are known to vary between various subregions in phase-space (i.e. a scintillator bar with significantly lower firing efficiency than its counterparts will have to be included here). Also one might note that now the yield is written as an integral over the phase-space. The aim of the measurement will still be the calculation of $\overline{\left(\frac{d^n\sigma}{d^nV}\right)}$ but its definition and significance will have to be somewhat modified (see below).

For the type of experiments performed at Jefferson Lab in Hall C one uses magnetic spectrometers to detect charged particles. For these type of devices a further improvement of eq. (4.13) would be to consider the influence of the *Spectrometer Acceptance* (see Section 4.3.5), i.e. the probability of detecting in the spectrometer a particle with given momentum, p, polar and azimuthal angles, θ and ϕ respectively, originating from a certain point of the (generally extended) target, y_{tar}:

$$N(\Delta V) = N_e N_T \varepsilon_1 \int_{\Delta V} \frac{d^n\sigma}{d^nV} \varepsilon_2(V) A(V) d^nV \tag{4.14}$$

where $A(V)$ is the spectrometer acceptance.

One will note that eq. (4.14) shows a much more complicated dependence of the cross-section on the measured observables than eq. (4.12). A successful calculation of the cross-section requires the knowledge of ε_2 and A at every point in the available phase-space.

The relations (4.12- 4.14) provide the framework for cross-section calculations. While further improvement of the general relations might still be possible let us now focus on the specific conditions of experiment **E93–018**.

The basic reaction studied was $e + p \to e' + K^+ + \Lambda/\Sigma^0$. The measurement of the focal plane quantities x_{fp}, y_{fp}, x'_{fp} and y'_{fp} enabled the calculation of the target quantities x'_{tar}, y'_{tar}, y_{tar}, and $\delta = (p - p_0)/p_0$ for each spectrometer via sets of known optics matrix elements. Naively one would be tempted to write the phase space for the reaction studied as:

$$\Delta V \equiv \Delta^6 V \equiv \Delta E_{e'} \Delta\Omega_{e'} \Delta p_{K^+} \Delta\Omega_{K^+} \tag{4.15}$$

Now, the known widths of the Λ and Σ^0 particles are 0.05 MeV and 0.10 MeV respectively, well below the few MeV resolution of the HMS-SOS spectrometer combination. This additional constraint would act like a δ function upon eq. 4.15, in fact lowering the independent size of the phase-space from six to five dimensions. A choice would be for example

$$\Delta V \equiv \Delta^5 V \equiv \Delta E_{e'} \Delta\Omega_{e'} \Delta\Omega_{K^+}, \tag{4.16}$$

where the constraint was used to perform the "integration" over p_{K^+}. This would be the approach taken in (almost) all theoretical papers.

Experimentally (at least in the **E93-018** conditions) one does not detect any of the leptoproduced hyperons, thus one is forced to identify the Λ and the Σ^0 reaction channels by inspecting the missing mass, M_x. For the identification of the missing mass ranges for Λ and for Σ^0 production respectively one is referred to Fig. 4.7. This hyperon identification procedure effectively means one has to change one of the "natural" variables from eq. 4.15 to one with M_x and this involves the use of the appropriate Jacobian. The integration over the desired range in M_x (using the Jacobian, evaluated at every point, of course) yields the five dimensional phase-space from eq. 4.16. In the present analysis the kaon momentum was the variable "exchanged" for the missing mass, thus the following Jacobian was used:

$$\frac{dM_x}{dp_{K^+}} = \frac{1}{2M_x}\frac{dM_x^2}{dp_{K^+}} = \frac{1}{M_x}\Big(\|\vec{q}\|\cos\theta_{\gamma K} - (\nu + m_p)\frac{p_{K^+}}{E_{K^+}}\Big) \tag{4.17}$$

with p_{K^+} and E_{K^+} the momentum and the energy of the kaon, M_x the missing mass, $\theta_{\gamma K}$ the angle between the kaon and the virtual photon, and $\vec{q}$ is the momentum of the virtual photon.

4.5.2 Extraction of $d\sigma^{CM}/d\Omega_{K^+}$.

While the previous section elaborated on the extraction of the five–fold (laboratory) differential cross–section, it is often more convenient to express the results in terms of the CM cross–section. This way one can make direct comparisons with previous (if any) or similar (say we are interested in comparing kaon and pion electroproduction) measurements. Also, all theoretical predictions are expressed, typically, as CM quantities.

One can express the Laboratory cross-section in terms of the CM cross–section via:

$$\frac{d^5\sigma}{d\Omega_{e'}d\Omega_{K^+}dE_{e'}} = \Gamma \frac{d\cos\theta^*}{d\cos\theta}\frac{d\sigma^{CM}}{d\Omega_{K^+}} \tag{4.18}$$

where the virtual photon flux Γ expressed as:

$$\Gamma = \frac{\alpha}{4\pi^2}\ \frac{E'\ (W^2 - M^2)}{EMQ^2\ (1-\varepsilon)} \tag{4.19}$$

and $\frac{d\cos\theta^*}{d\cos\theta}$ is simply the Jacobian between the CM (θ^*) and the Laboratory (θ) angle between the virtual photon and the kaon[15]. $\frac{d\sigma^{CM}}{d\Omega_{K^+}}$ represents the CM (sometimes called "reduced") cross-section.

After computing the laboratory cross–section, eq. (4.18) was used to compute the reduced cross–section for each kinematic point. Note that, in the present analysis, the laboratory cross–section was already bin centered, so the virtual photon flux and the angular Jacobian needed to be evaluated only for the center of the bins considered.

4.5.3 Rosenbluth (L/T) Separation.

In the previous sections it was shown how to extract the 5–fold (laboratory) cross–section from the raw data and how to use the virtual photon flux and the angular Jacobian to subsequently compute the CM (reduced) cross–section.

[15]Sometimes the subscript γK is added to the θ and/or θ^* angles for clarity.

The only other condition that needed to be met in order to proceed with the separation of the longitudinal and transverse components of the cross–section (i.e. the Rosenbluth separation) was to insure that the two interference terms, σ_{LT} and σ_{TT} completely cancel out for all of the kinematic settings measured. As shown by eq. (1.5) the two interference terms have respectively a $\cos\phi$, and a $\cos 2\phi$ dependence on the angle between the scattering and production planes. Depending on the size and shape of the angular coverage in ϕ, several scenarios were possible:

1 For complete 0–2π coverage in ϕ for all ε points , symmetric around $\theta_{\gamma K}$, the interference terms completely canceled out and one could proceed with the Rosenbluth separation.

2 For incomplete coverage in ϕ the interference terms would not cancel out (at least not completely) and one needed to estimate their contribution before proceeding further. This will tended to increase the size of the systematic uncertainty, as well as add some unwanted model dependence to the Rosenbluth separation (as our experimental knowledge of the interference terms was extremely poor, one would have had to rely on a theoretical model to get an estimate).

3 For cases where the ϕ coverage is complete (0–2π) but did not show circular symmetry around $\theta_{\gamma K}$ one had to either throw away some of the data to regain the conditions of point one or to again rely on a model to estimate the contribution of the interference terms in the unseparated cross-section.

In view of the above the $\theta_{\gamma K}$ and ϕ (or t and ϕ) coverage of the **E93-018** data was extensively studied. In Fig. 4.32 the results of such a study are shown for the $Q^2 = 1$ (GeV/c)^2 settings[16]. The experimental data is plotted as a function of $-t$ (the radius of the plot) and ϕ (the polar angle of the plot). The three panels correspond in order to the low-, middle-, and high- ε points measured. One can clearly see that there is complete ϕ coverage and that the data shows a nice circular symmetry. Also one might want to note that the t coverage is quite similar for all three ε points (so no artificial, data wasting, t cut

[16]Similar results, obtained for the other Q^2 settings, were left out due to space considerations.

need to be imposed). After ensuring the complete cancellation of the interference terms, the CM cross–sections measured at each Q^2 setting formed a system of linear equations as shown in (1.6). Since in **E93-018** three different ε points were measured for each Q^2 setting, this system is over-determined and a fitting algorithm was used to separate σ_L and σ_T.

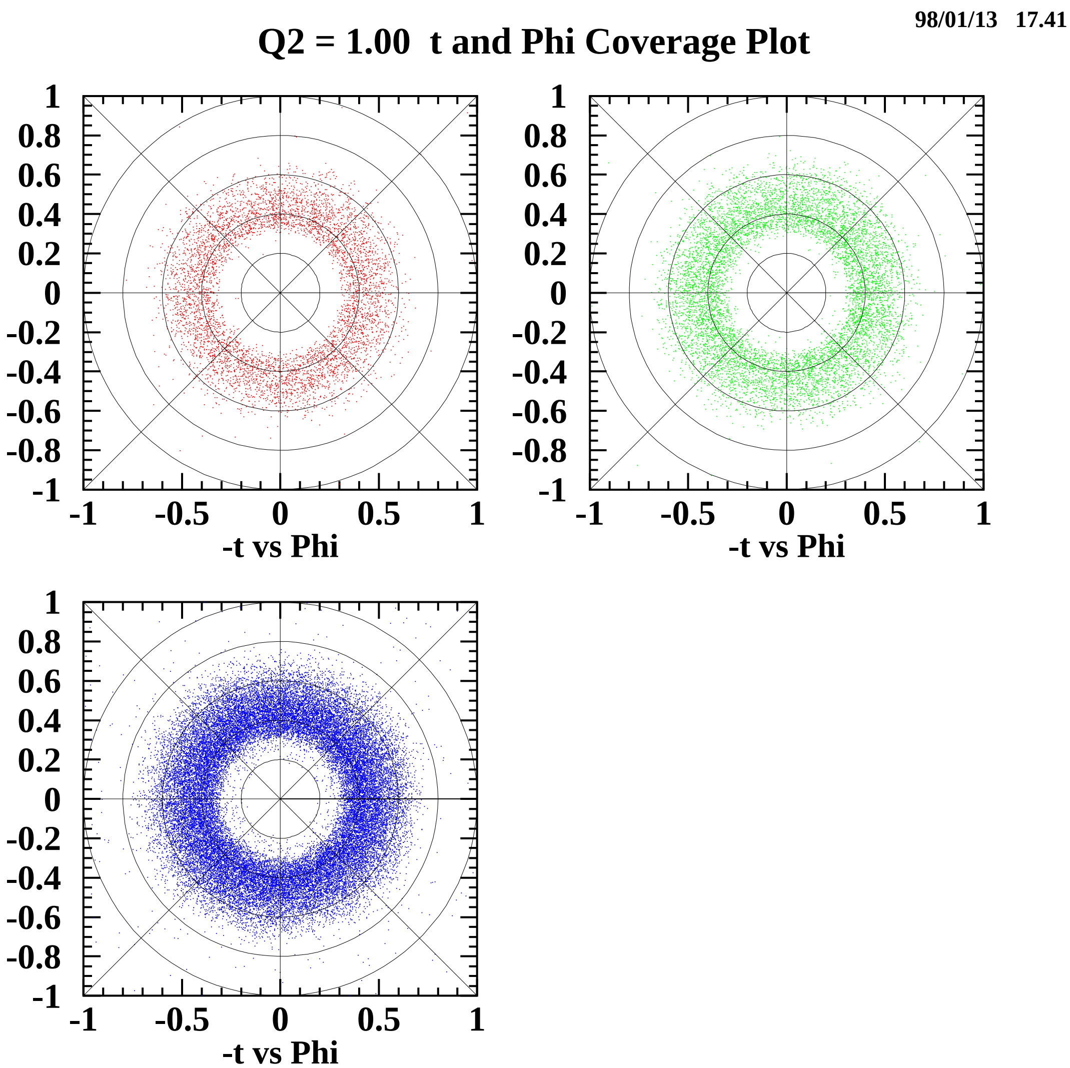

Figure 4.32: **E93-018** experimental ϕ and t coverage for the $Q^2 = 1$ (GeV/c)^2 kinematic points (for the Λ channel). The radius of the plot is $-t$ (GeV/c)^2 while the polar angle is ϕ. The three panels correspond, in order, to the low-, middle-, and high- ε points measured.

4.6 Error Analysis

This section provides an in-depth discussion of the various experimental and/or theoretical uncertainties that affect the physics analysis, in particular the extraction of the longitudinal and transverse parts of the cross-section, as well as on the ratio R $= \sigma_L/\sigma_T$.

4.6.1 Fitting and Data Modeling

The data analysis process often involves the fitting of experimentally measured dependent and independent quantities to one/several model(s). This subsection serves a dual purpose: first the (general) relevant mathematical apparatus is reviewed; then the focus of the discussion is shifted to the particular requirements/conditions of the **E93-018** analysis, namely the extraction of R from the experimental data.

Let (x_i, y_i) $i = 1, \ldots, N$, $i \in N^*$ be a set of measured quantities/set of data points. Let $y(x) = y(x; a_1, \ldots, a_M)$ be a generic model with $\{a_j\}$, $j = 1, \ldots, M$, $j \in N^*$ adjustable parameters. In general $N \geq M$, otherwise the system is underdetermined, i.e. the parameters of the model cannot be fixed from the experimental data (too few data points and/or too many parameters in the model).

What is needed is a method to find "fitted" values for a_j's using the available data. Instead of venturing in the most general answer to this problem (which would be the realm of *maximum likelihood estimators*), the discussion will continue in the framework of the "General Linear Least Squares" method. The crux of this approach is to restrict the form of the model M to:

$$y(x) = \sum_{k=1}^{M} a_k X_k(x) \tag{4.20}$$

where $X_1(x), \ldots, X_M(x)$ are arbitrary fixed functions of x, called *basis functions.* Note that the discussion is still very general because the term "linear" only refers to dependence (of the model) on the parameters a_j, the functions X_k can be highly non-linear functions of x. For this particular class of functions one can now form the merit function, χ^2

$$\chi^2 = \sum_{i=1}^{N} \Big[\frac{y_i - \sum_{k=1}^{M} a_k X_k(x_i)}{\sigma_i}\Big]^2 \tag{4.21}$$

where σ_i denotes the measurement error of the ith data point, presumed known[17]. Several techniques, like the "Normal Equations Method" or the "Singular Value Decomposition Method"[18] can be used to minimize χ^2.

4.6.2 Fitting to a Straight Line

A very particular and very simple choice of the fitting model is the straight-line model. Given a set of N data points (x_i, y_i) one simply wants to fit

$$y(x) = y(x; a, b) = a + bx \tag{4.22}$$

As before, the uncertainties σ_i[19] associated with the measurements y_i are assumed known and that the x_i's are known exactly. For this particular case χ^2 becomes

$$\chi^2 = \sum_{i=1}^{N} \Big[\frac{y_i - a - bx}{\sigma_i}\Big]^2 \tag{4.23}$$

χ^2 is minimized when its partial derivatives with respect to a and b vanish.

$$\begin{aligned} 0 &= \frac{\partial \chi^2}{\partial a} = -2 \sum_{i=1}^{N} \frac{y_i - a - bx_i}{\sigma_i^2} \\ 0 &= \frac{\partial \chi^2}{\partial b} = -2 \sum_{i=1}^{N} \frac{x_i(y_i - a - bx_i)}{\sigma_i^2} \end{aligned} \tag{4.24}$$

A more elegant expression of 4.24 can be obtained using the following quantities:

$$\begin{aligned} S \equiv \sum_{i=1}^{N} \frac{1}{\sigma_i^2} \quad S_x \equiv \sum_{i=1}^{N} \frac{x_i}{\sigma_i^2} \quad S_y \equiv \sum_{i=1}^{N} \frac{y_i}{\sigma_i^2} \\ S_{xx} \equiv \sum_{i=1}^{N} \frac{x_i^2}{\sigma_i^2} \quad S_{xy} \equiv \sum_{i=1}^{N} \frac{x_i y_i}{\sigma_i^2} \end{aligned} \tag{4.25}$$

[17] If measurement errors are not known, they may all be set to the constant value of $\sigma = 1$ and the procedure can be carried-out the same way; however the goodness-of-fit cannot be computed in such a case (the assumption that "the fit is good" is already made when fixing all errors constant).

[18] These, and other χ^2 minimization techniques, are extensively documented in many numerical methods books [52, 61].

[19] For normally distributed measurement errors this merit function will yield the maximum likelihood estimators for a and b; if errors are not normally distributed the estimations will not be maximum likelihood; however they may still be of some practical use.

With this notation eq. 4.24 becomes

$$\begin{aligned} aS + bS_x &= S_y \\ aS_x + bS_{xx} &= S_{xy} \end{aligned} \tag{4.26}$$

If one now introduces $\Delta \equiv SS_{xx} - (S_x)^2$ the solution of (4.26) is simply

$$\begin{aligned} a &= \frac{S_{xx}S_y - S_xS_{xy}}{\Delta} \\ b &= \frac{SS_{xy} - S_xS_y}{\Delta} \end{aligned} \tag{4.27}$$

Taking the derivatives of a and b with respect to y_i

$$\begin{aligned} \frac{\partial a}{\partial y_i} &= \frac{S_{xx} - S_xx_i}{\sigma_i^2\Delta} \\ \frac{\partial b}{\partial y_i} &= \frac{Sx_i - S_x}{\sigma_i^2\Delta} \end{aligned} \tag{4.28}$$

and summing over all data points one gets the variances in the estimates of a and b:

$$\begin{aligned} \sigma_a^2 &= S_{xx}/\Delta \\ \sigma_b^2 &= S/\Delta \end{aligned} \tag{4.29}$$

Of course, given the way they are computed, a and b are not independent and one can express their *covariance* (i.e. a measure of the correlation between a and b) as

$$Cov(a, b) \equiv -S_x/\Delta \tag{4.30}$$

To complete the discussion one additional number is needed, i.e. the "goodness-of-fit". This is the probability Q, of finding by chance a value of χ^2 as poor as the one given by eq. (4.23). In terms of the incomplete gamma function Γ_q one has

$$Q = \Gamma_q\Big(\frac{N-2}{2}, \frac{\chi^2}{2}\Big). \tag{4.31}$$

4.6.3 Error Matrix. Definition. Usage

In previous section(s) the basics of model fitting and error calculation were reviewed. Appropriate formulas were given for finding the set of parameters that minimize a certain merit function (namely χ^2) and their associated errors. This approach should be adequate for most simple situations.

In the analysis of nuclear/high-energy experimental data, however, one often encounters slightly more complicated situations: the number of dependent and/or independent variables, as well as the number of parameters in a theoretical model become (very) big (usually both can happen at the same time). In such a situation a matricial approach might be tried, defining the so-called "error matrix". Given a set of measured quantities $(x_1, x_2, \ldots, x_N)$, the corresponding uncertainties $(\sigma_1, \sigma_2, \ldots, \sigma_N)$, and the covariances $cov_{ij} \equiv cov(x_i, x_j)$, all presumed known, the error matrix is

$$\boldsymbol{M} = \begin{pmatrix} \sigma_1^2 & cov_{12} & cov_{13} & \ldots & cov_{1N} \\ cov_{12} & \sigma_2^2 & cov_{23} & \ldots & \ldots \\ \ldots & \ldots & \ldots & \ldots & \ldots \\ \ldots & \ldots & \ldots & \ldots & \sigma_N^2 \end{pmatrix}. \tag{4.32}$$

A couple of immediate observations can be made: first, the matrix $\mathbf{M}$ is symmetric, and second, for totally uncorrelated errors ($cov_{ij} = 0 \;\; \forall i, \;\; \forall j$) the matrix reduces to a diagonal matrix. The main situations where the use of the error matrix (4.32) is really useful are:

1. computing the uncertainty of any other quantity expressed as a function of $(x_1, x_2, \ldots, x_N)$,
2. changing to a new set of variables $(x'_1, x'_2, \ldots, x'_N)$,
3. computing the uncertainty of any quantity expressed as a function of the new set of variables $(x'_1, x'_2, \ldots, x'_N)$.

Case 1. Let $y = f(x_1, \ldots, x_N)$ be the quantity of interest. Let $\boldsymbol{D}$ be the vector holding the partial derivatives of f with respect to the parameters x_i,

$$\boldsymbol{D} = \left(\frac{\partial f}{\partial x_1} \quad \ldots \quad \frac{\partial f}{\partial x_N} \right), \tag{4.33}$$

and let $\boldsymbol{D^T}$ be its transpose. Then, for the uncertainty in y one has

$$\sigma_y^2 = \boldsymbol{D^T M D}. \tag{4.34}$$

Case 2. With the same notations as above, let now $\boldsymbol{M'}$ be the new error matrix, $\boldsymbol{T}$ the matrix transformation from the set (x_i) to the set (x'_i) and $\boldsymbol{T^T}$ its transpose. The following relation is true

$$\boldsymbol{M'} = \boldsymbol{T^T M T}. \tag{4.35}$$

Case 3. For any $y = g(x'_1, \ldots, x'_N)$ one can combine the results from 4.34 and 4.35 to get

$$\sigma_y^2 = \boldsymbol{D^T T^T M T D}. \tag{4.36}$$

4.6.4 Extraction of σ_L, σ_T, and R

As shown in previous chapter(s), under a well-defined set of assumptions, the total (CM) cross-section for the kaon electroproduction process can be written as

$$\sigma_{Total}^{CM} = \sigma_T + \varepsilon \sigma_L \tag{4.37}$$

Using the fitting techniques outlined above, one can extract the separated parts of the cross-section, σ_T and σ_L, out of the **E93-018** data. Another quantity of interest for the physics analysis and interpretation of the data is the ratio $R = \sigma_L/\sigma_T$. Because they are extracted through a fitting procedure, the final values for the quantities of interest (σ_L, σ_T, etc.) are dependent not only on the measured cross–section but also on the uncertainties in the cross–section measurement as well.

The sources of uncertainties in **E93-018** can be broken-down into three main types:

1 Random errors (these include statistical (counting) uncertainties as well as all random fluctuations in beam energy and position, target density, fiducial efficiencies, dead time, etc.),

2 Correlated systematic errors (these include all correction that are known to be correlated with one/more parameters that vary between the various ε settings considered in a fit). For example the errors associated with the absolute error on the central electron scattering angle will be highly correlated with the ε setting (via the rapidly varying Mott cross–section),

3 Scale–type systematic errors (these include all corrections that are identical for all ε points considered in a fit. An example of this would be the absolute normalization of the charge measurement, (most) of the decay correction,etc.).

The purely random uncertainties and the correlated errors propagate in the final answer using the so-called error matrix technique, outlined above. Note that for the correlated errors one needs to rely on the (presumed) known functional dependence in order to obtain the error on the unseparated cross–section. In the present analysis the two available models for the cross–section were used for this purpose.

The scale errors propagate directly into σ_T and σ_L, with no effect whatsoever in R [62] (thus making R the most precise quantity measured in this experiment). This is a great advantage, especially if one takes into account that the larger uncertainty sources in **E93-018** are of the scale type.

For the two variable case, say variables a and b, (4.32) becomes

$$M = \begin{pmatrix} \sigma_a^2 & cov(a,b) \\ cov(a,b) & \sigma_b^2 \end{pmatrix}. \tag{4.38}$$

One can use eq. (4.38) to evaluate the error on the extracted σ_L/σ_T ratio, R, by introducing $\partial R/\partial\sigma_L = 1/a$ and $\partial R/\partial\sigma_T = -1/a^2$. Carrying-out the necessary matrix manipulations and dividing in the end both sides with R^2 one gets:

$$\left(\frac{\sigma_R}{R}\right)^2 = \left(\frac{\sigma_a}{a}\right)^2 + \left(\frac{\sigma_b}{b}\right)^2 - \left(\frac{2cov(a,b)}{ab}\right) \tag{4.39}$$

This last relation was used throughout the present analysis to estimate the errors on R[20]. Table 4.8 summarizes the sources of systematic uncertainties for the present **E93-018**

[20] As an inside note one might note that in the present analysis the contribution of the covariance term was less than one percent for all cases.

$p(e, e'K^+)\Lambda$ analysis, the size of these uncertainties, as well as the mode(s) in which they were evaluated. While most of the entries in the table are self–explanatory, additional explanations might be needed for the uncertainties that appear here for the first time (and also to clarify some of the notations used in the table). Entries 1–5 in Table 4.8 are uncertainties that relate to the absolute knowledge of the kinematic parameters of the measurement. A model cross–section was used to estimate these uncertainties when allowing a 10^{-3} variation of the central HMS/SOS momenta and beam energy, and a one mr variation for the central spectrometer angles. Entry number nine, "Cblk", is the coincidence blocking, documented in section 4.4.3. Entry number 14 is the radiative correction (also previously explained). Entries 15 and 16 refer respectively to the subtraction of random coincidence and target wall contribution, while the "B.C." in entry 17 stands for "Bin Centering". In Table 4.6.4 the point–to–point systematic uncertainties (i.e. the quadratic sum of random and correlated uncertainties), and the statistical uncertainties are listed for all kinematic points measured during **E93-018** in the Λ channel.

4.7 Results

After having shown how to correctly identify the sample of coincident electron–kaon events, how to apply various cuts and correction factors, etc., in this section we present our results for kaon electroproduction in the $e + p \rightarrow e' + K^+ + \Lambda$ reaction.

4.7.1 Unseparated $(d\sigma/d\Omega)^{CM}$ Results

The main purpose of the present analysis was to separate the longitudinal and transverse parts of the kaon electroproduction cross–section in the $e+p \rightarrow e' + K^+ + \Lambda$ reaction via the Rosenbluth technique described in section 4.6. In Table 4.10 the unseparated cross–sections are shown for every Q^2 and ε combination measured[21]. Both the statistical and the point–to–point systematic uncertainties given in Table 4.10 are relative to the measured cross–section. An additional ~5% scale uncertainty needs to be added when quoting absolute values for the separated σ_L and σ_T values.

[21] The other kinematical quantities of interest not shown in Table 4.10 were listed earlier in Table 1.1.

#	Source of Uncertainty	Uncertainty Type and Value (%) Rand +Corr	Scale Type	Observations
1	Beam Energy	0.2-0.7	-	Allow 1.e-3 change from “nominal” value.
2	HMS Mom.	0.0-0.2	-	Allow 1.e-3 change from “nominal” value.
3	HMS Angle	0.3-1.0	-	Allow 1 mr change from “nominal” value.
4	SOS Mom.	0.1-0.3	-	Allow 1.e-3 change from “nominal” value.
5	SOS Angle	< 0.1	-	Allow 1 mr change from “nominal” value.
6	Acceptance	1.6-2.4	1.0	Data vs MC while varying cuts up to $\pm 20\%$.
7	HMS Eff.	0.5	-	Eff. vs Rate. Also run-to-run.
8	SOS Eff.	0.5	-	Eff. vs Rate. Also run-to-run.
9	Cblk	0.4	-	Cblk vs Total Rate. Residuals...
10	Dead Time	0.2	-	DT vs Rate. Also from redundant HMS/SOS info.
11	Decay	0.6	3.0	Monte Carlo of the decay in the hut...
12	Target	0.6	0.5	Luminosity scans; spread in I_{beam}.
13	Charge	0.5	1.0	BCM calibration; variations between BCM2 and BCM3.
14	Rad. Corr.	0.5	2.0	Data/MC for different M_x cuts (in the tail).
15	Random	-	0.5	Real/Random yields. Counts below Λ threshold.
16	MT Target	-	0.5	MT/LH2 yields. Counts below Λ threshold.
17	B.C.	0.3	2.0	Model diff. Also between kinematic points.
18	Other	-	...	
19	**TOTAL**	**2.1-3.0**	**6.0**	

Table 4.8: Summary of all sources of systematic uncertainty in the **E93-018** $p(e,e'K^+)\Lambda$ analysis. Error Types (by column): **Rand** - Random; **Corr** - Correlated; **Scale** - Scale Type.

ε	$Q^2 = 0.52$		$Q^2 = 0.75$		$Q^2 = 1.00$		$Q^2 = 2.00$	
	p-to-p	stat.	p-to-p	stat.	p-to-p	stat.	p-to-p	stat.
low-	2.1	1.3	2.2	1.4	2.7	1.6	2.8	2.0
mid-	2.2	1.1	2.2	0.9	2.8	1.4	2.9	1.9
high-	2.2	0.9	2.3	0.8	2.9	0.8	3.0	1.5

Table 4.9: Sources of uncertainty in the **E93-018** $p(e,e'K^+)\Lambda$ analysis. The p-to-p column includes (in quadrature) both the random point-to-point and the correlated point-to-point uncertainties, the stat. column represent the counting (statistical) uncertainties for each point. The overall scale uncertainty is ~ 5 %.

Q^2 $(\mathrm{GeV/c})^2$	ε	$(d\sigma/d\Omega)^{CM}$ (nb/sr)	$(\Delta\sigma/\sigma)_{\mathrm{stat}}$ (%)	$(\Delta\sigma/\sigma)_{\mathrm{syst}}$ (%)
0.52	0.55	452.2	1.3	2.1
0.52	0.77	497.2	1.1	2.3
0.52	0.87	536.8	0.9	2.2
0.75	0.46	287.7	1.4	2.2
0.75	0.72	340.5	0.9	2.2
0.75	0.83	358.2	0.8	2.3
1.00	0.38	249.7	1.6	2.7
1.00	0.67	272.0	1.4	2.8
1.00	0.81	299.3	0.8	7.0
2.00	0.37	90.8	2.0	2.8
2.00	0.48	98.3	1.9	2.9
2.00	0.62	101.6	1.5	3.0

Table 4.10: **E93-018** measured $e + p \rightarrow e' + K^+ + \Lambda$ unseparated cross–sections used for the Rosenbluth separations.

As an useful intermediate step (towards the Rosenbluth separation of the response functions) the present unseparated cross–section measurements were checked against the existing world data set for the $e+p \rightarrow e' + K^+ + \Lambda$ reaction (i.e. the data shown in 1.6). This comparison is shown in Fig. (4.33) where the CM (unseparated) cross–section is shown as a function of Q^2. Before commenting on the agreement or lack thereof between various data sets (including the present **E93-018** results), one needs to be reminded that there are a number of rather important assumptions/approximations that need to be made in order to obtain Fig. 4.33:

(a) In order to compare data from different experiments (**E93-018** included), the results had to be extrapolated to a common kinematic point. Following the precedent set by Bebek et al in [2] all data shown in Fig. 4.33 were extrapolated to W = 2.15 GeV. This W extrapolation is based on the assumption (experimentally verified by the photoproduction data [63, 64]) that all relevant matrix elements are W–independent, thus, the only W dependence of the CM cross–section arises simply from the phase–space integration. While there is general agreement on the need to extrapolate the data (in W),

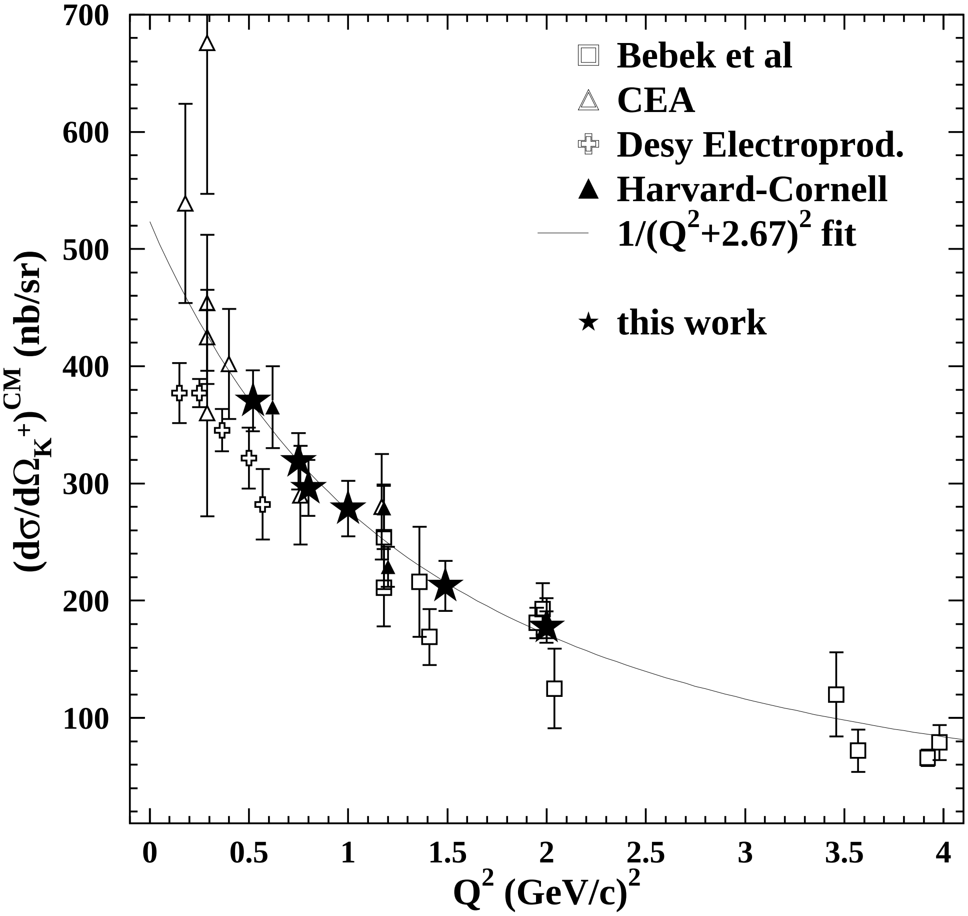

Figure 4.33: The Q^2 dependence of the unseparated (CM) differential cross–section for the reaction $e + p \rightarrow e' + K^+ + \Lambda$, as measured during **E93-018** (star symbols) and in previous data (rectangle, cross, open and filled triangle symbols). The curve shown is an eye–guiding, dipole fit through the **E93-018** data points.

various groups disagree on how this should be achieved: some groups favor a "theoretical" extrapolation based on the phase–space considerations outlined above [21, 2, 22] and use

$$\frac{\vec{p}_{K^*}}{W(W^2 - m_p^2)} \tag{4.40}$$

(here m_p is, as before, the proton mass and $\vec{p}_{K^*}$ the kaon momentum in the CM frame) to scale the data, while other groups rely on the measured W–dependence of their own data (so a more "experimental" approach) for the W extrapolation [24, 20]. As the W coverage of the **E93-018** data was very limited, the W–dependence of eq. 4.40 was used.

(b) The **E93-018** data was also extrapolated in t using an exponential function as indicated in [45]. This t extrapolation of the cross–section might seem somewhat counter–intuitive at first, if one assumes measurements are made at $t_{\rm min}$. However, in practice, in order to perform any measurement, one needs a non–zero phase–space. This means one has to integrate over a region around $\theta^* = 0°$ (in other words over some t bin, not centered, but at best bounded at one edge by $t_{\rm min}$):

$$\int_{t_{\rm min}}^{t_1} \frac{d\sigma}{dt} dt = (t_1 - t_{\rm min}) \frac{d\sigma}{dt}(\tau) \tag{4.41}$$

with $\tau \in (t_{\rm min}, t_{\rm max})$. As kaon electroproduction experiments are typically statistics–limited, the temptation is to make larger rather than smaller bins, thus approximating τ by $t_{\rm min}$ is not a good choice; therefore the need to extrapolate in t (alternatively one can simply quote the θ^* interval for each data point - as was done in earlier experiments [2, 22, 24], thus leaving the t setting undefined).

(c) Lastly, for the **E93-018** data at Q^2 = 0.52, 0.75, 1.00, and 2.00 (GeV/c)^2, only the high–ε points are shown in Fig. 4.33 (to match as closely as possible the existing data which was taken, almost exclusively, at high ε). The Q^2 = 0.8 (GeV/c)^2 point is a limited statistics run (i.e. $\sim$ 2.5 hours of beam time) measured, as feasibility study, in the spring of 1996, during (and courtesy of) the Jefferson Lab E91-013 experiment (spokesperson D. F. Geesaman), while the Q^2 =1.5 (GeV/c)^2 entry represents one of the test settings measured during the detector check–up phase of **E93-018** . The error bars shown represent the total uncertainties (i.e. the sum in quadrature of the statistical, point–to–point, and scale-type uncertainties).

Bearing in mind the three caveats listed above, one finds a good agreement between existing data and the current **E93-018** measurement. The data, as a whole, shows a pronounced decrease of the cross–section with increasing Q^2. To emphasize this trend, an eye–guiding, dipole–type fit, $1/(2.67+Q^2)^2$, through the **E93-018** data is also shown in Fig. 4.33. More importantly, the uncertainties of the present measurement are lower, or at least they are at the same level with those of the world data set. Furthermore, for the **E93-018** data, the biggest contribution to the uncertainties shown in Fig. 4.33 is the overall normalization (scale) error, which has minimal impact in the σ_L and σ_T uncertainties (and will not affect at all the σ_L/σ_T ratio).

4.7.2 σ_L, σ_T, and R Results

As was repeatedly mentioned earlier, the Rosenbluth separation of the longitudinal and transverse parts of the kaon electroproduction cross–section in the $e + p \rightarrow e' + K^+ + \Lambda$ reaction is the first step towards a more in–depth testing of the various theoretical models available. Using the techniques outlined in section 4.6 for the result $d\sigma/d\Omega^* = \sigma_T + \varepsilon\sigma_L$, all the ε points measured for each Q^2 setting were fit to a line. The slope of this line yields the value of σ_L while the intercept at the origin (i.e. ε=0) represents the transverse part of the cross–section, σ_T. The results of these fits are shown in Fig. 4.34 (Q^2 = 0.52, and 0.75 (GeV/c)^2), and in Fig. 4.35 (Q^2 = 1.0, and 2.0 (GeV/c)^2). The extracted σ_L, σ_T, and R values, as well as their total absolute uncertainties are summarized in Table 4.11. The last column of Table 4.11 lists the χ^2 per degree of freedom for each fit. For both Fig. 4.34 and Fig. 4.35 the inner error bars represent the total point–to–point uncertainties (i.e. the sum in quadrature of the counting and point–to–point systematic uncertainties), while the outer error bars represent the total absolute uncertainty (i.e. the scale uncertainties added in quadrature to the total point–to–point uncertainties)[22]. Note that, as shown section 4.6, only the point–to–point uncertainties need to be taken into account in the

[22]The systematic uncertainty assigned to the low–ε point at Q^2 =1.00 (GeV/c)^2 is larger (compared to the other data points) due to the large uncertainty in the total charge. The source of this large uncertainty is the sensitivity of the Hall C BCM electronics to temperature variations, coupled with the failure of the electronics room air conditioning system during the time this kinematic point was measured.

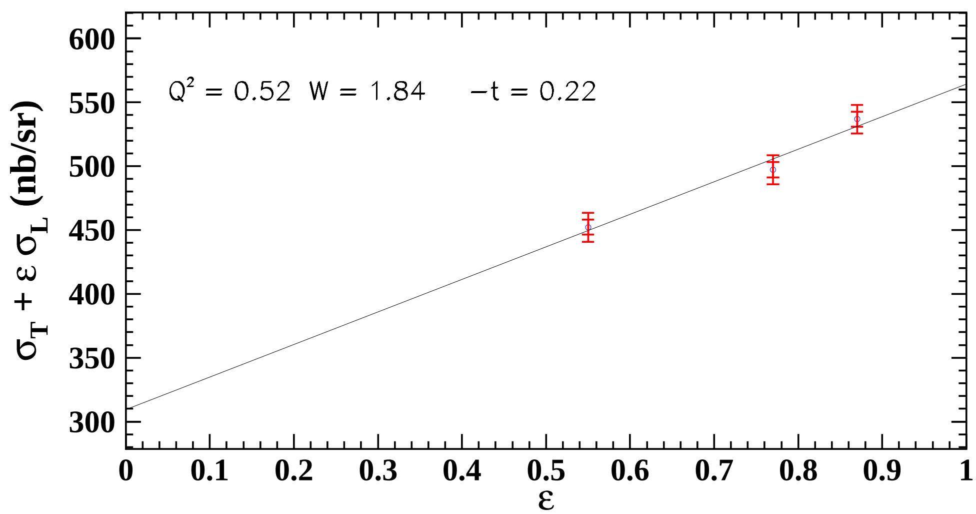

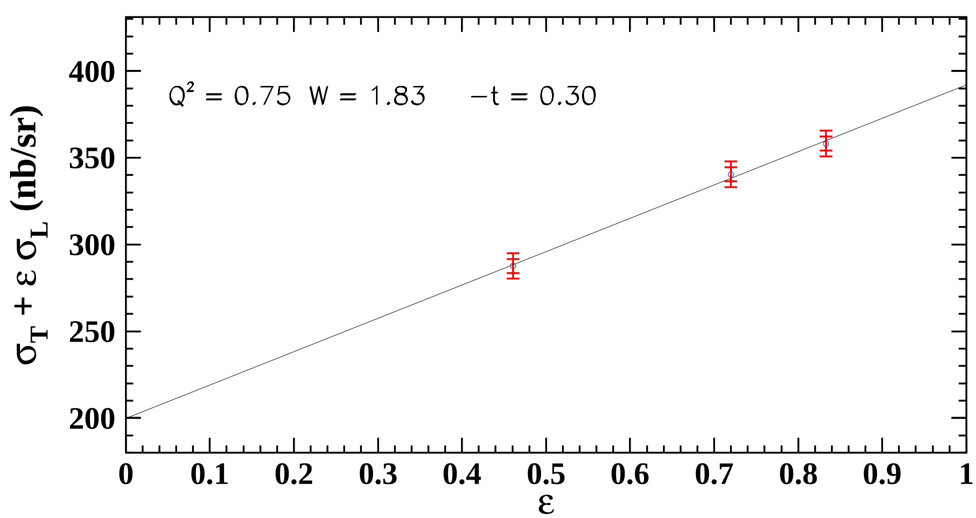

Figure 4.34: Rosenbluth separations for the $Q^2 = 0.52$ and 0.75 $(\mathrm{GeV/c})^2$ settings measured in the **E93-018** experiment.

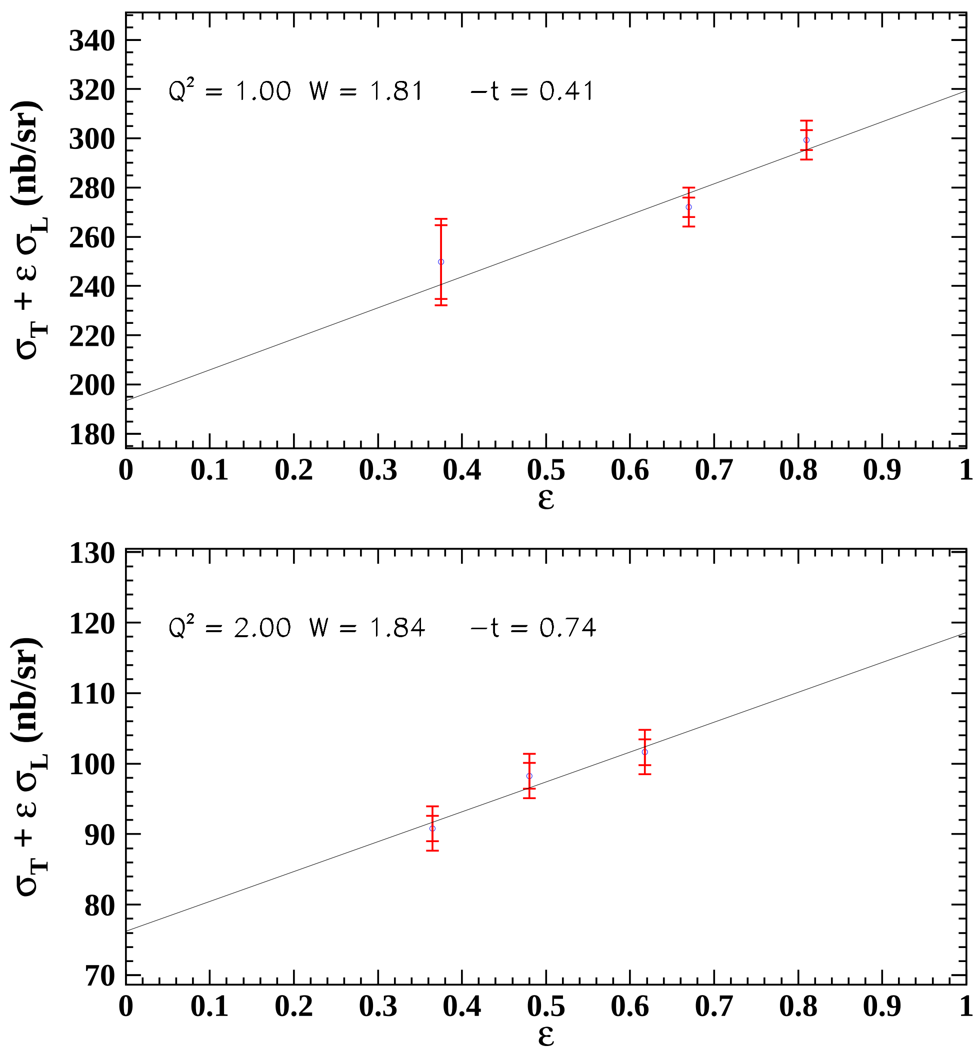

Figure 4.35: Rosenbluth separations for the $Q^2 = 1.00$ and 2.00 (GeV/c)^2 settings measured in the **E93-018** experiment.

Q^2 $(GeV/c)^2$	σ_T [nb/sr]	σ_L [nb/sr]	R	$\chi^2/D.F.$
0.52	309.6 ± 39.0	254.6 ± 50.2	0.82 ± 0.18	0.864
0.75	199.9 ± 21.2	192.0 ± 29.0	0.96 ± 0.16	1.625
1.00	193.4 ± 38.3	125.9 ± 51.2	0.65 ± 0.29	1.048
2.00	76.2 ± 9.6	42.4 ± 18.0	0.56 ± 0.24	0.432

Table 4.11: Separated transverse and longitudinal cross-sections, and their ratio (and their uncertainties) for the $^1H(e, e'K^+)\Lambda$ process as measured in Experiment E93-018. The uncertainty quoted is the total absolute uncertainty. The last column shows the χ^2 per degree of freedom for each fit.

fitting procedure. Then the scale uncertainty is added (in quadrature) to the σ_L and σ_T errors from the fit. As the fitting procedure typically finds $\sim 20\%$ (sometimes larger) uncertainties for the separated cross–sections, the influence of the scale uncertainty in the final $\Delta\sigma_L$ and $\Delta\sigma_T$ is minimal. The additivity property of χ^2 [62] was used to check the validity of the L/T fits. The combined χ^2 from all four Rosenbluth separations shown in Fig. 4.34 and 4.35 is 3.97, for 4 degrees of freedom (i.e. $4 \times 3 - 4 \times 2 = 12 - 8 = 4$), giving an excellent χ^2 per degree of freedom (χ^2/D.F. $= 0.99$). While the relatively low value of χ^2/D.F. reflects a conservative estimate of the systematic uncertainties, one might want to note that in recently published work involving Rosenbluth separations (mainly in DIS experiments) global χ^2/D.F. values as low as 0.9 [62] (for the L/T separation in SLAC DIS data on hydrogen) or even 0.7 [65] are quoted.

In the context of the present **E93-018** analysis it has been speculated that the SOS (i.e. kaon arm) acceptance uncertainties need to be excluded from the point–to–point uncertainties used in the L/T fit, because the hadron arm momentum was kept fixed for all ε settings measured for a given Q^2. However, the y_{tar} acceptance of the spectrometer changes from setting to setting (because the central SOS angle changes) and, given the y'_{tar}–y_{tar} and x'_{tar}–y_{tar} correlations [66], it is impossible to study separately only the y_{tar} dependence of the acceptance function, especially given the limited amount of y_{tar} calibration data available. Thus, as shown in the Monte Carlo simulation section, separate acceptance functions were generated for each setting and the total (i.e. full contributions from both the HMS and the SOS acceptances) acceptance uncertainty was used, even though it leads to a slight overestimate of the point–to–point uncertainties (thus the smaller χ^2).

The separated σ_L values are shown in Fig. 4.36 as a function of Q^2, while in Fig. 4.37 the Q^2 dependence of the transverse cross–section, σ_T, is shown. Both σ_L and σ_T show a pronounced, hyperbola–like decrease with Q^2. While the Q^2 behavior of σ_T is expected (after all, extrapolating σ_T in Q^2 values should lead to the photoproduction cross–section in the limit $Q^2 \to 0$), the Q^2 dependence of σ_L is somewhat puzzling: Given its definition σ_L should equal zero for $Q^2 = 0$ (GeV/c)^2 (i.e. real photons have no longitudinal polarization). L/T measurements at Q^2 values below 0.5 (GeV/c)^2 are required to pin down this expected rise of the longitudinal part of the cross–section with increasing Q^2. In both Fig. 4.36 and Fig. 4.37 a number of theoretical curves are also shown. The thin curves correspond to the Saclay–Lyon model, in its 1996 version [1], the medium thickness lines correspond to the latest Williams, Ji and Cotanch calculation (WJC) [67], while the thicker curves correspond to the Regge model of Vanderhaeghen, Guidal and Laget (VGL98) [17, 18, 19]. In practice the WJC curves had to be scaled up by a factor of ~ 4.5 [23].

As it can be seen in Fig. 4.36, the SL model shows a flat σ_L vs Q^2 dependence (after the initial rise from $Q^2 = 0$ predicted by all models), completely missing the trend shown by the experimental data. The latest WJC calculation, shows a pronounced rise of σ_L then a gradual decrease with increasing Q^2, in good agreement with the data. The VGL model shows a similar Q^2 dependence as the WJC model, although the maximum is not as pronounced. While it is clear that the latest WJC calculation provides the best agreement with the σ_L data, the Regge model also provides a good description of the experimental points, whereas the SL model completely misses the Q^2 behavior of the longitudinal cross–section. It is worth mentioning that, in this latest WJC model shown in Fig. 4.36, Williams and collaborators, among other improvement of their model, changed their kaon (and K^*) propagators from Feynman– to Regge–poles. Given this

[23] This is partially explained by the slight difference in the definition of σ_L and σ_T as used in the WJC calculations.

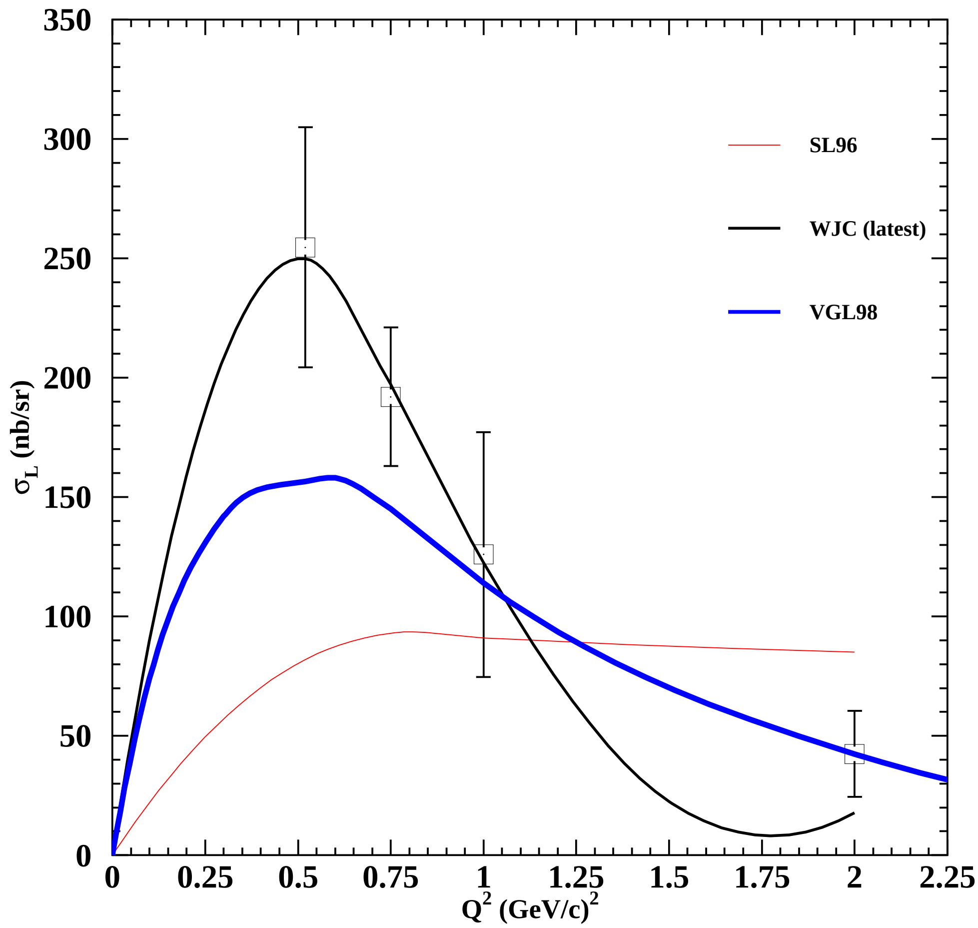

Figure 4.36: Q^2 dependence of the longitudinal cross–section, σ_L. Calculations based on the Saclay–Lyon (SL96), VGL (VGL98), as well as the latest WJC model are also shown (see text for details).

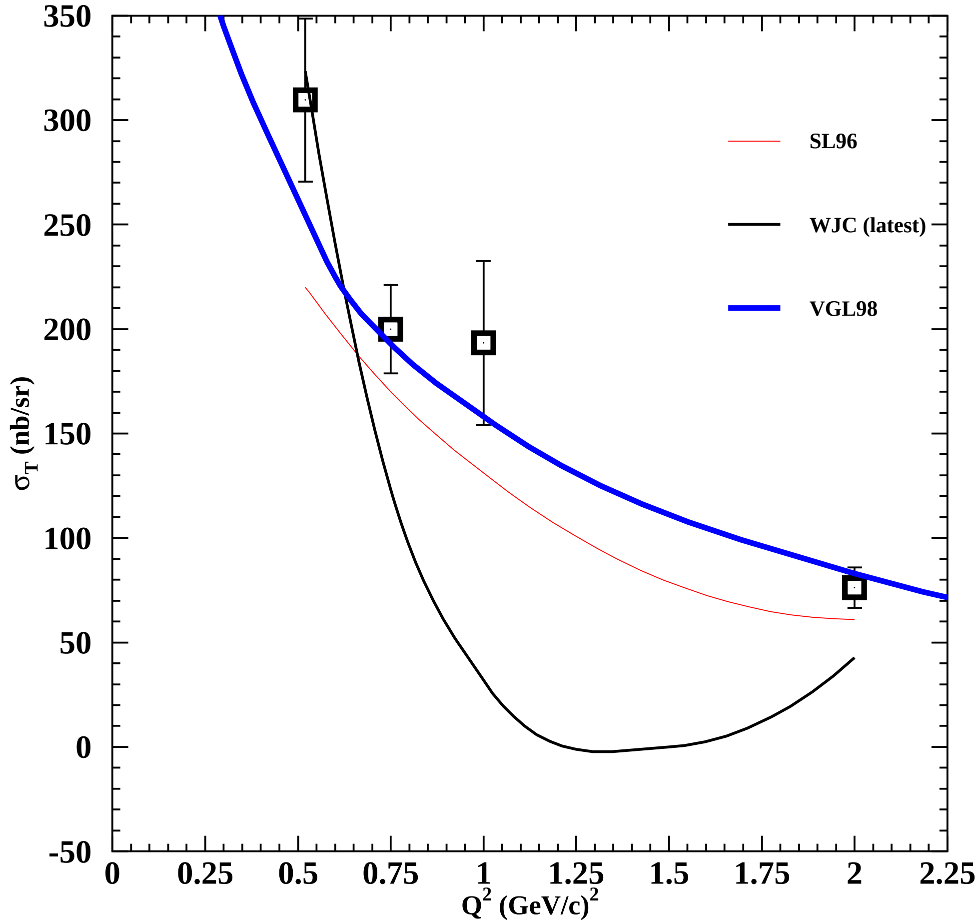

Figure 4.37: Q^2 dependence of σ_T, as measured during **E93-018** . Three model calculations are shown for comparison. Notations are the same as in Fig. 4.36.

remark and also considering that one expects σ_L to be dominated (at least at low t values) by the kaon exchange term; it seems that, in the Q^2 range studied in **E93–018**, a model using Regge–type poles (for the K^+ exchange) is likely to provide a more accurate description of the σ_L data rather than a model using Feynman–type poles.

For σ_T it is rather hard to *a priori* predict which type of process(es) will tend to dominate a given Q^2 range. Certainly the K^* exchange is expected to play a role, as do the various s–channel resonance exchange terms. Examining the curves in Fig. 4.37 one finds that the WJC calculation greatly undershoots the data, whereas both the SL and the VGL models correctly reproduce the Q^2 behavior of σ_T (the SL curve seems to be systematically lower by $\sim 15\%$ but it is still consistent with the data within the experimental uncertainties). Considering that the main difference between the WJC and the SL models is the inclusion of resonances up to spin 5/2 in the latter (whereas the former stops at spin 3/2 resonances), it seems likely that the higher mass/spin resonances have a sizeable contribution in σ_T. According to Regge theory, all the resonances lying on the n trajectory are included in the VGL model, which is, possibly, why the VGL model provides the best description of the σ_T data.

Considering both the σ_L and the σ_T data simultaneously, one finds that overall the Regge model provides the best representation for the separated cross–sections, while the two isobaric models shown fall short either in describing σ_L (SL model) or σ_T (WJC model).

It has been advocated [1] that the σ_L/σ_T ratio, R, is the best quantity in which to perform data versus model comparisons. Experimentally, R is insensitive to some of the larger sources of uncertainty (i.e. scale–type errors), while theoretically it was shown that in R the sensitivity to some important quantities, such as the form factor, is maximized. In particular, for the present **E93-018** analysis, a model–dependent extraction of the form factor is possible just by studying R.

In Fig. 4.38 the R results of the present analysis are plotted alongside the earlier measurements of Bebek et al. [21][24]. In contrast with the Bebek et al. measurement,

[24] As a word of caution, in performing their L/T separation, Bebek et al. used, for their high-ε point, both proton and deuteron data to increase statistics. Thus, technically, the present measurement is the

the uncertainties of the present **E93-018** data are significantly smaller (by a factor of $\sim 3)^{25}$. The present data extends the world knowledge of the σ_L/σ_T ratio towards lower values of Q^2, more than doubling the number of data points (i.e. from 3 to 7). Given the precision of the data and the range in Q^2 covered by the present measurement (and also taking into account the $Q^2 = 3.5$ (GeV/c)^2 Bebek point), one begins to distinguish a certain Q^2 behavior for R, namely it increases (from zero, see earlier discussion on σ_L), then gently flattens out in the $Q^2 = 0.75$–1.0 (GeV/c)^2 region, then decreases with increasing Q^2.

Several theoretical calculations for R are shown in Fig. 4.38. The isobaric models are shown with thin lines as follows:

- Solid line, label: WJC (old) – an older Williams, Ji, and Cotanch calculation based on the model developed in [48];

- Dashed line, label: SL – the Saclay–Lyon model (1996 version) as described in [1];

- Dotted line, label: BMH – the model due to Bennhold and collaborators;

- Dash–dotted line, label: WJC (new) – the latest WJC model (including the Reggeization of the kaon poles, as explained earlier).

With thicker lines three different predictions of the Regge model of Laget et al. (i.e. the VGL model) are shown. The differences between these lines are solely due to the differences in the *ansätze* used for the K^+ and K^* form factor parameterizations. The numbers shown next to each line correspond to the values (in GeV/c) of the cutoff parameter Λ used in the monopole–type parameterizations of the K^+ and K^* form factors (recall that the VGL model uses $1/(1+Q^2/\Lambda^2)$ for the K^2 and K^* form factors). The Q^2 dependence of the ratio R seen in the data is very well reproduced by the Regge model prediction whereas the isobaric models (WJC (old), SL) show a continuous increase of

first L/T separation in the $e + p \to e' + K^+ + \Lambda$ reaction.

[25] Note that in order to accommodate the size of the error bars for the highest Q^2 point of the old measurement, the vertical scale had to be extended to unphysical negative values of R.

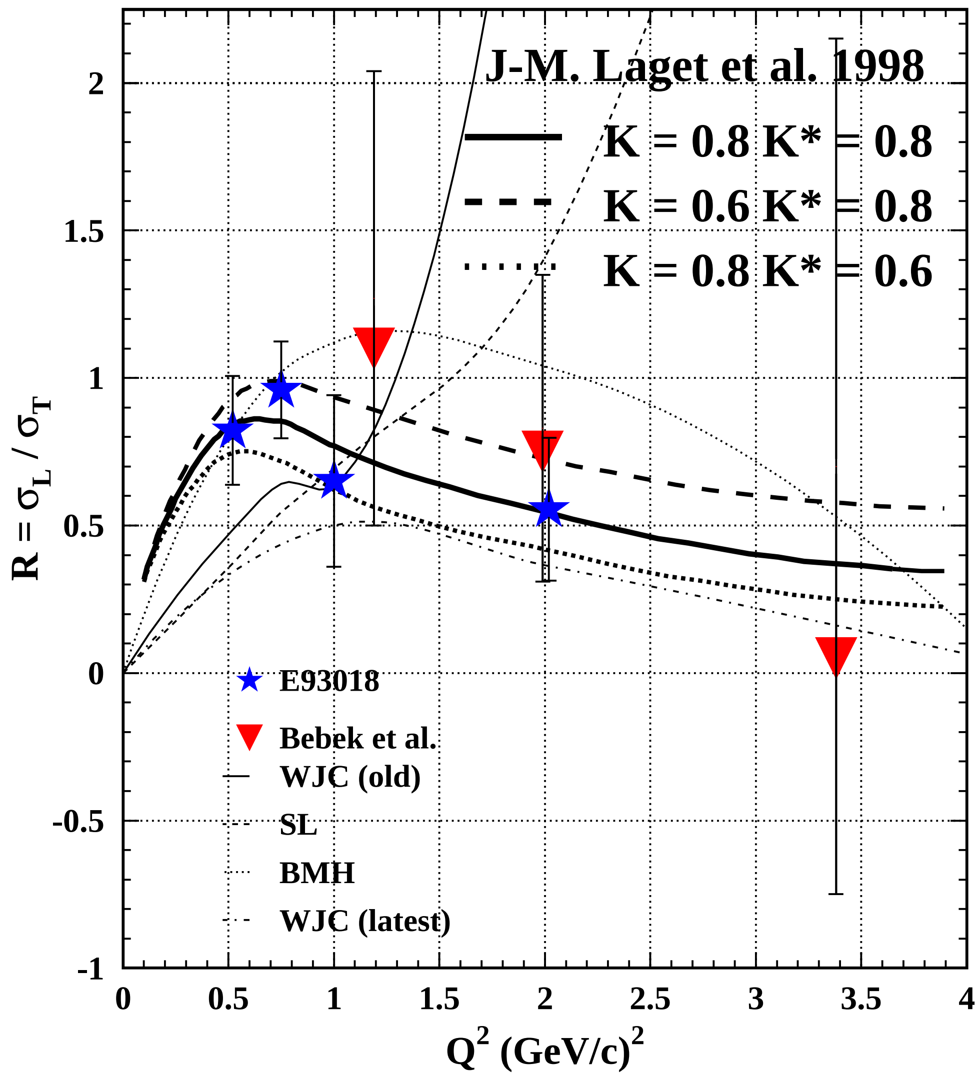

Figure 4.38: Q^2 dependence of the ratio σ_L/σ_T=R. Isobaric model calculations are shown for two versions of the WJC model, the SL and the BMH models (thin lines), as are three different variations of the VGL Regge model (thick lines). See text for more in–depth explanations.

R with Q^2. The BMH [16] model is somewhere in the middle, showing an almost flat[26] (perhaps slightly dipping) evolution in Q^2, although it too misses high (at about the 1 σ level) the larger Q^2 experimental points. While the newer WJC calculation reproduces well the Q^2 trend of the data, this model seems to be systematically lower than the data (perhaps due to the σ_T discrepancy discussed above).

While one cannot make the claim that the present data completely rejects the isobaric models discussed (after all, both the isobaric models and the Regge models try to achieve the same thing: take into account high mass, high–spin resonances as intermediate states, although they accomplish this task in different ways), the precision of the present measurement requires at least a revision of the basic assumptions and ingredients used in the isobaric calculations. Some possible explanations for the discrepancies observed could be related to:

- The particular way in which the gauge invariance is restored in the isobaric models. As the kaon exchange diagram is known not to be gauge invariant, the particular way in which gauge invariance is restored (i.e. adding diagrams in the s channel) can be a source of trouble.

- The behavior of the kaon (or K^*, K^1) form factors might differ in reality from the parameterizations considered in the models.

- As most of the coupling constants involved are poorly known, depending on their relative strength, the contribution of the K^* ($K1$) exchange (especially for large t's) might be larger/smaller than previously thought. Tests conducted with the WJC model in which the K^* exchange was turned "off" resulted in an even more dramatic increase of R with Q^2.

- The branching ratios of various resonances to decays in strange fragments are also poorly known. Thus, one can easily overestimate/underestimate the contribution of one or more resonances to the total cross–section.

[26] While R is plotted in Fig. 4.38 up to values of Q^2 of 4 (GeV/c)^2, all comments are based only on the Q^2 range measured during **E93–018**.

- Relating to the previous point and perhaps more exciting is the possibility that the effects seen arise from the contribution of previously unknown resonances (i.e. the so–called missing resonances) that might have significant $K^+\Lambda$ branching ratios [68].

As the isobaric models involve fitting several[27] (highly) non–linear parameters using old data that is very scarce and carries, for the most part, large error bars, there is the general danger of running into severe computing problems (i.e. "converging" to an artificial, local minimum, instead of the absolute minimum) that might limit the reliability and predictive power of the isobaric models.

Finally, one can interpret Fig. 4.38 as a model–dependent way of gaining knowledge on the kaon form–factor, $F_{K^+}(Q^2)$ in the following way: Assume one focusses on a model that seems to reproduce well the experimental data. Within the confines of the chosen model, one can then vary only the parameter(s) used for the kaon (K^*, $K1$, if applicable) form factor to obtain different theoretical predictions. The "ansatz" which results in the best match between experiment and theory can be interpreted as a model–dependent extraction/measurement of the kaon form factor.

For the **E93-018** data shown in Fig. 4.38, and choosing VGL model[28], one finds the curve with $\Lambda_{K^+} = \Lambda_{K^*} = 0.800$ GeV/c as the best match for the experimental data. As the other two VGL curves also reproduce the data reasonably well, a ~ 20 % uncertainty should be associated with the quoted value of Λ_{K^+}.

4.7.3 Preliminary t–Dependence Results and The Kaon Form Factor

Besides the kinematics shown in Table 1.1, in the second part of the **E93-018** experiment, $(e, e'K^+)$ data was acquired for three Q^2 settings around $Q^2 = 1.0$ (GeV/c)^2, aiming to study the t dependence of the cross–section. Similar to the L/T study discussed above, for each Q^2 setting, measurements were undertaken for three different ε values. The

[27] 8 to 20 or more parameters, depending on the particular model/reaction studied.

[28] Note that we do not endorse here the Regge model as "right", just that it "fits well" the data.

Q^2 $[GeV/c]^2$	E_e $[GeV]$	$E_{e'}$ $[GeV]$	p_k $[GeV/c]$	θ_e $[°]$	θ_γ $[°]$	W $[GeV/c]$	ε	x	$-t$ $[GeV/c]^2$
1.25	3.245	1.244	1.385	32.31	16.80	1.84	0.59	0.33	0.47
1.25	3.545	1.544	1.385	27.65	18.21	1.84	0.66	0.33	0.47
1.25	4.045	2.044	1.385	22.42	19.88	1.84	0.75	0.33	0.47
1.00	3.245	1.278	1.430	28.43	16.00	1.89	0.62	0.27	0.34
1.00	3.545	1.578	1.430	24.41	17.19	1.89	0.69	0.27	0.34
1.00	4.045	2.078	1.430	19.86	18.66	1.89	0.77	0.27	0.34
0.75	3.245	1.329	1.440	24.07	15.06	1.93	0.65	0.21	0.24
0.75	3.545	1.629	1.440	20.76	15.95	1.93	0.72	0.21	0.24
0.75	4.045	2.129	1.440	16.97	17.20	1.93	0.79	0.21	0.24

Table 4.12: Nominal (central) values of the kinematic variables for Experiment' **E93-018** t–dependence study.

relevant kinematics are shown in Table 4.12 while the preliminary results of this analysis are discussed below. Assuming that at low t the cross–section is dominated by the kaon exchange diagram (the so–called pole domination), it can be shown [69] that the longitudinal part of the cross–section is, at the kaon pole ($t = m_K^2$), proportional to

$$\sigma_L \simeq \frac{-2tQ^2}{(t - m_K^2)^2} k(eg_{K\Lambda N})^2 F_K^2(Q^2) \tag{4.42}$$

where k is a kinematic factor, e is the fine structure constant, $g_{K\Lambda N}$ is the coupling constant for the KΛN vertex, and F_K is the kaon form factor. If one were to measure/separate σ_L for a range of t values at constant Q^2, then, the extrapolation of the data to the kaon pole[29] should yield a measurement of the (squared) kaon form factor (of course after the removal of all other dependences shown in eq. (4.42)).

In Fig. 4.39 the CM unseparated cross–section for the $e + p \to e' + K^+ + \Lambda$ reaction is shown, as a function of t, for the high- (squares), middle- (crosses), and low- (stars) values of ε measured at $Q^2 = 0.75$ (GeV/c)^2 (i.e. the last three kinematics shown in Table 4.12). The horizontal error bars reflect the size of the binning in t (bin centering was performed, as explained in the data analysis chapter, within each t bin). The fact that the CM cross–section shows a steep rise with decreasing (in absolute value) t is generally interpreted [70]

[29] This technique (and its variations) are generally known as the Chew–Low extrapolation technique.

as a sign of the (kaon) pole dominance, while other authors [18] claim that even values of t as high as 2 GeV^2 should be usable for form factor extraction. As equation (4.42) requires the knowledge of σ_L as a function of t, Rosenbluth separations were performed for every t bin. Due to the fact that the $\Delta\varepsilon$ range available in this t–dependence study were relatively small, the $\Delta\sigma_L$ uncertainties are sensibly larger than those quoted in Table 4.11 for the first part of the experiment, at about the 30–40 % level. The original analysis plan was to combine all t–dependence data around $Q^2 = 1$ $(\text{GeV/c})^2$ (extrapolating in Q^2 using the formulas shown, for example, in [45]) to obtain a reasonably large set of (σ_L,t) pairs (eventually increasing the t range as different Q^2 settings overlap only partially in t), then perform the Chew–Low extrapolation to the pole and extract the form factor. However this approach presented two major problems:

(a) Combining different settings involves extrapolating in Q^2 according to some function. As part of the Q^2 dependence (at least) of the cross–section is expected to arise from the kaon form factor, it has been argued that the use of a Q^2–dependent extrapolating function already implies some knowledge of the form factor. This problem can be "solved" by iterating the analysis until the kaon form factor extracted from the Chew–Low extrapolation and the one implied by the extrapolating function become consistent.

(b) Second, and perhaps more important, is the observation that some of the quantities present in eq. 4.42 are not so well known. Specifically, the value of the $g_{K\Lambda N}/4\pi$ coupling constant, as quoted by various groups [1], could be as low as 0.51 or as high as 4.17, almost an order of magnitude variation. In principle it is agreed (see the introduction part for the general requirements for kaon photo- and electroproduction models) that the SU(3) prediction (-3.7) should be respected at the $\pm$ 20 % level. As one order of magnitude theoretical uncertainty in the extraction of the form factor was deemed unacceptable, a more viable analysis technique was sought.

The solution to the two problems listed above, as implemented in the present analysis is shown in Fig. 4.40: The top two panels show the measured t dependence of σ_L for two different Q^2 settings (0.75 and 1.00 $(\text{GeV/c})^2$). The corresponding (σ_L, t) pairs are listed in Table 4.13. The lines shown are the best linear fit through the experimental data (second and third order polynomials were tried, but the χ^2/D.F. obtained in each case

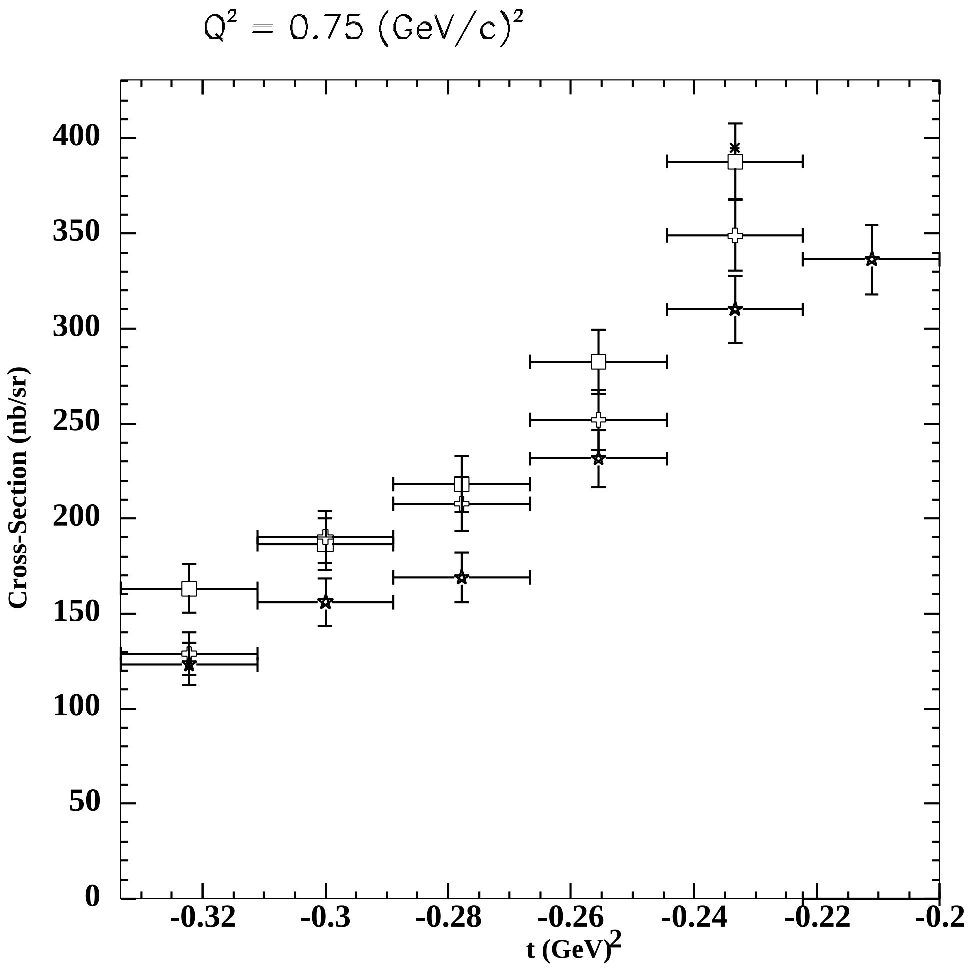

Figure 4.39: The t dependence of the CM (unseparated) cross–section for the $e + p \to e' + K^+ + \Lambda$ reaction. The three distributions shown correspond to the low- (stars), middle- (crosses), and high- ((squares) ε settings measured for $Q^2 = 0.75$ (GeV/c)^2.

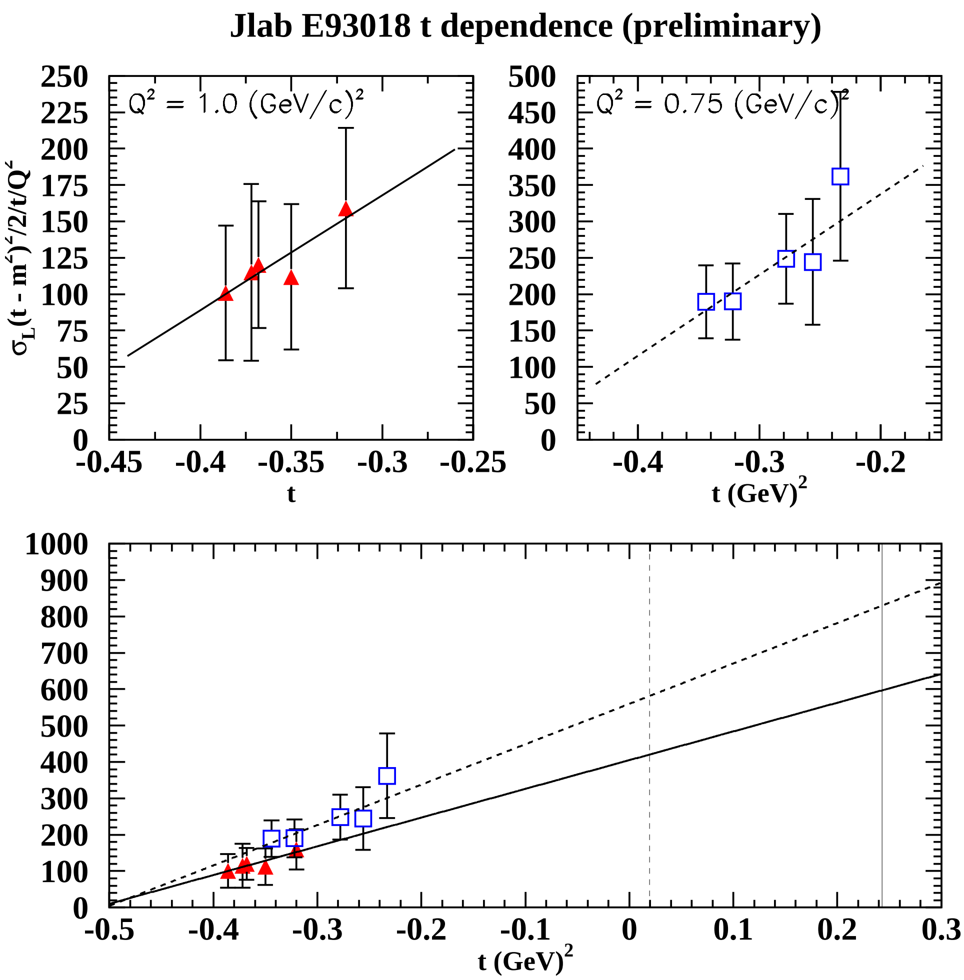

Figure 4.40: Chew–Low extrapolation technique used for the extraction of the kaon form factor. The top two panels show $\sigma_L(t - m_K^2)/2/t/Q^2$ as a function of t for $Q^2 = 1.00$ (GeV/c)^2 (left panel) and for $Q^2 = 0.75$ (GeV/c)^2 (right panel). The curves shown are the best linear least square fits through the data. The bottom plot illustrates the extrapolation of the fitted curve to the kaon pole ($t = m_K^2$).

Q^2 $(\mathrm{GeV/c})^2$	t $(\mathrm{GeV})^2$	$\sigma_L \pm \Delta\sigma_L$ (nb/sr)
0.75	-0.344	283.0 ± 75.0
0.75	-0.322	286.8 ± 79.0
0.75	-0.278	381.0 ± 94.8
0.75	-0.256	375.9 ± 132.8
0.75	-0.233	556.9 ± 178.4
1.00	-0.386	196.2 ± 90.0
1.00	-0.372	225.8 ± 119.1
1.00	-0.368	236.5 ± 85.8
1.00	-0.350	222.3 ± 99.1
1.00	-0.320	320.6 ± 111.2

Table 4.13: Extracted σ_L values used in the t extrapolation.

was larger than that of the linear fit). Note that the quantity shown on the vertical scale is the product $\sigma_L(t-m_K^2)/2/t/Q^2$, i.e. only the well known dependences[30] were removed from eq. (4.42). In the bottom plot of Fig. 4.40 the extrapolation in t of the linear fits to the kaon pole is shown. The intercept of the fitting curve at the kaon pole $(t = m_K^2)$ should be $\simeq k(eg_{K\Lambda N})^2 F_K^2(Q^2)$. Taking the ratio of these intercepts, r_{pole}, all the dependences will cancel out, except for the form factor. Thus, effectively, r_{pole} equals the ratio of the kaon form factors, evaluated for the two Q^2 points:

$$r_{\mathrm{pole}} = \frac{F_K^2(0.75)}{F_K^2(1.00)} \tag{4.43}$$

Assuming a monopole–type parameterization for the kaon form–factor (consistent with the VGL model used in the previous section to extract a model–dependent kaon form factor), $F_K^2(Q^2) = 1/(1+Q^2/\Lambda_{K^+}^2)$, the Λ cutoff parameter was calculated using the intercept ratio shown in Fig. 4.40. The value obtained[31], $\Lambda_{K^+}^{\mathrm{t-dep.}} = 820$ Mev/c, is **consistent** with the model–dependent extraction of the kaon form factor shown in the previous

[30]The fine structure constant is also well known but for convenience it was not divided out from the data.

[31]The superscript on the Λ parameter merely flags the fact that this result came from the t–dependence data of **E93–018**.

(sub)section. The uncertainty in $\Lambda_{K^+}^{\mathrm{t-dep.}}$ is at the $\pm$ 20 % level, due mainly to the small range in ε available for the Rosenbluth separation (used to obtain σ_L) and also to the limited range in t spanned by the **E93-018** data. Figure 4.41 expands the Q^2 scale of Fig. 4.41 to show both the old Amendolia et al. [3] data, as well as the present result. The solid, dashed, and dotted curves shown are three parameterizations for the form factor due to Ji and Cotanch [71]; namely a relativistic quark model prediction (solid line), a vector meson dominance model (dashed line) based on ρ exchange, and another vector meson dominance model (dotted line) that includes Φ exchange. The dashed–dotted curve shown is a prediction of the gauge invariant, covariant model of Buck, Williams, and Ito [72] that makes use of solutions of the coupled Bethe–Salpeter and Dyson–Schwinger equations.

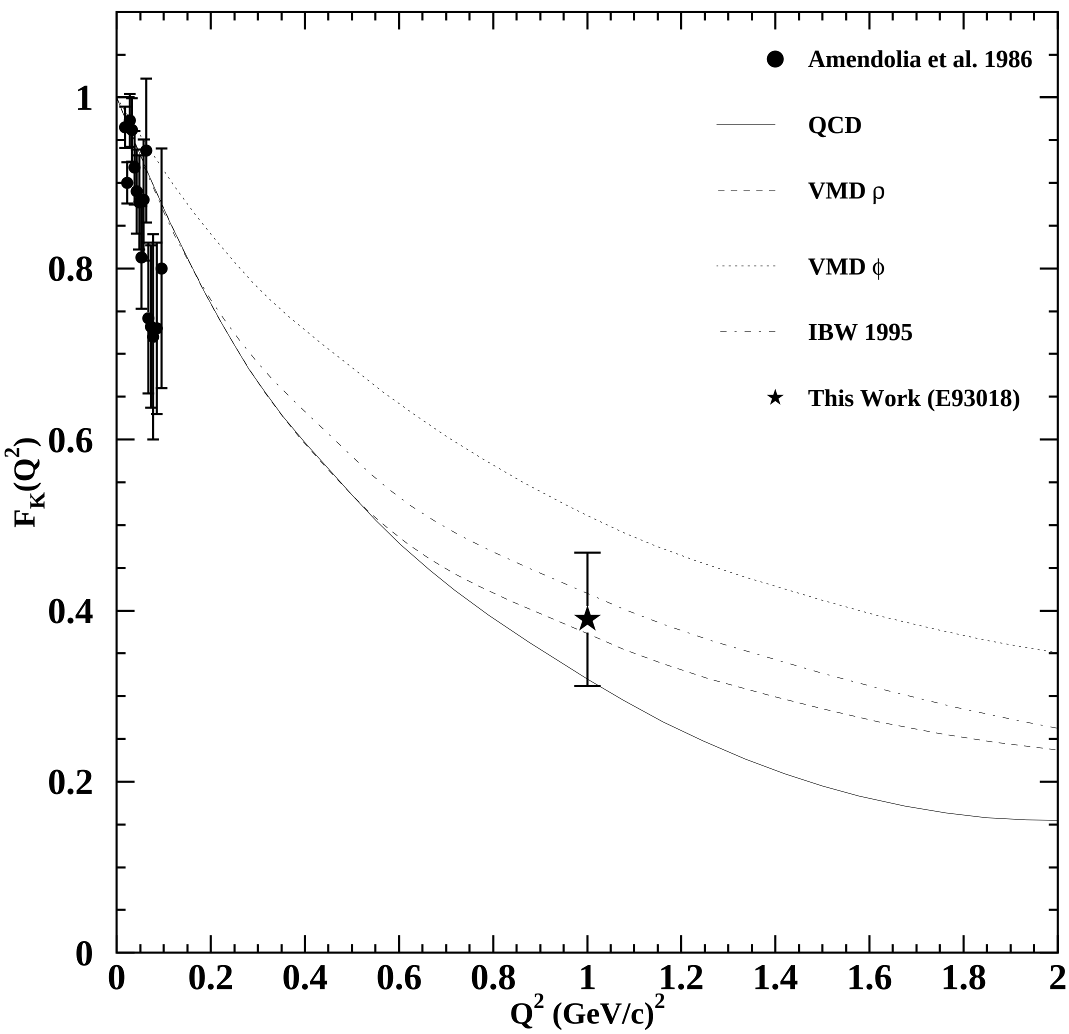

Figure 4.41: Kaon form factor as a function of Q^2. The present extraction of $F_{K^+}(Q^2)$ is shown at $Q^2 = 1.0$ (GeV/c)^2 (whereas the data at $Q^2 < 0.1$ (GeV/c)^2 is from [3]). The four curves represent different parameterizations of the kaon form factor (see text for details).

SUMMARY AND CONCLUSIONS

The $e + p \to e' + K^+ + \Lambda$ reaction was studied as a function of the four momentum transfer, Q^2, and the virtual photon polarization, ε. For four selected Q^2 settings in the 0.5–2.0 $(\mathrm{GeV/c})^2$ range the longitudinal and the transverse components of the cross–section were separated via the Rosenbluth technique[1] with a good precision in σ_L and σ_T. The t–dependence of the cross–section was studied for values of Q^2 around 1.0 $(\mathrm{GeV/c})^2$.

Extensive comparisons between the present data and various isobaric and Regge model predictions were made in terms of σ_L, σ_T, and their ratio, R. Several discrepancies between data and theoretical calculations were thus revealed. This prompted several groups to reconsider and review the basic assumptions and input parameters (form factors, coupling constants, etc.) of their models.

The kaon form factor F_{K+} was extracted in two independent ways:

(a) by varying the form factor parameterization of a model describing reasonably well the L/T data (model dependent extraction);

(b) by extrapolating the measured t dependence of the cross–section to the kaon pole via a variation of the Chew–Low extrapolation technique.

The results of the two extractions were shown to be consistent with each other within their respective uncertainties.

[1]Considering the earlier note regarding the use of deuterium data by Bebek et al. for their lower ε points, the present analysis truly constitutes the world's *first* L/T separation in the $p(e, e'K^+)\Lambda$ reaction, thus the "first" appearing in the title of this work.

While the current **E93-018** analysis revealed discrepancies with some of the existing models and served to correct them (as well as constrain future models), the available data is not enough to unambiguously identify the source(s) of these discrepancies. Kaon electro– and photoproduction experiments expanding and enlarging the scope of the present measurement are approved for running at Jefferson Lab, and at other laboratories throughout the world (GRAAL, MAMI, etc.).

Appendix A

PATHLENGTH CORRECTION PARAMETERIZATIONS

The pathlength corrections are designed to account for the difference between the central ray through a spectrometer and a given ray. A more detailed discussion about the usefullness of pathlenght corrections is given in [44]. The pathlength corrections, as implemented in the Hall C `Engine`, are parameterized in terms of the focal plane quantities as follows [1]:

```
*
*  New Pathlength corrections
*

*** HMS ***
      new_hpath= 12.462*hsxpfp+0.1138*hsxpfp*hsxfp-0.0154*hsxfp
     &     -72.292*hsxpfp**2-0.0000544*hsxfp**2-116.52*hsypfp**2
*
*** SOS ***
      new_spath= 2.923*ssxpfp - 6.1065*ssxpfp**2 + 0.006908*ssxfp
     &  *ssxpfp+0.001225*ssxfp -0.0000324*ssxfp**2 -21.936*ssypfp**2
*
```

[1]Using “standard” Hall C notations as explained in [41].

Appendix B

LIST OF COINCIDENCE NTUPLE VARIABLES

The full list of the coincidence varibles used in the present analysis is given here. Notations and units for the different variables are as defined in [41].

```
   subroutine c_Ntuple_init(ABORT,err)
*----------------------------------------------------------------------
*
*     Purpose : Books an COIN Ntuple; defines structure of it
*
**********begin insert description of contents of COIN tuple ******
...
     c_Ntuple_tag(m)= 'cointime'      ! Corrected Coincidence Time
      c_Ntuple_tag(m)= 'beamx'        ! Beam X Position
      c_Ntuple_tag(m)= 'beamy'        ! Beam Y Position
      c_Ntuple_tag(m)= 'beamxp'       ! Beam X Angle
      c_Ntuple_tag(m)= 'beamyp'       ! Beam Y Angle
      c_Ntuple_tag(m)= 'hsxfp'        ! HMS Focal Plane x (cm)
      c_Ntuple_tag(m)= 'hsyfp'        !  y (cm)
      c_Ntuple_tag(m)= 'hsxpfp'       ! xprime
      c_Ntuple_tag(m)= 'hsypfp'       ! yprime
      c_Ntuple_tag(m)= 'ssxfp'        ! SOS Focal Plane x (cm)
      c_Ntuple_tag(m)= 'ssyfp'        ! y (cm)
      c_Ntuple_tag(m)= 'ssxpfp'       ! xprime
      c_Ntuple_tag(m)= 'ssypfp'       ! yprime
      c_Ntuple_tag(m)= 'hsytar'       ! HMS Target
      c_Ntuple_tag(m)= 'hsxptar'      !
```

```
      c_Ntuple_tag(m)= 'hsyptar'      !
      c_Ntuple_tag(m)= 'hsdelta'      !
      c_Ntuple_tag(m)= 'ssytar'       ! SOS Target
      c_Ntuple_tag(m)= 'ssxptar'      !
      c_Ntuple_tag(m)= 'ssyptar'      !
      c_Ntuple_tag(m)= 'ssdelta'      !
      c_Ntuple_tag(m)= 'hcer_npe'     ! HMS Particle Id.
      c_Ntuple_tag(m)= 'hsshtrk'      !
      c_Ntuple_tag(m)= 'hsprtrk'      !
      c_Ntuple_tag(m)= 'hsbeta'       !
      c_Ntuple_tag(m)= 'hsdedx1'      !
      c_Ntuple_tag(m)= 'scer_npe'     ! SOS Particle Id.
      c_Ntuple_tag(m)= 'saer_npe'     !
      c_Ntuple_tag(m)= 'ssshtrk'      !
      c_Ntuple_tag(m)= 'ssprtrk'      !
      c_Ntuple_tag(m)= 'ssbeta'       !
      c_Ntuple_tag(m)= 'ssdedx1'      !
      c_Ntuple_tag(m)= 'charge'       ! Charge of last Scaler Event
      c_Ntuple_tag(m)= 'eventID'      ! CODA event ID#

***********end insert description of contents of COIN tuple********
...
      RETURN
      END
```

Bibliography

[1] J. C. David et al., Phys. Rev. C **53**, 2613 (1996).

[2] C. J. Bebek et al., Phys. Rev. D **15**, 594 (1977).

[3] S. R. Amendolia et al., Phys. Lett. B **178**, 435 (1986).

[4] J. D. Walecka, Invited talk, The Niels Bohr Institute, Copenhagen, 1993.

[5] G. D. Rochester and C. C. Butler, Nature **160**, 855 (1947).

[6] F. Halzen and A. D. Martin, *Quarks and Leptons* (John Wiley & Sons, 1984).

[7] M. Gell-Mann, Phys. Lett. **8**, 214 (1964).

[8] G. Zweig, CERN Technical report CERN–TH–412 , CERN, 1964.

[9] R. A. Adelseck and B. Saghai, Phys. Rev. C **42**, 108 (1990).

[10] J. Cohen, Int. J. Mod. Phys. **A4**, 1 (1989).

[11] W. E. Kleppinger and J. D. Walecka, Ann. Phys. **146**, 349 (1983).

[12] S. Nozawa and T. S. H. Lee, Nucl. Phys. (1990).

[13] O. K. Baker, Jefferson Lab. E93–018 Proposal, 1993.

[14] R. A. Williams, C. R. Ji, , and S. R. Cotanch, Phys. Rev. C **46**, 1617 (1992).

[15] R. A. Williams, C. R. Ji, and S. R. Cotanch, Phys. Rev. C **43**, 452 (1991).

[16] T. Mart, C. Bennhold, and C. E. Hyde-Wright, Phys. Rev. C **51**, R1074 (1995).

[17] M. Guidal, J. M. Laget, and M. Vanderhaeghen, Phys. Lett. B **400**, 6 (1997).

[18] M. Guidal, J. M. Laget, and M. Vanderhaeghen, Nucl. Phys. **A627**, 645 (1997).

[19] M. Vanderhaeghen, M. Guidal, and J. M. Laget, Phys. Rev. C **57**, 1454 (1998).

[20] P. Brauel, Ph.D. Dissertation, Hamburg, 1978.

[21] C. J. Bebek et al., Phys. Rev. D **15**, 3082 (1977).

[22] C. J. Bebek et al., Phys. Rev. D **17**, 1693 (1978).

[23] C. N. Brown et al., Phys. Rev. Lett. **28**, 1086 (1972).

[24] P. Brauel et al., Z. Phys. C **3**, 101 (1979).

[25] P. Gueye, M. Tiefenback, and C. Yan, CEBAF Internal Report, 1997 (unpublished).

[26] G. Niculescu, CEBAF Internal Report, 1995 (unpublished).

[27] J. Cobb and J. Murray, Nucl. Instrum. Meth. **46**, 99 (1967).

[28] M. Berz, Technical report MSUCL–977, Michigan State University, 1995 (unpublished).

[29] J. R. Arrington, Ph.D. Dissertation, Caltech, 1998.

[30] K. A. Assamagan, D. Dutta, and P. Welch, CEBAF Internal Report, 1996 (unpublished).

[31] O. K. Baker et al., Nucl. Instrum. Meth. **A367**, 92 (1995).

[32] J. Litt and R. Meunier, Ann. Rev. Nucl. Sci. **23**, 1 (1973).

[33] R. Smythe, CEBAF Technical report, 1995 (unpublished).

[34] P. B. Cushman, *Instrumentation in High Energy Physics* (World Scientific, 1993).

[35] C. A. Heusch, Nucl. Inst. Meth. **A248**, 157 (1986).

[36] H. Mkrtchyan, Private communication, 1996.

[37] G. Hayes et al., in *Proc. of the TOOLS 8 Conference* (Prentice Hall, 1992).

[38] G. Hayes et al., in *Proc. of the CHEP Conference* (edited by S. Loken, 1994).

[39] D. Abbott et al., in *Proc. of the IEEE Conference on Real-Time Computer Applications in Nuclear, Particle, and Plasma Physics* (edited by R. Fox, 1995).

[40] *, Introduction to Q, LAMPF Technical report, 1972 (unpublished).

[41] D. F. Geesaman and S. Wood, Hall C internal report, 1994 (unpublished).

[42] I. Niculescu, Hall C internal report, 1997 (unpublished).

[43] I. Niculescu, Ph.D. Dissertation, Hampton University, expected 1999.

[44] G. Niculescu, CEBAF Internal Report, 1996 (unpublished).

[45] T. Angelescu et al., Fizika B **5**, 113 (1996).

[46] N. C. R. Makins, Ph.D. Dissertation, MIT, 1994.

[47] M. Gary and W. Krumpelmann, Z. Phys. A **322**, 689 (1985).

[48] R. A. Williams, Ph.D. Dissertation, North Carolina State University, 1993.

[49] R. Ent, Private communication, 1996.

[50] L. W. Mo and Y. S. Tsai, Rev. Mod. Phys. **41**, 205 (1969).

[51] H. Ackermann et al., Nucl. Phys. B **137**, 294 (1978).

[52] W. H. Press et al., *Numerical Recipes* (Cambridge University Press, 1996).

[53] J. Allison, Comp. Phys. Comm. **77**, 377 (1993).

[54] *, Phys. Rev. D **50**, 1173 (1994).

[55] E. Hwang, Master's Thesis, Hampton University, 1991.

[56] A. Kerman, H. McManus, and R. Thaler, Ann. Phys. **8**, 551 (1959).

[57] W.Weise, Il Nuovo Cimento **102A**, 265 (1989).

[58] R. A. et al., Phys. Rev. D **4**, 3235 (1971).

[59] J. Reinhold, Private communication, 1998.

[60] K. Gustafsson, CEBAF Internal Report (unpublished).

[61] G. E. Forsythe, M. A. Malcolm, and C. B. Moler, *Computer Methods for Mathematical Computations* (Prentice–Hall, NY, 1977).

[62] L. W. Whitlow, Technical report, SLAC–357, 1990 (unpublished).

[63] T. Azemoon et al., Nucl. Phys. B **39**, 413 (1972).

[64] A. M. Boyarski et al., Phys. Rev. Lett **22**, 1131 (1969).

[65] S. Dasu et al., Phys. Rev. D **49**, 5641 (1990).

[66] J. Cha, Ph.D. Dissertation, Hampton University, expected 1999.

[67] R. A. Williams, Private communication, 1998.

[68] K. Hicks and M. Mestayer, Jefferson Lab **E93–030** proposal, 1993.

[69] D. Mack, Jefferson Lab **E93–021** proposal, 1993.

[70] R. C. E. Devenish and D. H. Lyth, Phys. Rev. D **5**, 47 (1972).

[71] C. R. Ji and S. R. Cotanch, Phys. Rev. D **41**, 1449 (1990).

[72] W. W. Buck, R. A. Williams, and Hiroshi Ito, Phys. Lett B **351**, 24 (1995).

Appendix C

VITA

Gabriel Niculescu was born in Bucharest, Romania, on November 15, 1966, as the first child of Niculae and Florica Niculescu. He graduated from the Mathematics and Physics High School No. 3 in June 1985, and, after accomplishing his military duties, became a physics student at Bucharest University, Bucharest, Romania, in the Fall of 1986. In 1989 he was married to Maria Ioana Niculescu (formerly Beşliu). In the Summer of 1991 he received his "engineer physicist" diploma (Master's equivalent) from Bucharest University. In 1992 he began his graduate studies at Hampton University, Hampton, Virginia, from which he received his Ph. D. degree in December 1998. He and his family currently live in Newport News, Virginia.